MAGNETIC FIELD SENSOR UTILIZING MAGNETO IMPEDANCE IN THIN FILM MULTI-LAYERS

by

PAUL DELOOZE

Thesis submitted to the University of Plymouth

in partial fulfilment for the degree of

DOCTOR OF PHILOSOPHY

2007

ABSTRACT

MAGNETIC FIELD SENSOR UTILIZING MAGNETO IMPEDANCE IN THIN FILM MULTI-LAYERS

Since the discovery of the Magneto Impedance (MI) effect in 1994 there has been a global increase in the research devoted to understanding the effect. In certain magnetic materials, the impedance change, often referred to as the MI ratio, is in the range of 50 to 100% for an excitation current in the MHz frequency range for external magnetic fields of a few Oe. The use of thin film multilayer structures allows the increase of sensitivity and the reduction of size for MI effect to be integrated with micro magnetic sensor technologies.

In the present work, we explain the origins of the MI effect and its versatile nature for the development of sub nano Tesla magnetic field sensors. The matrix like nature of the MI effect allows a variety of MI characteristics to be implemented in a thin film, which allows the structure to be tailored for maximum sensitivity in the chosen field sensing application.

In the case of a simple transverse magnetic anisotropy, the diagonal components of the MI matrix are symmetric and the off diagonal components are anti-symmetric with respect to the dc longitudinal field. The asymmetry in the MI behaviour can be related to either a certain asymmetric arrangement of the dc magnetization (crossed anisotropy), or a contribution to the measured voltage due to the ac cross-magnetization process, which is represented as an off-diagonal component.

These asymmetrical characteristics are useful in producing linear bi-directional field sensors without DC biasing. In attempt to find optimal film systems with respect to relative impedance change, sensitivity, linearity, operational frequency range, and dimensions, thin film multi-layers, consisting of a magnetic / conductor / magnetic material configuration were fabricated. Variations in magnetic compositions, geometries, structures and magnetic configurations (transverse, longitudinal or cross anisotropy) and additional insulations layers were produced.

Planar coil thin film multi-layers were constructed to utilize the more magnetic complex asymmetric characteristics of the MI effect. An experimental configuration was developed in order to measure all components of the MI matrix within the thin films and standardise their sensitivity using the MI ratio.

Two sub nano Tesla magnetic field sensors were developed during the course of this work based on the fabricated thin films. The first sensor concentrates on utilizing two asymmetrical Magneto Impedance (AMI) elements combined differentially. The sensor is driven by a sinusoidal current of 90 MHz biased with a dc bias current. For AMI film element of 5mm long, 40μm wide and having anisotropy angle of 45° the field detection resolution is in the magnitude of 1μ Oe for both ac and dc for fields of ~ 2Oe magnitude. The maximum response speed is in the order of 1MHz. The use of MI to the measurement low frequency fields such as bio-medical signals drove the design of the second sensor.

Extensive research was undertaken to improve the phase noise of the oscillator and sensitivity of the detection mechanism using novel RF techniques to improve the sensitivity at high frequencies, and secondly a method to improve the low frequency sensitivity by AC biasing the MI element with a magnetic field.

A thin film multilayer MI sensor was produced based on the measurement of the modulation of the incident reflected power due to an external AC magnetic field. Direct field measurement performance at 1kHz produced a resolution of 3.73×10^{-7} Oe, AC biased performance at 5kHz of a 20Hz field was a resolution of 5.27×10^{-6} Oe, and at 10Hz of 9.33×10^{-6} Oe. With continued improvement of the electronic components utilized in this novel method of Magneto Impedance sensor presented in this work, the possibility of measuring bio magnetic signals of the human body at room temperature becomes a distinct reality.

AUTHOR'S DECLARATION

At no time during the registration for the degree of Doctor of Philosophy has author been registered for any other University awards.

Authors study and research were financed with the aid of a studentship from an EPSRC award scheme from 03/2002 – 03/2005. A programme of advanced study was undertaken including a list of guided reading and advanced thematic seminars in the measuring techniques and magnetic sensors.

The work contained in this thesis was presented at several international conferences and thematic schools. Four papers have been published in research journals.

Number of words in this thesis is **46970** .

Signature:

Date: _____01.04.2007_____

List of Published papers:

[1]   P. Delooze, L. V. Panina, D. J. Mapps, K. Ueno, and H. Sano, *"CoFeB-Cu layered film with crossed anisotropy for asymmetrical magneto impedance"* IEEE Trans. Magn. vol. 39, pp. 3307–3309, Sept. 2003.

[2]   P. Delooze, L. V. Panina, D. J. Mapps, K. Ueno, and H. Sano, *"Effect of transverse magnetic field on thin-film magneto impedance and application to magnetic recording"*, Elsevier Science, 2003.

[3]   P. Delooze, L. V. Panina, D. J. Mapps, K. Ueno, and H. Sano, *"Sub-nano tesla resolution differential magnetic field sensor utilizing asymmetrical magnetoimpedance in multilayer films"* IEEE Trans. Magn. vol. 40, pp. 2664–2666, July. 2004.

[4]   P. Delooze, L. V. Panina, D. J. Mapps ,*"AC biased sub-nano-tesla magnetic field sensor for low-frequency applications utilizing magneto impedance in multilayer films"* IEEE Trans. Magn. vol. 41, pp. 3652 - 3654, 2005.

Conference attended:

CNRS Thematic school *"High sensitive magnetometer"*, November 4th - 8th 2002, PortBail, France.

The IEEE International Magnetics Conference, Intermag 2003, March 30th – April 3rd 2003, Boston, Massachusetts.

9th Joint MMM / IEEE International Magnetics Conference, Intermag 2004, January 5th – January 9th 2004, Anaheim, California.

The IEEE International Magnetics Conference, Intermag 2005, April 4th – April 8th 2005, Nagoya, Japan.

ACKNOWLEDGEMENTS

TABLE OF CONTENTS

TABLE OF FIGURES

Chapter 1. Introduction

Miniature magnetic-sensor technology is a rapidly growing industry. Sensitive and rapid-response sensors are in great demand for advanced intelligent measurement and control systems. This demand has been satisfied in some areas by magneto-resistance (MR), giant magneto-resistance (GMR), fluxgate and other technologies [1]-[3]. A relatively new magnetic sensor technology based on the Magneto Impedance (MI) effect has the potential to overtake some of the other emergent sensor systems in term of performance and low cost [4]-[6]. MI sensors combine such desirable characteristics as high sensitivity, miniature size, fast response, and low power consumption, which make them unique in the magnetic sensor family.

The MI sensing performance is based on large changes in the complex-valued impedance at high frequencies under the application of a DC (or low frequency) magnetic field [7]. The ratio of the percent change of the impedance, called the MI ratio, reaches the value up to 150 % at MHz frequencies in amorphous micro wires having circumferential (or helical) anisotropy. The characteristic magnetic fields required to cause this impedance change are in the range of 1-5 Oe. Then, the MI sensitivity is at least one order of magnitude higher than that of GMR materials. However, the MI-wires have much greater dimensions: 10-50 micron in diameter and a few mm in length. With decreasing sensor-element size, the maintenance of ultra high sensitivity becomes a problem. Special thin-film structures have been proposed to be employed to improve the MI performance in miniature elements (thickness < 1 μm, in-plane size < 200 μm and length < 5000 μm) [8]-[9]. The basic structure consists of two outer soft magnetic layers separated by a non magnetic highly conductive layer. The system with amorphous magnetic layers allows the MI ratio to be increased up to several hundred percents. *The present work further advances MI in multi-layers investigating structures with different magnetic anisotropy with the purpose to optimise the MI characteristics with respect to sensitivity, linearity and element size; and to integrate the fabricated MI elements into a specially designed high frequency oscillation circuit which constitutes a magnetic sensor.*

In electrically uniform materials subjected to a DC magnetic field, MI originates from the dependence of the skin depth on the transverse permeability. In multi-layer structures having a highly conductive inner film, a very large change in impedance can occur at quite

low frequencies when the inductance caused by the outer magnetic layers becomes sufficiently high. This results in multi-fold enhancement of the MI ratio and a considerable extension of the operational frequency range. Furthermore, special types of magnetic anisotropy can be realized in layered systems [10]. In this work, much attention is drawn to cross-anisotropy films which exhibit asymmetric MI characteristics. This feature is crucially important to obtain a linear voltage response with enhanced sensitivity, without requiring large power consumption, and is of particular interest for magnetic-sensor applications.

The importance of the anisotropy to the MI effect has been understood from the onset of MI research. The amorphous ferromagnetic microwires were the first materials which demonstrated a wide variety of the MI field behaviors for the different magnetic anisotropies. For films, the required anisotropy could be established by sputtering in the presence of a large magnetic field of certain orientation. Annealing frequently helps to establish the required type of the anisotropy and domain structure, as internal stresses and other defects caused by the sputtering process may result in unexpected magnetic structures. In this work films with different anisotropies are considered: transverse, longitudinal and crossed. The case of the crossed anisotropy is more complicated, involving considerable modifications of MI under the DC bias current and it makes it possible to realize linear sensing without using external bias fields.

The MI effect is investigated utilizing RF techniques based on measurements of S-parameters with the help of a HP vector analyzer. For the development of a miniature magnetic sensor, the MI element has to be integrated within a high frequency circuit. Achievements were made in active reduction of the oscillator noise and the AC biasing of the MI element which allowed the measurement of low frequency magnetic fields to a number of orders of magnitude smaller than previously developed techniques. The achieved sensitivities are the order of 10^{-7} Oe for high frequency fields and 10^{-5} Oe for low frequency fields in the order of 10 Hz.

The work is organised as follows. Chapter 2 begins by reviewing some of the essential physical properties of ferromagnetism, as this topic covers the magnetic state of materials used in the thin films investigated in this thesis. The intrinsic magnetisation of ferromagnetic metals through the discussion of phenomenology of magnetic anisotropy of various types will be introduced. Secondly, the domain structure of thin films and movement of domain walls will be illustrated.

Some simple single domain models of reversible and irreversible magnetization will be illustrated based on the Stoner-Wohlfarth model. In order to develop a background understanding of the Magneto Impedance (MI) effect, a quasi-static model for susceptibility as a response to a small AC easy-axis driving field in the presence of an arbitrary DC magnetic field applied in the transverse direction will be presented. This configuration is typical of the Magneto Impedance effect, and the corresponding susceptibility is referred to as transverse (with respect to the DC field and AC current creating the driving field). It will then be further elaborated to include the frequency dependence and contribution of domain wall movements to the effective transverse susceptibility.

Chapter 3 provides a review of underlying physical effects for MI in magnetic/metallic multi-layers, by modelling the impedance of a single layer thin film for arbitrary frequencies including the case of a strong skin effect. It is then shown that the case of multi-layer structures having a highly conductive inner film is different in that a very large change in impedance can occur at lower frequencies when the skin effect is not essential. This can result in a large enhancement of the MI ratio and a considerable extension of the operational frequency range into the lower frequency band compared to single layer films. The versatility of the multi-layer will be illustrated through the development of different magnetic configurations through inducement of specific anisotropies in the magnetic layers. Through the introduction of a coil to the multi-layer, cross magnetisation or off-diagonal impedances can be measured, making possible the investigation of the full surface impedance tensor. Practical estimations of the effect of the sample dimensions on MI are made before the introduction of Asymmetrical Magneto Impedance (AMI) in both dynamical and static configurations.

Chapter 4 aims to provide background information on the general manufacturing processes involved in the production of thin-films and the methods utilized in this work to produce the thin film multi-layers possessing the required properties (alloy composition, geometry, magnetic anisotropy). Firstly, the concept of sputtering as the means of depositing the material is introduced. Next, the means of shaping the thin film to desired dimensions and structure are discussed through the use of masks and etching. Lastly, inducing anisotropy in the thin film is discussed, whether during the sputtering process or post manufacturing with heat or current annealing treatments.

Chapter 5 outlines the experimental method and measurements undertaken on the thin film multi-layers produced during the course of this work. The chapter begins by giving fundamental background information on the many methods of measuring the complex impedance of a network, before giving a description of the experimental configuration and method used in the measurements presented. Our experimental investigations cover NiFe /Au / NiFe multi-layers including that with integrated planar coil, amorphous CoFeB / Cu / CoFeB multi-layers, multi-layers with additional insulation layers, including full variations in geometry and dimensions.

Chapter 6 will continue discussing the experimental process; this time shifting our attention to the special magnetic configuration of static crossed anisotropy that can be created in multi-layer thin films, which produces asymmetrical MI in the presence of a bias current. Furthermore, the possibility of obtaining asymmetry is investigated in multi-layers with an additional planar coil sputtered around the film.

Chapter 7 will present a review on several types of magnetic sensors, which are based on different physical principles. It aims to demonstrate that a sensor based on the MI effect would be extremely versatile, as it combines the many attributes of other sensors, and would be suitable from general field sensing to resolutions down to 10^{-7} Oe which typically would require the use of sophisticated sensing techniques, such as a SQUID magnetometer. It also presents a review of historical MI sensors and their technologies.

Chapter 8 will be devoted to the development of novel high sensitivity MI sensors and reporting of their results. Throughout the course of the work it will be shown that Magneto Impedance has the potential to be a very sensitive magnetic transducer in an electronic sensor device. However, the transfer of theoretical measurements into a practical commercial sensing device that can produce a superior performance to current industrial sensors in a number of critical areas is an ongoing challenge. Beginning with theoretical modelling of oscillators and power detection devices, including their sources of noise and limitations, a stage by stage development process of two Magneto Impedance sensing devices, each designed to operate with a different magnetic anisotropy multi-layer will be presented. Detailed measurements of their performance and operation will be illustrated, leading to the presentation of results in which the magnitude, resolution and frequency of AC and DC magnetic fields measured set new benchmarks for a Magneto Impedance sensing device.

References

[1]   D. Robbes, C. Dolabdjian, S. Saez, Y. Monfort, G. Kaiser and P. Ciureanu, *"Highly sensitive uncooled magnetometers: state of art. Superconductive magnetic Hybrid magnetometers, an alternative to SQUIDs?"*, *IEEE Trans App Superconductivity.* **11** (2001), 629-634.

[2]   D.J. Mapps, Magnetoresistive sensors, *Sens Actual A: Phys* **59** (1997), 9-19.

[3]   F. Primdahl, *"The fluxgate mechanism, part I: The gating curves of parallel and orthogonal fluxgates"*, *IEEE Trans Magn* **6** (1970), 376-383.

[4]   K. Mohri, L.V. Panina, T. Uchiyama, K. Bushida and M. Noda, *"Sensitive and quick response micro-magnetic sensor utilizing magneto-impedance in co-rich amorphous wires"*, *IEEE Trans Magn* **31** (1995), 1266-1275.

[5]   K. Mohri, T. Uchiyama and L.V. Panina, *"Recent advances of micro magnetic sensors and sensing application"*, *Sens Actual A: Phys* **59** (1997), 1-8.

[6]   M. Vazquez and A. Hernando, *"A soft magnetic wire for sensor applications"*, *J Phys D: Appl Phys* **29** (1996), 939-949.

[7]   L.V. Panina and K. Mohri, *"Magneto-impedance effect in amorphous wires"*, *Appl Phys Lett* **65** (1994), 1189-1191.

[8]   T. Morikawa, Y. Nishibe, H. Yamadera, Y. Nonomura, M. Takeuchi and Y. Taga, *"Giant magneto-impedance effect in layered thin films"*, *IEEE Trans Magn* **33** (1997), 4367-4369.

[9]   T. Morikawa, Y. Nishibe, H. Yamadera, Y. Nonomura, M. Takeuchi, J. Sakata and Y. Taga, *"Enhancement of giant magneto-impedance in layered film by insulator separation"*, *IEEE Trans Magn* **32** (1996), 4965-4967.

[10]   K. Hika, L.V. Panina and K. Mohri, "*Magneto-impedance in sandwich film for magnetic sensor heads*", *IEEE Trans Magn* **32** (1996), 4594-4596.

[11]   L.V. Panina, D.P. Makhnovskiy and K. Mohri, "*Analysis of magneto-impedance in multilayers with cross-anisotropy*", *J Mag Soc Jpn*, **23**, (1999), 925-931.

Chapter 2. Background research

This chapter provides a review of some of the essential physical properties of ferromagnetism, as this topic covers the magnetic state of materials used in the thin films investigated in this thesis, such as the 3d-metal crystals of iron, nickel and cobalt or amorphous ferromagnetic alloys. It begins by investigating the intrinsic magnetization of ferromagnetic metals through the discussion of phenomenon of magnetic anisotropy, including any differing properties of the thin film compared to a bulk material such as shape anisotropy. The domain structure of thin films and movement of domain walls are illustrated.

After the ferromagnetic review, some simple single domain models of reversible and irreversible magnetization are illustrated based on the Stoner-Wohlfarth model. To develop a background understanding of the Magneto Impedance (MI) effect, a quasi-static model for susceptibility as a response to a small AC easy-axis driving field in the presence of an arbitrary DC magnetic field applied in the transverse direction is presented. This configuration is typical of the Magneto Impedance effect, and the corresponding susceptibility is referred to as transverse (with respect to the DC field and AC current creating the driving field). It is next elaborated to include the frequency dependence and contribution of domain wall movements to the effective transverse susceptibility.

2.1   Choice of Magnetic units

In a course of study of magnetism it is necessary to consider basic magnetic quantities and the units in which they are expressed, ways of making magnetic measurements, theories of magnetism, and the magnetic behaviour of materials.   The study of the subject is complicated by the unfortunate existence of three systems of units in magnetism and several other systems of units which are variants of these.

The three main unit systems are the Gaussian or CGS system and two MKS unit systems, the Sommerfeld convention and the Kennelly convention; these are shown in the Fig 2.1 below.   Each of these unit systems has certain advantages and disadvantages.   The CGS and MKS systems of magnetic units have different philosophies.   The CGS system took an approach based on magneto-statics and the concept of the magnetic pole, while the MKS system takes an electrodynamics approach to magnetism based on electric currents.   The CGS system uses a combination of e.m.u (electromagnetic units) and e.s.u. (electrostatic units) and the MKS system uses the SI (Système International d'Unités, or International System of Units).

In this thesis, it has been chosen to express the various magnetic quantities using the centimetre, gram, second (CGS) unit system rather than metre, kilogram, second (MKS) units system.   This choice has been made due to the majority of the published works on Magneto Impedance being expressed through the CGS system, and through the process of background reading and study during this PhD of these publications; this system has been adopted as the norm.

The table below illustrates how the quantities of magnetism are expressed in the different magnetic systems and how their naming conventions differ.   The value of the permeability of free space, μ_0 in the MKS system is given as 4π x 10^{-7} Weber / Ampere meter.

However there is no common agreement as to how the basic relation of the field equation, B should be written in the MKS system and three other forms exist.   The variant illustrated in the table is the most commonly used form the field equation.

Quantity		MKS (Sommerfeld)	MKS (Kennelly)	CGS (Guassian)
Field	H	A m^{-1}	A m^{-1}	Oersteds
Induction	B	Tesla	Tesla	Gauss
Magnetization	M	A m^{-1}		emu cc^{-1}
Intensity of magnetization	I		Tesla	
Flux	Φ	Weber	Weber	Maxwell
Moment	m	A m^2	Weber meter	Emu
Pole strength	p	A m	Weber	emu cm^{-1}
Field equation		$\mathbf{B} = \mu_0 (\mathbf{H} + \mathbf{M})$	$\mathbf{B} = \mu_0 \mathbf{H} + \mathbf{I}$	$\mathbf{B} = \mathbf{H} + 4\pi\mathbf{M}$
Energy of moment (in free space)		$E = -\mu_0 \mathbf{m} \cdot \mathbf{H}$	$E = -\mathbf{m} \cdot \mathbf{H}$	$E = -\mathbf{m} \cdot \mathbf{H}$
Torque on moment (in free space)		$\boldsymbol{\tau} = \mu_0 \mathbf{m} \times \mathbf{H}$	$\boldsymbol{\tau} = \mathbf{m} \times \mathbf{H}$	$\boldsymbol{\tau} = \mathbf{m} \times \mathbf{H}$

Figure 2.1   Principle unit systems currently used in magnetism, from [8].

2.2   Phenomenology of magnetic anisotropy

Magnetic materials tend to display a directional dependence of their properties, and this is a consequence of their magnetic anisotropy. This term simply means that the magnetic properties depend on the direction in which they are measured; a thorough knowledge of anisotropy is thus the key to understanding the magnetic material.

There are several kinds of anisotropy: Crystal anisotropy (also called magnetocrystalline anisotropy), shape anisotropy, stress anisotropy and work induced anisotropy such as by magnetic annealing.

2.2.1   Crystalline anisotropy

If a single crystal sample is cut in the form of a disc with axis parallel to the plane $\{110\}$, this sample will then have the directions of the form $\langle 100 \rangle, \langle 110 \rangle$ and $\langle 111 \rangle$ as diameters, as shown in Fig. 2.2 for the plane $(1\bar{1}0)$. The measurements of the magnetization curves along these diameters, in the plane of the disc, will then give information about three important crystallographic directions. For example Iron is used as an illustration, which has a body-centred cubic structure. For Iron, the magnetization curves show that saturation can be achieved with quite low fields in the $\langle 100 \rangle$ direction, in the range of a few tens of Oersteds, in comparison to the other directions which required hundreds of Oersteds to saturate. Accordingly, $\langle 100 \rangle$ direction is called the "easy direction" of magnetization. This in turn tells us that the domains in demagnetized iron are spontaneously magnetized to saturation in directions of the form $\langle 100 \rangle$ then a possible domain structure for a demagnetized crystal disc cut parallel to (001) is shown in Fig. 2.3 (a). Simplified, it has four kinds of domains, magnetized parallel to four of the six easy directions, namely $[010]$, $[100]$, $[0\bar{1}0]$ and $[\bar{1}00]$.
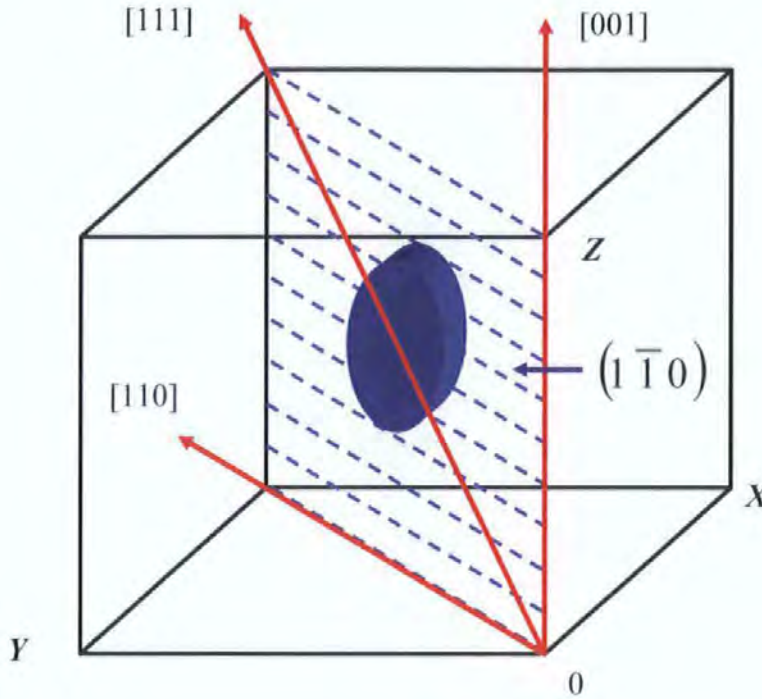
Figure 2.2   Illustration of principle crystallographic axes in a single crystal of Iron.

If a field is now applied in the $[010]$ direction, the $[010]$ domain will grow in volume by the mechanism of domain-wall motion, as shown in Fig. 2.3 (b). Continued application of the field eliminates all but the favoured domain and the crystal is now saturated. This saturation has been accomplished by the application of a low field required for domain wall movement. This illustrates that generally the direction of easy magnetization of a crystal is the direction of spontaneous domain magnetization in the demagnetized state. [2]

In order to saturate iron in a $\langle 110 \rangle$ direction, fairly high fields in the order of hundreds of Oersteds are required. For this orientation of field, the domain structure changes as shown in Fig. 2.4. Domain wall motion in a low field occurs until there are only two domains left (with the same projection of the magnetisation onto the field direction, Fig. 2.4 (c), each with the same potential energy. The only way in which the magnetization can increase further in the direction of the field is by rotation of the $\mathbf{M}_s$ vector of each domain until it is parallel with the applied field. This process is called domain rotation. Domain rotation typically requires fairly high fields, because the field is then acting against the force of the crystal

anisotropy, which is fairly strong. Crystal anisotropy may therefore be regarded as a force which tends to bind the magnetization to certain directions of a crystal. When the rotation process is complete (Fig. 2.4 d), the domain wall in (c) disappears and the crystal is saturated.

Because the applied field must do work against the anisotropy force to turn the magnetization vector away from an easy direction, there must be energy stored in any crystal in which $\mathbf{M}_S$ points in a non-easy direction. This is called the crystal anisotropy energy U_K. This can be expressed in terms of a series expansion of the direction cosines of $\mathbf{M}_S$ relative to the crystal axes. In a cubic crystal, let $\mathbf{M}_S$ make angles a,b,c with the crystal axes, and let $\alpha_1, \alpha_2, \alpha_3$ be the cosines of these angles, then

$$U_K = K_0 + K_1(\alpha_1^2\alpha_2^2 + \alpha_2^2\alpha_3^2 + \alpha_3^2\alpha_1^2) + K_2(\alpha_1^2\alpha_2^2\alpha_3^2) + \ldots \ldots \qquad (2.1)$$

where $K_0, K_1, K_2 \ldots$ are constants for a particular material and are expressed in ergs/cm^3. The higher order terms generally are not needed, and sometimes K_2 is so small that it can be neglected. The first term, which is K_0, is independent of angle and is usually ignored, because there normally is only an interest in the change in the energy U_K when the vector $\mathbf{M}_S$ rotates from one direction to another.

When K_2 is zero, the direction of the easy magnetization is determined by the sign of K_1. If K_1 is positive, then $U_{100} < U_{110} < U_{111}$, and $\langle 100 \rangle$ is the easy direction because U_K is a minimum when $\mathbf{M}_S$ is in that direction. If K_1 is negative, $U_{111} < U_{110} < U_{100}$ and $\langle 111 \rangle$ is the easy direction of magnetization. When K_2 is not zero, the easy direction is determined by the values of both K_1 and K_2.
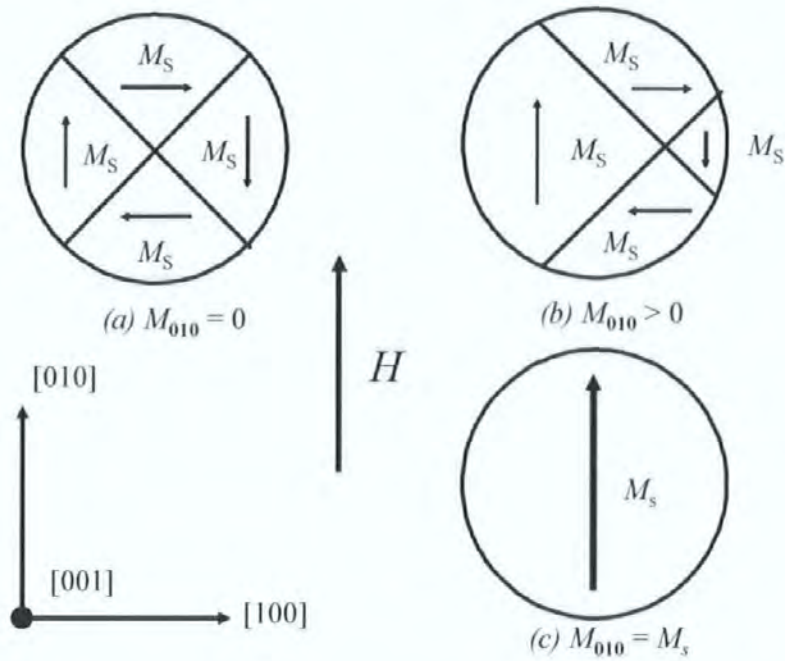
Figure 2.3   Changes in the domain structure of a crystal of iron by external field
H *in the direction* $[010]$.
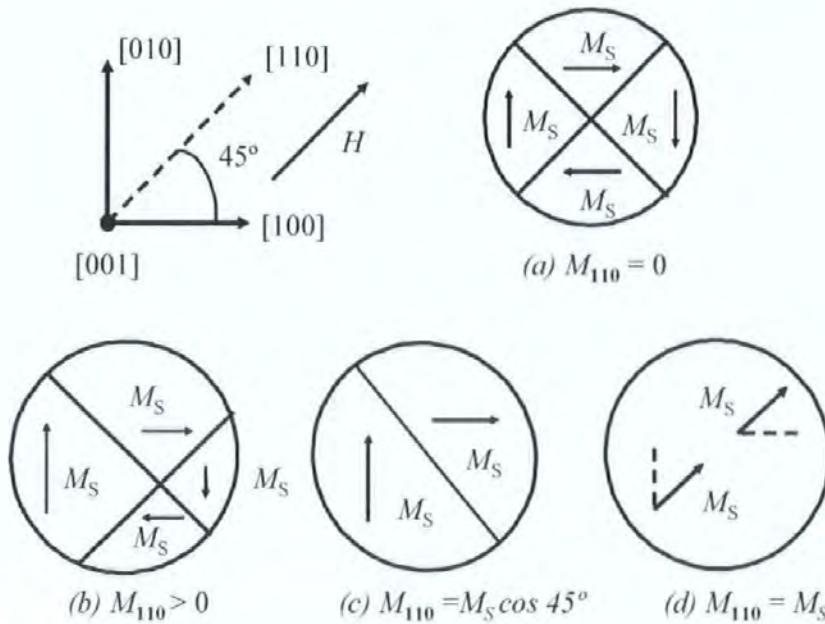
Figure 2.4   Changes in the domain structure of a crystal of iron by external field
H *in the direction* $[110]$.

In certain kinds of crystals, such as hexagonal closed packed crystals of cobalt, the anisotropy can be considered to be uniaxial, that is the hexagonal c axis is the easy direction of magnetization and any direction in the basal plane is found to be equally hard. Under these circumstances the anisotropy energy U_K depends on only a single angle, the angle θ between the vector $\mathbf{M}_S$ and the c axis. Therefore,

$$U_K = K'_0 + K'_1 \cos^2 \theta + K'_2 \cos^4 \theta + ... \tag{2.2}$$

However, it is customary to write the equation for U_K in hexagonal crystals in powers of $\sin \theta$. Putting $\cos^2 \theta = 1 - \sin^2 \theta$ into Eq. (2.2), it is shown that

$$U_K = K_0 + K_1 \sin^2 \theta + K_2 \sin^4 \theta + ... \tag{2.3}$$

When K_1 is positive and $K_2 > -K_1$, the energy U_K has a minimum for $\theta = 0$, and the c axis is the easy axis of magnetization. A crystal with a single axis, along which the magnetization points can either be up or down, is referred to as a uniaxial crystal. Its domain structure in the demagnetized state is particularly simple, as shown in Fig. 2.5
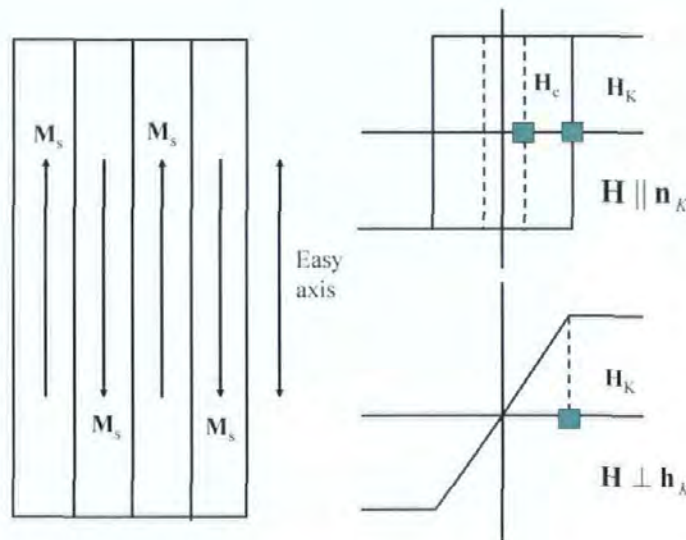
Figure 2.5   *Domain structure of a uniaxial crystal, magnetization loops for fields applied parallel and perpendicular to the anisotropy axis* $\mathbf{n}_K$.

The energy U_K will have a minimum for $\theta = 90°$ if K_1 is negative and $K_2 \triangleleft |K_1|/2$, or if K_1 is positive and $K_2 < -K_1$. The basal plane is then the easy plane of magnetization and the c axis is the hard axis of magnetization.

Referring to Fig. 2.5, the field H_c is known as a coercive field, and the field H_K is known as the anisotropy field. Typically, $H_K \gg H_c$. In the opposite case, the magnetisation in the parallel configuration ($\mathbf{H} \| \mathbf{n}_k$) will flip by irreversible rotational process at the field $H = H_K$. The magnitude of the anisotropy field can be most conveniently determined by the magnetization of a uniaxial crystal when the field is applied in a direction at right angles to the easy axis. The rotational processes of magnetisation in uniaxial crystals will ow be illustrated briefly. When the field is strong enough to rotate $\mathbf{M}_s$ away from the easy axis by an angle θ, the anisotropy energy is found from Eq. (2.3) and the Zeeman energy (energy of a magnetic body in an external field) is:

$$U_H = -M_s H \cos(\pi/2 - \theta) \tag{2.4}$$

The condition for the minimum (maximum) total energy is

$$\frac{\partial(U_K + U_H)}{\partial \theta} = 0$$

$$2K_1 \sin\theta \cos\theta + 4K_2 \sin^3\theta \cos\theta - M_s H \cos\theta = 0 \tag{2.5}$$

One solution of this equation is $\cos\theta = 0$, which describes the saturation along the field. The other solution is found from:

$$2K_1 \sin\theta + 4K_2 \sin^3\theta - M_s H = 0 \tag{2.6}$$

which describes the intermediate case and approach to saturation at $\sin\theta = 1$. The external field needed to reach saturation corresponds to the anisotropy field H_K and is expressed as:

$$H_K = \frac{2K_1 + 4K_2}{M_S}$$ (2.7)

If K_2 is small, the magnetization curve becomes a straight line as shown in Fig. 2.5 $H \perp n_k$ with the anisotropy field,

$$H_K = \frac{2K_1}{M_S}$$ (2.8)

A more detailed approach to the magnetisation behaviour when the field is applied at an arbitrary angle with respect to the anisotropy axis is carried out in section 2.4.

In amorphous materials, this intrinsic crystal anisotropy is not preserved, since the crystal field rapidly averages to "zero" on a macroscopic scale owing to the absence of the long-scale atomic ordering. On a local scale, it can be assumed that there is some "crystalline" anisotropy because of interactions between nearest neighbours, which will be, however, very short range, and therefore the average macroscopic crystal anisotropy is close to, or equal to, zero. In this case, other types of magnetic anisotropy should be considered.

2.2.2 Shape anisotropy

The shape anisotropy results from the demagnetising fields that occur within a magnetised material of a finite size due to the existence of magnetic poles at the boundaries. The shape of the sample has the effect of creating directions in which it is easier to magnetise the sample, and this is governed by the demagnetising field, H_d which in the material points in the opposite direction to the magnetization. For instance, a smaller field is required to magnetise a long cylindrical magnetic rod along its length, because of the smaller demagnetising field, compared to the magnetic field required to magnetise the rod along a diameter. If this is considered in terms of magnetic poles, the strength of the demagnetising field depends upon the separation between these opposite magnetic poles. The poles generated at the ends of a rod are much further apart, giving rise to a small demagnetising field, whereas the magnetic poles will be much closer together when the rod is magnetised across its diameter, thus producing a larger demagnetising field. The demagnetising field depends

solely on the magnetization and the demagnetising factor, and is expressed, for a uniformly magnetized object of ellipsoidal shape which creates a uniform internal demagnetizing field, as:

$$\mathbf{H}_d = \tilde{N}_d \mathbf{M} \tag{2.9}$$

Where $\tilde{N}_d$ is the demagnetising factor tensor that is mainly dependent on the shape of the body, and $\mathbf{M}$ is the magnetization vector.
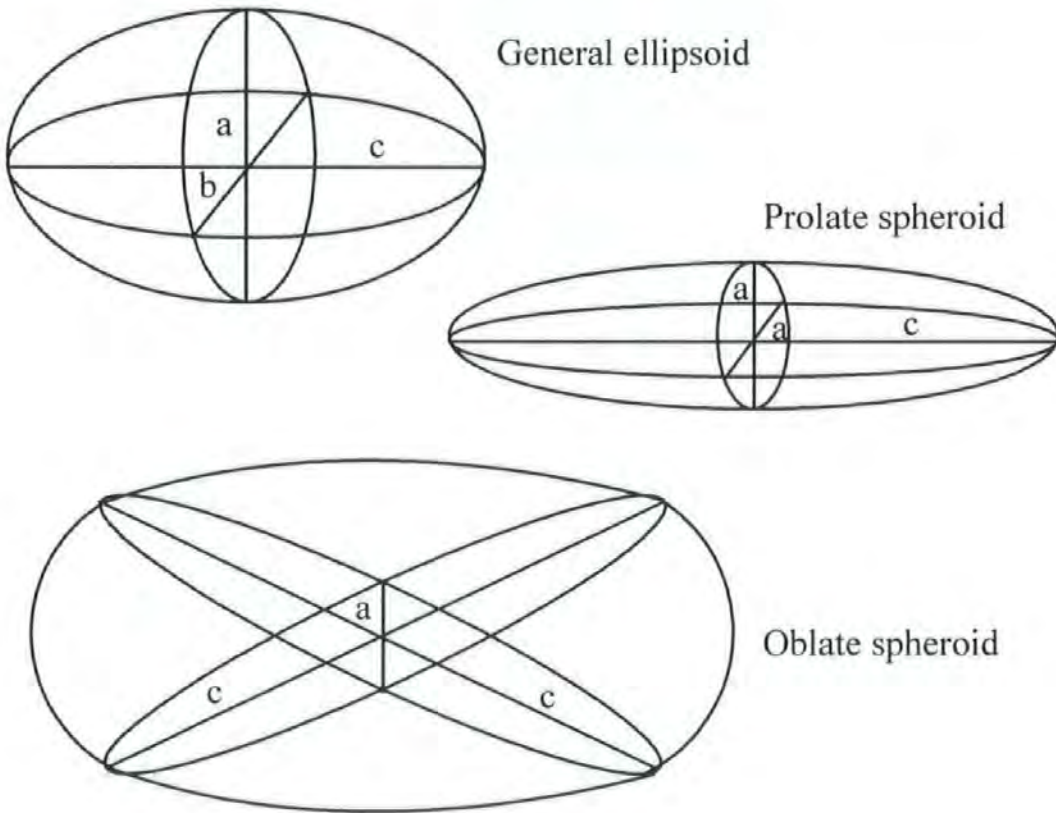
Figure 2.6   Ellipsoids, from [2].

Calculations of demagnetizing factors for general ellipsoids shown in Fig. 2.6 have been made in [7]. The general ellipsoid has three unequal axes $2a$, $2b$, $2c$ and a section perpendicular to any axis is an ellipse. Of more practical interest are the special cases of the prolate spheroid, formed by rotating an ellipse about its major axis $2c$; then $a = b$, resulting in a rod or cylinder shape for $c \gg a$, and the oblate spheroid formed by rotating about the minor axis $2a$, with $b = c$ with a limiting shape of a thin disc for $a \ll b$. If the magnetization is along the ellipsoid axis then $\tilde{N}_d$ is a diagonal tensor with N_a, N_b and N_c being particular

17

values for magnetization along the a, b or c axes. For any ellipsoid, the condition $N_a + N_b + N_c = 4\pi$ is true. [2].

The demagnetization factor of a prolate spheroid $a = b \neq c$, with $c/a = r$ is expressed as,

$$N_c = \frac{4\pi}{\left(r^2 - 1\right)}\left[\frac{r}{\sqrt{r^2 - 1}}\ln\left(r + \sqrt{r^2 - 1}\right) - 1\right], \qquad (2.10)$$

$$N_a = N_b = \frac{4\pi - N_c}{2} \qquad (2.11)$$

When r is very large, as in the case of a very long cylinder, then

$$N_a = N_b \approx 2\pi \qquad (2.12)$$

$$N_c \approx \frac{4\pi}{r^2}\left(\ln 2r - 1\right) \qquad (2.13)$$

As r approaches infinity N_c approaches zero.

For the demagnetization factor of the oblate spheroid $a \neq b = c$, with $c/a = r$,

$$N_a = \frac{4\pi r^2}{\left(r^2 - 1\right)}\left[1 - \sqrt{\frac{1}{r^2 - 1}}\sin^{-1}\frac{\sqrt{r^2 - 1}}{r}\right], \qquad (2.14)$$

$$N_b = N_c = \frac{4\pi - N_a}{2} \qquad (2.15)$$

When r is very large (approximation of a thin disc), then

$$N_a \approx 4\pi \qquad (2.16)$$

$$N_b = N_c \approx \pi^2 / r \qquad (2.17)$$

As r approaches infinity N_b and N_c approach zero.

The shape anisotropy has an importance in thin films. If magnetisation goes out of the film plane, there can be a significant demagnetization field according to Eq. (2.16). Then, the magnetization usually lays in-plane for a film in the absence of perpendicular crystal anisotropy [3]. In general, a thin film can be approximated by the oblate ellipsoid; this allows one to determine approximately the demagnetising factors for a thin film system.

Using Eq. (2.14), and some typical values for the size of a thin film used as sensor elements of $a = 1.5 \mu m$ and $c = 200 \mu m$ giving $r = 133.3$ the demagnetising factor, $N_a = 12.56601$ and in the plane of the film is $N_b = N_c = 2.2657 \times 10^{-3}$.

Hence the easy-axis is in the plane of the film, whilst the hard axis is perpendicular to the plane of the film. This means that any competing anisotropy, or an applied field, must overcome the demagnetising field that is nearly equal to the magnetic induction $4\pi M$ Eq. (2.9), in order to rotate the magnetization out of the plane of the film.

It is therefore important to be aware of the shape anisotropy in the design process of thin films in situations where the in-plane dimensions of the film approach the thickness of the film, by reducing the width of the sample for example, since the in-plane demagnetising field will no longer be negligible. [8]

2.2.3   Stress anisotropy

When the state of magnetization of a magnetic material is altered by an external magnetic field, it also experiences a change in its physical dimensions, provided that part or all of the magnetization process occurs by magnetization rotation as opposed to domain wall displacement. This change in dimension gives rise to a strain that is referred to as the magnetostriction λ Eq. (2.18)

$$\lambda = \frac{\Delta l}{l} \qquad\qquad (2.18)$$

Where l is the length of the sample before the applied field and Δl is the change in length along the magnetization caused by the applied field. The magnetostriction is due to the spin-orbit coupling which is also responsible for the Magneto crystalline anisotropy and they are both intrinsically related [2]. This type of magnetostriction is known as longitudinal or linear magnetostriction. The magnetostrictive strain λ increases as a function of applied field up to the point of magnetic saturation and is known as the saturation magnetostriction, λ_s. It is defined as the fractional change in length between the demagnetised state and the magnetically saturated state. The reason is that the crystal lattice inside each domain is spontaneously deformed in the direction of the domain magnetization and its strain axis rotates with the rotation of the domain magnetization. The magnetostrictive strain can have values which are either positive, negative, or in some cases, nearly zero depending upon the composition of the material. This means that, on application of a magnetic field, a positively magnetostrictive material will elongate in the direction of the magnetization caused by the applied field, whereas it will contract if it is negatively magnetostrictive. It is found that λ_s is anisotropic for crystalline materials and is therefore defined relative to the crystal axis along which the magnetization lies. In case of isotropic magnetostriction (as in amorphous materials) a simple expression relates the magnetostrictive elongation changes with the magnetization direction governed by the applied magnetic field:

$$\lambda(\theta) = (\frac{\delta l}{l})_{sat} - (\frac{\delta l}{l})_{0} = \frac{3}{2}\lambda_s \left(1 - \cos^2\theta\right) \qquad\qquad (2.19)$$

Here θ is the angle between the easy magnetization axis and the direction of the applied field. The maximum magnetostrictive strain has the value of $1.5\lambda_s$ as the spontaneous strain in the domain and will occur when the magnetization is rotated through 90^0 from magnetic saturation.

An important effect that is related to the magnetostriction is the inverse magnetostrictive or magnetoelastic effect. A stress applied to a ferromagnetic material will affect the direction of the domain magnetization through the magnetostriction. The preferred directions for the magnetization induced by stress depend on the sign of λ_s and the type of stress. For materials with $\lambda_s > 0$ the magnetization will rotate so as to lie along the direction of the uniaxial tensile stress, whereas it will lie perpendicular to a uniaxial compressive stress. The reverse is true for materials with $\lambda_s < 0$.

These effects are important to consider when inducing magnetic anisotropy into a thin film sample through heat treatments.

2.3   Domain structure in thin films

A ferromagnetic material usually consists of domains in any bulk material in the absence of external fields. The arrangement or configurations of the domains in the sample depend on a number of different factors. However, without the presence of external fields, domain structures are configured primarily to reduce the magneto static energy that is associated with the stray field emanating from the magnetic sample. This section will give an overview of domains in uniaxial crystals and thin films, general domain wall structure and domain wall motion.

Firstly it is necessary to give an explanation for the formation and relative arrangement of domains in any given specimen. It has been found that magneto static energy plays a primary role.

2.3.1   Domain structure of uniaxial crystals

Consider a large single crystal of a uniaxial substance. Suppose it is entirely one domain, spontaneously magnetized parallel to the easy axis, as shown in Fig. 2.7 (a). Then the free poles form on the ends, and these poles are the source of a large **H** field. The magneto static energy of the crystal is $(1/8\pi) \int H^2 dv$, evaluated over all space where **H** is appreciable.

This considerable energy can be approximately halved, if the crystal splits into two domains magnetized in the opposite directions as in Fig. 2.7 (b), because this brings north and south poles closer together to one another, thus decreasing the spatial extent of the **H** field. If the crystal splits into four domains as in Fig. 2.7 (c), the magnetostatic energy again decreases, to about one-forth of its original value, and so on. But this division into smaller and smaller domains cannot continue indefinitely, because each wall formed in the crystal adds energy. Eventually an equilibrium domain size will be reached.

A still larger reduction in magnetostatic energy will result if the unlike poles on each end of the crystal are "mixed" more. This can be done if the domain walls become curved rather than flat, although still parallel to the easy axis as shown in Fig. 2.8 (a). A section of such a crystal parallel to the easy axis will show straight lines separating the domains, and a section normal to the easy axis will show curved lines. Curvature of the walls increases the wall area, and this type of domain structure is therefore found mainly in very thin crystals. In thick crystals, wall curvature involves too much extra wall energy, and another method of

reducing magnetostatic energy is favoured, as shown in Fig. 2.8 (b). Here spike-shaped domains of reversed magnetization are formed at the surface. This has the desired effect of producing a fine mixture of opposite poles on the end surfaces without adding too much wall energy, because the spike domains are short. However, there is a discontinuity in the normal component of $\mathbf{M}_s$ on the walls of the spike domains, and free north poles must form there. These interior poles are the source of a $\mathbf{H}$ field and therefore contribute to the magnetostatic energy. The number and size of the spike domains will be such as to balance the reduction in main magnetostatic energy due to the surface poles against the increase in wall energy and in magnetostatic energy due to interior poles.
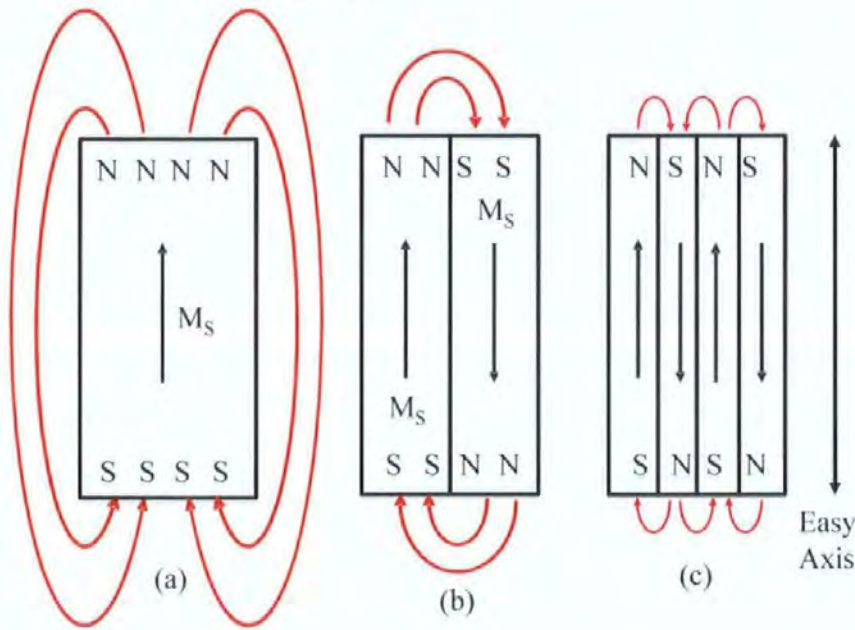
Figure 2.7   Divisions into domains to reduce magnetostatic energy (ignoring closure domains).
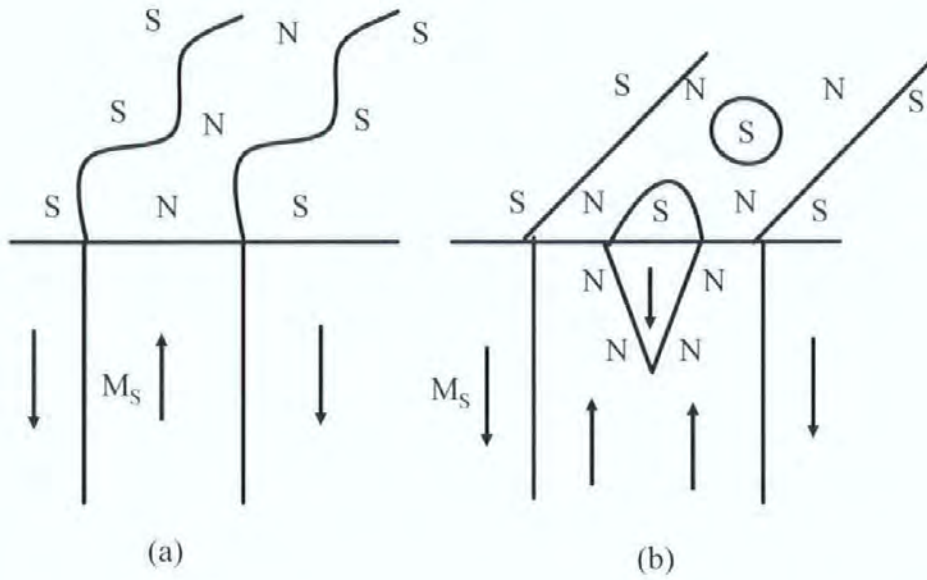
Figure 2.8   Curved walls and surface spike domains.

2.3.2   Domain wall structure

Domain walls are the interface between regions in which the spontaneous magnetization has different directions. At or within the wall the magnetization must change direction. An assumption could be made that the change of direction of magnetization would be abrupt, occurring from one atom to the next as shown in Fig. 2.9. A row of atoms is shown parallel to x, with the 180° domain wall lying in the yz plane; the easy axis is $\pm y$. But the exchange energy in a ferromagnet is a minimum only when adjacent spins are parallel. Therefore, the wall of Fig. 2.9 would have a large exchange energy associated with it, because the spins are anti parallel. This exchange energy can be decreased if the 180° change in spin direction to take place gradually over N atoms, so that the angle ϕ between adjacent spins, equal to π/N, has some small value, for example $\phi = 30°$ for 6 atoms. The total exchange energy is then reduced because it varies as ϕ^2 rather than ϕ.
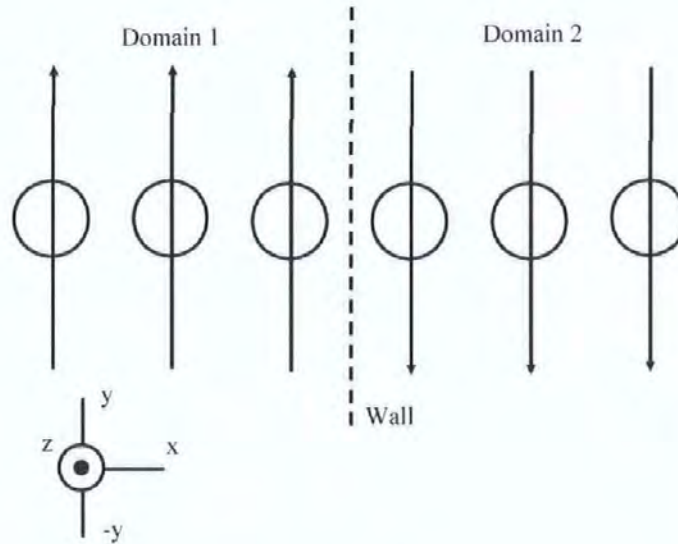
Figure 2.9   An infinitely thin 180° wall.

But, the spins within the wall under going this rotation are pointing in non easy directions, so that the crystal anisotropy energy within the wall is higher than it is in adjoining domains. While the exchange energy tries to make the wall as wide as possible, in order to make the angle ϕ between adjacent spins as small as possible, the anisotropy energy tries to make the wall thin, in order to reduce the number of spins pointing in the non easy direction. (The hypothetical wall in Fig. 2.9 has no extra anisotropy energy).

As a result of this competition the wall has a certain finite width and a certain structure. Also the wall has certain energy per unit area of its surface, because the spins in it are not quite parallel to one another and not parallel to an easy axis. The first theoretical examination of the structure of a domain wall was made by Bloch in 1932, and domain walls with the magnetization rotating in the plane of the wall are often called *Bloch walls*, to distinguish them from the types of domain walls in thin films where magnetization may rotate in the plane transverse to the wall plane.

2.3.3 Domain walls in thin films

The magnetization in thin films lies in the plane of the film, because a huge demagnetizing field $\mathbf{H}_d \left(= 4\pi \mathbf{M}_s \approx 10 kOe \right)$ would act normal to the plane of the film if $\mathbf{M}_s$ were turned in that direction. Domains in the film extend completely through the film thickness, and the walls between them are mainly of the 180° kind, roughly parallel to the easy axis of the film.

However, two new kinds of domain walls can exist in thin films. The first is called a *Néel wall,* because it was first suggested on the theoretical grounds by Néel in 1955. Ordinary walls such as those found in bulk materials can also exist in thin films; they are then specifically called Bloch walls to distinguish them from Néel walls.

Néel showed that the energy per unit area γ of a Bloch wall is not a constant of the material but depends also on the thickness of the specimen, when the thickness is less than a few thousand angstroms. The magnetostatic energy of the wall then becomes appreciable, relative to the usual exchange and anisotropy energy. Free poles are formed where the wall intersects the surface, as indicated in Fig. 2.10 where only the central spin in the wall is shown; when the specimen thickness t is of the same order of magnitude as the wall thickness δ, the field created by these poles constitutes appreciable magnetostatic energy. To calculate this energy Néel approximated the actual wall, a non-uniformly magnetized rectangular block in which the spins continuously rotate from the direction $+ y$ to $- y$, by a uniformly magnetized elliptic cylinder. This is shown in Fig. 2.10 (b); its major axis c is infinite. When magnetized along the a axis, its demagnetizing coefficient is

$$N_a = \frac{4\pi b}{a + b} \tag{2.20}$$

and when magnetized along b,

$$N_b = \frac{4\pi a}{a+b} \tag{2.21}$$

The magnetostatic energy density of the wall is then,

$$U_{ms} = \frac{1}{2} N_t M_S^2 \text{ erg/cm}^3 \qquad = \frac{1}{2}\left(\frac{4\pi\delta}{t+\delta}\right) M_S^2 \tag{2.22}$$

This must be multiplied by δ to obtain the magnetostatic energy per unit area of the wall in the yz plane:

$$\gamma_{ms,B} = \frac{2\pi\delta^2 M_S^2}{t+\delta} \text{ erg/cm}^2 \tag{2.23}$$

This energy is negligible when t/δ is large, as in bulk specimens, but no when it is of the order of unity or less.
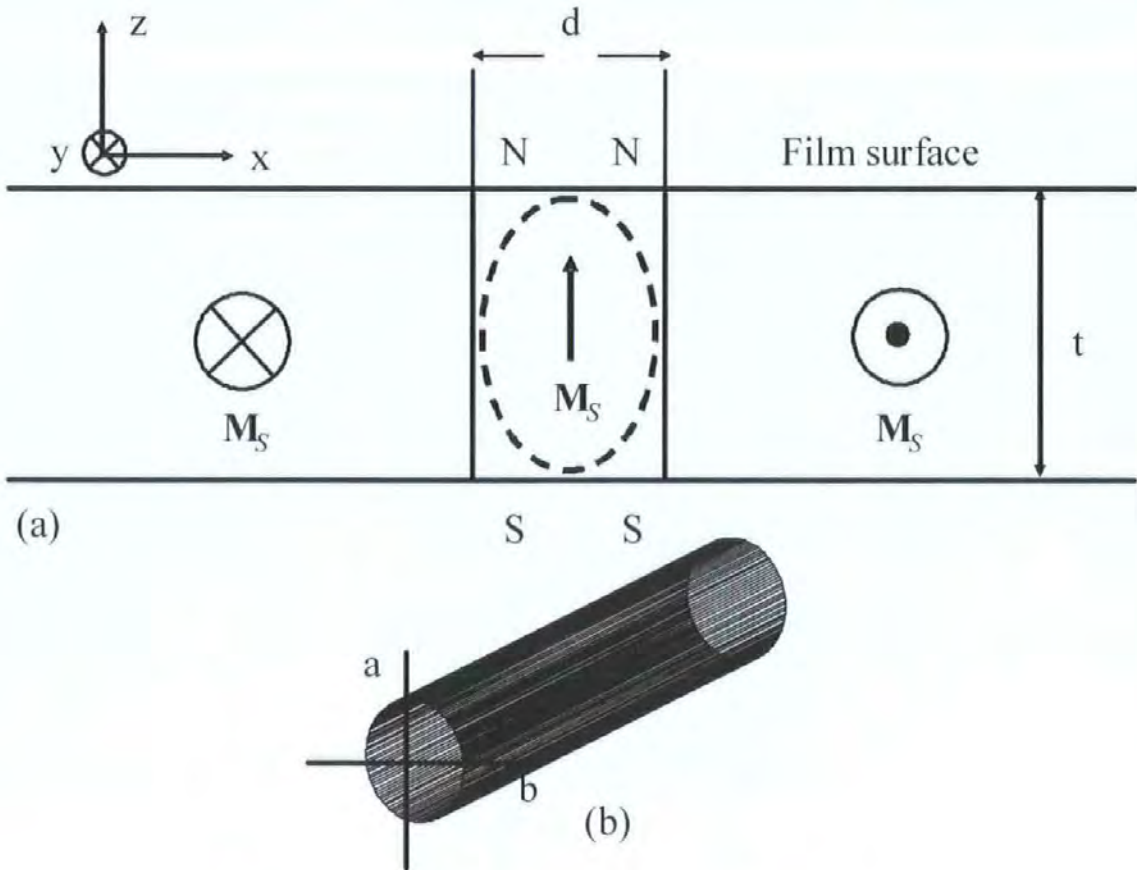
Figure 2.10   (a) cross section of 180° Bloch wall in thin film. (b) Elliptic cylinder

When the film thickness t is small, the magnetostatic energy of the wall can be reduced if the spins in the wall rotate, not about the wall normal x, but about the film normal z. The result is a Néel wall. Free poles are then formed, not on the film surface, but on the wall surface, and spins everywhere in the film, both within the domains and within walls, are parallel to the film surface a shown in Fig. 2.11

Again approximating the wall by an elliptic cylinder and find that its magnetostatic energy is

$$\gamma_{ms,N} = \frac{2\pi t \delta M_S^2}{t+\delta} \ \text{erg/cm}^2 \tag{2.24}$$

The ratio of magnetostatic energies of the two kinds of wall is then

$$\frac{\gamma_{ms,B}}{\gamma_{ms,N}} = \frac{\delta}{t} \tag{2.25}$$

This expression states that the magnetostatic energy of a Néel wall is less than that of a Bloch wall when the film thickness t becomes less than the wall thickness δ. This is not exact just because of assumptions in its derivation, but also because δ varies with film thickness, it is necessary to calculate the total wall energy γ, which contains magnetostatic, exchange, and anisotropy terms. Including these terms, it can be seen that the total energy of a Néel wall, as well as the magnetostatic energy, is less than that of a Bloch wall when the film is very thin, less than about 500 Å. The widths of Bloch and Néel walls also vary in different ways with film thickness: the thinner the film, the narrower the Bloch wall and the wider the Néel wall.
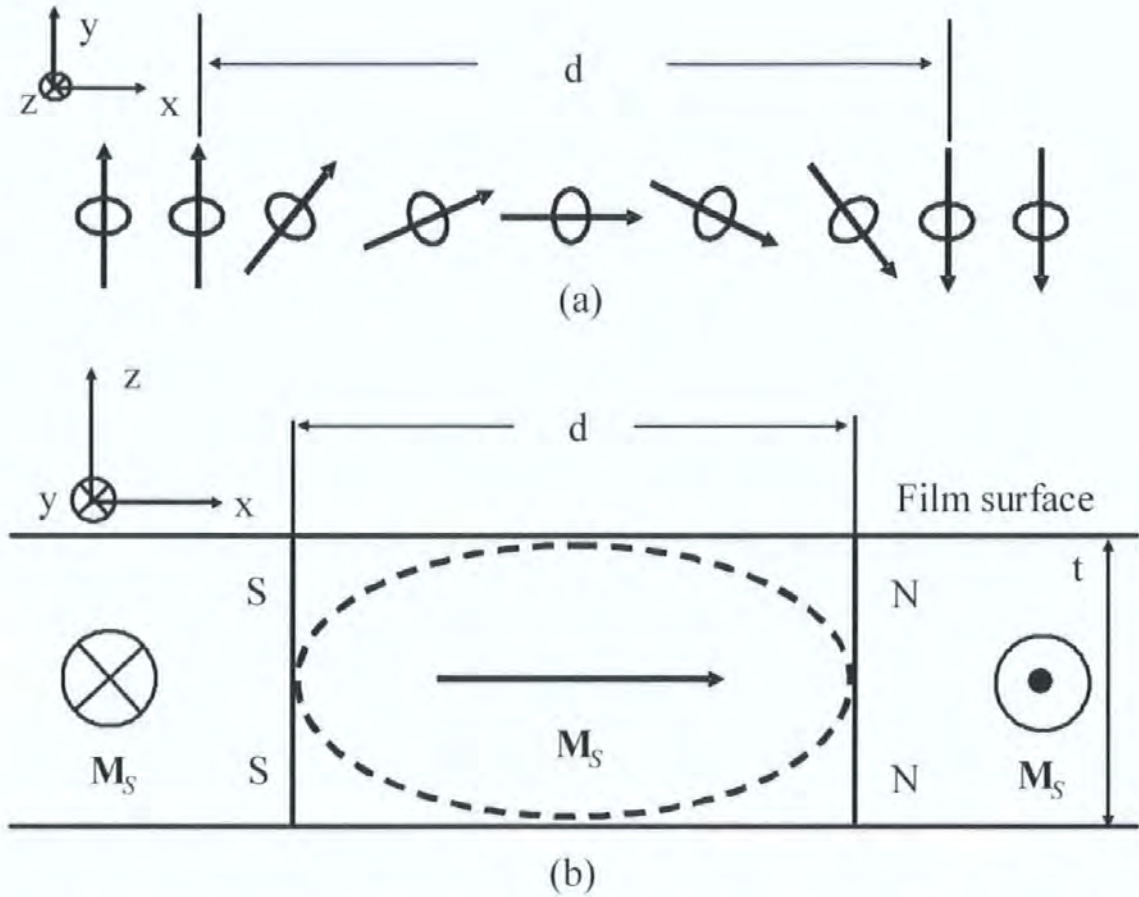
Figure 2.11   Structure of a Néel wall. (a) Section parallel to film surface. (b) Cross section of wall.

The second new kind of wall observed in thin films is the *cross tie wall*, first seen by Hubert. It consists of a special kind of Néel wall, crossed at regular intervals by Néel wall segments. Its energy is less than that of a Bloch wall of a Néel wall in a certain range of film thickness; the cross tie wall therefore constitutes a transition form between Bloch walls of very thick films and the Néel walls of very thin films.

Its structure is shown in Fig. 2.12, a Néel wall is shown, separating two oppositely magnetized domains. It is not a normal Néel wall because it consists of segments of opposite polarity; these have formed in an attempt to mix the north and south poles of the wall surface more closely and thus reduce magnetostatic energy.

The regions within the wall where the polarity changes, marked with small circles, and where the magnetization is normal to the film surface, are called *Bloch wall segments*.

However, this hypothetical wall would have a very large energy, because the fields due to the poles on the wall, sometimes called stray fields, are anti parallel to the domain magnetization in the regions opposite the Bloch lines marked A. As a result, spike walls form in these regions, as shown in Fig. 2.12 (b), and the stray fields close in a clockwise direction between the cross ties.
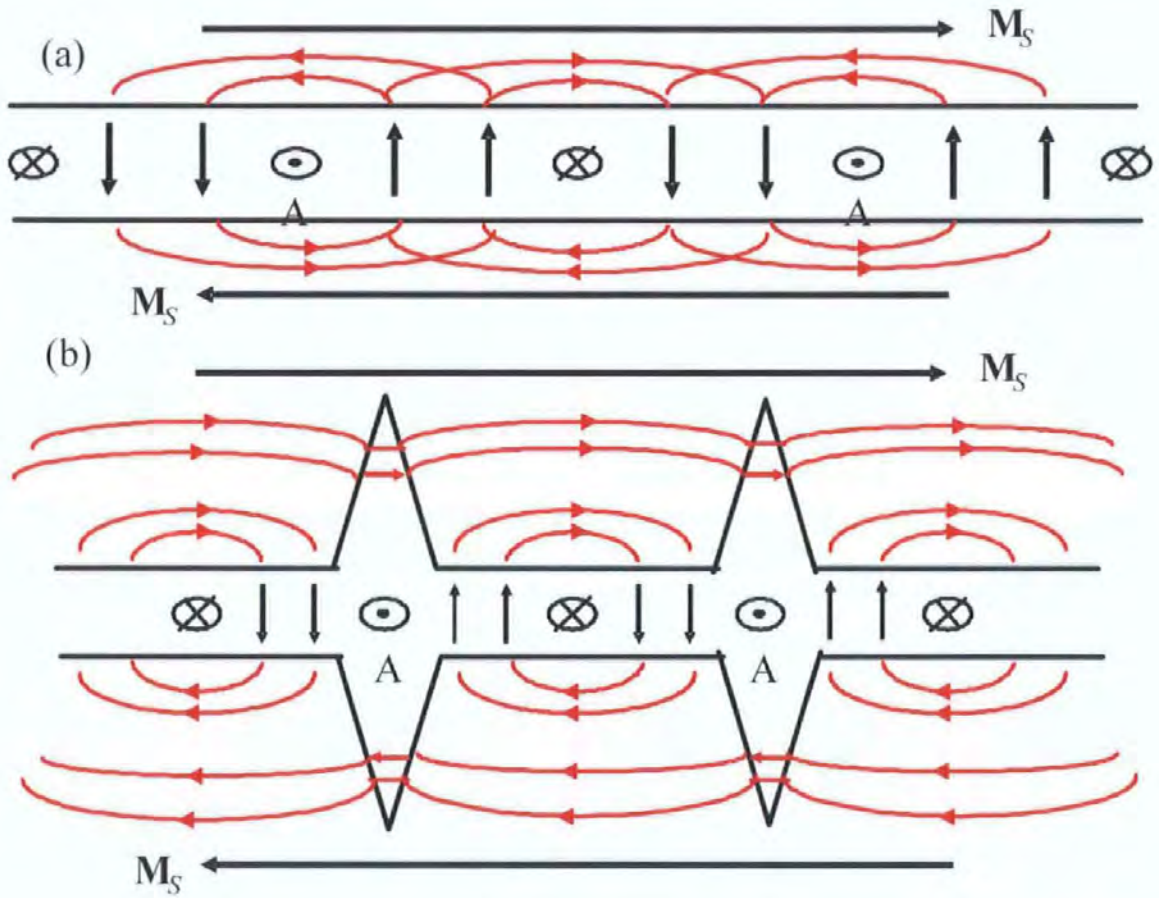
Figure 2.12   Sections parallel to film surface of (a) hypothetical Néel wall with sections of opposite polarity, and (b) cross-tie wall.

2.4   Model of the magnetization process

After giving a general overview of the basic properties of a ferromagnetic material, simple models of the magnetization processes can be described.

In order to analyse the magnetization dynamics in ferromagnetic films, it is required to establish the equilibrium magnetic structure, which can be done through the minimisation of the free energy of the thin film sample. The total magnetic energy is made up of a number of different terms from the anisotropic properties of the material and external fields. The following energy terms are considered to make important contributions: magnetocrystalline energy, U_K, magnetostatic energy from shape anisotropy, U_{sh}, magneto elastic energy associated with stress anisotropy, U_{me}, and energy due to an external magnetic field, H, U_H.

$$U_E = U_K + U_{sh} + U_{me} + U_H \tag{2.26}$$

The first three terms constitute the effective anisotropy which defines the equilibrium direction of the magnetization inside domains in the absence of the external fields. The equilibrium magnetization in the case of a single domain film structure with the effective uniaxial anisotropy by minimising the total energy with respect to the magnetization angle (known as Stoner-Wohlfarth model) will be considered next. This was shown before in section 2.2.1 for the specific case of a perpendicular applied field with respect to the easy axis. To obtain more general results, a model of an oblate spheroid as the approximation of the shape of a thin film will be used.
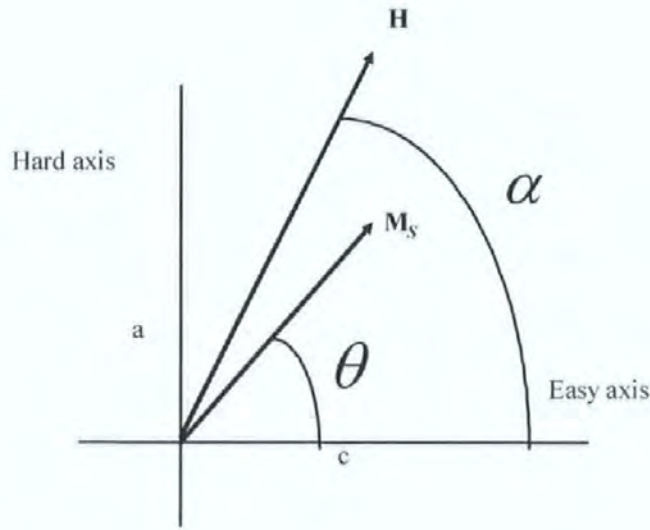
Figure 2.13   Direction of magnetization with respect to applied field and easy axis.

As shown in the figure above, The *a* axis is the hard axis and *c* is an easy axis of magnetization. Rotation occurs in plane. α is defined as the angle between **H** and the easy axis and θ as the angle between $\mathbf{M}_S$ and the easy axis, the anisotropy energy is given by

$$U_K = K_u \sin^2 \theta \tag{2.27},$$

the Zeeman energy is

$$U_H = HM_S \cos(\alpha - \theta) \tag{2.28},$$

and the total energy is

$$U = U_K + U_H = K_u \sin^2 \theta - HM_S \cos(\alpha - \theta) \tag{2.29}$$

The equilibrium position of M_S is given by

$$\frac{dU}{d\theta} = 2K_u \sin\theta \cos\theta - HM_S \sin(\alpha - \theta) = 0 \tag{2.30},$$

and the magnetization resolved in the field direction is given by

$$M = M_S \cos(\alpha - \theta) \tag{2.31}$$

Suppose the field is normal to the easy axis, so that α is $90°$. Then,

$$2K_u \sin\theta\cos\theta = HM_S \cos\theta \text{ and } M = M_S \sin\theta \qquad (2.32)$$

therefore,

$$2K_u(M/M_S) = HM_S \qquad (2.33)$$

Put $M/M_S = m$, reduced magnetization. Then,

$$m = H(M_S/2K_u) \qquad (2.34)$$

This shows that the magnetization is a linear function of H, with no hysteresis. Saturation is achieved when $H = H_K = 2K_u/M_S$ or the anisotropy field, as shown in Eq. (2.9) previously. If h = reduced field $= H/H_K = HM_S/2K_u$, then $m = h$ when α is $90°$.

For the general case Eq. (2.30) and (2.31) may now be written

$$\sin\theta\cos\theta - h\sin(\alpha-\theta) = 0 \qquad (2.35)$$

$$m = \cos(\alpha-\theta) \qquad (2.36)$$

Suppose now that the field is along the easy axis $(\alpha = 0)$, and that H and M both point along the positive direction of the axis. Let H be reduced to zero and then increased in the negative direction $(\alpha = 180°)$. Although H and M are now anti-parallel which leads to increase in energy, the magnetisation will not flip because of the existence of the energy barrier. A certain amount of the negative field is needed to realise the magnetisation flip from the position with $\theta = 0$ to $\theta = 180°$. To find this critical value, the solution to Eq. 2.35 can be used which describes all the energy extremums. The critical field is found from the condition that the local energy minimum (metastable state) becomes unstable, which is governed by the sign of the second derivative.

If $d^2U/d\theta^2$ is positive, the equilibrium is stable; if it is negative the equilibrium is unstable; if it is zero, a condition of stability is just changing to one of instability.

Thus the critical field is found by setting

$$\frac{d^2U}{d\theta^2} = \cos^2\theta - \sin^2\theta + h\cos(\alpha - \theta) = 0 \qquad (2.37)$$

Simultaneous solutions of Eq. (2.35) and (2.37) lead to the following equations, from which the critical field h_c and the critical angle θ_c, at which the magnetization will flip, may be calculated:

$$\tan^3\theta_c = -\tan\alpha, \qquad (2.38)$$

$$h_c^2 = 1 - \frac{3}{4}\sin^2 2\theta_c. \qquad (2.39)$$

When $\alpha = 180°$, $h_c = 1$, or $H = H_K$. The hysteresis loop is then rectangular, as shown in Fig. 2.14.

The reduced magnetization m as a function of reduced field h for an intermediate angle, say $\alpha = 20°$ is calculated as follows. For positive values of h, the angle θ will vary between 0 and $20°$. For selected values of θ in this range, corresponding values of h and m are found from Eq. (2.35) and (2.36). When h is negative, $\alpha = 180° - 20° = 160°$, and Eq. (2.39) gives the critical value θ_c at which the magnetization will flip. Values of h and m are again found from Eq. (2.35) and (2.36), with α equal to $160°$, for selected values of θ in the range 0 to θ_c.

Figure 2.14 shows hysteresis loops calculated for various values of α. In general, these loops consist of reversible and irreversible portions and therefore that reversible and irreversible changes in magnetization can occur by domain rotation as well as by domain wall motion. The portion of the total change of m due to irreversible jumps varies from a maximum at $\alpha = 0°$ to zero at $\alpha = 90°$. The critical value of reduced field h_c, at which the $\mathbf{M}_S$ vector flips from one orientation to another, decreases from 1 at $\alpha = 0$ to a minimum of 0.5 at $\alpha = 45°$ and then increases to 1 again as α approaches $90°$; these critical values are equal to any two values of α, such as $20°$ and $70°$, symmetrically located about $\alpha = 45°$. On the other hand, the reduced intrinsic coercivity h_{ci} (the value of h which reduces m to zero) decreases from 1 at $\alpha = 0°$ to zero at $\alpha = 90°$. For values of α between 0 and $90°$, cyclic variation of $\mathbf{H}$ in a fixed direction has a curious result: $\mathbf{M}_S$ makes one complete revolution per cycle, although it does not rotate continuously in the same direction
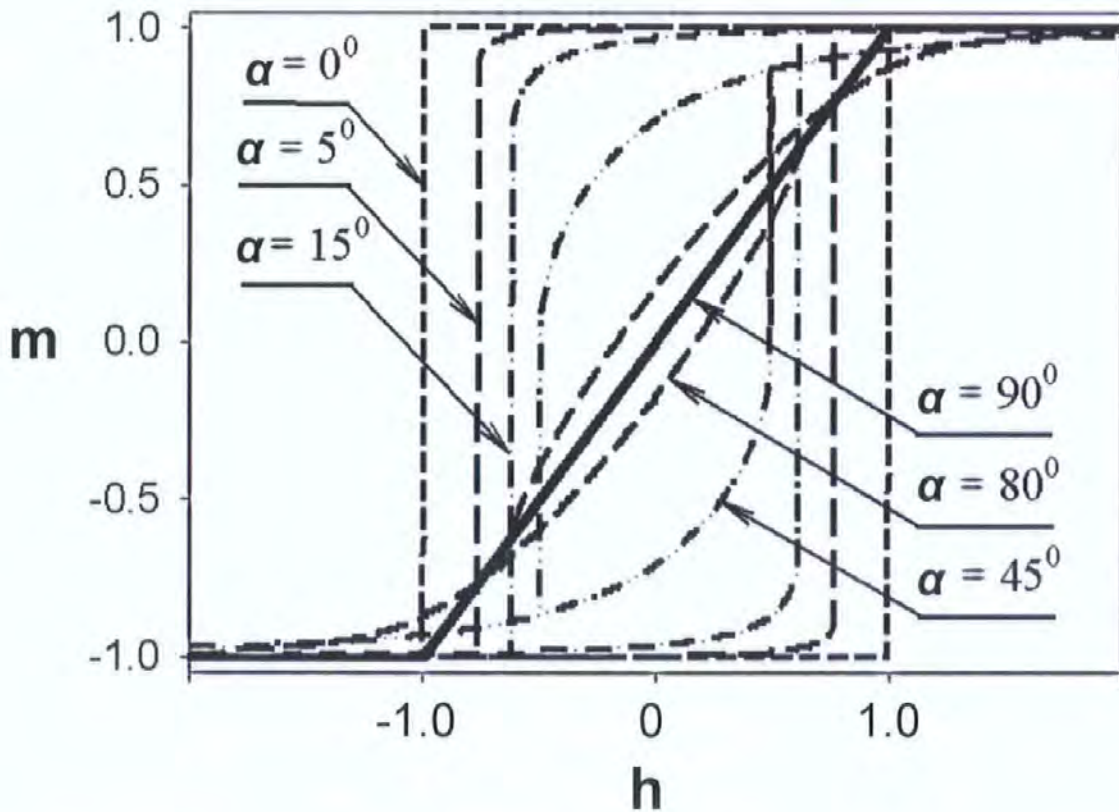
Figure 2.14 Rotational hysteresis loops for uniaxial anisotropy (α = angle between field and easy axis).

2.5   Further magnetic properties

The previous sections had described general models of the magnetic properties for static fields. This approach will be further developed to produce a quasi-static model for the magnetization change (which is described in terms of the susceptibility) due to a small AC field applied in the direction of the easy magnetization, and in the presence of a DC magnetic field of arbitrarily magnitude along the hard axis. This configuration is typical of the magneto Impedance effect as will be explained later. At this stage, it is intended to demonstrate the behaviour of the susceptibility as a function of the hard axis field.

2.5.1   Linear model for the easy-axis magnetization in the presence of the orthogonal field

To illustrate the behaviour of the quasi-static magnetization $m = \chi H_{ac}$, where χ is the susceptibility, caused by a small easy axis driving field H_{ac} in the presence of a hard axis field H_{ex}, a development of the previous model has been employed. By considering a single layer film having a transverse anisotropy along its width which may have anti-parallel domains with 180^0 domain walls. The equilibrium magnetization with the angle θ_0 with respect to n_k is set by the balance of the transverse anisotropy and the hard axis field, which is then changed by applying H_{ac} as shown in Fig. 2.15 To simplify the model, it is assumed that there is no domain wall bowing caused by the field H_{ex}. Additionally it is assumed that the magnetization process occurs purely by moment rotation.

36

Easy Axis

$\mathbf{H}_K$

$\mathbf{M}_{ac}$

$\delta\theta$

$\mathbf{M}_0$

θ_0

$\mathbf{H}_{ac}$

$\mathbf{H}_{ex}$

Hard Axis
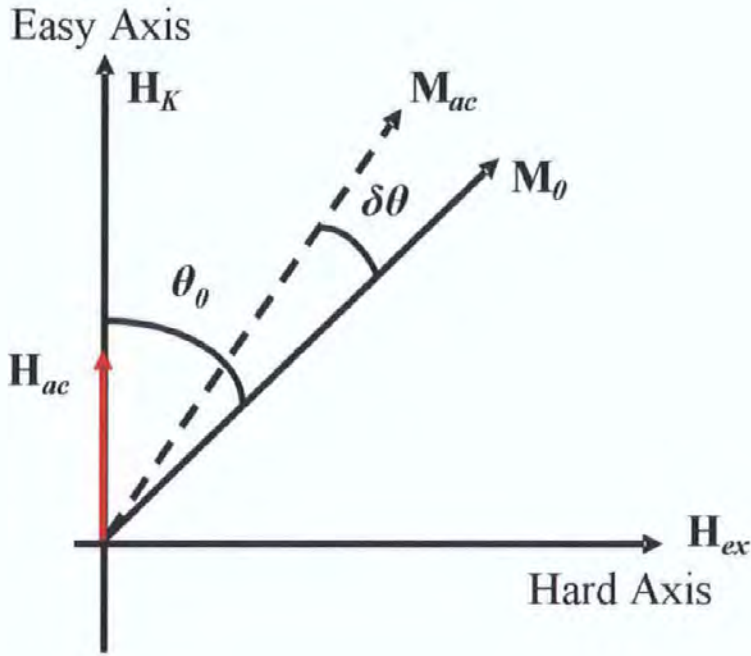
Figure 2.15   Simplified domain model used to illustrate the susceptibility with respect to H_{ac} in a magnetic layer of a thin film.

The transverse susceptibility (with respect to the film length and H_{ex}) under the conditions of these assumptions can be written as:

$$\chi_t = \frac{\partial M_{ac}}{\partial H_{ac}} \tag{2.40}$$

Where the change in the transverse magnetization M_{ac} is simply the oscillation of the magnetization vector M_0 in the transverse direction, due to the field H_{ac}, described by the variation in the angle $\theta = \theta_0 - \delta\theta(H_{ac})$ (see Fig. 2.15). Considering this change to be small, in the linear approximation the magnetization M_{ac} is expressed as

$$M_{ac} = M_0(\cos\theta_0 + \delta\theta\sin\theta_0) \tag{2.41},$$

which defines the transverse susceptibility:

$$\chi_t = M_0 \sin\theta_0 \frac{\delta\theta}{H_{ac}}$$

(2.42)

The equilibrium angle θ_0 of the magnetization vector $\mathbf{M}_0$ is determined from Eq. (2.30) with the anisotropy angle $\alpha = \pi/2$

$$\sin\theta_0 = \frac{H_{ex}}{H_K}, \quad H_{ex} < H_K = 2K_u/M_0;$$

$$\sin\theta_0 = 1, \quad H_{ex} \geq H_K$$

(2.43)

To find the changes in θ when a small field H_{ac} is applied, a linear equation for the energy minimisation will be considered. The total energy in the presence of the two orthogonal fields is written as

$$U_0 = -K_u \cos^2\theta - M_0 H_{ac} \cos\theta - M_0 H_{ex} \sin\theta$$

(2.44)

Minimising Eq. (2.44) with respect to θ obtains the following expression

$$\frac{\partial U_0}{\partial\theta} = H_K \sin\theta\cos\theta + H_{ac}\sin\theta - H_{ex}\cos\theta = 0$$

(2.45)

Substituting $\theta = \theta_0 - \delta\theta$ into Eq. 2.45 gives

$$\frac{1}{2}\sin 2(\theta_0 - \delta\theta) + \frac{H_{ac}}{H_K}\sin(\theta_0 - \delta\theta) - \frac{H_{ex}}{H_K}\cos(\theta_0 - \delta\theta)$$

(2.46)

Expanding Eq. (2.46) in series of $\delta\theta$, and taking the linear terms after some algebraic manipulation, the following is obtained:

$$\delta\theta = \frac{H_{ac}}{H_K}\left[\frac{\sin\theta_0}{\cos 2\theta_0 + \frac{H_{ex}}{H_K}\sin\theta_0}\right]$$

(2.47)

38

Substituting Eq. (2.47) together with the solution for the equilibrium angle θ_{ex} Eq. (2.43) into Eq. (2.42) completes the problem of finding the transverse susceptibility:

$$\chi_t = \frac{M_0 H_{ex}^{2}}{H_K (H_K^{2} - H_{ex}^{2})}, \qquad (|H_{ex}| < H_K) \tag{2.48}$$

$$\chi_t = \frac{M_0}{|H_{ex}| - H_K}, \qquad (|H_{ex}| > H_K) \tag{2.49}$$

Figure 2.16 shows the field plot of the transverse susceptibility calculated from Eq. (2.48) & (2.49). Due to the simplicity of the model the susceptibility diverges as H_{ex} approaches H_K (which is equal to 10 Oe in the present calculation) but it is clear that there is a significant change in transverse susceptibility which occurs in the presence of the hard axis field nearly equal to the anisotropy field.
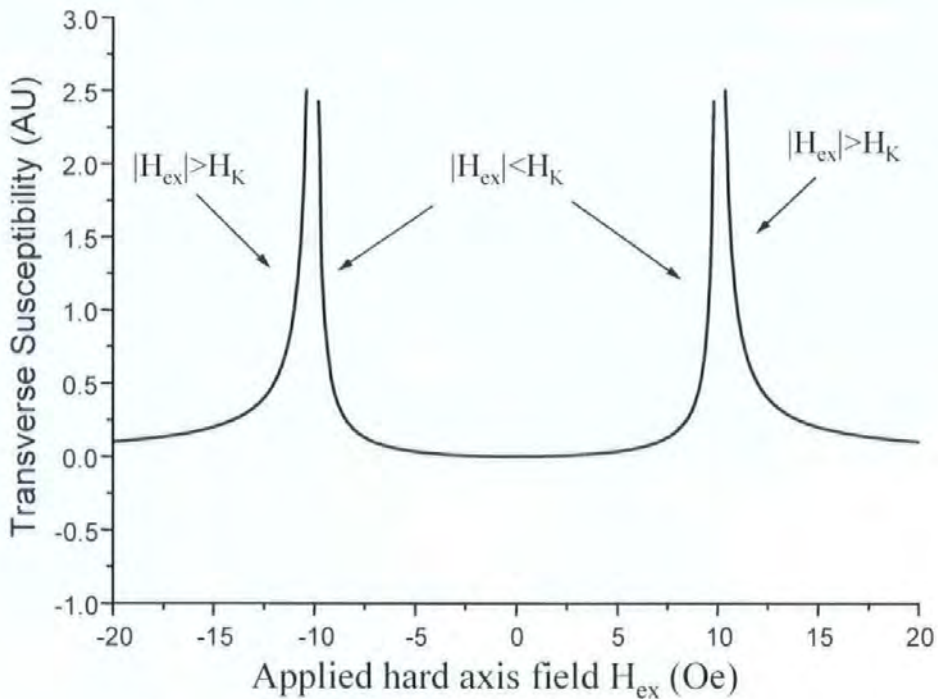
Figure 2.16   Illustration to show the effect of a hard axis field on the easy axis susceptibility.

This shows an ideal model within which the approach to H_K is not possible to determine, however, this model shows a very steep change in the permeability when the orthogonal field of the order of the anisotropy field is applied. In reality the peak value in the susceptibility will be defined by imperfections like the distribution of the anisotropy axes, and relaxation processes.

2.6   Magnetization dynamics

This section will consider the effects of dynamic magnetization. Firstly the effects of eddy currents are considered. These not only affect the operation of many kinds of magnetic devices and machines; they also influence magnetic measurements. It is therefore important that the nature of eddy currents be understood. Secondly the velocity of magnetization change by domain wall motion will be considered, including the internal friction or damping of magnetic materials, due to the oscillatory motion of domain walls. Finally the effect of the domain wall motion and oscillation to be developed to produce the frequency dependence of the transverse susceptibility of a thin film.

2.6.1   Dynamic susceptibility due to wall motion

Magnetization dynamics can occur by domain wall motion and / or rotation. In some specimens and in certain ranges of applied field, only one mechanism is operative; in others both operate. In this section only the wall motion mechanism and other factors that influence wall velocity will be examined.

Let a field **H** be applied parallel to a 180° wall and to the $\mathbf{M}_S$ vector in one of the adjacent domains. The field then exerts a force per unit area, or pressure, on the wall equal to $2HM_S$. Suppose that, when $H = 0$, the wall is initially located at a potential energy minimum. Then the equation of motion of the wall per unit area is

$$m\frac{d^2x}{dt^2} + \beta\frac{dx}{dt} + \alpha x = 2M_S H \tag{2.51}$$

where x describes the position of the wall.

If **H** is a weak alternating field, the wall will oscillate back and forth about its initial position. The first term in this equation, the mass per unit area m of the wall and its

acceleration, represents the inertia of the wall, or the resistance of the spins to sudden rotation. This term is not usually important. The second term represents the resistance to motion which is proportional to velocity, and β is accordingly called the viscous damping parameter which can be due to eddy currents or spin relaxation. The third term αx represents the force due to material imperfections such as micro stress or inclusions, and α is related to the shape of the potential-energy minimum in which the wall is located. The value of α determines the field required to move the wall out of the energy minimum and the ensemble of α values for the whole specimen determines the coercive force H_c, which is required for extensive wall movement.

The solution of Eq. (2.51) for a small alternating field $H = h\exp(-j\omega t)$ is of the form

$$x = \frac{2M_s}{\alpha - j\omega\beta} h$$

Here the first term in (2.51) is neglected.

The wall displacement x is related with the susceptibility as $\chi = (xM_s/d)/h$, where $2d$ is the domain size. The initial domain wall susceptibility is determined by,

$$\chi^0 = \frac{M_s^2}{\alpha d} \tag{2.52}$$

Then, the dynamical domain wall susceptibility is expressed as

$$\chi = \frac{M_s^2/d\alpha}{1 - j\omega\beta/\alpha} = \frac{\chi^0}{1 - j\omega/\omega_r} \tag{2.53}$$

Where Eq. (2.52) is used for the initial susceptibility.

The parameter $\omega_r = \alpha/\beta = M_s^2/d\chi^0\beta$ is the relaxation time for domain damping. Considering that in metallic ferromagnetics the main source of relaxation is related with the eddy currents, it can be calculated for a particular domain structure and sample geometry.

The damping effect of eddy currents on wall mobility can be understood from a simple model. Local wall displacements generate eddy currents circulating in and near a moving

domain wall, which creates the field H_{mi} as shown in Fig. 2.17. This field is in the opposite direction to the applied field H^0 to move the walls, because the true field actually acting on the wall is now less than H^0, the velocity of the wall is now less than it would be if the eddy currents did not exist, i.e. the wall motion is damped.
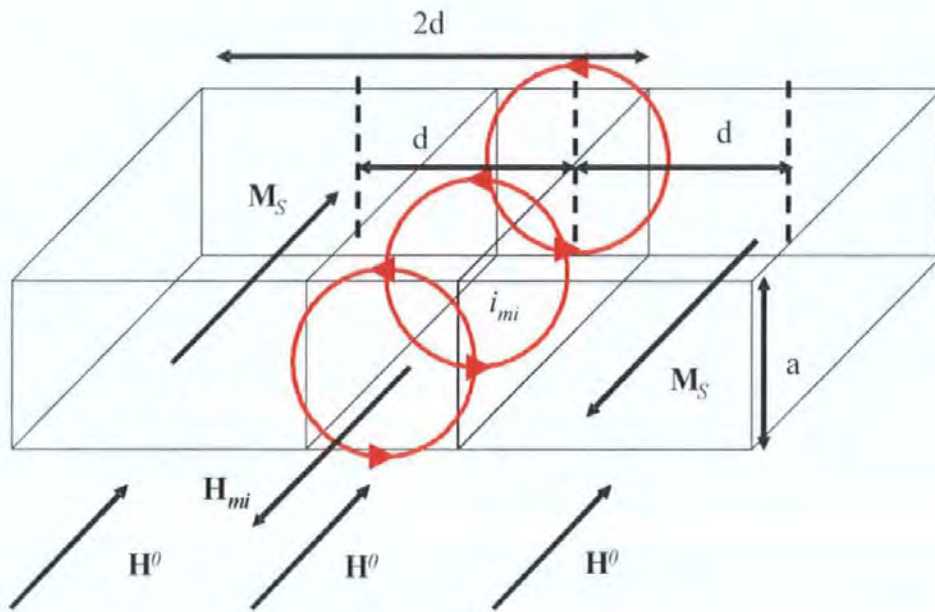
Figure 2.17   Micro eddy currents associated with a moving domain wall.

Now considering the dynamic permeability for thin film geometry with stripe domain structure following the model developed in [9]. The domains cross the entire film periodically with spacing 2d as shown in Fig. 2.17.   The dynamical magnetic susceptibility χ_{dw} due to domain wall movements taking into account the eddy current damping is defined from,

$$< \chi_{dw}^0 H >= \chi_{dw} < H^0 > \tag{2.54}$$

Where $< ..... >$ indicates averaging over the volume larger than the domain spacing, χ_{dw}^0 is the static domain wall susceptibility, H^0 is an external driving field, and H is the total microscopic field including H_{mi} generated by the eddy currents. It assumed that the domain wall shifts as a whole under the influence of the averaged field $< H >$.

It can be shown that Eq. (2.55) results in the same frequency dependence as obtained from Eq. (2.51) but gives the explicit form of the relaxation frequency

$$\chi_{dw} = \frac{\chi_{dw}^{0} <H>}{H^{0}} = \frac{\chi_{dw}^{0}}{1 - j\,\omega/\omega_{dw}} ,$$

(2.55)

$$\omega_{dw} = \frac{c^{2}}{64\pi^{2} \chi_{dw}^{0}.\sigma\alpha d \sum_{n} g_{n}} ,$$

(2.56)

and where,

$$g_{n} = \frac{4\coth\left[\dfrac{(2n+1)\pi d}{2a}\right]}{\pi^{3}(2n+1)^{3}}$$

(2.57)

It can be seen that with increasing frequency beyond the characteristic frequency of the domain wall relaxation ω_{dw}, the susceptibility value is greatly reduced. The estimation for an amorphous film of a few microns thickness gives the value of the domain relaxation frequency in the range of 100kHz. Therefore, for MHz frequencies the wall motion becomes strongly damped and the main contribution to the permeability will be due to rotation which in general is characterised by much faster relaxation.

2.6.2. Dynamic permeability due to magnetisation rotation.

In general, the rotational susceptibility is found from the solution of Lanadu-Lifshitz equation for the magnetization dynamics. In the case of a small AC magnetic field causing the rotation, a liner approximation is used which is further simplified for the local relationship between the magnetisation and the field (neglecting non uniform exchange effects). Even in this case for arbitrary angle between the DC magnetisation and anisotropy, this equation is rather complicated. It will result in a frequency dependent non-diagonal tensor $(\hat{\chi}_{rot})$ [9]. This leads to a description of the effective transverse permeability μ_{ef} that comprises of χ_{dw} and some components of $\hat{\chi}_{rot}$ [9]. In the case of a stripe domain structure in the presence of a hard axis field H_{ex}, the effective transverse permeability is expressed as,

$$\mu_{ef} = 1 + 4\pi(\chi_{dw} + \sin^2\psi\chi_{rot})$$

(2.58)

$$4\pi\chi_{rot} = \frac{(\Omega_1 + \Omega_M + j\tau\omega)(\Omega_2 + j\tau\omega) - \omega^2}{(\Omega_1 + j\tau\omega)(\Omega_2 + j\tau\omega) - \omega^2} - 1,$$

$$\Omega_1 = \gamma H_K(h\cos\psi + \cos 2(\alpha - \psi)),$$

(2.59)

$$\Omega_2 = \Omega_{II} + \Omega_M, \Omega_M = \gamma 4\pi M_s, \quad h = H_{ex}/H_K,$$

$$\Omega_{II} = \gamma H_K(h\cos\psi + \cos^2(\alpha - \psi)).$$

Here τ is a spin relaxation parameter, γ is the gyro magnetic constant and ψ is the angle between the equilibrium magnetization and external field H_{ex}. For $\omega = 0$ and $\alpha = \pi/2$ expression (2.59) reduces to the static value given by Eq. (2.48) and (2.49).

The relaxation frequency for the rotational processes estimated for CoSiB amorphous alloys is in the range of 30-60 MHz. Therefore, this contribution will be dominant at frequencies of tens of MHz.

In the intermediate frequency range, both contributions originated by wall motion and moment rotation should be considered. Regarding the dependence of the permeability upon an external DC magnetic field applied in the hard direction, the behaviour can be quite complicated in this frequency range.

Typically, the static domain permeability χ^0_{dw} shows a peak at zero field whereas the rotational permeability peaks at H_{ex} close to the anisotropy field [9]. It means that with increasing frequency the field plots of the permeability will typically change from those having a central peak to plots with two symmetrical peaks situated at the anisotropy field. Further increase in frequency moves the peaks towards even higher fields due to the effect of relaxation.

References

[1]   S.Chikazumi, *"Physics of Magnetism"*, R.E. Krieger Publishing Company, (1978).

[2]   B.D. Cullity, *"Introduction to magnetic materials"*, Addison-Wesley, (1972).

[3]   D. Craik, *"Magnetism - principles and applications"*, Wiley & Sons, p94 (1995).

[4]   W. F. Brown, Phys. Rev. 60, 139 (1941).

[5]   L. Néel, C. R. Acad. Science 228, 664 (1949).

[6]   C. Kittel, *"Introduction to Solid State Physics"*, John Wily & Sons Inc., New York, (1971).

[7]   E. C. Stoner and E. P. Wohlfarth, Phil. Trans. Roy. Soc. **A 240**, 599 (1948).

[8]   D. Jiles, *"Introduction to Magnetism and Magnetic Materials"*, Chapman and Hall, 2nd edition, (1998).

[9]   L.V. Panina, K. Mohri, T. Uchiyama, M. Noda, *"Giant-Magneto Impedance in Co-Rich Amorphous Wires and Films"* IEEE Trans. Magn. MAG-31(2) 1249, (1995).

Chapter 3. Magneto Impedance in thin films

When a ferromagnetic material carrying a low intensity, high frequency alternating current is subjected to an external magnetic field, it may exhibit a sharp change in its electrical Impedance with the relative change running into more than one hundred percent. This effect is known as the *Magneto Impedance* (MI) or the *Giant Magneto Impedance* (GMI) effect. In an electrically uniform material, the changes in the Impedance are a consequence of the AC current redistribution in the presence of the external magnetic field H_{ex} due to changes in the static magnetic structure of the material and its dynamic permeability μ_{ef}. Correspondingly, relatively high frequencies are essential to insure that the skin effect is strong and the current is not uniform across the conductor. Typically, the MI effect is larger and more sensitive if the external field H_{ex} causes the directional changes in the static magnetisation. Then a magnetic system with transverse anisotropy with respect to the AC current and H_{ex} is needed to realise a large and sensitive MI. In this case, the effective permeability of the material in the direction of the field produced by the current is most sensitive with respect to H_{ex} as was demonstrated in Section 2.6.

Since its discovery in 1994 [1,2] in amorphous micro wires, the MI effect has been extensively researched due to its importance for developing new types of high performance magnetic field sensors [3-6], the variety of MI materials has increased significantly, including amorphous films, magnetic/metallic multi-layers and nanocrystalline materials in the form of wires, ribbons and film [7-12]. MI in film systems is of a particular interest mainly because of miniaturisation and compatibility with integrated circuit technology. MI sensors developed in this work mainly utilize layered film systems.

This chapter begins by modelling the Impedance of a single layer thin film for arbitrary frequencies including the case of a strong skin effect. The Impedance is then considered in the next development of thin films, the multi-layer, which allows the development of different magnetic configurations through inducement of specific anisotropies in the magnetic layers.

Through the introduction of a coil to the multi-layer, cross magnetisation or off-diagonal impedances can be measured, making possible the investigation of the full surface Impedance tensor. Practical considerations of the samples dimensions on the Impedance are considered, before the introduction of Asymmetrical Magneto Impedance (AMI) in both dynamical and static configurations.

3.1   Magneto Impedance in a single layer magnetic conductor

Firstly, a general analysis of the MI (Magneto Impedance) effect in a simple single layer ferromagnetic conductor with a transverse magnetisation (with respect to the applied current direction) will be considered. The process will be considered in the configuration of an AC current and DC external magnetic field being parallel to one another.

When an alternating current $i = i_0 \exp(-j\omega t)$ flows through a magnetic conductor, it generates a transverse magnetic field, which in turn causes a corresponding magnetisation. When the frequency of this applied current is large enough it causes the current to flow near the surface of the material, which reduces the effective cross-sectional area of the material. A mathematical description of the skin effect has been obtained from classical electrodynamics. For a flat conductor carrying a sinusoidal alternating current, the penetration or skin depth, δ, is given by the well known expression: [13]

$$\delta_m = \frac{c}{\sqrt{2\pi\omega\sigma\mu_y}} \tag{3.1}$$

Where σ is the conductivity of the magnetic medium and μ_y is the effective transverse permeability. Equation (3.1) is strictly valid for a material with scalar type of the permeability μ. However, it can be generalised for certain cases of tensor $\hat{\mu}$, for example, when it is of a quasi-diagonal form in the coordinate system with the z-axis along the current. This case can be realised in films with transverse anisotropy and transverse domain structure with respect to the z-direction.

At low frequencies when the skin effect is weak in the magnetic conductor, the change in transverse magnetisation generates an additional inductive voltage V_L across the conductor, where R is the DC resistance of the conductor:

$$V = RI + V_L \tag{3.2}$$

In the case of a transverse domain structure, the current induced magnetisation is due to domain motion and magnetisation rotation. Both these contributions to the transverse permeability may be large, which results in relatively large values of the induced voltage. Moreover, both magnetisation processes can be sensitively affected by H_{ex}. However, as the frequency increases and the skin effect becomes stronger and more effective in the magnetic conductor, the current is distributed near the surface of a conductor, changing the total voltage V including both the resistive and inductive components. The current distribution is governed not only by the shape of the conductor and frequency but also the transverse magnetization dependency on H_{ex}. As a result, the total voltage can show a large magnetic response. The change in an AC voltage with the application of the field can be analysed in terms of the field dependence of the complex Impedance,

$$Z = R(\omega, \mu(\omega, H_{ex})) + jX(\omega, \mu(\omega, H_{ex})) \tag{3.3}$$

At low frequencies, when the skin effect is negligible, the first order term in an expansion of $Z(\omega)$ in powers of frequency is responsible for the voltage field dependence. This term is represented by an internal inductance, which is proportional to the static transverse permeability. When the skin effect is strong, the total Impedance including resistance R and reactance X, is field dependant through the penetration depth.

48
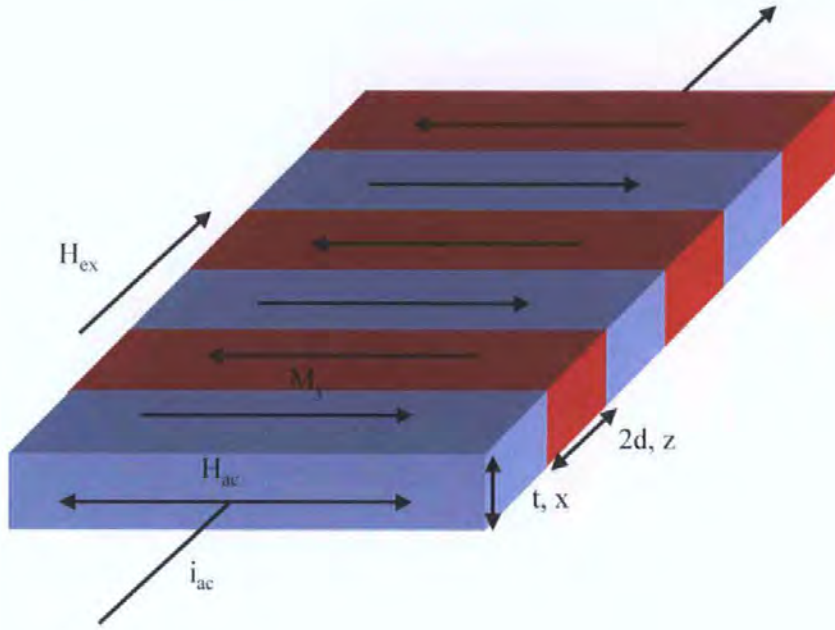
Figure 3.1   Transverse domain structure in a single layer film.

For the simple geometry of the thin film shown in Fig. 3.1, the Impedance can be calculated for any frequency, without neglecting the skin effect, in the case of homogeneous magnetisation changing linearly with the AC magnetisation field, as [13]

$$Z = R_{dc} \cdot jkt \coth(jkt)$$
$$k = \frac{(1+j)}{\delta_m} \tag{3.4}$$

Where R_{dc} is the DC resistance, and t the thickness of the conductor.

It follows from expressions (3.1) and (3.4) that the total Impedance of a magnetic conductor again is dependent upon the effective permeability, controlled through the skin depth. For films with a transverse domain structure as in Fig. 3.1 the effective permeability arises from two contributions: domain wall movement and rotation of the domain magnetization. These processes typically have a different dependence on the external magnetic field. The domain processes are more efficient at zero H_{ex} which causes the film to be uniformly magnetized along its length. On the other hand, the rotational processes are

stronger at H_{ex} of the order of the anisotropy field as was explained in section 2.6.2. These contributions also have a different frequency behavior.

At low frequencies, the domain wall movement dominates the permeability, whereas at higher frequencies the domain wall movement is strongly damped by microscopic eddy currents, and the magnetisation rotation contribution becomes dominant. This may result in different field behavior of the Impedance which has a single peak at zero field for lower frequencies and two symmetrical peaks at the anisotropy field for higher frequencies.

In early works, sensitivities of 8%/ Oe and a maximum change of around 65% have been reported in [14] for a CoFeB magnetic layer of dimensions 4μm thickness, 300μm width and 10mm length.

3.2   Magneto Impedance in multi-layer films

As shown in the last section, in electrically uniform materials subjected to a DC magnetic field, the MI effect originates from the dependence of the skin depth on the transverse permeability. Therefore, for thin films with the thickness of less than a few microns, very high frequencies (towards the GHz range) would be needed to obtain noticeable change in the Impedance.

In multi-layer structures having a highly conductive inner film, a very large change in Impedance can occur at lower frequencies when the inductance caused by the outer magnetic layers becomes sufficiently high in comparison with the DC resistance of the inner layer. This can result in a large enhancement of the MI ratio and a considerable extension of the operational frequency range into the lower frequency band compared to single layer films.

Although the magnetic layers are made of the same ferromagnetic alloy material, it is possible to create a different magnetic anisotropy within each layer. In particular, the configuration when the anisotropy axes are directed at an angle $\pm\alpha$ to the z axis, respectively for the upper ($x > 0$) and lower ($x < 0$) magnetic layers.

Through the variation of the angle $\pm\alpha$, special types of magnetic anisotropy can be realized in layered systems [15 -17]. Multi-layers with a transverse anisotropy $\pm\alpha=90°$ can

produce an antisymmetric response manifested through the measurement of off-diagonal terms in the surface Impedance tensor. Crossed-anisotropy films exhibit asymmetric MI characteristics (with respect to H_{ex}) in the presence of DC bias current I_b which induces a circulatory magnetic field $H_b(x > 0) = -H_b(x < 0)$. All these special MI characteristics are important to improve the sensor linearity.

In these sections, a symmetrical three-layer film model has been considered that reflects all the essential features of MI behaviour in multi-layered materials. Within this model, different magnetic configurations can be discussed.

The magnetic multi-layer consists of an inner conductive lead (labelled C) of a thickness $2d_1$ and two identical magnetic layers (F) of a thickness d_2 along the x-axis. The layers are parallel to the yz plane having a width b (y-axis) and length l (z-axis). An external DC magnetic field or sense field H_{ex} is applied parallel to the z-axis. Additionally, a DC bias current I_b can be also used to modify the static magnetic structure. A schematic diagram of this model is illustrated in Fig. 3.2.
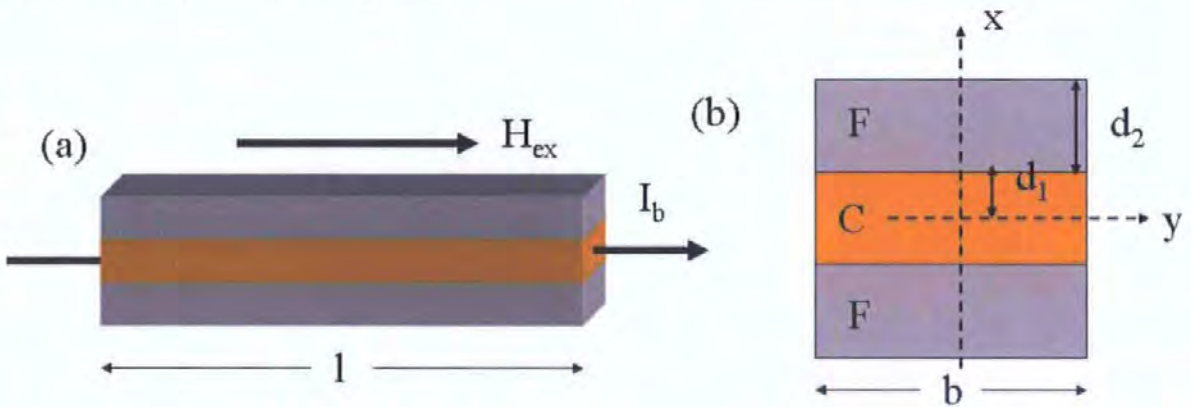
Figure 3.2   Schematic drawing of 3-layer MI film showing principal directions and quantities used. (a) general view, (b) cross-section of the film.

3.2.1 Impedance of a 3-layer film with transverse anisotropy

The first model to be investigated is the impedance of the 3-layer structure shown in Fig. 3.2, when it is excited by an alternating current $i = i_0 \exp(-j\omega t)$ flowing along the z-axis. The magnetic anisotropy is set so that $\alpha = 90°$ in the magnetic layers, leading to a transverse anisotropy in respect to the applied sense field H_{ex}.

The layer thickness d_1 and d_2 are such that the skin effect can be neglected. An assumption can be made that if the inner lead conductivity σ_1 is considerably higher than the conductivity σ_2 of the magnetic layers, in combination when their respective film thickness satisfying $\sigma_1 d_1 \gg \sigma_2 d_2$, that the current can be considered to mainly flow in the conductive lead.

With that assumption, the expression for the Impedance can be written in the form

$$Z = R_m - j\frac{\omega\Phi}{ci}, \tag{3.5}$$

Where $R_m = \dfrac{l}{2\sigma_1 d_1 b}$ is the resistance of the inner conductor,

Φ is the total transverse magnetic flux generated by the driving current i in the magnetic layers, and c is the velocity of light. If the film is treated as infinitely long in the y and z directions (neglecting edge effects), then the AC magnetic field h within the magnetic layers can be considered uniform.

$$\Phi = (\hat{\mu}h)_y d_2 l, \tag{3.6}$$

Where $\hat{\mu}$ is the AC permeability tensor. In general, the field h has x- and y-components due to the tensor form of the permeability. The value of the y-component is related to the current as $|h_y| = \dfrac{2\pi i}{cb}$, and the relation between h_y and h_x is determined from the condition that the normal magnetic flux is zero (i.e., $(\hat{\mu}h)_x = 0$); accordingly,

$$\Phi = \tilde{\mu}_{yy} h_y d_2 l = \tilde{\mu}_{yy} d_2 \frac{2\pi i l}{cb},$$

(3.7)

$$\tilde{\mu}_{yy} = \mu_{yy} + \frac{\mu_{xy}^2}{\mu_{xx} - 1}.$$

After using (3.7), the Impedance can be written in the form,

$$Z = R_m \left(1 - 2j\tilde{\mu}_{yy} \frac{d_1 d_2}{\delta_1^2} \right),$$

(3.8)

Where $\delta_1 = \dfrac{c}{\sqrt{2\pi\sigma_1\omega}}$ is the skin depth in the metallic inner layer.

Expression (3.8) shows that the MI ratio in the layered film can be very large even at relatively low frequencies when the skin effect is not substantial, and has a linear dependence on $\tilde{\mu}_{yy}$.

The Impedance for the geometry shown in Fig. 3.2 can be calculated exactly for any frequency, without neglecting the skin effect [15-18] by solving the Maxwell equations in each layer and imposing proper boundary conditions and continuity conditions at the interfaces. However for a film of 1 μm thickness with $\sigma_1 d_1 / \sigma_2 d_2 \approx 50$ (as for a CoSiB/Cu/CoSiB configuration of multi-layers with amorphous magnetic films), the approximate solution almost coincides with the exact one up to a frequency of 1 GHz.

3.2.2   Surface Impedance tensor

Considering a multi-layer film, shown in Fig. 3.2, in the presence of a small DC current sufficient to eliminate domain structure. In this case the permeability of magnetic layers has a general tensor form with non zero components $\mu_{yz} = \mu_{zy} \neq 0$. It means that the circulatory magnetic field (h_y) induced by current will now produce not only the corresponding circulatory magnetisation (m_y) but also a longitudinal magnetisation (m_z) Therefore, the AC current i induces a voltage V_f between the film ends (due to magnetisation m_y) and an additional coil voltage V_c caused by m_z. Similarly, if the film is placed in a variable longitudinal field h_{ex} induced by a coil current i_c, not only a longitudinal magnetisation is induced, but also a circulatory magnetisation contributing to V_f, as shown in Fig. 3.3(c) The crossed magnetisation processes $m_y(h_z)$ and $m_z(h_y)$ related to the voltages V_f, V_c are known as the inverse Wiedemann and the Matteucci effects [13], which typically are studied at low frequencies and require a helical type of anisotropy. With increasing frequency, the induced voltages become of the same order and are very sensitive to the longitudinal field, H_{ex} which allows for some unusual field effects.

The relationship between the generalized voltage (V_f, V_c) as response to excitation (i, i_c) is conveniently described through the introduction of the surface Impedance tensor $\hat{\varsigma}$ [15, 17, 20]. The tensor $\hat{\varsigma}$, is described through a two dimensional matrix of so called diagonal and off-diagonal terms. It relates the variable electric $\mathbf{e}_t$ and magnetic $\mathbf{h}_t$ fields taken on the external surfaces $x = \pm d$ ($d = d_1 + d_2$).
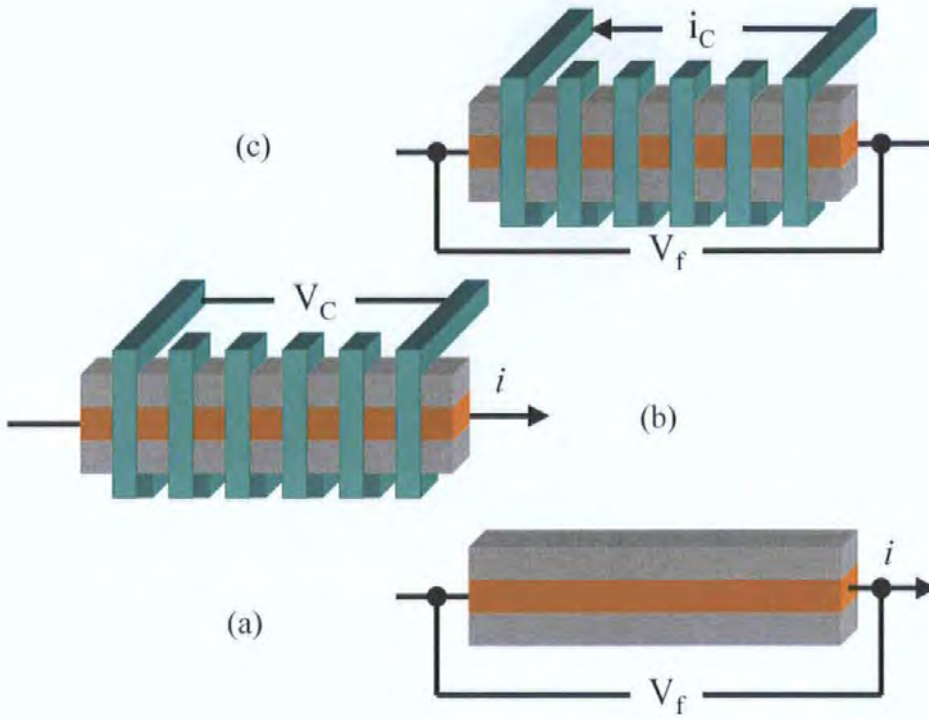
Figure 3.3   Methods of AC voltage excitation.

Thus,

$$\mathbf{e}_{t\alpha} = \varsigma_{\alpha\beta}(\mathbf{h}_t \times \mathbf{n})_\beta, \qquad \alpha, \beta = z, y, \tag{3.9}$$

Where **n** is a unit vector directed inside the film, while $\mathbf{e}_t$ and $\mathbf{h}_t$ are tangential to the surface. The voltage V_f is determined by the surface value of the longitudinal electric field $e_z(d) = e_z(-d)$ and is related to the fields h_y generated by the current flowing in the sample i and $h_z = h_{ex}$ by the current flowing in the coil i_c via the surface Impedance tensor components ς_{zz} and ς_{zy} as follows:

$$V_f = (\varsigma_{zz}h_y - \varsigma_{zy}h_{ex})l \qquad (3.10)$$

$$h_y = \left(\frac{2\pi}{cb}\right)i, \quad h_{ex} = \frac{4\pi n_1 i_c}{c}, \qquad (3.11)$$

Where n_1 is the number of turns per unit length in the excitation coil.

The coil voltage V_c is associated with the circulatory electric field $e_y(d) = e_y(-d)$ and can be expressed as

$$V_c = 2bN_2(\varsigma_{yz}h_y - \varsigma_{yy}h_{ex}), \qquad (3.12)$$

Where N_2 is the number of turns in the detection coil.

So generally two coils will be required, the excitation coil for producing h_{ex} and the pick-up coil for detection of V_c. Eq. (3.10) and (3.12) can be written in terms of currents i and i_c

$$\begin{pmatrix} V_f/l \\ V_c/2bN_2 \end{pmatrix} = \begin{pmatrix} \varsigma_{zz} & -\varsigma_{zz} \\ \varsigma_{yz} & \varsigma_{yy} \end{pmatrix}\begin{pmatrix} Ai \\ Bi_c \end{pmatrix}, \qquad (3.13)$$

Where the parameters $A = h_y/i$ and $B = h_{ex}/i_c$ are given by (3.11).

The surface Impedance tensor can be easily found in the low-frequency approximation. Here by analysing ς_{zz} and $\varsigma_{yz} = \varsigma_{zy}$ components. The parameter ς_{zz} or diagonal Impedance is obtained by comparing Eq. (3.8) and (3.13) where $i_c = 0$:

$$\varsigma_{zz} = Z/A = \varsigma_0\left(1 - 2j\tilde{\mu}_{yy}\frac{d_1 d_2}{\delta_1^2}\right), \quad \varsigma_0 = \frac{c}{4\pi\sigma_1 d_1} \qquad (3.14)$$

The off-diagonal component, ς_{yz}, can be found by considering the coil voltage V_c induced by the film current i. This voltage is related to the longitudinal magnetic flux:

$$V_c = -j\omega N_2 (2d_2 b)(\hat{\mu}h)_z .$$ (3.15)

When comparing Eq. (3.15) and (3.13) taken with $i_c = 0$ one can obtain

$$\varsigma_{yz} = \frac{V_c}{2bN_2 Ai} = -j\frac{\omega d_2 \tilde{\mu}_{zy}}{c}$$ (3.16)

$$\tilde{\mu}_{zy} = \mu_{zy} - \mu_{zx}\mu_{xy}/\mu_{xx}$$

3.2.3   Exact solution of the surface Impedance tensor

The calculation of $\hat{\varsigma}$ that is valid for any frequency is based on the solution of the Maxwell equations for the fields **e** and **h**, together with the equation of motion for the magnetisation vector **M**. The theoretical aspects of the problem can be very complicated and generally require approximations.

Typically, a linear approximation with respect to the time-variable parameters **e**, **h** and $m = M - M_0$ (where M_0 is the static magnetisation) is used. On assuming a local relationship between **m** and **h** ($m = \hat{\chi}$ **h**), the problem is simplified to finding the solutions of Maxwell's equations with a given AC permeability tensor $\hat{\mu} = 1 + 4\pi\hat{\chi}$, which corresponds to neglecting the exchange effects.

Further assumptions about $\hat{\mu}$ are needed. The permeability depends on many factors, including the domain configuration, anisotropy and stress distribution, and the mode of magnetisation (domain wall motion or magnetisation rotation). These factors can be very complicated in real materials, making modelling very difficult. The problem is simplified if the domain structure is not considered (in practice, it can be eliminated by a proper DC bias) and if M_0 is constant in the films. Then, $\hat{\mu}$ is determined by the magnetic moment rotation and is independent of the position.

Furthermore, the tensor $\hat{\mu}$ has a general form that reduces to a quasi-diagonal form in the primed co-ordinate system with the axis $z'\|\mathbf{M}_0$, shown in Fig. 3.4.
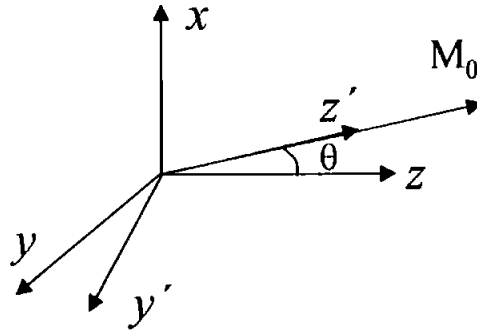
Figure 3.4   Original xyz *and primed* xy'z' *co-ordinate systems. Using primed coordinates reduces the permeability tensor to quasi-diagonal form.*

In the case of a uniform precession of the total magnetisation vector $\mathbf{M}$ around $\mathbf{M}_0$, the susceptibility tensor in the primed coordinates (x, y', z') is of the form

$$\hat{\chi} = \begin{pmatrix} \chi_1 & -j\chi_a & 0 \\ j\chi_a & \chi_2 & 0 \\ 0 & 0 & 0 \end{pmatrix} \qquad (3.17)$$

This form can be easily obtained from the linearised Landau-Lifshitz equation describing the magnetisation dynamics. The expressions for χ_1, χ_2, χ_a depend on a specific magnetic configuration [16].

By restricting the consideration of magnetisation rotation dynamics only if the domain wall displacements are strongly damped. Then, (3.17) determines the permeability tensor $\hat{\mu} = 1 + 4\pi\hat{\chi}$. To calculate the normalized parameters $\tilde{\mu}_{xx}$ and $\tilde{\mu}_{zy}$ which appear in expressions (3.14) and (3.16) for the Impedance components, the tensor $\hat{\mu}$ has to be written in the original coordinates x, y, z, which yields:

$$\tilde{\mu}_{yy} = 1 + 4\pi\chi\cos^2\theta \qquad\qquad (3.18)$$

$$\tilde{\mu}_{zy} = -4\pi\chi\sin\theta\cos\theta , \qquad\qquad (3.19)$$

$$\chi = \chi_2 - \frac{4\pi\chi_a^2}{1 + 4\pi\chi_1}$$

where θ is the angle between the DC magnetisation M_0 and the z axis.

3.2.4 Magneto Impedance effect in practical samples

For a practical multi-layer sample, the effect of in-plane width on MI has to be considered. If the edge effect is neglected (approximation of an infinite width), the magnetic flux generated by the current flowing along the inner lead is confined within the outer magnetic layers. In a realistic multi-layer of finite width, the flux leaks across the inner conductor [18], [21], [22]. This process eventually results in the considerable drop in MI ratio, if the film width is smaller than some critical value depending on the transverse permeability and the thickness of the magnetic and conductive layers. This process is similar to that resulting in a drop in the efficiency of inductive recording heads [23], [24].

The effect of the flux leakage across the conductive layer is found to be described by an effective "AC demagnetising" factor g that reduces the permeability and makes it less sensitive to the DC field H_{ex} when the film width b is decreased. In the low-frequency approximation when the skin effect is neglected the parameter g is given by:

$$g(k) = \frac{1}{(k_1\lambda)^2}\left(1 - (k\lambda)^2 \frac{kb\sinh kb}{kb\sinh kb + 2(k_1\lambda)^2(1 - \cosh kb)}\right) \qquad\qquad (3.20)$$

$$k^2 = 1/\lambda^2 - k_1^2, \quad \lambda^2 = d\,1 d\,2\tilde{\mu}_{yy}, \quad k_1 = (1 + j)/\delta_1$$

For $kb >> 1$ (or $b/ \lambda >> 1$) the function g tends to be unity. It means that the parameter $b* = 1/k$ plays the role of a critical width: for $b < b*$ all the film dimensions b, d_1 and d_2 influence the value of the Impedance. In the low- frequency limit, $b* = \sqrt{d_1 d_2 \tilde{\mu}_{yy}}$. Typical parameters for the structures of interest are $d1 \approx d2 \approx 0.1 - 0.5 \mu m$, $2b \approx 10 - 50 \mu m$ and $\mu_t \approx 10^3$, for which $b* \approx 3 - 15 \mu m$ is comparable to the half-width, which means that the size effects can not be neglected.

Figure 3.5 shows the plots of the Impedance change vs. frequency with the film width b as a parameter for magnetic films with transverse anisotropy [18]. The function $|(Z(H_{ex})|$ has a maximum at $H_{ex} \approx H_K$, associated with that for the rotational transverse permeability $\tilde{\mu}_{yy}$. Therefore, the introduced parameter gives the maximum Impedance change. The magnetic and electric parameters taken for the calculations correspond to amorphous CoFeSiB/Cu/CoFeSiB sputtered multi-layers [25], [26].

For a wide film ($b > 100$ μm for $d = 0.5$ μm or $b > 10$ μm for $d = 0.1$ μm), the results are very close to those obtained for an infinite in-plane film. With decreasing b, the Impedance change ratio decreases substantially: for example, for 100 μm-wide films, $\Delta Z/Z$ reaches more than 300% at a frequency of 150 MHz, whereas its value is only about 70% for $b = 10$ μm at this frequency. The decrease in MI is stronger at lower frequencies where the critical width $b*$ is larger. In the foregoing example, $\Delta Z/Z$ recovers up to 200% at a frequency of 900 MHz. As a result, the Impedance plots do not show flat regions for small values of b.
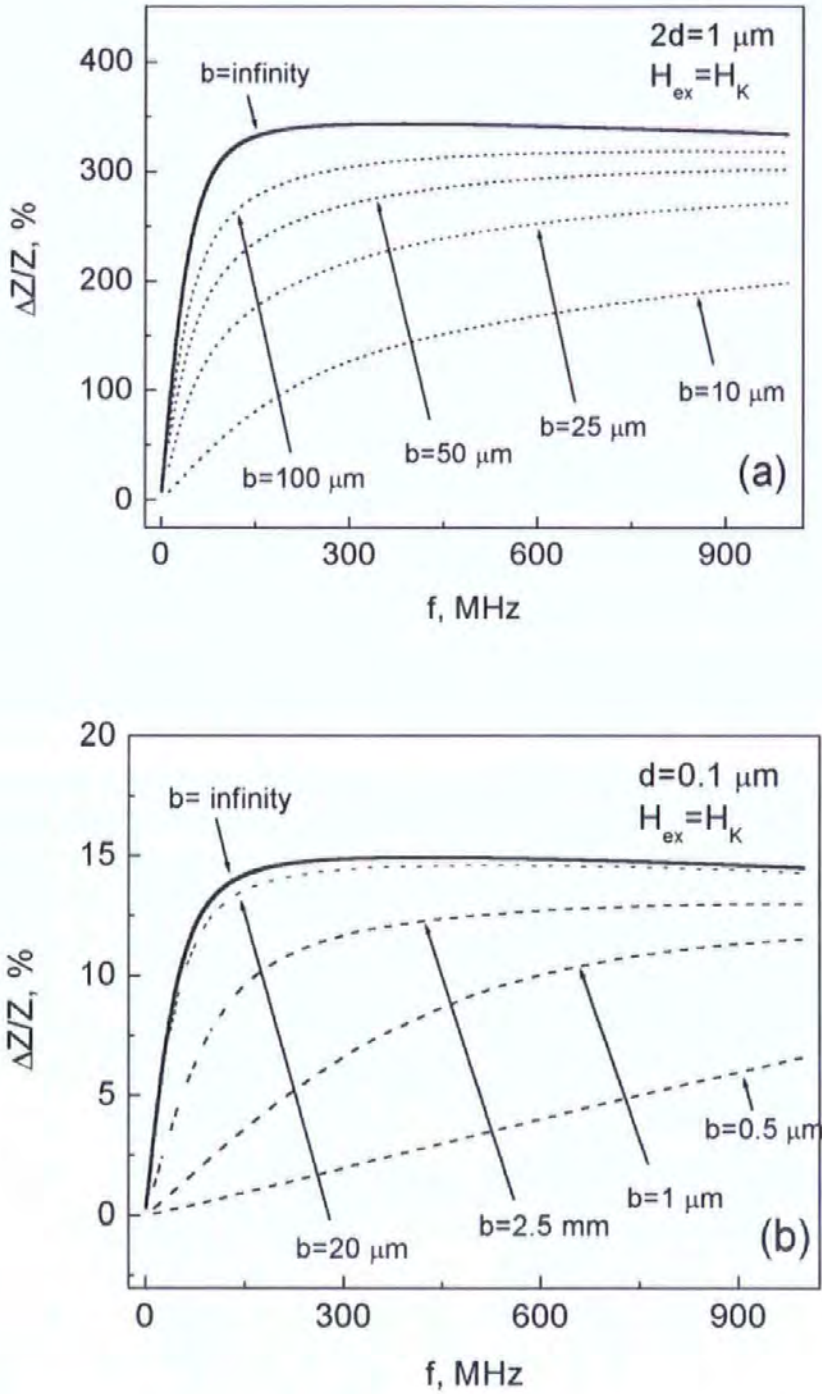
Figure 3.5   Maximum Impedance change ratio $\Delta Z / Z = |(Z(H_K) - Z(0)) / Z(0)|$ in a sandwich structure with transverse anisotropy as a function of frequency with the width b as a parameter. $d_1 = d_2 = 0.25 \ \mu m$ in (a) and $d_1 = d_2 = 0.05 \ \mu m$ in (b).

3.3 Asymmetrical Magneto Impedance (AMI) in multi-layer films

The field behaviour of the surface Impedance tensor and therefore the voltage responses are associated with that of the permeability tensor. From Eq. (3.18) and (3.19) it follows that the permeability parameters $\tilde{\mu}_{yy}$ (diagonal) and $\tilde{\mu}_{zy}$ (off-diagonal) depend on the angle θ of the static magnetisation M_0. Therefore, in multi-layer structures with an asymmetric arrangement of M_0 with respect to H_{ex} the Impedance will also show an asymmetric behaviour with respect to H_{ex}. This asymmetric response has been defined as the Asymmetric Magneto Impedance effect, or AMI. [15]-[17], [27].

AMI can be produced in multi-layer structures with cross-anisotropy in the presence of the DC bias current I_b.

However, the other important conclusion from section 3.2.3 is that the components of the surface Impedance tensor $\hat{\varsigma}$ have a different symmetry with respect to the DC magnetisation. The diagonal components do not change when the direction of M_0 is reversed, whereas the off-diagonal components do. Therefore, AMI can also be found if the voltage response in Eq. (3.10) is represented by the combination of ς_{zz} and ς_{zy}, which is not associated with that for $M_0(H_{ex})$ [27]-[29].

3.3.1   Dynamical AMI in multi-layer films with transverse anisotropy

By considering the role that the off-diagonal component ς_{zy} plays in producing asymmetry in the total voltage response V_f. According to Eq. (3.10), the ς_{zy} contribution to V_f appears in the presence of the AC bias field h_{ex}, produced by the coil current. As this asymmetry is produced only by the presence of an AC bias field it has been termed as dynamical AMI.

Considering a film with a transverse anisotropy, since this case does not have asymmetry in respect to $M_0(H_{ex})$. The transverse domain structure can be removed by the application of a small DC current inducing the transverse bias field H_b. Excitation is with both AC current and H_{ex} induced by the coil around the film. Then, the total voltage is described by Eq. 3.19. In this form, the diagonal components are symmetric, and off-diagonal are asymmetric. As a result, the total voltage exhibits asymmetry because $\varsigma_{zz}(H_{ex}) = \varsigma_{zz}(-H_{ex})$, but $\varsigma_{zy}(H_{ex}) = -\varsigma_{zy}(-H_{ex})$.

Figure 3.6 shows plots of the real parts of ς_{zz} and ς_{zy} vs. H_{ex}, at a frequency of 120 MHz. The parameters used correspond to amorphous CoSiB/Cu/CoSiB multi-layers: $2d = 1\square$m and $2d_1 = d_2$. The field behaviour of the diagonal component ς_{zz} is characterized by two symmetrical peaks when H_{ex} is equal to $1.3\,H_K$, shown in Fig. 3.6(a). However, the off-diagonal component ς_{zy} shown in Fig. 3.6b is anti-symmetric with respect to H_{ex}. Under the application of sufficient DC bias current I_b, the diagonal component shown in (a) is suppressed and the overall voltage response is anti-symmetric as shown in (b)
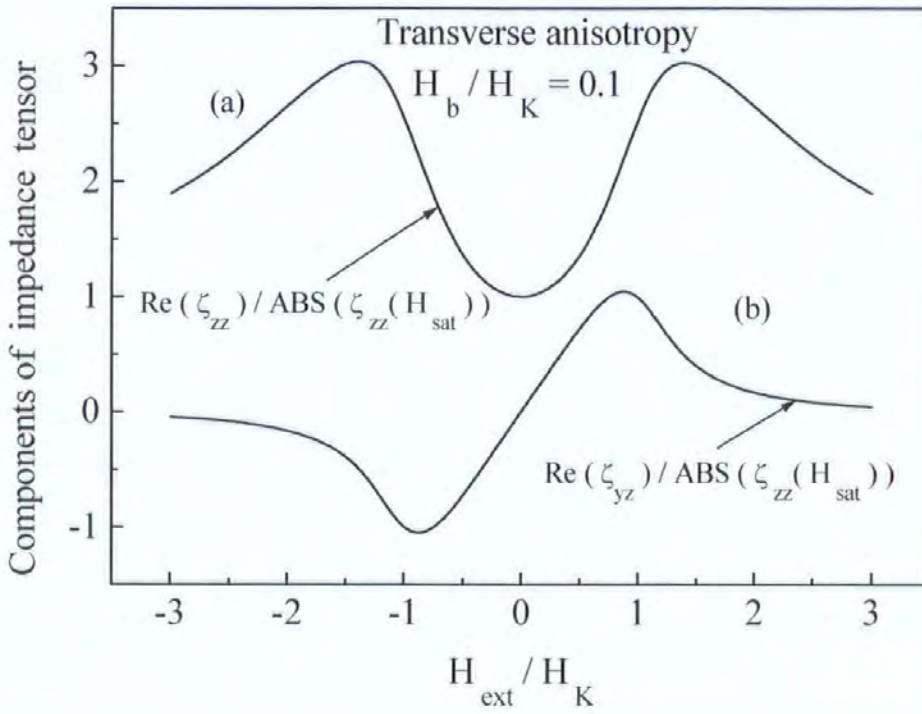
Figure 3.6   Surface Impedance tensor and voltage response in a film attached to a coil (transverse anisotropy).

3.3.2   Static AMI in multi-layer films with crossed anisotropy

In this section, AMI due to an asymmetric magnetisation reversal is discussed [15]-[17], [27]. A particular magnetic configuration can be realized in the multi-layer structure by combining a crossed- anisotropy and DC bias current producing a circulatory bias field H_b. The rotational magnetisation process is illustrated in Fig. 3.7 as calculated from Stoner-Wohlfarth model described in section 2.4. The magnetisation loops are given for different values of H_b.
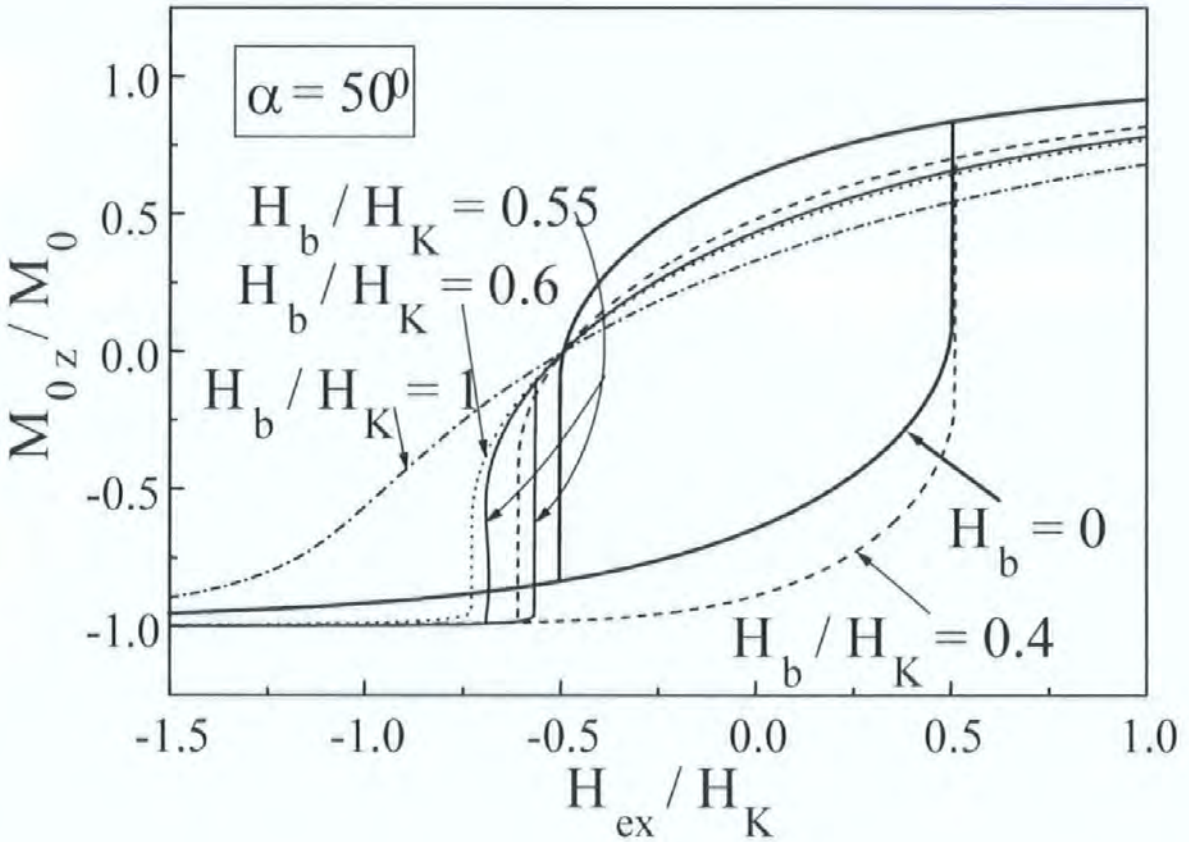
Figure 3.7   Magnetisation curves $M_{0z}(H_{ex})$ in a wire with a helical anisotropy ($\alpha = 50°$) for different magnitudes of DC bias field H_b.

Reversal of M_0 by rotation is possible, since the magnetisation vector during its rotation is held parallel to the surface, without going through high-energy demagnetisation states. It is seen that the DC bias causes a transition from a symmetric hysteresis curve to an asymmetric hysteretic one at a critical field $H_b = H^* = H_K \cos\alpha$.

The Impedance characteristics reflect this behaviour as shown in Fig. 3.8, where the plots of ς_{zz} vs. H_{ex} are given in [16]. For H_b slightly larger than H^*, the field sensitivity of the Impedance change is especially high, and the nominal change can be more than 100% for negative fields, when H_{ex} is changed by only $0.1 H_K$. The other components of the Impedance tensor exhibit a similar behaviour. This type of static asymmetry will be investigated experimentally through the construction of crossed anisotropy multi-layers, it is practically easier to realise than dynamical asymmetry as it does not required the planar coil to measure off diagonal components.
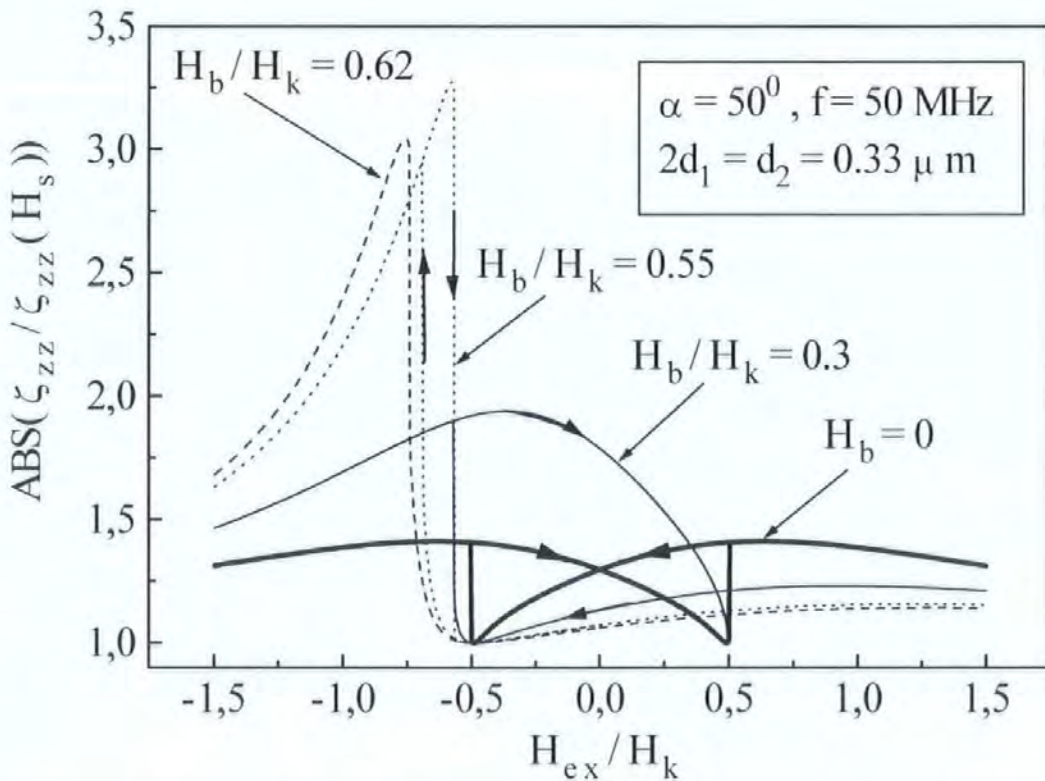
Figure 3.8   Modifications in the longitudinal Impedance ς_{zz} vs. H_{ex} under the effect of DC bias $0 \le H_b/H_K \le 1$, when $\alpha = 50°$.

References

[1]   L. V. Pamina and K. Mohri, Apply. Phys. Lett. 65, 1189 (1994).

[2]   R. S. Beach and A. E. Berkowitz, *"Sensitive field- and frequency-dependent impedance spectra of amorphous FeCoSiB wire and ribbon"* J. Appl. Phys. 76, 6209 (1994).

[3]   L. V. Panina, K. Mohri, K. Bushida, and M. Noda, *"Giant magneto-impedance and magneto-inductive effects in amorphous alloys"* J. Appl. Phys. 76, 6198 (1994).

[4]   L. V. Panina and K. Mohri, *"Magneto-impedance in multilayer films"* Sensors and Actuators A 81, 71 (2000).

[5]   K. Mohri, T. Uchiyama, L. P. Shen, C. M. Cai, and L. V. Panina, *"Amorphous wire and CMOS IC-based sensitive micro-magnetic sensors (MI sensor and SI sensor) for intelligent measurements and controls "* J. Magn. Magn. Mater 249, 351 (2002).

[6]   K. Mohri, T. Uchiyama, L. P. Shen, C. M. Cai, and L. V. Panina, *"Sensitive micro magnetic sensor family utilizing magneto-impedance (MI) and stress-impedance (SI) effects for intelligent measurements and controls"* Sensors and Actuators A 91, 85 (2001).

[7]   Ahn, S. J., Kim, C. G., Park, C. G., and Yu, S. C. 2001, *Mater. Sci. Eng. A*, vol. 304,   p. 1026.

[8]   Pirota, K. R., Schoenmaker, J., Sartorelli, M. L., Knobel, M., Gutierrez, J., and Barandiaran, J. M. 1999c, *Mater. Sci. Forum*, vol. 302-303, p. 229.

[9]   Sommer, R. L. and Chien, C. L. 1995, *Appl. Phys. Lett.*, vol. 67, p. 3346.

[10]   Antonov, A., Iakubov, I. T., and Lagar'kov, A. N. 1997, *IEEE Trans. Magn.*, vol. 33, p. 3367.

[11]   Zhou, Y., Yu, J. Q., Zhao, X. L., and Cai, B. C. 2001, *J. Appl. Phys.*, vol. 89, p. 1816.

[12]   Guo, H. Q., Kronmuller, H., Dragon, T., Cheng, Z. H., and Shen, B. G. *"Influence of nanocrystallization on the evolution of domain patterns and the magnetoimpedance effect in amorphous Fe73.5Cu1Nb3Si13.5B9 ribbons"* 2001, *J. Appl. Phys.*, vol. 89, p. 514.

[13]   L. V. Panina, K. Mohri, T. Uchiyama and M. Noda, *"Giant magneto-impedance in Co-rich amorphous wires and films"* IEEE Trans. Magn. 31, 1249 (1995).

[14]   T. Uchiyama, K. Mohri, L. V. Panina and K. Furuno, *"Magneto-impedance in sputtered amorphous films for micro magnetic sensor"* IEEE Trans. Magn. 31, 3182 (1995).

[15]   D.P. Makhnovskiy, A.S. Antonov, A.N. Lagar'kov and L.V. Panina, *"Field-dependent surface Impedance of a bilayer film with an antisymmetric bias magnetisation"*, *J Appl Phys* 84 (1998), 5698-5702.

[16]   L.V. Panina, D.P. Makhnovskiy and K. Mohri, *"Analysis of magneto-impedance in multilayers with cross-anisotropy"*, *J Mag Soc Jpn*, 23, (1999), 925-931.

[17]   D.P. Makhnovskiy, L.V. Panina, A.N Lagar'kov and K. Mohri, *"Effect of antisymmetric bias field on magneto-Impedance in multilayers with crossed anisotropy"*, *Sens Actual A: Phys* 81 (2000), 106-110.

[18]   L.V. Panina, D. Zarechnuk, D.P. Makhnovskiy and D.J. Mapps, "*Two-dimensional analysis of magneto impedance in magnetic/metallic multi-layers*", *J Appl Phys* **89** (2001), 7221-7223.

[19]   M. Vazquez and A. Hernando, "*A soft magnetic wire for sensor applications*", *J Phys D: Appl Phys* **29** (1996), 939-949.

[20]   D.P. Makhnovskiy, L.V. Panina and D.J. Mapps, "*Field-dependent surface Impedance tensor in amorphous wires with two types of magnetic anisotropy: helical and circumferential*", *Phys Rev B* **63** (2001), 144424-144441.

[21]   V. Korenivski, "*GHz magnetic film inductors*", *J Magn Magn Mater* **215-216** (2000), 800-806.

[22]   D.P. Makhnovskiy and L.V. Panina, "*Size effect on magneto-Impedance in layered films*", *Sens Actuat A: Phys* **81** (2000), 91-94.

[23]   A. Paton, "*Analysis of the efficiency of thin-film magnetic recording heads*", *J Appl Phys* **42** (1971), 5868-5870.

[24]   R. W. Cross, S.E. Russek, S.C. Sanders, M.R. Parker, J.A. Barnard and S.A. Hossain, "*Size and self-field effects in giant magnetoresistive thin-film devices*", *IEEE Trans Magn* **30** (1994), 3825-3827.

[25]   T. Morikawa, Y. Nishibe, H. Yamadera, Y. Nonomura, M. Takeuchi and Y. Taga, "Giant *magneto-Impedance effect in layered thin films*", *IEEE Trans Magn* **33** (1997), 4367-4369.

[26]   T. Morikawa, Y. Nishibe, H. Yamadera, Y. Nonomura, M. Takeuchi, J. Sakata and Y. Taga, "*Enhancement of giant magneto-Impedance in layered film by insulator separation*", *IEEE Trans Magn* **32** (1996), 4965-4967.

[27]   L.V. Panina, D.P. Makhnovskiy and K. Mohri, "*Mechanism of asymmetrical magnetoimpedance in amorphous wires*", *J Appl Phys* **85** (1999), 5444-5446.

[28]   D.P. Makhnovskiy, L.V Panina and D.J. Mapps, "*Asymmetrical magneto-Impedance in a sandwich film with a transverse anisotropy using an AC bias*", *J Magn Magn Mater* **215** (2000), 629-633.

[29]   K. Gunji, L.V. Panina and K. Mohri, "*Asymmetrical Magneto-Impedance in amorphous wires with helical current excitation*", *J Mag Soc Jpn* **21** (1997), 793-797.

Chapter 4. Thin film technology

This chapter provides background information on the general manufacturing processes involved in the production of thin films and the methods by which thin film multi-layers were prepared for this work. Firstly, the concept of sputtering as the means of depositing the material, which constitutes a film, is introduced, with further detail on the equipment required for the process. Next, the means of shaping the thin film to desired dimensions and structure are discussed through the use of masks and etching. Lastly, inducing anisotropy in the thin film is discussed, whether during the sputtering process or post manufacturing with heat or current annealing treatments.

All thin films prepared in this work were manufactured at the CRIST (Centre for Information Storage Technologies) micro magnetic clean room at Plymouth University, which has sputtering and evaporating equipment such as two Nordiko NM2000 systems with deposition controlled down to several nanometres, CVC ion milling system for dry etching, an OAI 500 mask aligner capable of resolving line widths down to 0.8 of a micron, optical lithography, annealing furnace, electron and optical microscopy, basic optical and microwave measurement equipment.

4.1   Thin film fabrication methods

As a general background to the manufacturing methods involved in thin film production an overview of the methods utilized are presented. There are a number of different industry standard processes that are available for the fabrication of thin-films, with the most common deposition technique being sputtering. Sputtering is the removal of material from a target to deposit it in the form of a condensed coating on a substrate. This process is carried out within a vacuum chamber that contains two electrodes, the target (cathode) and the substrate (anode).

The close packed atoms at the surface layer of the target are subjected to a bombardment of high velocity atomic sized particles. The majority of these incident ion collisions agitate and free surface atoms, through the transfer of momentum. The sputtered target atoms are ejected and mobilise in straight lines to condense on the substrate surface. Some of the bombarding ions are reflected back and are neutralised, but may still have sufficient energy to reach the substrate were the film is being deposited. This can be a source of substrate bombardment (back scattering) that can affect the resulting properties of the film. Secondary electrons which are emitted either join the oscillating plasma gas, which causes the continuous ionisation of the gas needed to sustain the incident ions for sputtering, or they liberate their energy in the form of heat on colliding with the substrate or other parts of the chamber. The process is schematically shown in Fig 4.1(a)

In order to obtain the fast moving atomic-sized particles required for this process, the target is immersed in a "gas plasma" or "glow discharge" with a high negative voltage applied to its surface. An inert gas such as argon is introduced into the vacuum chamber at some specified pressure, and the gas particles are ionised in an electric field, which produces the plasma. The high negative voltage at the surface of the target attracts the ions from the plasma, creating the bombardment of high velocity particles necessary to free the target surface atoms. The process needs to take place in a vacuum so that the number of gas molecules between the target and substrate is low, hence reducing the chance of any collisions between the dislodged target atoms and gas molecules, which prevents condensation on the substrate.
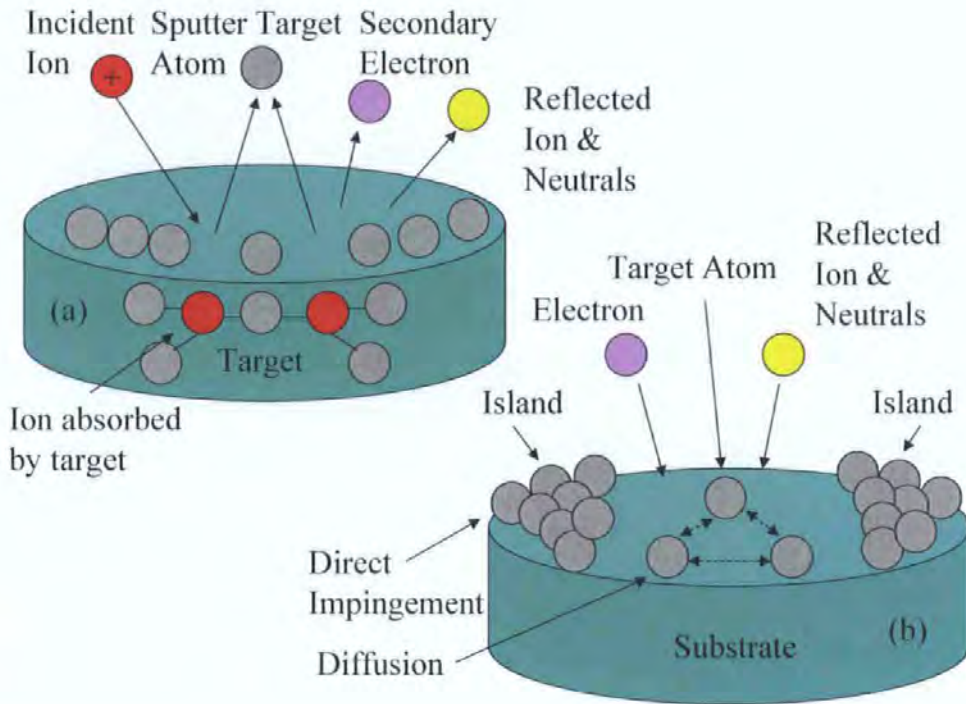
Figure 4.1   Illustration of the sputtering process at the target (a), and film generation at the substrate (b).

The condensation coefficient for a particular sputtered material is determined by several factors. These include the bonding energy between the atoms and the substrate, the substrate temperature and the rate of arrival of atoms at the substrate. The structure of the film grown on the substrate is extremely sensitive to the deposition conditions.

Once at the substrate, the sputtered atoms from the target jump around from one absorption site to another until they combine with another atom and become more stable and less mobile, or evaporate off. This process continues with the atoms combining to make larger groups that have even lower mobility, with their ability to jump around and thus evaporate becoming slimmer. As more atoms combine the nucleation stage of the thin-film growth begins, leading to the formation of quasi-stable "islands" each consisting of tens or hundreds of atoms. These islands grow in size, eventually touching (coalescence stage), finally reaching continuity. During the coalescence stage the film will typically have hills and

valleys, and continuity of the film may not occur until an average film thickness of several hundred Angstroms is reached

Other types of particles besides the target atoms can also bombard the substrate, which can affect the growth of the film. Unwanted neutral reflected atoms and gas particles have enough energy to sputter the film or become integrated into the film itself. These particles are a problem, as they cannot be manipulated by the use of electric or magnetic fields. In addition to these neutral particles, the substrate can also suffer bombardment from reflected gas ions. Control of these particles can be achieved by applying a bias to the substrate, leading to the technique of bias sputtering. All particles impinging on the substrate, including electrons, will liberate energy in the form of heat, increasing the temperature of the substrate which affects the mobility of the target atoms and hence the depositing film. The basic processes occurring at the surface of the substrate are shown in Fig. 4.1(b).

The high energies involved in the sputtering process makes it a very reliable method of deposition, particularly for alloys. Film characteristics such as composition and homogeneity are critical for many thin-film applications, and sputtering offers a wider range of control over the thin film properties than any other deposition method. Physical properties such as grain structure, film stress, adhesion, step coverage, uniformity, and film composition can be varied in the sputtering process by controlling such parameters as sputtering pressure, temperature, power and substrate bias voltage. Although sputtering is one of the most versatile of all the deposition methods, its rates of deposition are relatively slow (50Å-500Å per minute), and the cost of the sputtering equipment is generally higher than for most other coating processes.

4.1.1   R.F. sputtering process

For films produced locally in the CRIST facility, a Nordiko NM 2000 radio frequency (RF) magnetron sputtering system was used. A schematic diagram of the system is shown in Fig. 4.2. A picture of the actual system is shown in Fig. 4.3. The process information in this section is described from work initially carried out in [1], which served as a training document for CRIST in the operation of the equipment for manufacture of the films prepared in this work.

Before sputtering can commence, the chamber is firstly evacuated by the rotary pump. When an adequate base pressure is achieved, the diffusion pump is used to evacuate the chamber to the higher vacuum required. RF sputtering is more widely used than DC sputtering, as it is more efficient and can be used to deposit insulators. If a low frequency alternating voltage was applied to the electrodes in a chamber the ions would still be mobile enough to complete a DC discharge at each electrode on each half cycle, requiring a source of secondary electrons at both electrodes to be sustained. With applied voltages at frequencies above 50 kHz and up to the MHz region the minimum pressure at which a discharge will be sustained is reduced. At these frequencies, electrons oscillate in the glow space, acquiring enough energy from the RF field to generate ionising collisions. In this respect the RF glow discharge is very different to the DC glow discharge as the dependence on secondary electrons is reduced and thus the breakdown voltage is lower. As RF can be coupled through non conductors, insulators can be sputtered.
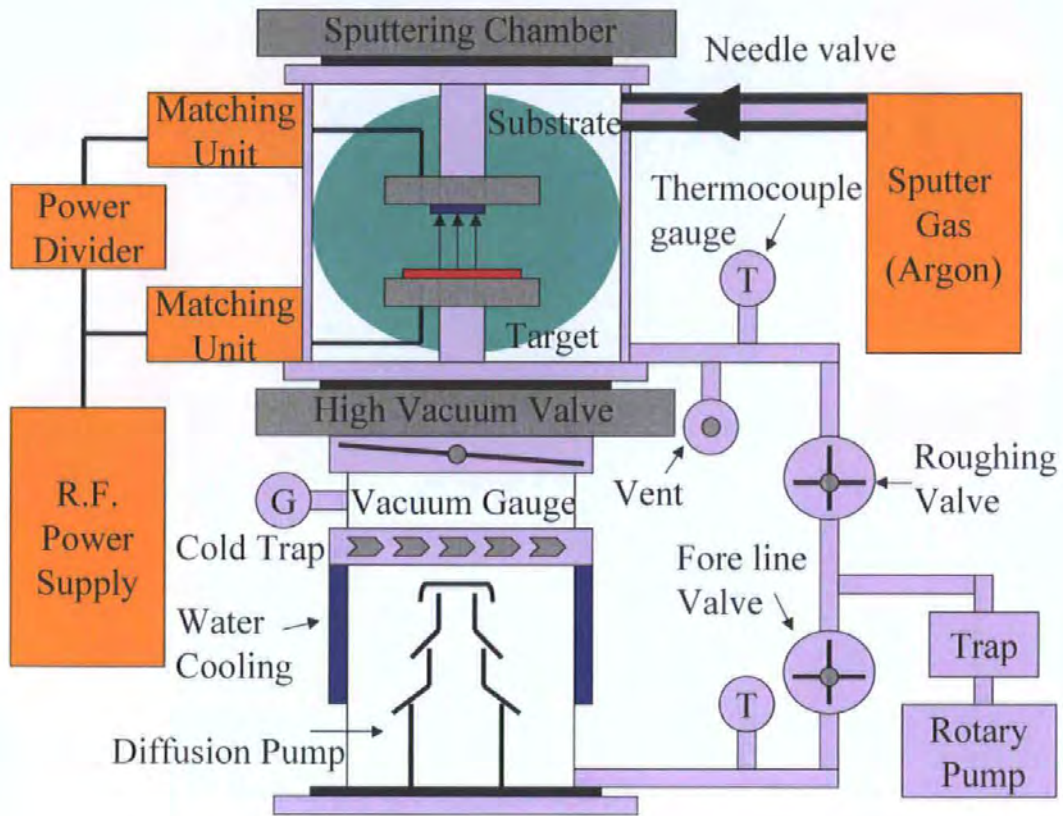
Figure 4.2   Schematic diagram illustrating the R.F. sputtering system.
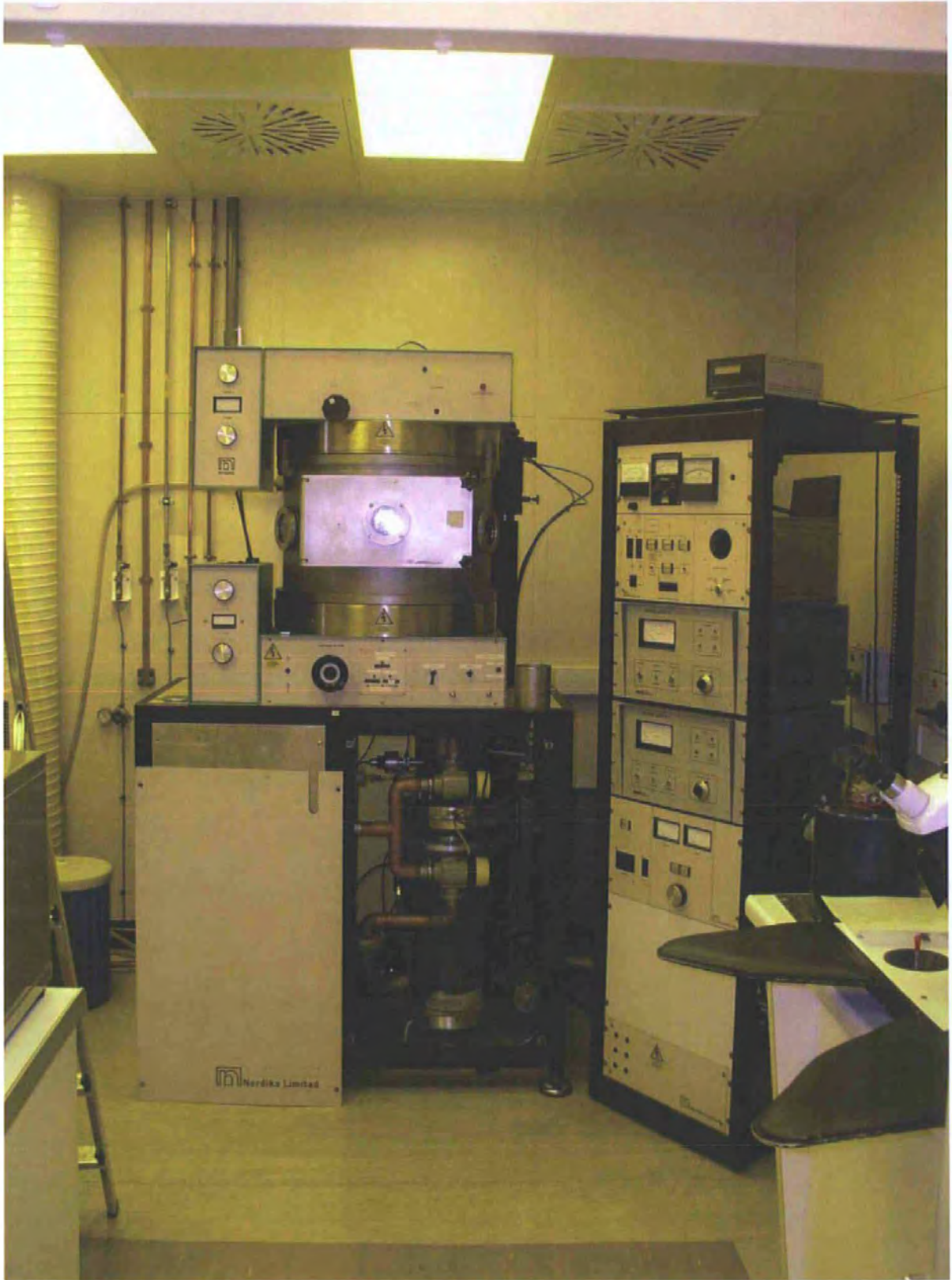
Figure 4.3   Nordiko NM2000 sputtering system installed in CRIST.

4.1.2   Substrate preparation

In order to ensure the quality, reproducibility, and adhesion of the deposited films, substrate cleanliness is essential. Once removed from their packaging the substrates were thoroughly wiped with hot detergent (neutracon) using a soft clean room cloth to remove grease marks and any particle debris stuck to the surface. After rinsing in deionised water, the substrates were placed in an ultrasonic bath containing a hot solution of diluted detergent and cleaned for a further 15 minutes. After a final and thorough rinse, the substrates were dried with a Nitrogen gun and then examined under a microscope. If not completely clean, the cleaning process was repeated. Finally, the substrates are placed in an oven to dry at a temperature of 135°C for half an hour before being transferred to the sputtering chamber. Before deposition, the substrate was sputter etched to remove any contaminants that may still remain after the cleaning process.

4.2   Induced anisotropy

Two different methods of inducing an anisotropy in the thin film sample are illustrated in this section, firstly during the deposition process, and secondly after the deposition process. It is necessary to induce different types of anisotropy to allow different magnetic conditions to be produced in the thin films. It was used to produce the strongly defined transverse anisotropy in the multi-layers prepared for this work

4.2.1   Magnetic anisotropy induced during the deposition process

Inducing a uniaxial anisotropy by the application of a magnetic field parallel to the plane of the depositing film is a widely used technique. It has been used successfully in thin film based works [2-4] where it has been preferable to align the domain magnetisation in a particular direction during the deposition. This removes the need to anneal the thin film in the presence of magnetic field at a much higher temperature to induce the required magnetic anisotropy.

The origin of this uniaxial anisotropy is due to the directional ordering of like atom (e.g. Fe-Fe). This ordering process if undertaken during the deposition process occurs at an accelerated rate in comparison to magnetic annealing, even though the temperature of the depositing film is generally much lower in comparison. This is mainly due to the kinetic energies of the impinging sputtered atoms, which tend to be mobile at the surface of the film. This increased directional ordering makes it possible to induce much larger anisotropies in the depositing films, compared to conventional magnetic annealing were the directional ordering is not as high. Both transverse and longitudinal anisotropies in the films can be produced in this method. All of the layers of the thin film element can be sputtered in one cycle because the field direction is set to be constant for all layers. In order to induce a crossed anisotropy in a multi-layer thin film, the magnetic field is set at some angle with respect to the film length then the first lower magnetic layer and the conducting layer are sputtered. Next the thin film substrate is rotated so that the anisotropy of the upper magnetic layer is at an angle with respect to the previous lower magnetic layer. This means that all of the magnetic layers are not sputtered in one cycle and care must be taken to ensure conditions are maintained.

The magnetic field is usually provided by permanent magnets that are positioned on either side of the substrate or by a horseshoe type magnet arrangement. It is usual to shield the magnets by a grounded iron plate that prevents any stray field from the permanent magnets from altering the plasma dynamics. The shielding also prevents the magnets themselves from being sputtered. It is important that the applied field is parallel to the substrate surface and to minimize the number of flux lines which intersect (are not parallel to) the surface of the substrate and the plasma discharge. If the applied field is sufficiently large and parallel to the substrate as shown in Fig. 4.4(a), then any secondary electrons on a collision path with the depositing film will be prevented by the magnetic field, thus reducing the electron bombardment of the substrate. In the situation were the field lines have a transverse component to the substrate, there is an increase in the density of electrons arriving in the proximity of the substrate, which will increase the chance of electron bombardment of the substrate [5]. Obviously the application of a magnetic field will alter the sputtering dynamics and the surface mobility of the sputtered atoms, and this generally means that the sputtering parameters need to be re-calibrated to account for this change.

Stresses in thin films can also be extrinsically induced due to the differing thermal expansion coefficients of the film and substrate as the film/substrate system cools after the deposition and contracts by different amounts. A film, which is deposited onto a substrate that has a larger thermal expansion coefficient, will be placed in a state of compressive stress, whereas a substrate with a lower thermal expansion coefficient will place the deposited film in state of tensile stress. If the stress is either bi-axial or isotropic, a uniaxial perpendicular anisotropy may be induced, depending on the sign of the magneto restriction. For substrates and films with similar expansion coefficients that are deposited at low deposition temperatures, this problem is usually avoided.
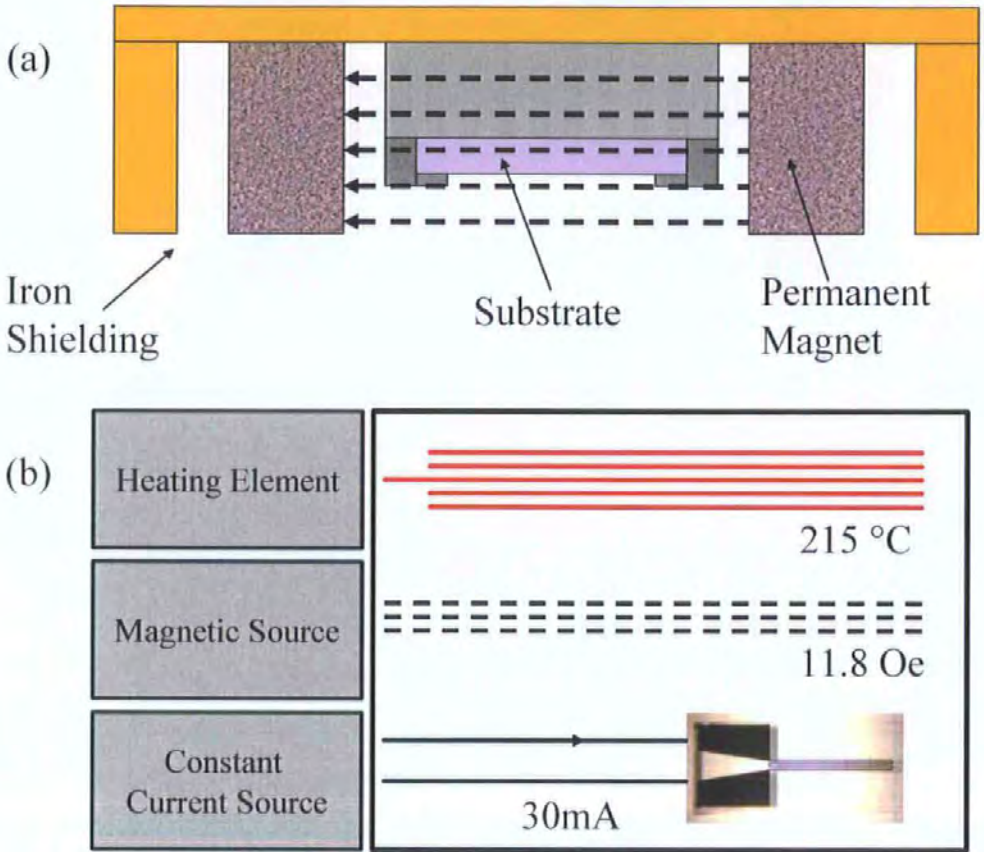
Figure 4.4   Illustration of (a) induced anisotropy during deposition, and (b) induced anisotropy through magnetic and current annealing.

Figure 4.5   Picture of the CRIST magnetic annealing system.

4.2.2 Magnetic anisotropy induced after deposition

Magnetic field annealing is a well-established method for inducing a uniaxial anisotropy in amorphous ribbons or films. It generally involves heating a magnetic sample below the Curie temperature, T_c, in the presence of a magnetic field that is sufficiently large to saturate the sample so as to ensure that a single domain exists. With the field annealing being carried out under a low vacuum, usually in a wire-wound furnace arrangement, such as illustrated in Fig. 4.4(b). A picture of a custom made annealing system used in the CRIST facility is shown in Fig. 4.5. The origin of this induced magnetic anisotropy has been attributed to the short-range directional ordering of atomic pairs (e.g. Fe-Fe). The high temperature allows atomic diffusion on a local scale so that a preferred orientation minimises the energy of the system of like atomic pairs and aligns them parallel with the magnetic field.

This directional order is frozen in place as the sample is allowed to cool in the presence of the magnetic field giving rise to an easy axis direction that is parallel to the magnetic field. The domain structure for such a demagnetised sample displays a strong preference for the domain walls to lie parallel to the induced easy axis. It has been found that the anisotropy induced by field annealing is not particularly strong in films [6]. But it has been found that the low anisotropy induced is sufficient to develop a well-defined domain structure. The uniaxial anisotropy induced by the field annealing is a reversible process; annealing the sample just above the Curie temperature in the absence of a magnetic field, will disorder the atomic pairs.

It is important that the sample is fully stress relieved before the field annealing process is undertaken, otherwise the stresses present will not allow a satisfactory field induced anisotropy to develop. The stress relief is commonly carried out at temperatures that are above the Curie temperature, but below the crystallisation temperature. The two steps are commonly performed in a single process, where the sample is first stress relieved at the upper temperature, and then magnetically annealed at the lower temperature for the required time.

The effect of annealing is clearly illustrated in section 5.3.2 with NiFe / Au multi-layers, the transverse anisotropy can be strongly defined in the films by use of the equipment of Fig. 4.5 after the sputtering process.

In the case of creating a crossed anisotropy in a multi-layer thin film, that is the anisotropy is crossed in the top layer with respect to that in the bottom layer, a special annealing process is required and would generally be carried out on individual elements of the substrate. Firstly a uniaxial transverse anisotropy is created in the thin film during the deposition process, then a combination of a weak longitudinal magnetic field and a DC current applied to sample under annealing, creating a helical type anisotropy [7-8]. The angle of anisotropy produced in the thin film can be varied by changing the magnitude of the applied DC current. This method was used by Stanley Electric Company Research and Design, Yokohama, Kanagawa 225, Japan, to produce the crossed anisotropy samples measured in this work.

4.3   Photolithography

Photolithography is the process of transferring geometric shapes on a mask to the surface of the thin film. After the substrate has been deposited with the required materials and layers to make up the thin film, it is necessary to use a photolithography process to transform the layer or layers to the required shapes and dimensions to make the required element. This section will cover the photolithography processes used in the CRIST facility during the course of this work to produce thin film multi-layer with and without planar coils.

4.3.1   Photo-mask plates

The masks used for the photolithography process were designed for an in-contact mask aligner illustrated in Fig. 4.6(a), with a plate size of 100 mm square. The lithography was central on the mask plate, designed to cover a 50 mm square substrate. The masks were made of extremely flat glass with an 800 Å thick Chromium layer deposited on one side. The Chromium layer was patterned with the mask design using electron beam lithography. The beam size was 1.8 μm and could achieve a line width control of 0.3μm. The masks were manufactured at Rutherfords electron beam lithography facility (EBLF).

The photo masks were designed to produce thin film structures of widths 200, 100, 50, 20 and 10 microns and lengths of 5 and 2mm. Each thin film structure had a 2mm by 1.5mm rectangular connection (bonding) pad at each end. Additional photo masks were produced to enable to manufacture of a thin film micro coil which would be helically wrapped around the original thin film element. The helical micro coil was constructed from two Au thin-film structures to give 10 or 23 turns (for 2 and 5mm thin films, respectively) with a 50 μm turn width. The film thicknesses of the lower and upper coil structures were 0.245μm and 0.7 μm respectively. The lower coil structure additionally featured two bonding pads for coil connection. The photo masks were designed during the work of [9], and are illustrated in Fig. 4.7.

4.3.2 Photo-resist process

For the manufacture of the thin films and micro coils in this process the photo-resists used were exclusively positive so that the patterns designed on the masks were duplicated in photo-resist on the substrate. The photo-resist was used in two ways:

1. As a covering mask so that the exposed regions could be etched (Fig. 4.8 a-e)

2. When hard baked the photo-resist was used as a planarising layer for step coverage or as insulation between metallization layers. The photo-resist was hard baked at 250 °C for 1 hour, after which it could not be removed.

The first stage is to spin the appropriate photo-resist for the required spin-on thickness to the substrate. Once the wafer is held onto the vacuum chuck the photo resist is dispensed onto the centre of the wafer through a filtered syringe. The spin speed is selected to be a constant 4000 rpm and the wafer is spun for at least 20 seconds to achieve optimum thickness uniformity across the substrate (Fig. 4.8 a). A Headway Research Inc AHT series Photo-resist spinner was used (Fig. 4.6b).

Once spun, the photo-resist is soft baked at 100 °C on a hot plate placed in an air flow oven for 1 minute. This process dissociates any residual solvent contained in the resist. A post exposure and developing oven bake of 120 °C for 30 minutes was used to improve the photo-resist to substrate adhesion before a chemical etching stage.

The photo-resist coated films were exposed to ultra-violet light using a Dage Precima in contact type mask aligner, illustrated in Fig. 4.6 (a). The substrate holder is floated using an air cushion so that the substrate and mask can be gently brought together, and their surfaces levelled. Once in contact and levelled, the air is turned off. After separation, the substrate can be moved by micrometers to align the mask and substrate features using an optical microscope. When aligned, the substrate and mask are held together by vacuum. The photo-resist not masked by the pattern on the mask is then exposed (Fig. 4.8 b). In order to achieve optimum line definition, the exposure time of the photo-resist was determined experimentally. The ultra-violet exposure source is a 200 watt mercury lamp with a timed shutter.

Once exposed the substrate was developed for 30 seconds to reveal the photo-resist pattern of the same design as the mask lithography (Fig. 4.8 c). After developing, the substrate is thoroughly rinsed in deionised water and dried with the nitrogen gun prior to etching.

After the film was etched (Fig. 4.8 d) the photo-resist was finally removed by a soaking in acetone, revealing the patterned geometry (Fig. 4.8 e). The substrate was then thoroughly rinsed and dried before the next process step. The substrate was soaked overnight, and/or submerged in heated photo-resist stripper or acetone when the resist proved difficult to remove. This could happen if the resist was partially baked during an ion milling or sputtered lift off process.

Figure 4.6   (a) Dage Precima in-contact mask aligner, (b) Headway Research Inc AHT series Photo-resist spinner.

MI element

Connection
pad

1.5mm   2mm   5mm

MI elements

5mm   2mm   5mm
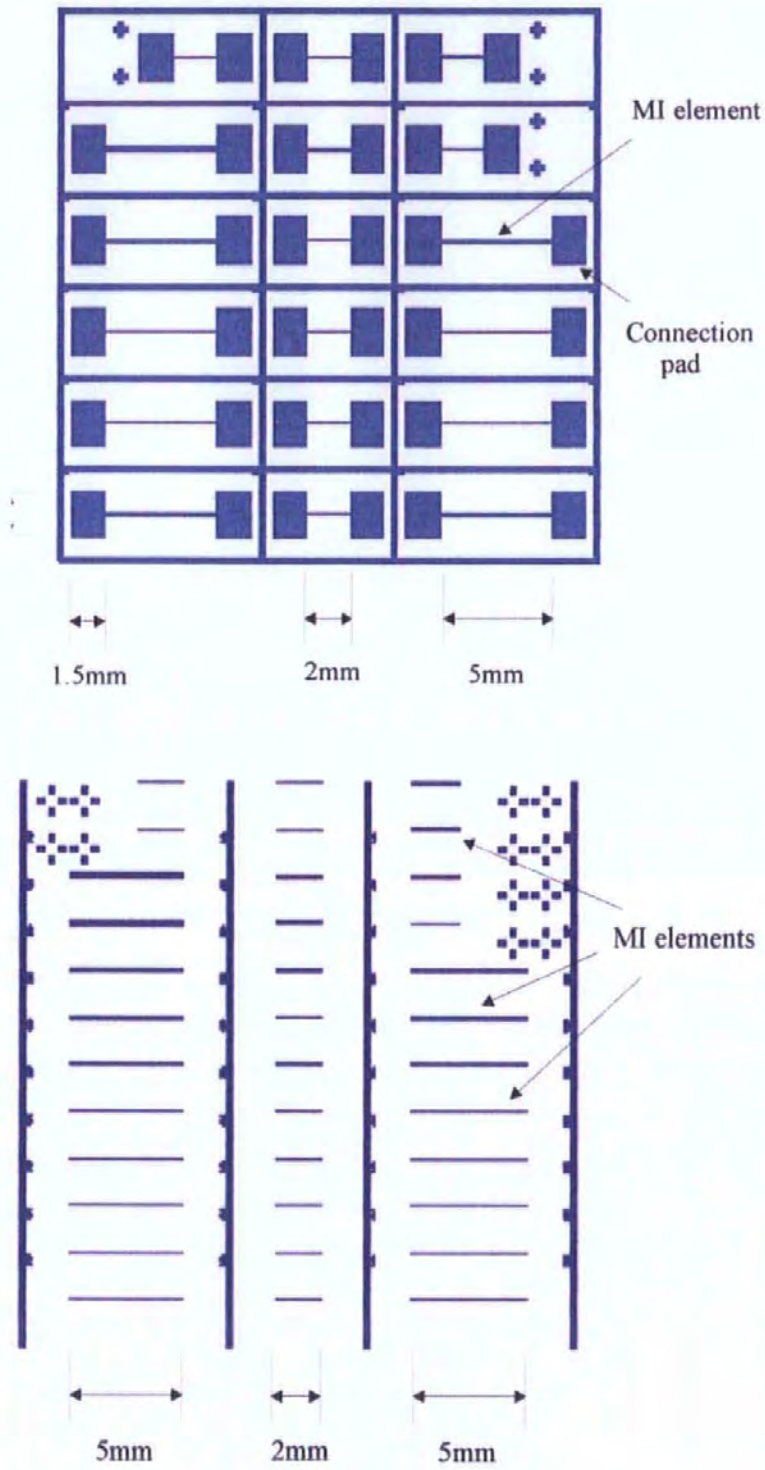
Figure 4.7   Positive photo resist masks from [9].

(a)

photo-resist

film

substrate

(b)

UV

(c)

(d)

(e)

(a) Spin on photo-resist

(b) Exposure

(c) Patterned photo-resist after developing

(d) Patterned film after etching

(e) Patterned film with photo-resist removed
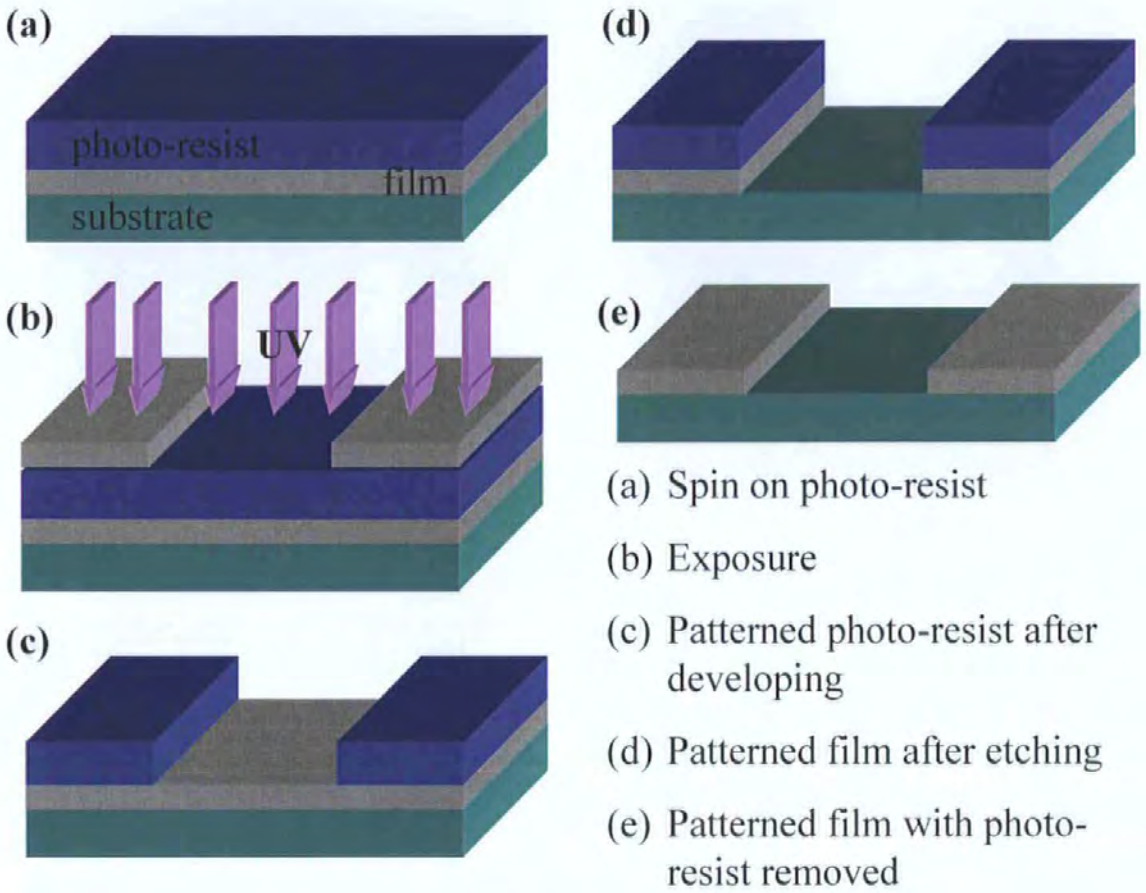
Figure 4.8   Generalised photo resist manufacture process of thin films.

4.3.3 Etching techniques

The samples were shaped using wet etching through the use of chemicals. Although cheap and simple to implement, wet etching is isotropic and so produces undercutting with poor line definition, however this is suitable for forming structures where edge tolerances are not critical. A table of the chemical formulation of the etchant used, and their operating temperatures are given in Fig. 4.9. Each etchant normally consists of an oxidising chemical and a chemical for dissolving the resulting oxide. After etching, the substrate is rinsed with deionised water and then the photo-resist is stripped. After a further rinse the substrate is finally dried with the Nitrogen gun.

Material	Etch Composition	Operating Temperature
Permalloy	2 parts Orthophosphoric acid	40°C
(NiFe)	2 parts Nitric acid	
	1 part Nickel Nitrate solution	
	10 parts de-ionised water	
Chromium	0.025kg Ammonium Ceric Nitrate	Ambient
	15ml Nitric acid	
	85ml de-ionised water	
Copper	0.2kg Ammonium Persulphate	Ambient
	11ml de-ionised water	
	5ml concentrated sulphuric acid	
Gold	400g Potassium Iodide	Ambient
	100g Iodine	
	400ml de-ionised water	

Figure 4.9   Table of wet etchants.

4.4   Fabrication of magnetic / conductive / magnetic layered films

In this section the exact stages of the processes developed in sections 4.1 to 4.3 will be described for the production of three layer magnetic / conductive / magnetic layered films with different types of anisotropy that were prepared for this work. The descriptions of the processes and methods in this section where adapted from the work carried out in [1] which served as reference manuals for the production of this type of thin films during the course of this work.

The substrates that were used in the RF magnetron deposition for the materials of the layered films were 50mm^2 CM5 quality glass microscope slides having a thickness of 0.8mm. These inexpensive slides are produced by a glass floating procedure. They have annealing and softening points of 535°C and 720°C. The base pressure attained in the sputtered chamber before the process was started was 2×10^{-7} bar, and the Ar gas pressure during the sputtering process was kept at 4.5×10^{-3} mbar. Each of the magnetic / conductive / magnetic material layers were sputtered consecutively to a thickness of 0.5 microns in the same continuous vacuum conditions, where the deposition rates for NiFe and Au for example were 2.35 Å/s and 5.75 Å/s respectively. The rates differed for each composition of magnetic and conductive material used. The total layer thickness was 1.5 microns. NiFe and CoSiB were chosen for the composition of the magnetic layers and Au was used for the conductive layer.

4.4.1   Transverse layered films

A substrate holder with an in-plane magnetic field of 60 Oe was used to induce an easy axis direction during film deposition. To induce a transverse anisotropy, the magnetic field was applied in the transverse direction with respect to the elements length.

After deposition the layers were patterned by conventional photolithography methods described in section 4.3 with an in-contact mask aligner with a ultra-violet exposure source. To produce the normal open magnetic structure, the photo-masks shown in Fig. 4.7 were utilised to produce multi-layers with widths of 200, 100, 50, 20 and 10 microns and lengths of 5 mm and 2 mm.

Chemical etching was used for both the magnetic layers and Au conduction layers in the fabrication of the layer structures. Au was used rather than Cu for the conduction layer in the structure because it was found to be more reliable and produced a much higher quality edge definition when chemically etched. It also produced the correct bonding surface to connect the multi-layer to its measuring cell using an Au bonder that was present in the CRIST facility.

The first photo mask used produced a positive photo-resist pattern of the completed layer structures with their connection pads on the surface of the layers. Both the upper magnetic and the Au conduction layers were chemically etched to this pattern as shown in Fig. 4.10 (a). After etching the upper magnetic layer, the remaining magnetic material pattern acted as a mask for etching the Au conductive under layer. For the final etching process a second photo-mask was required shown in Fig. 4.7. This mask produced a positive photo-resist pattern that only covered the multi-layer and not the connecting pads. During the final chemical etching process the lower magnetic layer was etched to this shape and the upper magnetic layer on top of the connection pads was removed, as shown in Fig. 4.10 (b).

To create closed and castellated structures, as illustrated in Fig 5.17, a slightly more complex method was required. The lower magnetic layer and conductive layers were sputtered together. Then the conductive layer was etched to a smaller thickness than the overall width with the normal mask. Instead of etching the lower magnetic layer to this pattern, a new magnetic layer is sputtered on top of the pre-etched conductive layer. This enables the magnetic layers to overlap the conductive layer. If a larger mask dimension, for example the 200μm width is used to etch the magnetic layers, the overlap remains and the magnetic circuit is closed. The top magnetic layer is etched as usual to reveal the conductive layer for the contacts. Further more if a larger castellated mask is used to etch the magnetic layers; the closed then open magnetic circuit structure can be produced. To add an Al_2O_2 insulation layer, it was simply sputtered to the required depth between the magnetic and conductive layers and shaped using photolithography and etching as normal.

As chemical etching is isotropic, a certain amount of undercutting (over-etching) and profile roughness was expected after each stage. Any undercutting that had occurred to the upper magnetic layer during the first etch process was masked against further undercutting

during the second photo-lithography process. Here, the second photo-resist layer covered the undercut edge of the upper layer. On completion of all etching processes of the layer structures the undercutting was found to be <2 microns and have an average profile roughness of <1 micron. Although not as accurate as the dry etching process, chemical etching proved to be as fast and generally reliable. With comparatively large sizes of the MI structures used in the course of this work, multi-layer widths of 20 microns and above, the undercutting and profile roughness were considered to be acceptable.

The transverse anisotropy for the manufactured layer films with 200 microns widths was accurately defined by the field direction within which the sputtering was carried out. However measurements of the longitudinal impedance of the samples with widths less than 200 microns (10 – 100) showed that the anisotropy is directed along its length in spite of the fact that sputtering was carried out in a strong transverse or crossed magnetic field of 60 Oe. This is clearly illustrated in Fig. 5.12 for a 100μm NiFe / Au sample in chapter 5.

This effect is most probably associated with the resulting mutual stress between the substrate and film layers during the sputtering process. After thermal treatment of the finished samples, the transverse were established in the same directions as the strong magnetic field as desired in the sputtering process. In order to decrease the dispersion of the transverse anisotropy direction all of the multi-layers were annealed in a strong transverse magnetic field of 100 Oe after the sputtering process.

The annealing system has a small vacuum chamber within which the wafer or individual multi-layer can be fixed securely. The chamber was evacuated down to a base pressure of 50 mTorr. The vacuum chamber is placed in an in-plane magnetic field with field strength of 100 Oe at its centre. The chamber would take approximately 2 hours to reach an annealing temperature of 450 °C and a similar time to cool back down to room temperature. Once the heating was removed the vacuum was kept until the chamber had cooled down to room temperature. After annealing, the wafer was diced manually using a diamond scriber into individual samples.

(a)

(b)
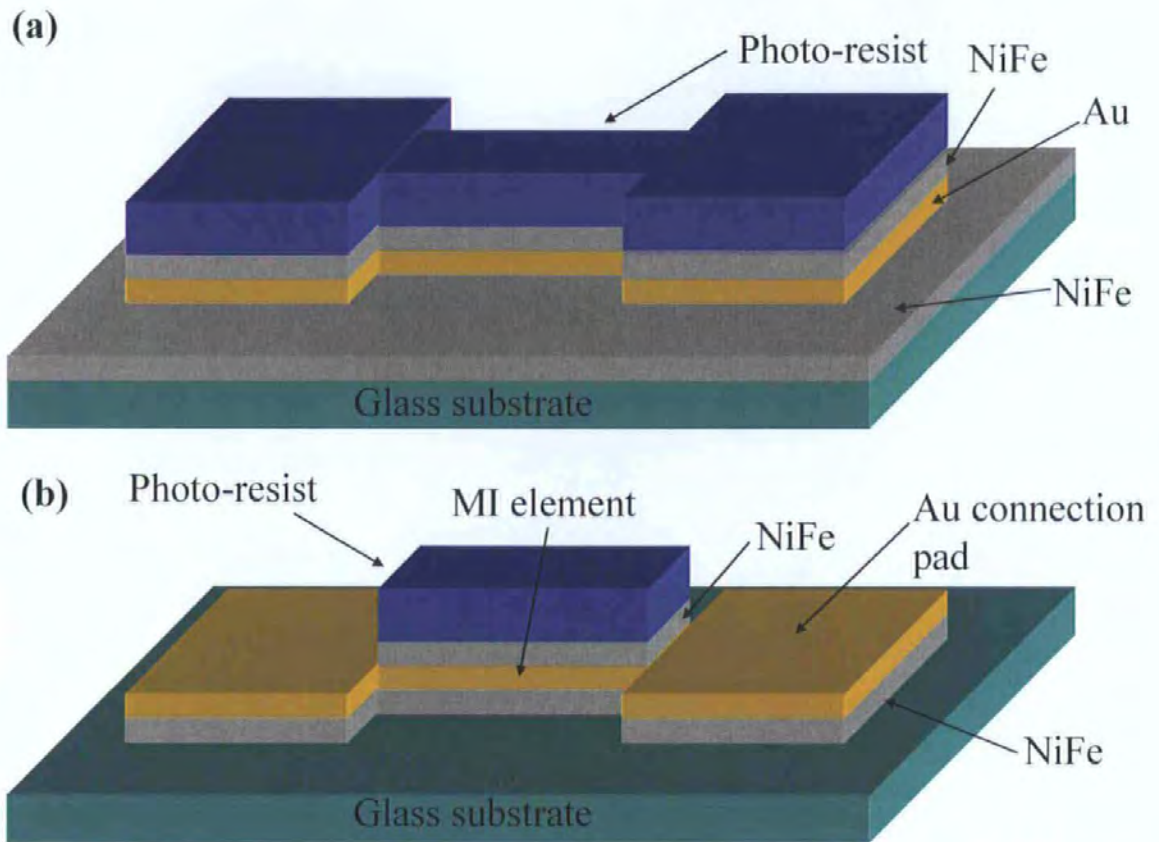
Figure 4.10   Photo resist manufacture process of an open structure NiFe / Au / NiFe multi-layer thin film.

4.4.2 Layered films with an helical micro coil

This section will discuss the additional processes that are involved to add a helical planar micro coil to the layered structure. The helical micro coil is added to a layered film with transverse anisotropy to enable the measurement of off-diagonal components of the surface impedance tensor. It is much more complicated to construct due to the number of layers and sputtering processes required to create the structure, only a limited number of successful thin films were able to be produced during the course of this work.

The helical coil multi-layer was constructed from a NiFe / Au / NiFe layered film core, with a thin-film micro coil wound helically around the core, along its length. Both the core and coil layers were deposited by means of RF sputtering. All sputtering conditions where the same as transverse layer process as shown in section 4.4.1, in the presence of a strong transverse magnetic field of 60 Oe. The final sample was annealed in the presence of a strong transverse magnetic field of 100 Oe to establish a transverse anisotropy. Cured photo resist was used to isolate the lower and upper coil structures from the core layers. The NiFe / Au / NiFe central layers were 5mm long, 50 microns in width, and had a total thickness of 1.5 microns. The helical microcoil around the multi-layer was constructed from two Au thin film structures to give 23 turns over a 5mm length with a 50 micron turn width. The film thicknesses of the lower and upper coil structures were 0.245 microns and 07 microns respectively.

The Fig. 4.11 (a) through 4.11 (f) show schematic cross-sections of the NiFe / Au / NiFe element and helical coil structures at key stages of fabrication, the schematics are arranged so that the layers are viewed along the length of the sample, through the centre of its width.

(a) Lower Au coil layer

(b) Al$_2$O$_3$ fill layer

(c) Lower photo-resist isolation layer

(d) NiFe/Au/NiFe MI Sandwich layers revealing Au bonding pads

(e) Upper photo-resist isolation layer

(f) Upper Au coil layer

Au   Al$_2$O$_3$ Photo resist   NiFe
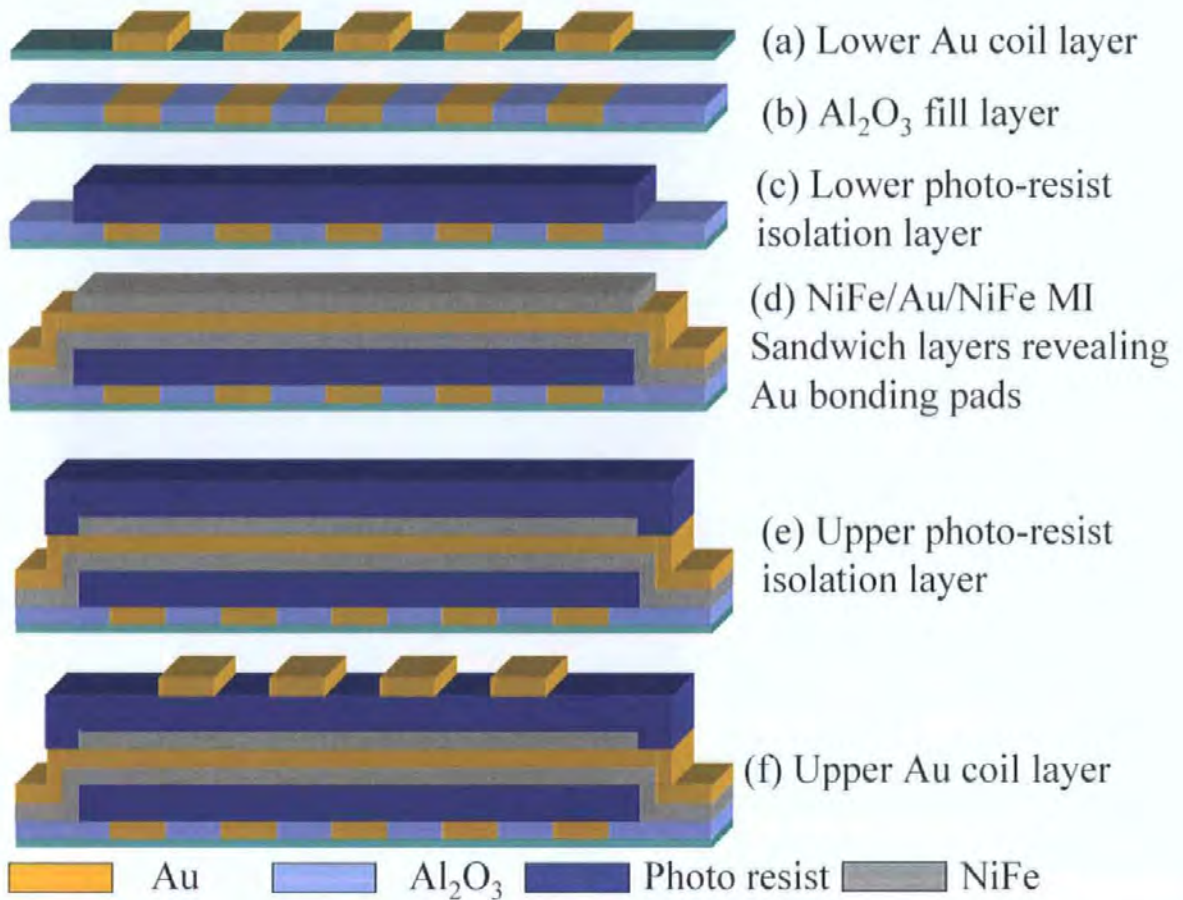
Figure 4.11   Illustration of the photo resist manufacture process of a multi-layer thin film with planar coil, neglecting undercutting.

Positive photo resist was used for every lithographic stage so the photo mask design was replicated in the photo resist once patterned. The sequence of the photo-masks used for fabricating the layered film and helical micro coil is shown in Fig. 4.12 (a) through 4.12 (e). Chemical etching was used for fabricating all metal layer structures of the sample. Again, Au was used for the conductor layer as it proved to be more reliable during the etching process and produced better edge definition.
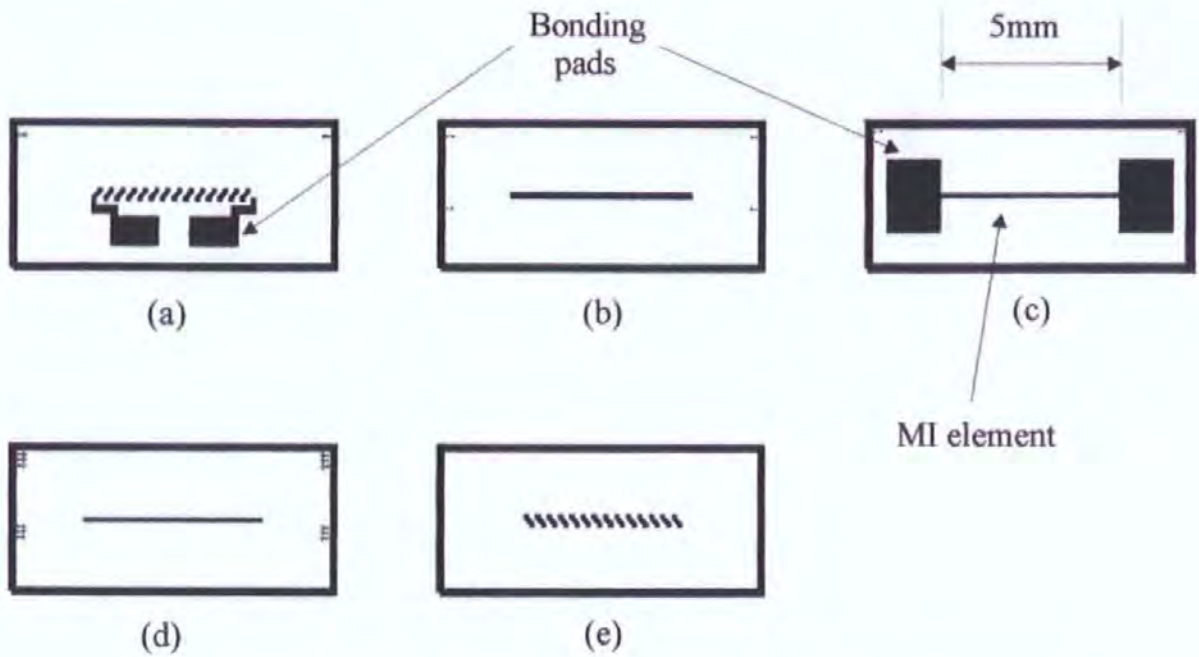
Figure 4.12   Positive photo resist masks for planar micro coil manufacture [9].

The first photo mask used in the fabrication process, shown in Fig. 4.12 (a) was used to produce the lower micro coil structure shown in Fig. 4.11 (a). Here, a 240nm thick layer of Au with a 5nm Cr adhesion layer was deposited, patterned and chemically etched to the geometry shown. After etching the Au and Cr, the patterned substrate was placed back into the sputtering chamber where a further 245nm of Al_2O_3 was deposited. The photo resist was then removed revealing the lower microcoil pattern with the Al_2O_3 layer filling the gaps between each element of the lower micro coil structure as shown in Fig. 4.11 (b).

This Al_2O_3 'lift off' process helped provide a more planar surface for the first isolation layer. For the next layer, AZ 1813 photo resist was spun and patterned on the substrate using photo mask in Fig. 4.12 (b). The photo resist was then hard baked to form the lower isolation layer. Once hard baked the AZ 1813 photo resist shrinks to an approximate thickness of 1 micron and provides a planerising isolation layer over the first micro coil structure, shown in Fig. 4.11 (c). Gentle inclines are formed at the photo resist edges that enable subsequent sputtered layers to traverse them more readily, maintaining good mechanical and electrical continuity. This was important for both the layer structure and the upper micro coil structure that were constructed above and over the isolation layers.

The NiFe / Au / NiFe layers were next to be deposited, patterned and etched to form the core. Using the photo mask in Fig. 4.12 (c), a positive photo resist pattern of the layered core with its connection pads was produced on the surface of the layers. Both the upper NiFe and the Au layers were then chemically etched to this pattern. The upper NiFe layer behaves as a mask for the Au under layer. To etch the lower NiFe layer of the film, a second photo mask was required as shown in Fig. 4.12 (d). This mask produced a positive photo resist pattern that only covered the core of the sample. Whilst etching the lower NiFe layer to form the layer core, the upper NiFe layer that had remained on top of the connection pads after the first etching process was removed, revealing the Au bonding pads. The resulting structure is shown in Fig. 4.11 (d). The undercutting from the chemical etching process was found to be in the same limits as with the original layer only samples.

Above the core layers a second isolation layer was required. Here, the photo mask and processing used was the same as for the lower isolation layer. Other than its bonding pads, the layer core was then completely encapsulated between the upper and lower isolation layers as shown in Fig. 4.12 (e). Finally, the upper micro coil layers of Au and Cr were deposited to a thickness of 500 nm and 200nm respectively.

These layers were then patterned and etched to produce the upper micro coil structure using the photo-mask in Fig. 4.12 (e) to produce the cross sectional pattern shown in Fig. 4.12 (f). The end of each part of the upper micro coil structure connected to those of the lower micro coil structure to form a helical micro coil and the layered core. In the case of the lower micro coil layer, its thickness was kept small to maximise the effect of the subsequent isolation and planarising layers. Whereas, for the upper micro coil layer, its thickness made large enough to ensure that good continuity was achieved at the edges over which each of the layers traversed. For the upper micro coil structure a thick Cr adhesion layer was used to cover and protect the exposed Au of the lower micro coil and the core structures chemically etching the upper micro coil Au layer.

As the process of sputtering and photolithography was learnt during the course of this work, numerous attempts were required to produce a range of different multi-layers in which to measure the range of characteristics of Magneto Impedance effect produced by the theoretical analysis. Transverse multi-layers in the standard dimensions of 200, 100, 50, 20 and 10μm were produced with NiFe and CoSiB magnetic layers and Au conductive layers. Further more, NiFe / Au multi-layers with insulation separation layers and NiFe / Au multi-layers with closed and castellated structures were also produced. Due to the manufacturing complexity a competitively few number of successful planar coil multi-layers were produced.

References

[1]   N.Fry, MPh Thesis, (Centre for Research in Information Storage Technology (CRIST), University of Plymouth, Plymouth, United Kingdom, 1996).

[2]   T.Uchiyama, K. Mohri, L.V. Panina, K. Furuno, "*Magneto Impedance- In Sputtered Amorphous Films For Micro Magnetic Sensor*" IEEE Trans. Magn. MAG-31(6) 3182, (1995).

[3]   L.V. Panina, K. Mohri, T. Uchiyama, M. Noda, "*Giant-Magneto Impedance in Co-Rich Amorphous Wires and Films*" IEEE Trans. Magn. MAG-31(2) 1249, (1995).

[4]   M. Senda, O. Ishii, Y. Koshimoto, T. Toshima, "*Thin-Film Magnetic Sensor using high frequency magneto-impedance (HFMI) effect*", IEEE Trans. Magn. MAG-30(6) 4611, (1994).

[5]   K. Ounadjela, G. Suran, J. SZtern, "*Control of the deposition temperature by the use of a magnetic field in r.f. sputtering*" Thin Solid Films (151) pp,397 (1987).

[6]   D. Garcia, J.L. Munoz, G. Kurlyandskaya, M. Vazquez, M. Ali, M.R.J. Gibbs, *"Magnetic domains and transverse induced anisotropy in magnetically soft CoFeB amorphous thin films"* IEEE Trans. Magn. MAG-34(4) 1153 (1998).

[7]   K. Ueno, H. Hiramoto, K. Mohri, T. Uchiyama, L.V. Panina, *"Sensitive asymmetrical MI effect in crossed anisotropy sputtered films"* IEEE Trans. Magn. MAG-36(5) 348 (2000).

[8]   P. Delooze, L.V. Panina, D. J. Mapps, K. Ueno, H. Sano, *"CoFeB-Cu layered film with crossed anisotropy for asymmetrical magneto impedance"* IEEE Trans. Magn. MAG-39(5) 3307 (2003).

[9]   D. Makhnovskiy, *"Diagonal and Off-Diagonal Magneto Impedance In Ferromagnetic Microwires and Thin Films"*, PhD Thesis, The University of Plymouth,(2003).

Chapter 5. Experimental measurement techniques of the Impedance in film systems and Magneto Impedance effect of transverse anisotropy multi-layers

This chapter outlines the experimental measurement techniques and the resulting measured results undertaken on the thin film multi-layers manufactured locally in the CRIST facility, and supplied by Stanley Electric Company Research and Design, Yokohama, Kanagawa 225, Japan.

The chapter begins by giving some fundamental background information on a method of measuring the complex Impedance of a multi-layer thin film, before giving a description of the experimental configuration and techniques used in the measurements presented.

In attempt to find optimal film systems with respect to relative Impedance change, sensitivity, linearity, operational frequency range, and dimensions, a number of candidate structures have been investigated varying in composition (NiFe /Au / NiFe, CoSiB / Au / CoSiB and CoFeB / Cu / CoFeB), magnetic configuration (transverse, longitudinal or cross anisotropy), geometry and dimensions. The effect of additional insulating layers between the inner conductor and outer magnetic layers have been considered as well. Measurements are taken over a range of frequencies from 1 to 100 MHz. In this chapter measurements on films having a transverse anisotropy will be undertaken (with respect to the external field and AC current). The case of a more magnetically complicated systems, as those with a cross anisotropy will be described in Section 6.

5.1   Fundamental principles of network analysis

This work will be concentrating on measuring the Impedance of the multi-layer thin films through characterisation of their effect on the amplitude and phase of swept frequency and swept power test signals. This measurement technique is called vector network analysis; the introductory information in this section is derived from [1, 2].

As the excitation intensity is small, the systems are considered to be linear, so the systems can only alter the waveform of the signals passing through them by altering the amplitude and phase relationships of the spectral components that make up the signal. Any sinusoid applied to the input of the thin film multi-layer will also appear at the output, and at the same frequency. In its fundamental form, network analysis involves the measurement of the complex-valued reflection and transmission coefficients of waves that travel along transmission lines. Using optical wavelengths as an analogy, when light strikes a clear lens (the incident energy), some of the light is reflected from the lens surface, but most of it continues through the lens (the transmitted energy) as illustrated in Fig. 5.1 (a). If the lens has mirrored surfaces, most of the light will be reflected and little or none will pass through it.

While the wavelengths are different for RF and microwave signals, the principle is the same. Network analyzers accurately measure the incident, reflected, and transmitted energy, e.g., the energy that is launched onto a transmission line, reflected back down the transmission line toward the source (due to impedance mismatch), and successfully transmitted to the terminating device (such as an antenna) as shown in Fig. 5.1 (b). For certain geometry, the reflection/transmission coefficients will uniquely depend on the surface Impedance of the sample under study. In our case the thin film multi-layer will have a complex-valued surface Impedance (of tensor form in general) that will be determined by materials, dimensions, geometry, magnetic properties and frequency (skin depth).
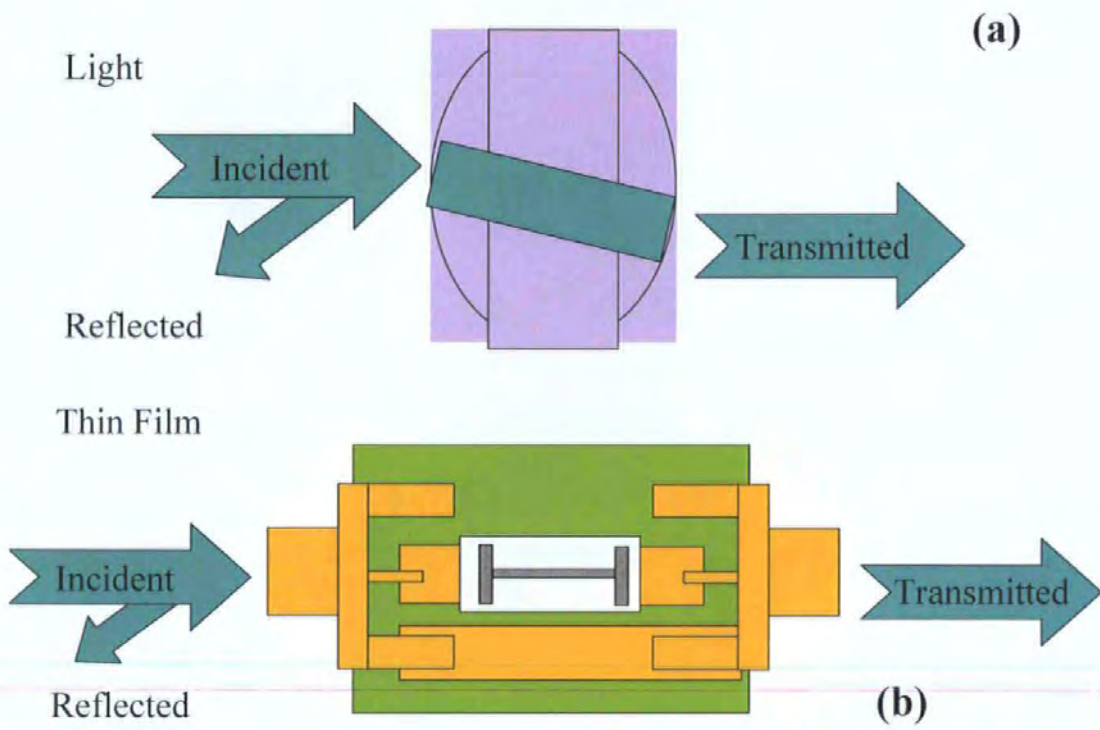
Figure 5.1   Light ray analogy to high frequency device characterisation.

5.1.1   Representation of Impedance measurements

The amount of reflection that occurs when characterizing a device depends on the Impedance that the incident signal "sees." Since any Impedance can be represented with real and imaginary parts (R+jX or G+jB), they can be plotted on a rectilinear grid known as the complex Impedance plane. Unfortunately, an open circuit appears at infinity on the real axis, and therefore cannot be shown.

The polar plot is useful because the entire Impedance plane is covered. However, instead of plotting Impedance directly, the complex reflection coefficient is displayed in vector form. The magnitude of the vector is the distance from the centre of the display, and phase is displayed as the angle of vector referenced to a flat line from the centre to the right-most edge. The drawback of polar plots is that Impedance values cannot be read directly from the display.

Since there is a one-to-one correspondence between complex Impedance and reflection coefficient, the positive real half of the complex Impedance plane can be mapped onto the polar display. The result is the Smith chart as illustrated in Fig. 5.2.

All values of reactance and all positive values of resistance from 0 to infinity fall within the outer circle of the Smith chart. On the Smith chart, loci of constant resistance appear as circles, while loci of constant reactance appear as arcs. Impedances on the Smith chart are always normalized to the characteristic Impedance of the component or system of interest, usually 50 ohms for RF and microwave systems and 75 ohms for broadcast and cable-television systems. A perfect termination appears in the centre of the Smith chart.

For our measurements, the Smith chart allows us to plot the values of Impedance of the thin film over a range of frequencies in one graphical form; the second important function is to allow the calculation of the required complex conjugate to match the Impedance at a certain frequency to 50 Ω.
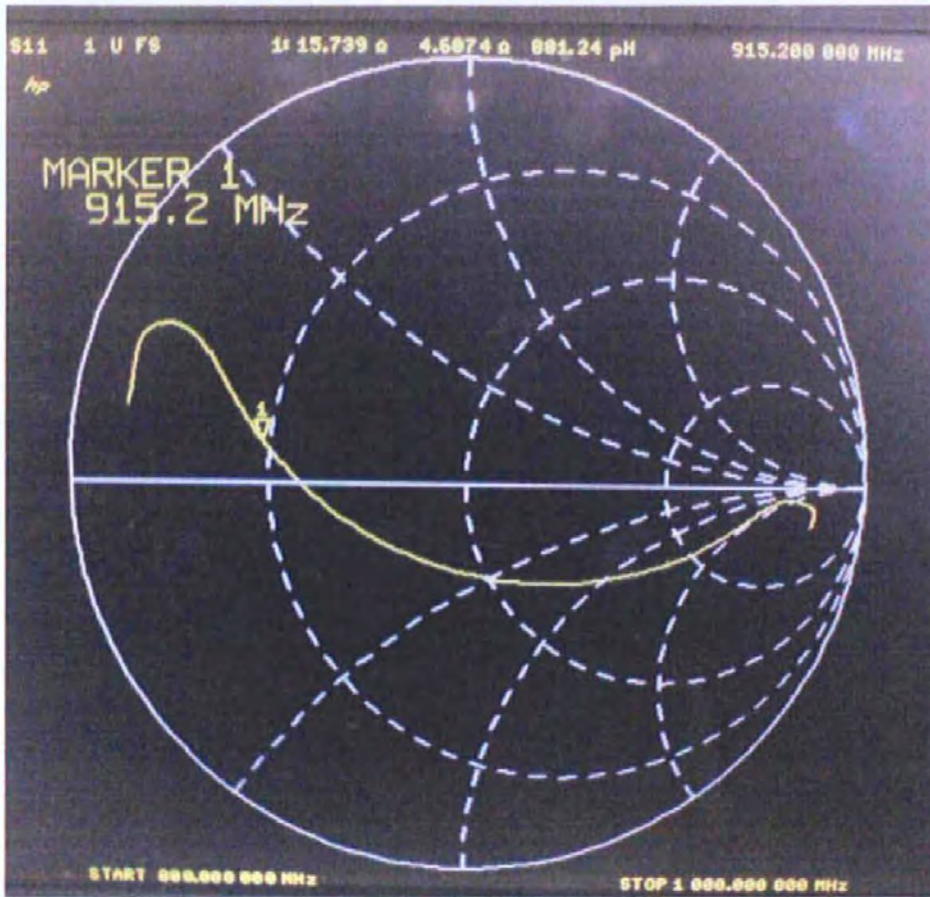
Figure 5.2   Illustration of a Smith chart representation of Impedance (S_{11}) on a Hewlett-Packard 8753E Vector Network Analyser.

5.1.2 Power transfer conditions

A perfectly matched condition must exist at a connection between two devices for maximum power transfer into a load, given a source resistance of R_S and a load resistance of R_L. This condition occurs when $R_L = R_S$, and is true whether the applied signal is a DC voltage source or a source of RF power. When the source Impedance is not purely resistive, maximum power transfer occurs when the load Impedance is equal to the complex conjugate of the source Impedance.

At higher frequencies, wavelengths are comparable to or smaller than the length of the conductors in a high-frequency circuit, and power transmission can be thought of in terms of travelling waves.

When the transmission line is terminated in its characteristic Impedance, maximum power is transferred to the load, and no reflected signal occurs. When the termination is not equal to the characteristic Impedance, that part of the signal that is not absorbed by the load is reflected back to the source. When the transmission line is terminated in a short circuit (which can sustain no voltage and therefore dissipates zero power), a reflected wave is launched back along the line toward the source. The reflected voltage wave must be equal in magnitude to the incident voltage wave and be 180 degrees out of phase with it at the plane of the load. The reflected and incident waves are equal in magnitude but travelling in the opposite directions.

If the transmission line is terminated in an open-circuit condition (which can sustain no current), the reflected current wave will be 180 degrees out of phase with the incident current wave, while the reflected voltage wave will be in phase with the incident voltage wave at the plane of the load. This guarantees that the current at the open will be zero. The reflected and incident current waves are equal in magnitude, but travelling in the opposite directions.

5.1.3   Network characterisation

In order to completely characterize an unknown linear two-port system such as the multi-layer thin film it is necessary to make measurements under various conditions and calculate a set of parameters. Since it is difficult to measure total current or voltage at higher frequencies, S-parameters are generally measured which represent the ratio of incident voltage to reflected or transmitted voltage as illustrated in Fig. 5.3. They are relatively simple to measure, and do not require connection of undesirable loads to the device. The parameters a_1, a_2 represent incident voltages of port 1 and port 2 of the system, and b_1, b_2 represent the reflected voltages at port 1 and port 2 of the system, respectively.
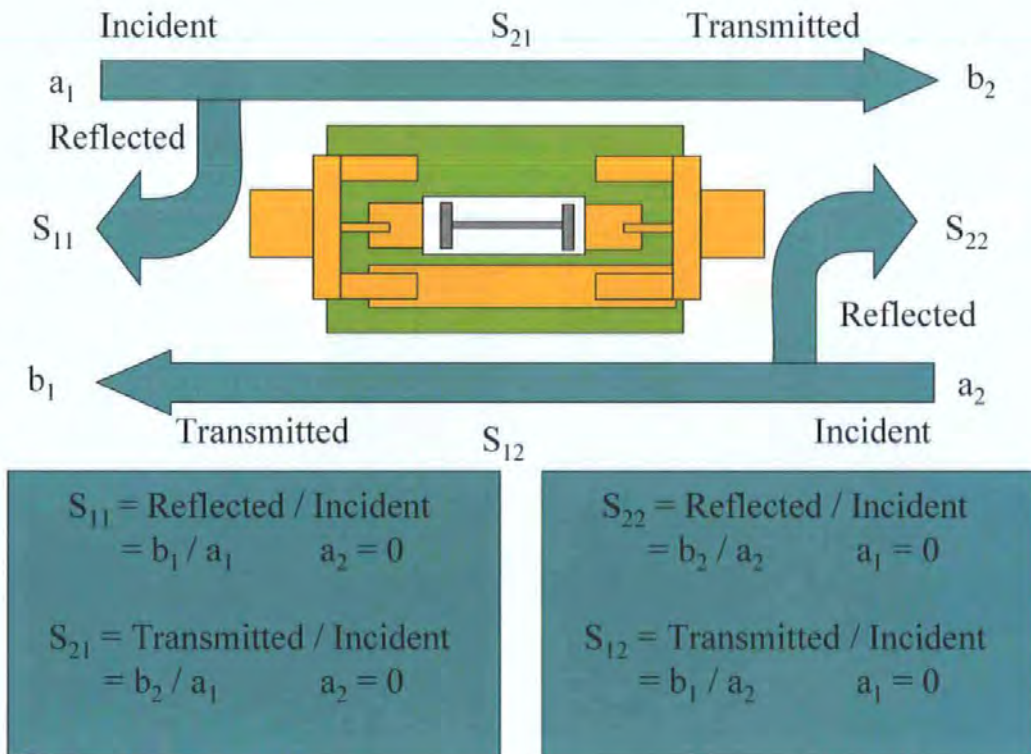
Figure 5.3   Measuring S-Parameters of a 2 port system.

The number of S-parameters for a given system is equal to the square of the number of ports. For example, a two-port system has four S-parameters. The numbering convention for S-parameters is that the first number following the S is the port at which energy emerges, and the second number is the port at which energy enters. Therefore S_{21} is a measure of power emerging from Port 2 as a result of applying an RF stimulus to Port 1. When the numbers are the same (e.g. S_{11}), a reflection measurement is indicated. Forward S-parameters are determined by measuring the magnitude and phase of the incident, reflected, and transmitted signals when the output is terminated in a load that is precisely equal to the characteristic Impedance of the test system.

The multi-layer film Impedance is related to the S- parameters by the following:

$$Z = Z_0 \frac{2(1 - S_{21})}{S_{21}} \qquad (5.1)$$

$$Z = Z_0 \frac{1 + S_{11}}{1 - S_{11}} \qquad (5.2),$$

where $Z = l\varsigma_{zz}/2b$, l is the film length, b is in–plane width, and $Z_0 = 50\Omega$ is the characteristic Impedance of the measurement system.

In the measurement of the Magneto Impedance effect of thin film multi-layers, which can have a tensor form as explained in Chapter 3, the longitudinal Impedance typically is measured using S_{11} parameter, whereas the off-diagonal Impedance (film system with a mounted coil) is more convenient to measure using the S_{21} parameter.

5.2   Experimental configuration and measurement

The surface Impedance tensor in the thin film multi-layers including both diagonal and off diagonal components is measured by means of a Hewlett-Packard 8753E Vector Network Analyser that is configured in two separate operating modes, depending on the component of Impedance to be measured. One port operation for S_{11} parameter measurement and two port mode for S_{21} parameter measurement

All samples are measured through connection to a specifically designed RF broadband Impedance matching measuring cell. The Network Analyser has two ports that are configured in the following way; port 1 produces the AC excitation current $i = i_0 \exp(-j\omega t)$ if connected to the sample or AC excitation field h_{ex} if connected to the planar coil around the sample. Correspondingly, port 2 measures the voltage over the sample V_f or the coil V_c depending on the configuration. This method is used to measure the off-diagonal component ς_{xy}, through the forward transmission parameter S_{21}. Additionally the network analyser can operate in a single port mode where the port 1 measures the S_{11} or reflection coefficient of the current $i = i_0 \exp(-j\omega t)$ applied to the sample. This method is not proper to use for the measurements of the off-diagonal Impedance since the reflection from the coil would give some additional contribution which is difficult to separate.

In order to characterise the effect of magnetic properties on the sample Impedance it is necessary to sweep both the frequency of excitation and the magnitude and direction of the external field. The analyser is only able to change the frequency of the current that it can apply to the sample; therefore, the external field must be produced by an additional device. The magnetic field H_{ex} is produced by a coil driven by a function generator and power amplifier. The operating processes of the analyser and function generator are synchronised by a computer programme written using VEE software, which is a Hewlett-Packard programming language. The frequency is scanned over 11 discrete point to cover an initial starting frequency a stop frequency and 9 equal divisions between those frequencies, for example 1MHz, 10MHz, 20MHz, etc up to 100MHz.

The magnetic field is driven in both positive and negative directions to produce a hysteresis plot. The function generator is utilised as a programmable stepwise DC source to provide the field scans. The S_{21} or S_{11} values obtained from one frequency scan, are saved in the analysers memory in the form of a column consisting of 11 points, that correspond to one particular value of H_{ex}. The total value matrix consists of columns of frequency (f) co-ordinate points and rows of field co-ordinate points (H_{ex}). This information is transferred to a PC at the end of the measurement and converted into an Excel spreadsheet for easy analysis.

The measured sample is placed onto an open-type cell made of copper-coated fibreglass printed circuit board (PCB), which has the following parameters: 1.8mm thickness, designated H in the illustration, average dielectric constant of $\varepsilon = 4.5$, and 30 μm thickness of copper on each side, designated T in the illustration. The width of the PCB track, usually the parameter to be resolved, is designated W in the illustration. These parameters can be used to calculate a 50Ω broadband match, which is required to minimise the effect of frequency on the measurement system itself. By considering the measurement cell as a microstrip transmission line as shown in Fig. 5.4, the Impedance of the strip line Z_0 is approximately given by the following equation.

$$Z_0 = \frac{87}{\sqrt{\varepsilon_r + 1.41}} \ln\left(\frac{5.98H}{0.8W + T}\right) \text{ Ohms} \tag{5.3}$$
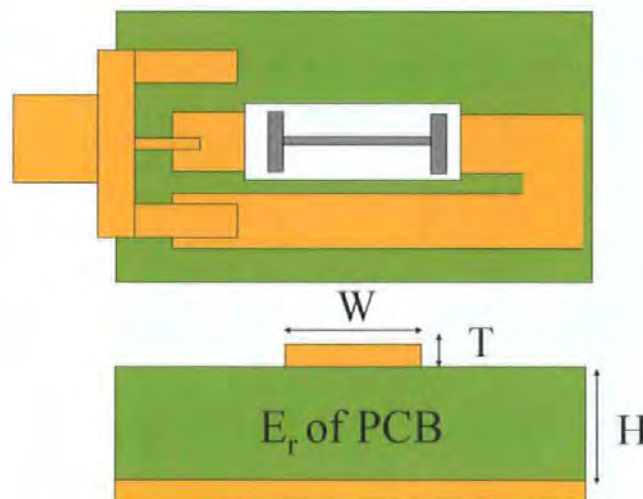
Figure 5.4   Micro strip parameters of measurement cell.

The connection stripes were etched on one side of the PCB and the other was kept copper coated for the transmission line ground plane. All connection stripes were etched as $W = 2.8$mm wide after calculation to provide Impedance in the order of 50-Ohms over a wide range of frequencies.

In measurement situations in which a DC bias was applied to sample, for example in the case of asymmetrical Magneto Impedance, blocking capacitors are required to prevent any DC bias current from entering the analyser, which could cause damage. The cell has input and output 3.5mm SMA connectors that are connected to the analyser via 3.5mm coaxial cables using 3.5mm to type-N adapters. The microwave track including the cables and the adapters were calibrated for both the two-port and one-port measurements accordingly over different frequency ranges, and saved as calibration ratios that are selected in the main programme before measuring.
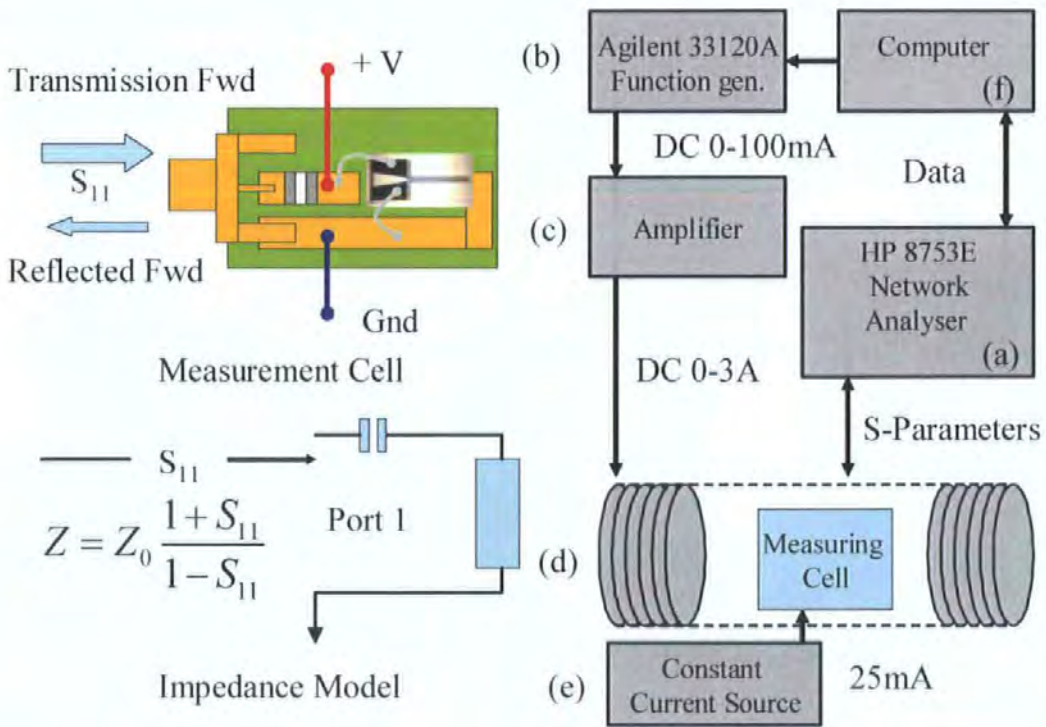
Figure 5.5   Illustration of the experimental configuration used to measure the Impedance of thin film samples.
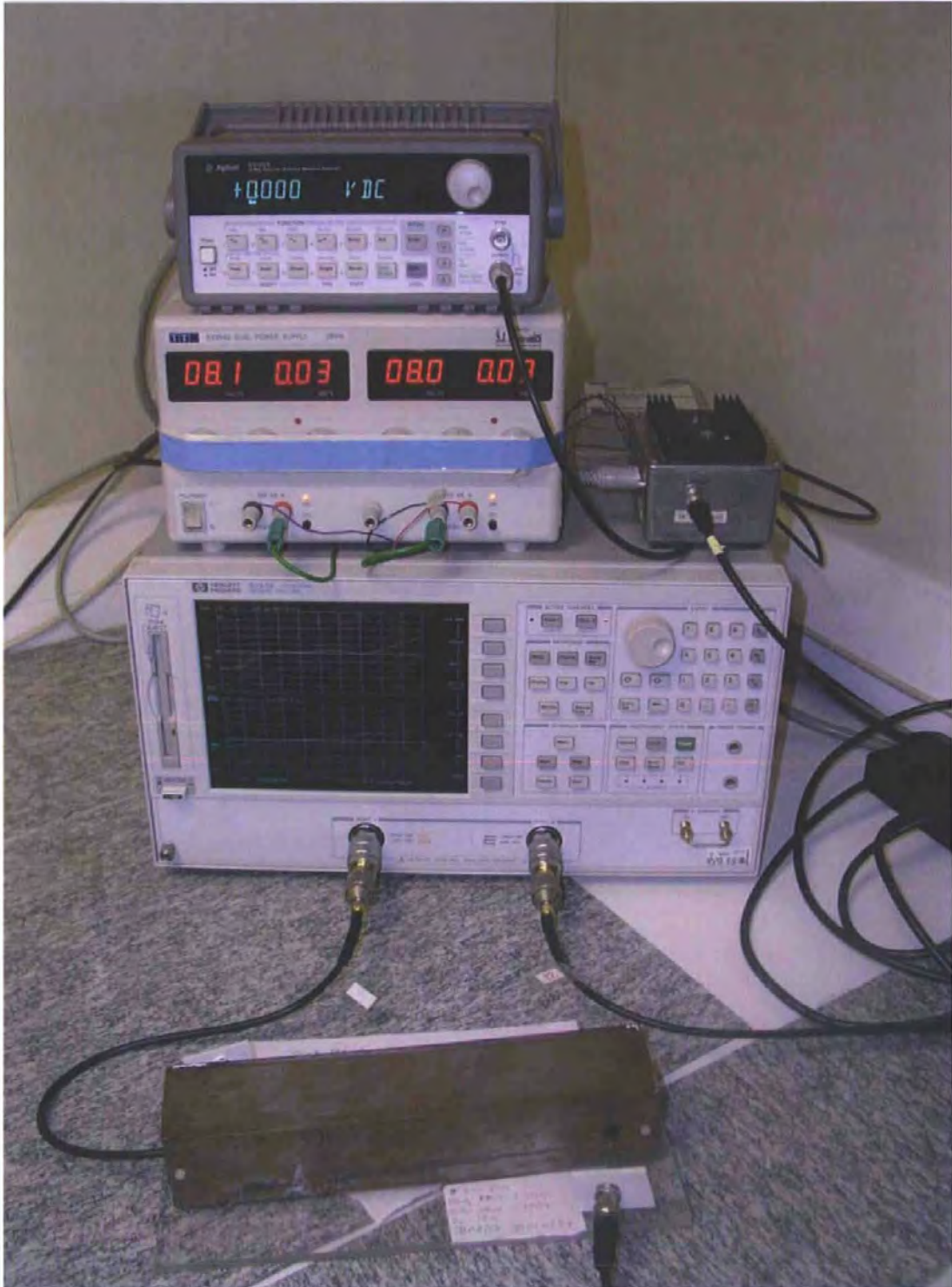
Figure 5.6   Actual experimental system apparatus.

5.3   Measurement of the Magneto Impedance effect in transverse anisotropy multi-layers in the frequency range of 1 to 100 MHz

To measure the diagonal component of Impedance of the samples the HP8753 was configured to produce a frequency sweep consisting of 11 points distributed in the frequency range of 1-100 MHz. The function generator was also configured to produce an output that has been calibrated to produce field strength of $\pm$ 50 Oe in 1000 equal steps in the large driving coil (H_{ex}). In order to determine the effect of an additional transverse bias field H_b in some multi-layers, for each set of 11 frequency measurements an increasing DC bias current was applied.

During the course of this work, one of the aims was to produce multi-layer thin films to experimentally confirm the theoretical predictions of very large Magneto Impedance effect in thin films with which would be important for sensor design. Initially, work began with the measurements of NiFe / Au multi-layers with transverse anisotropy. These systems were previously investigated in Ref. [4-9] and demonstrated very promising results. A number of multi-layers were fabricated of this composition with different dimensions to get further improvements on sensitivity and possible size reduction. Any effective performance increase of a secondary annealing process external to the manufacturing process was investigated by measuring NiFe /Au thin films pre and post annealing. In particular, annealing can be used to establish a required anisotropy as described in Chapter 4.

By taking reference from the improvement in performance of Magneto Resistive heads through changes to their multi-layer structure, closed and castellated loop magnetic flux configurations were created to measure if any additional performance could be transferred to Magneto Impedance thin film multi-layers.

With the effect of manufacturing, variations of basic in-plane structures established, experimentation in material composition of the multi-layer samples could be investigated. As described in Eq. (3.5) to (3.8) of chapter 3, the difference in the conductivity of the inner lead and the magnetic layers can affect the way in which the excitation current flows in the multi-layer structure, the effective permeability of the magnetic layer will also alter with magnetic composition. Both of these factors are able to directly influence the magnitude of the Magneto Impedance effect in the multi-layer. Further more, an insulating layer can be added between the inner lead and the magnetic layer to further influence the way in which the excitation current lows in the multi-layer structure and is also investigated.

Magneto Impedance ratio will be defined as

$$MI\% = \frac{(|Z| - |Z_{H\,max}|)}{|Z_{H\,max}|}$$

(5.4),

where $|Z_{H\,max}|$ is the magnitude of Impedance at the highest field strength used in that measurement, and the sample is considered to be magnetically saturated.

This ratio is used as means of eliminating an Impedance offset, consisting of the DC resistance of the multi-layer structure, which can alter with changes in the structure and composition of the multi-layer and the Impedance of the measurement cell itself, which alters with frequency. In the results of Fig. 5.7 show how this offset increases with frequency.

5.3.1 Magneto Impedance in NiFe / Au / NiFe multi-layers with transverse anisotropy

Firstly, a simple symmetrical 3-layer film systems of NiFe /Au / NiFe with open-loop magnetic flux configuration and with no insulation layer are considered. Variations in length and width of the in-plane dimensions of the multi-layer will be presented for a number of samples over the frequency range. Transverse anisotropy was induced during the sputtering process and the samples were annealed to relax any stress.

The results on MI in similar film systems have been previously reported in [4-9] demonstrating rather large variations. This is due to the effect of the measurement method, the sample quality, deviations of the anisotropy from the transverse direction, and also geometry. Therefore it is necessary to provide experimental results for a wide range of sample configurations all measured from the same experimental setup and method, to allow a direct comparison of the MI ratio.

Figure 5.7 demonstrates the magnitude of Impedance measured of a $100 \mu m$ in-plane width, 5mm length NiFe multi-layer in which a transverse anisotropy was established during the deposition and with further stress relaxation by annealing. As frequency increases the magnitude of the overall Impedance increases greatly even at zero field. This can not be attributed to the increase in Impedance with frequency since when the field is small the film Impedance is dominated by the DC resistance of the inner layer (see Eq. (3.5) in Chapter 3. The reason for this increase is the influence of the measurement cell itself which has greater inductive contributions.

Figure 5.7   Plots of |Z| Impedance vs. magnetic field in 5mm NiFe / Au /NiFe multi-layer with 100μm in-plane width, 1 to 40MHz (a), 50 to 100MHz (b).

Figure 5.8   Plot of MI ratio vs. magnetic field in 5mm NiFe / Au /NiFe multi-layer with 100μm in-plane width, 1 to 40MHz (a), 50 to 100MHz (b).

These samples show typical two-peak Impedance dependence to magnetic field of the longitudinal component of Impedance ς_{zz} when magnetic layers have a transverse anisotropy [3 - 8]. This is attributed to the behaviour of the rotational permeability as illustrated in Chapter 2, Fig. 2.16. In comparison to the magnitude of Impedance plots |Z|, the MI ratio shown in Fig. 5.8 is able to easily illustrate the greatest change of Impedance; this is essential for finding the most sensitive frequency of excitation for any particular material, dimension and geometry.

This sample displays two well defined peaks at $\pm H_K$ at lower frequencies, the anisotropy is around 10 Oe but with increasing frequency the peak shifts to higher fields which could be due to the effect of relaxation in combination with the anisotropy dispersion. The sensitivity to external field increases with frequency due to a larger inductive contribution from the magnetic layers to the total Impedance (compare with Eq. (3.5) from Chapter 3) reaching a peak at 80 MHz for this geometry and dimensions. A maximum 40% change in Impedance is observed in this sample.

With the reduction of the sample width by two to 50μm, as shown in Fig. 5.10, two interesting features are observed. A higher frequency of excitation current is required to establish a useful MI effect. This is due to the film edge effect resulting in the flux leakage through the inner layer as explained in Chapter 3. When the current frequency is below 50 MHz, the MI ratio is smaller than 20%. Additionally, the demagnetisation effect due to reduced width produces distortions in the linearity at low fields which is most evident at frequencies greater than 50 MHz. The sensitivity to external field increases with frequency as before, reaching a peak at 100 MHz for this geometry and dimension. A maximum 35% change in Impedance is observed in this sample, due to flux leakage and the demagnetisation effects.

119
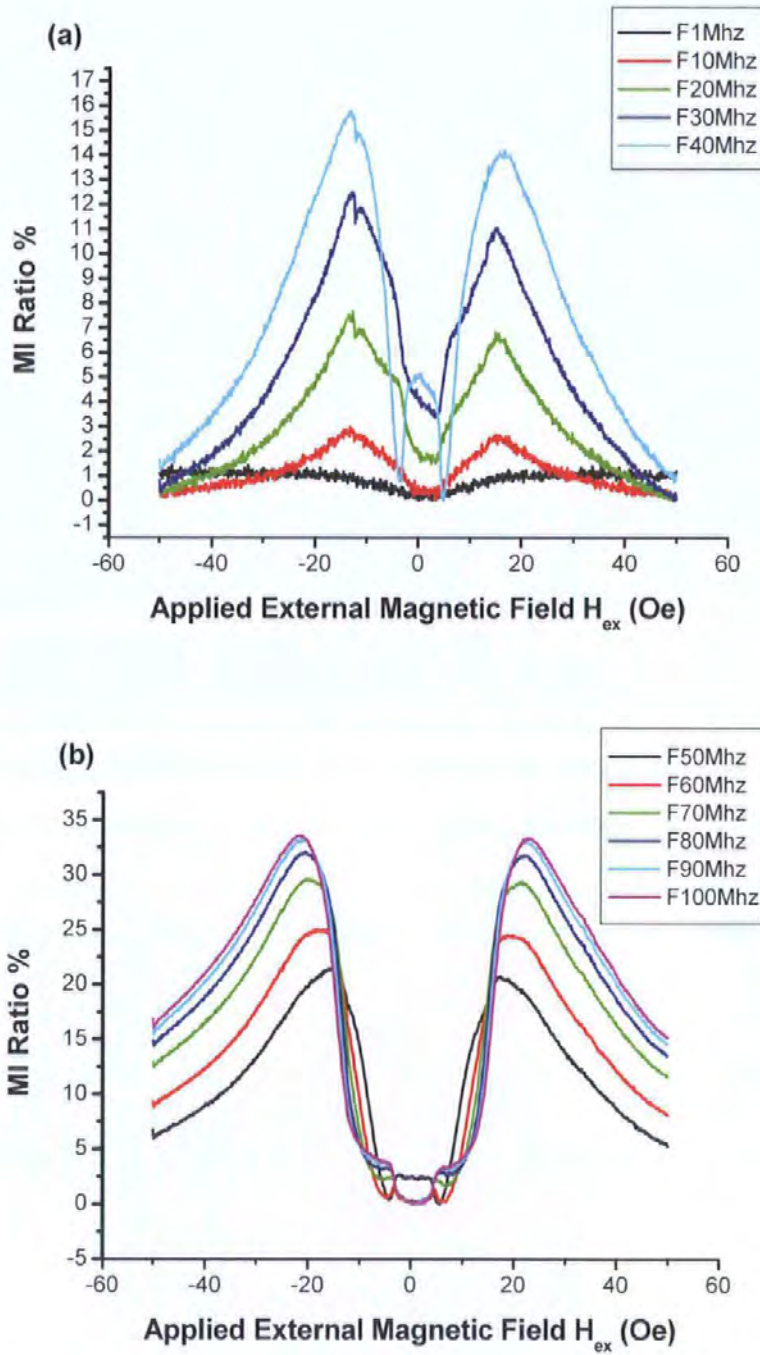
Figure 5.10   Plot of MI ratio vs. magnetic field in 5mm NiFe / Au /NiFe multi-layer with 50μm in-plane width, 1 to 40MHz (a), 50 to 100MHz (b).
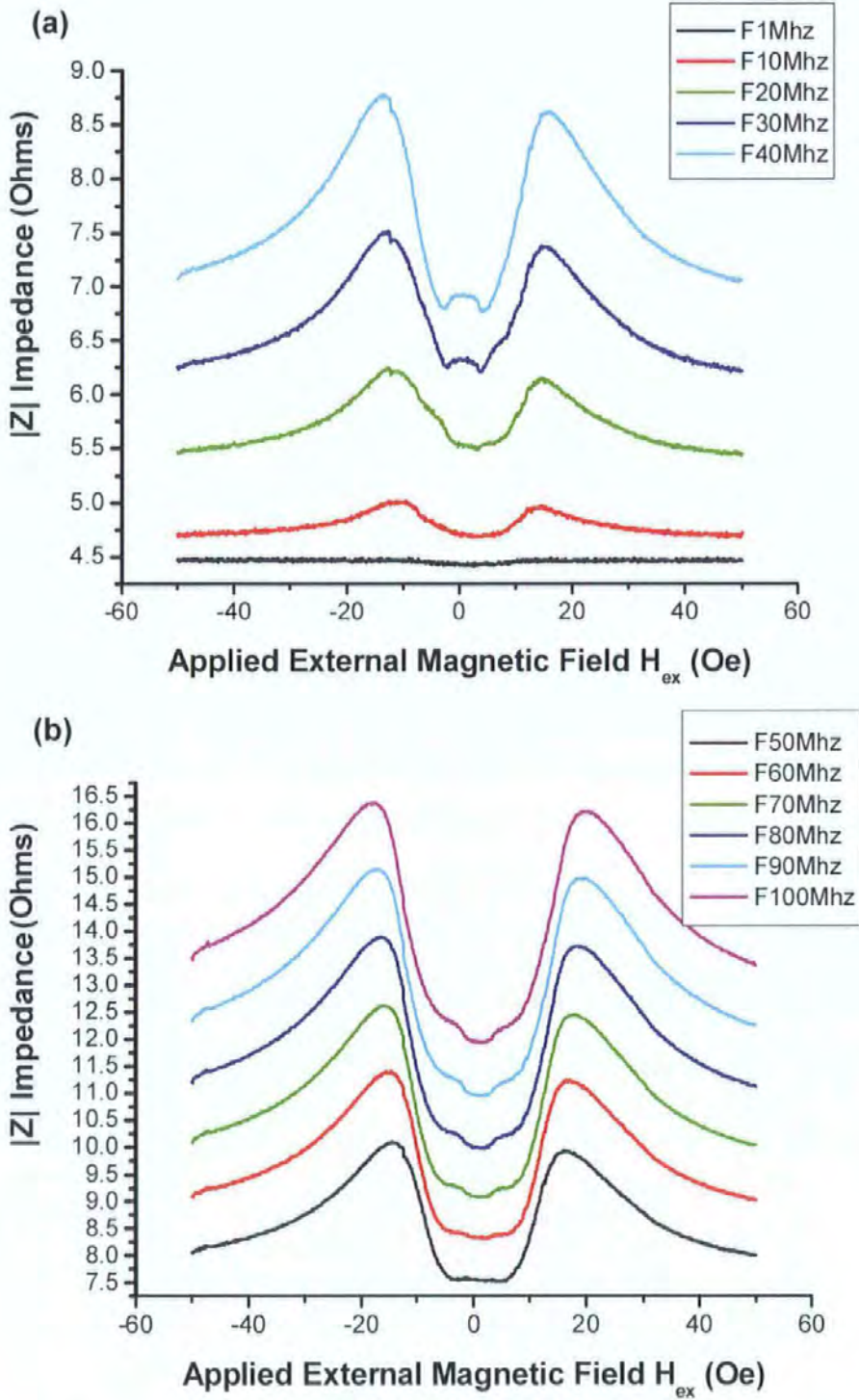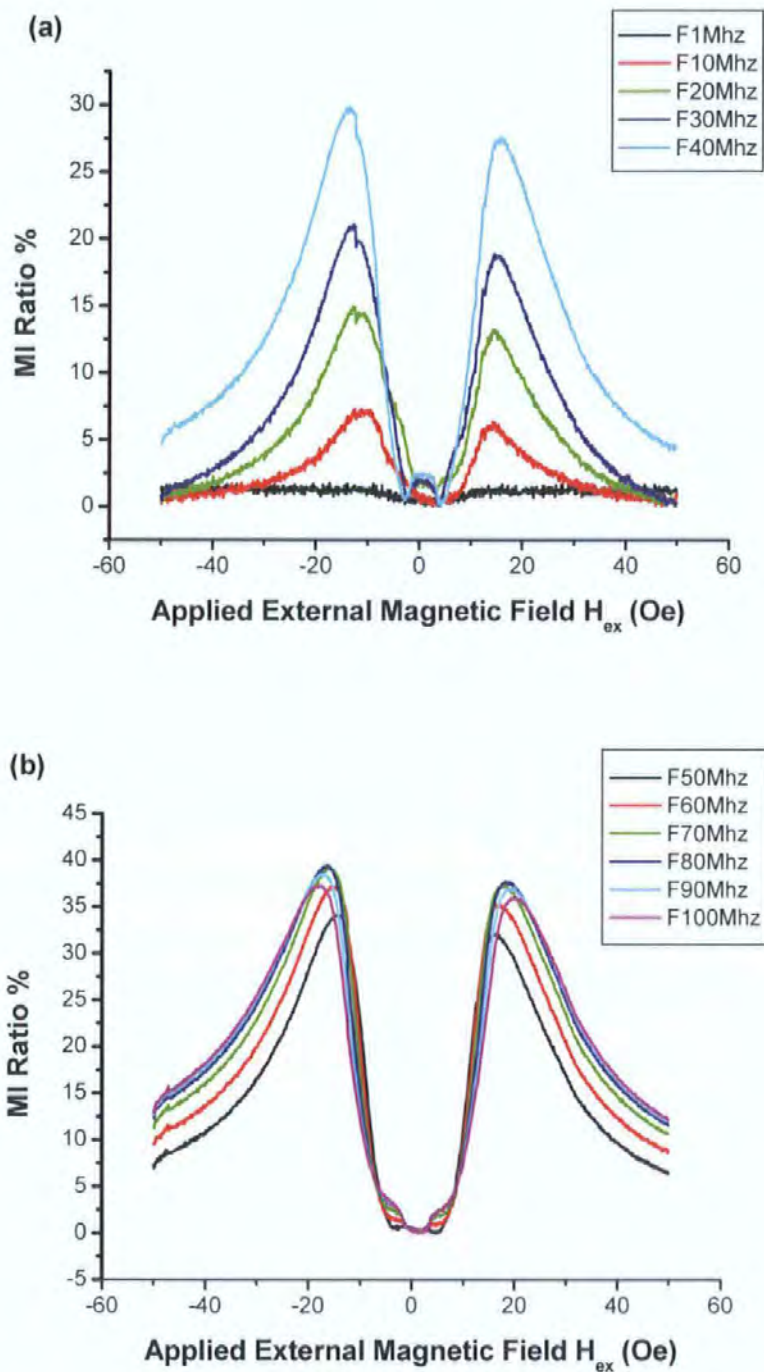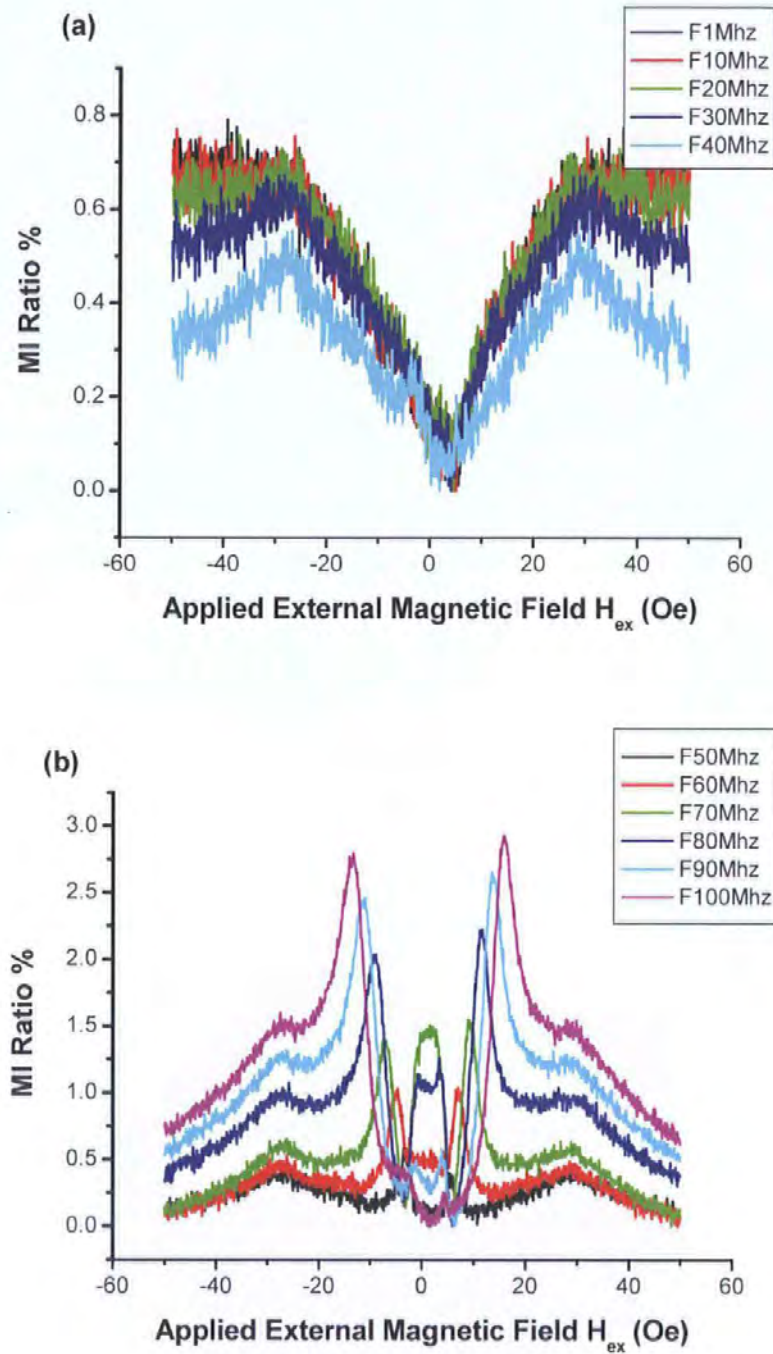
Figure 5.11   Plot of MI ratio vs. magnetic field in 5mm NiFe / Au /NiFe multi-layer with 20μm in-plane width 1 to 40MHz (a), 50 to 100MHz (b).

With a further reduction of the sample width down to 20µm, the in-plane edge effects have an even stronger influence on the magnetic response. The transverse response is severely degraded and not clearly defined even for an excitation frequency of 100MHz, and the sensitivity is severely reduced to only 3% for this geometry and dimensions.

5.3.2 Effect of sample annealing on Magneto Impedance in NiFe / Au / NiFe multi-layers

The next samples will be used as to show experimentally the effect of annealing on the NiFe / Au / NiFe multi-layers after the manufacturing process. The results of a 100µm in-plane width 5mm long sample are illustrated.

During sputtering the sample was exposed to a strong transverse magnetic field in the range of 60 Oe, which generally aligns the anisotropy of the sample. After the sputtering process, the sample cools and internal stresses from the material and the substrate have resulted in a movement of the easy anisotropy axis to the length of the sample. This produces a longitudinal anisotropy. Figure 5.12 shows the MI ratio vs. magnetic field for 'as-fabricated' samples. It is seen that they have completely different behaviour as compared with that seen in Fig. 5.7 to 5.10. The one-peak behaviour is typical of a longitudinal anisotropy [3]. It gives evidence that although, during the deposition a strong magnetic field was applied to set the anisotropy, its direction in 'as-produced' samples does not necessarily coincide with the direction of the field. The longitudinal anisotropy is not typically desired since it can be seen from Fig. 5.12 both the MI ratio and sensitivity are smaller than in the case of transverse anisotropy films. Also there is not much of an improvement in MI characteristics with increasing frequency. Therefore, further post-production treatments are needed to obtain films with high MI ratios. This problem occurs when the in-plane size is smaller than 100µm, which is important for producing miniature thin films for sensor applications.

After manufacturing the sample wafer was annealed in a high vacuum annealing furnace, which was developed after the production of the multi-layers illustrated in Fig. 5.7 to 5.10. This provided an improvement in performance to the existing annealing technique used previously. The device is shown in Fig. 4.5 of chapter 4. The sample is slowly brought up to and beyond the Curie temperature in a vacuum oven, whilst being exposed to a large transverse magnetic field, then slowly brought back down to room temperature. Cooling in

the presence of the transverse field reduces the effects of the tensile stresses between the substrate and material system. After this annealing process, the samples from the wafer showed a very accurate transverse in-plane magnetization structure in respect to the length of the sample, as the peaks are much sharper than in the previous samples shown in Fig. 5.7, which would be consistent with lower dispersion of anisotropy angle through out the material of the sample. Additionally, a lower anisotropy field of about 7 Oe was achieved. As a result a higher MI ratio with a maximum of 55% was observed. These results are shown in Fig. 5.13.

Figure 5.12   Plot of MI ratio vs. magnetic field in 5mm NiFe / Au 100μ in-plane width multi-layer, pre annealing, 1 to 40MHz (a), 50 to 100MHz (b).

Figure 5.13   Plot of MI ratio vs. magnetic field in 5mm NiFe / Au 100μ in-plane width multi-layer after high vacuum annealing, 1 to 40MHz (a), 50 to 100MHz (b).

5.3.3 Magneto Impedance in NiFe / Au / NiFe multi-layers with insulation layers

We will now consider NiFe / Al_2O_2 / Au / Al_2O_2 / NiFe multi-layers with open-loop magnetic flux configuration with an insulation layer of Al_2O_2 between the magnetic and conductor layers. The Al_2O_2 has a thickness of a few nanometers. The insulation layers were proposed for use in multi-layers in [12] for further improvements of the MI behaviour due to better separation of magnetic layers to prevent diffusion between the layers which would equalise the conductivity of the layers.

This multi-layer displays two well defined peaks at $\pm H_K$ at lower frequencies, the anisotropy is around 10 Oe but with increasing frequency the peak shifts to higher fields which could be due to the effect of relaxation in combination with the anisotropy dispersion. The sensitivity to external field increases with frequency due to a larger inductive contribution from the magnetic layers to the total Impedance as shown by Eq. (3.5) from Chapter 3. The MI ratio peaks at 60MHz with some reduction with further increase in frequency. The maximum MI ratio for this system with insulation layer was improved to 75%. Even on reduction of the length to 2mm the peak MI ratio was still very high in the range of 40% at 60 MHz, as illustrated in Fig. 5.15.

Figure 5.16 illustrates a small sample of 2mm length and 50μm in-plane width; however with the additional insulation layer, the general properties remain the same as the larger in-plane width samples, the edge effects are not present, which is a significant improvement on a non insulated NiFe / Au system of the same dimensions. The peak MI ratio is only slightly reduced to 30% at 100MHz. The magnitude of the MI ratio is in the order of the 5mm by 100μm in-plane width NiFe / Au multi-layer of Fig. 5.10 illustrating that the insulating layer significantly reduces the effect of demagnetizing and shape effects on very narrow magnetic structures which is important for producing smaller, more sensitive multi-layers.
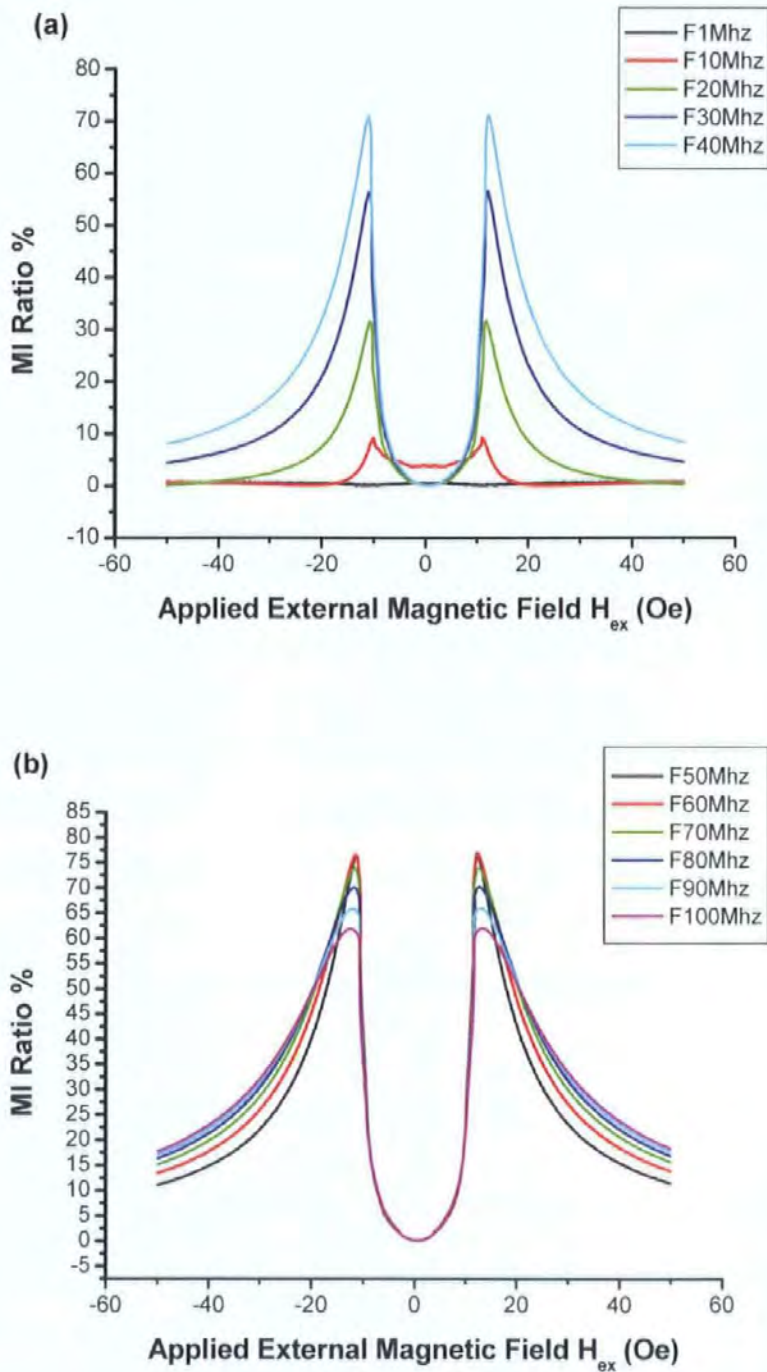
Figure 5.14   Plot of MI ratio vs. magnetic field in 5mm NiFe / Al$_2$O$_2$ / Au 100μ in-plane width multi-layer, 1 to 40MHz (a), 50 to 100MHz (b).
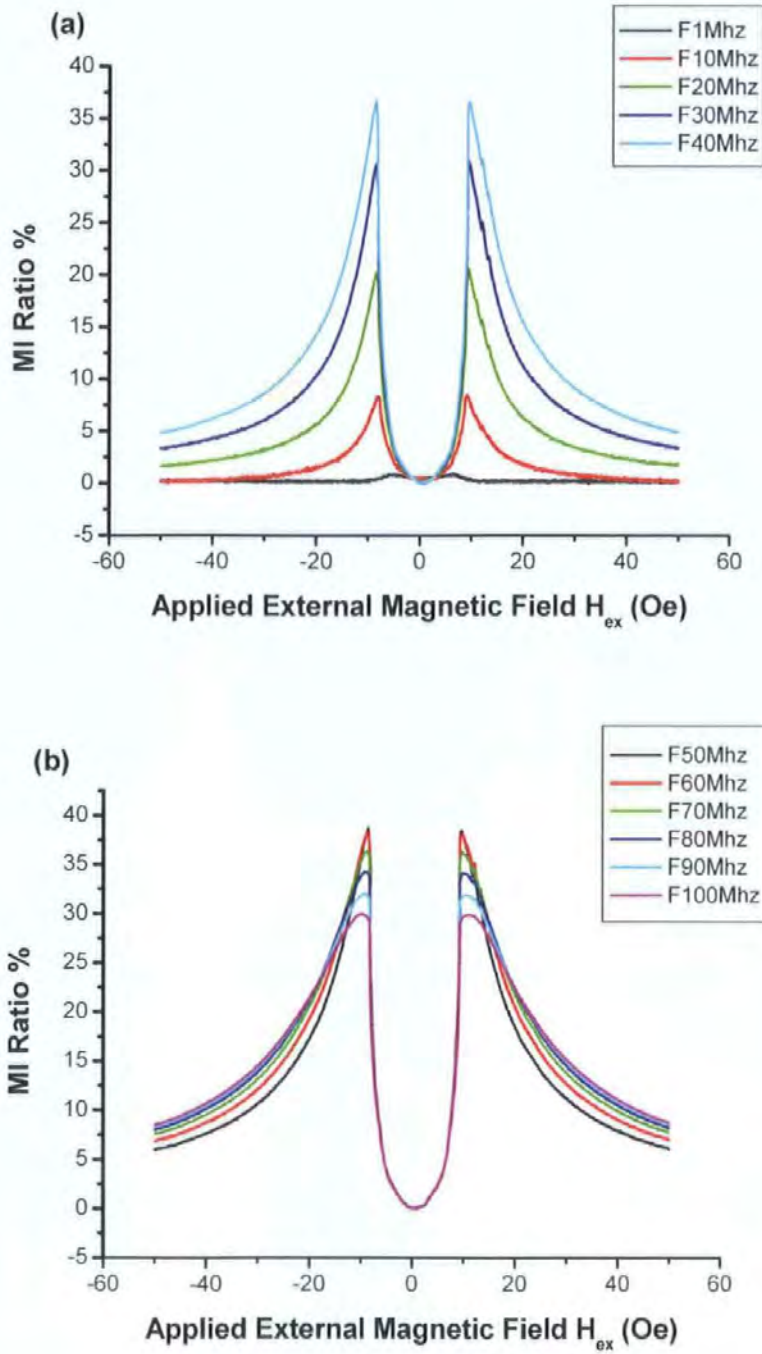
Figure 5.15   Plot of MI ratio vs. magnetic field in 2mm NiFe / Al₂O₂ / Au 100μ in-plane width multi-layer, 1 to 40MHz (a), 50 to 100MHz (b).
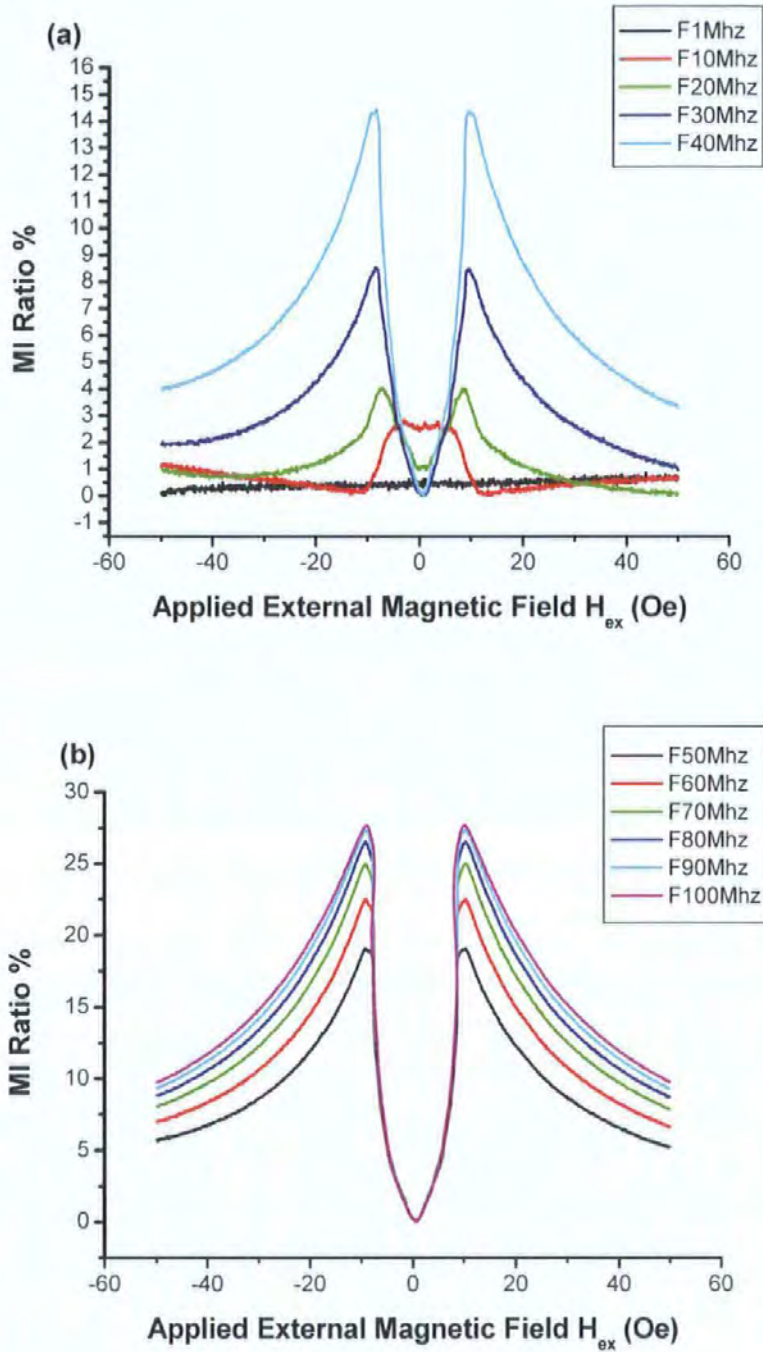
Figure 5.16   Plot of MI ratio vs. magnetic field in 2mm NiFe / Al$_2$O$_2$ / Au 50μ in-plane width multi-layer, 1 to 40MHz (a), 50 to 100MHz (b).

5.3.4   Magneto Impedance in NiFe / Au / NiFe multi-layers with different structures

In this section NiFe /Au NiFe multi-layers with closed or castellated loop magnetic flux configurations, at a fixed dimension and no insulation layer are considered. All samples had the following dimensions, layer thickness 0.5 μm, 5 mm length and 100μm in-plane width.
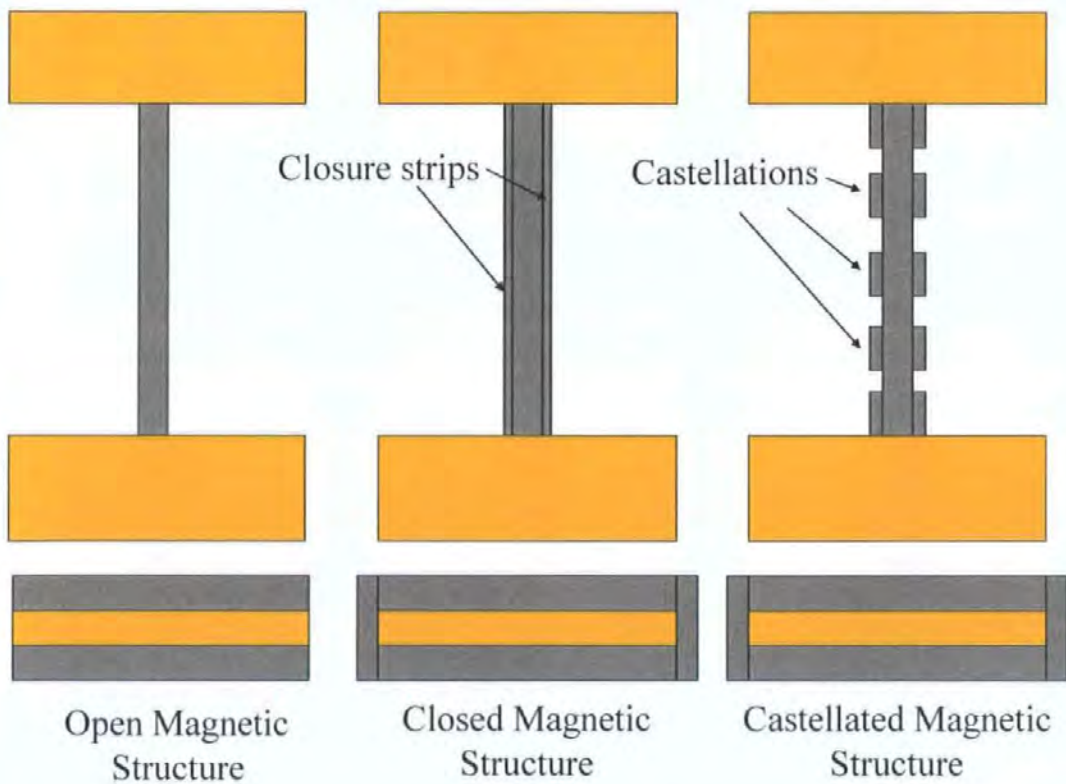
Figure 5.17   NiFe / Au / NiFe magnetic layer flux configurations.

The open loop magnetic flux configuration illustrated in Fig 5.17 was the normal configuration of the magnetic layers measured previously in this work and in Ref. [4-9], where the magnetic layer dimensions are the same as the conducting layer. With the closed magnetic flux configuration magnetic structure, the two magnetic layers are joined to produce a complete magnetic circuit, by simply not etching away the NiFe layers to the same photolithography mask as the conduction layer. With the castellated magnetic flux configuration, the NiFe layers have an additional shape added to them, on both the top and bottom layers, they are still closed, but small sections are removed, to give a "castellated effect", similar to the tops of a castle tower.

The multi-layers displays two well defined peaks at $\pm H_K$ at lower frequencies, the anisotropy is around 7 Oe but with increasing frequency the peak shifts to higher fields which could be due to the effect of relaxation in combination with the anisotropy dispersion. The sensitivity to external field increases with frequency due to a larger inductive contribution from the magnetic layers to the total Impedance. The characteristics of the closed loop illustrated in Fig. 5.18 are similar to an open loop system. However, there is a small distortion on the linear region, which is not present in the open structure. The peak MI ratio of 45% is comparable to the open loop system. The characteristics of the castellated system are illustrated in Fig. 5.19. Again it is similar open structure: the castellated loop has produced a larger distortion in the linear region at 2.5Oe. This distortion increases in magnitude with frequency until it is quite pronounced at 100MHz.

Changing the magnetic flux configuration of the magnetic structure, did not increase the sensitivity of the multi-layer film structure, and created negative effects to the linearity of the response. Therefore for highest linear sensitivity the open loop magnetic flux configuration is preferred.
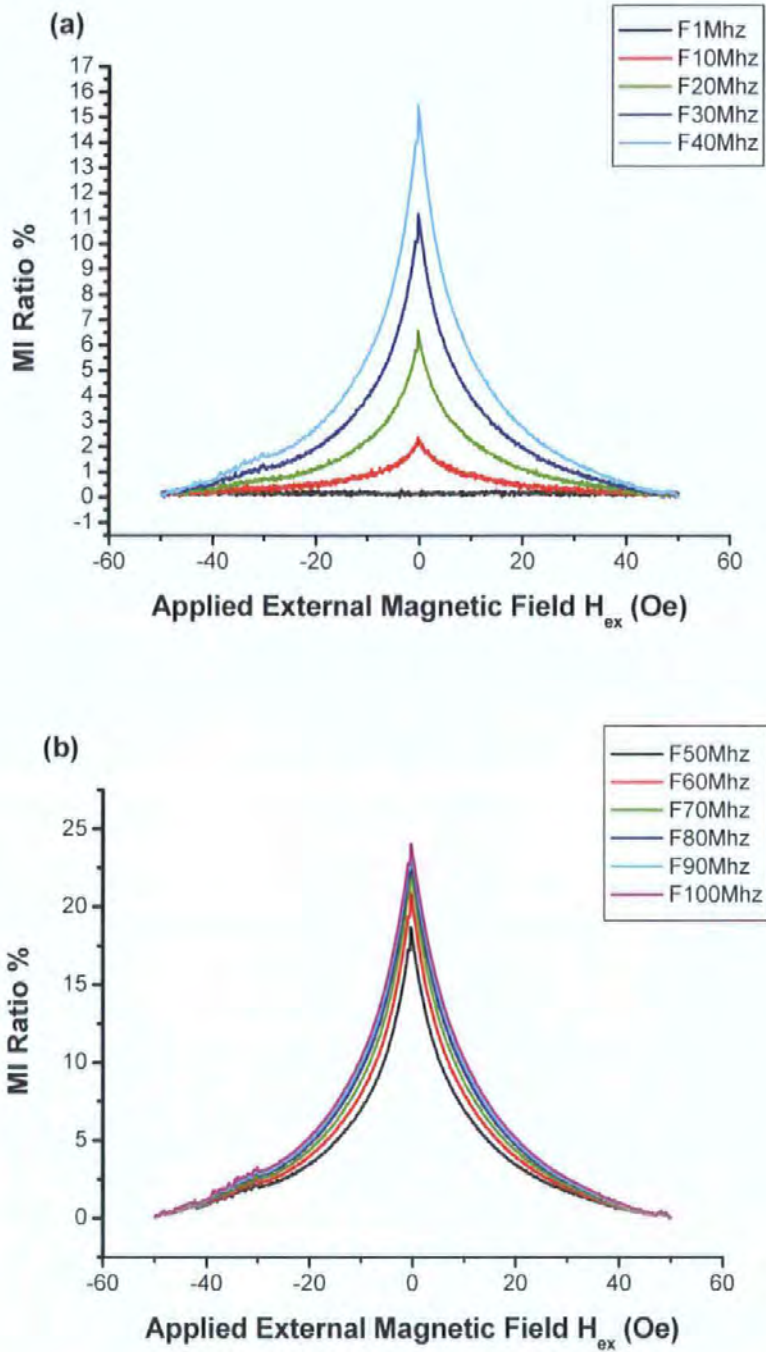
Figure 5.18   Plot of MI ratio vs. magnetic field in 5mm NiFe / Au 100μ in-plane width closed loop multi-layer, 1 to 40MHz (a), 50 to 100MHz (b).
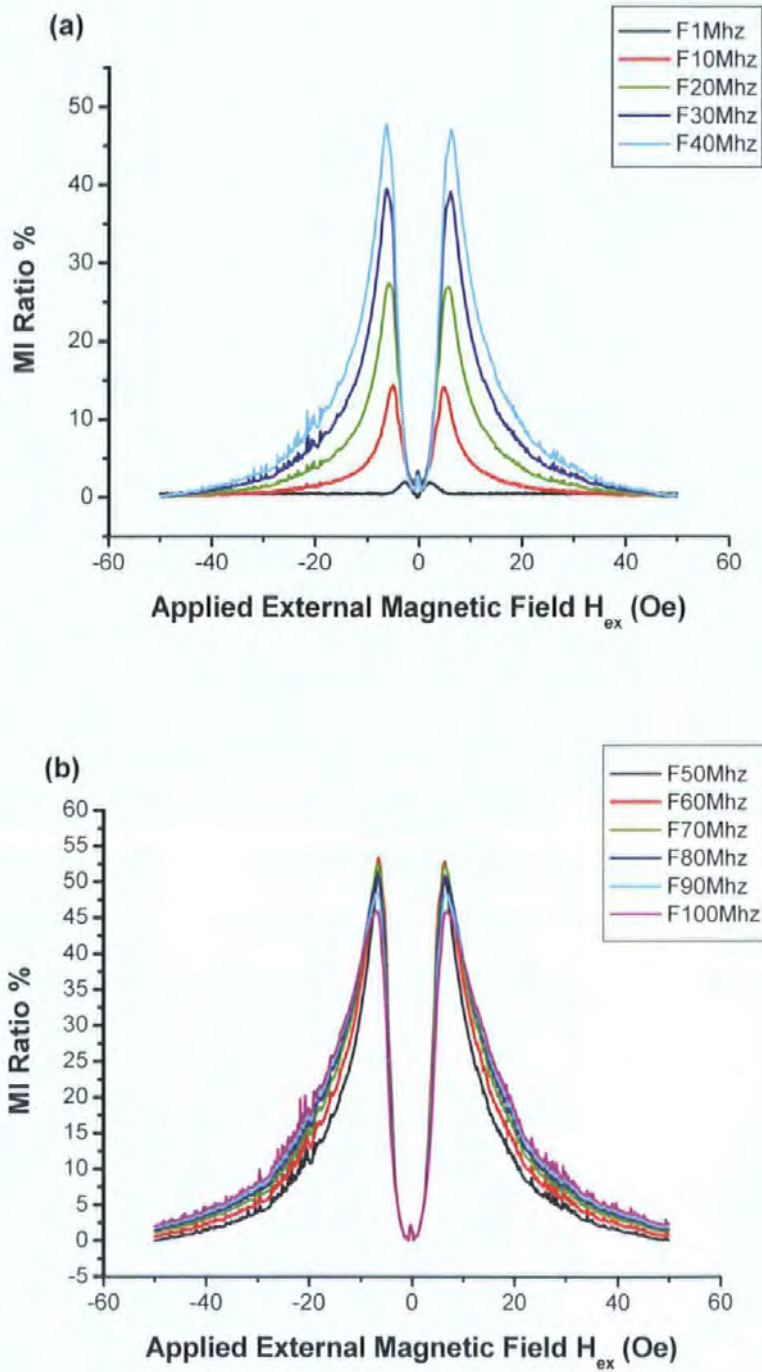
Figure 5.19   Plot of MI ratio vs. magnetic field in 5mm NiFe / Au 100μ in-plane width castellated loop multi-layer, 1 to 40MHz (a), 50 to 100MHz (b).

5.3.5 Magneto Impedance in multi-layers with alternative soft magnetic materials

The multi-layer structures used in these measurements use alternative soft magnetic layers in comparison to NiFe. Two alternative types are presented in this section, $Co_{70.2}Fe_{7.8}B_{22}$ which were supplied by Stanley Electric Company Research and Design, Yokohama, Kanagawa 225, Japan, and CoSiB manufactured locally in CRIST. Similar results have been shown with other amorphous magnetic layered materials and have presented in Ref. [13 to14].

The thin films prepared by Stanley Electric Company consisted of two outer magnetic layers with a $Co_{70.2}Fe_{7.8}B_{22}$ composition and a Cu inner lead sputtered onto a glass substrate. Each layer thickness is 0.5μm and the in-plane width of the sample is 50μm. The uniaxial transverse anisotropy was induced during the sputtering process, and was enhanced with a heat annealing treatment. No insulation layer was present in these samples. In order to increase the length of the sample within a small area, the sample was sputtered in a serpentine configuration, as shown in Fig. 5.20.
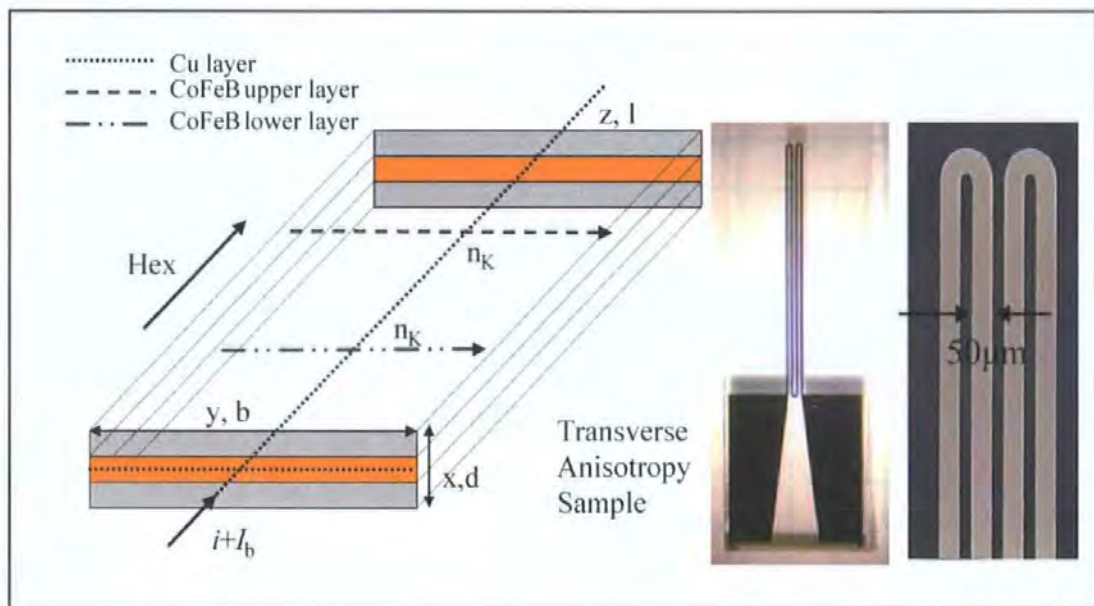
Figure 5.20   Transverse film structure and principle quantities and directions, sample in-plane view.

134

The serpentine geometry multi-layer displays two well defined peaks at $\pm H_K$ at lower frequencies, the anisotropy is around 10 Oe but with increasing frequency the peak shifts to higher fields of around 15 Oe, which could be due to the effect of relaxation in combination with the anisotropy dispersion. The sensitivity to external field increases with frequency due to a larger inductive contribution from the magnetic layers to the total Impedance as with the NiFe multi-layer samples. The MI ratio peaks at 50MHz, as illustrated in Fig. 5.21, before reducing with any further frequency increase. The most apparent difference between the materials is the significant increase in peak MI ratio. The MI ratio shown in Fig. 5.21 is nearly 240% at 50MHz, which is over four times more sensitive than NiFe/Au multi-layers illustrated in Fig. 5.10 through 5.19. This makes this configuration of magnetic material very sensitive at low frequencies, due to a sensitive change of permeability and much larger difference in conductivity (about 50) compared to around 10 of NiFe / Au between the magnetic and conductor layers as shown in Eq. (3.5.) through (3.8)
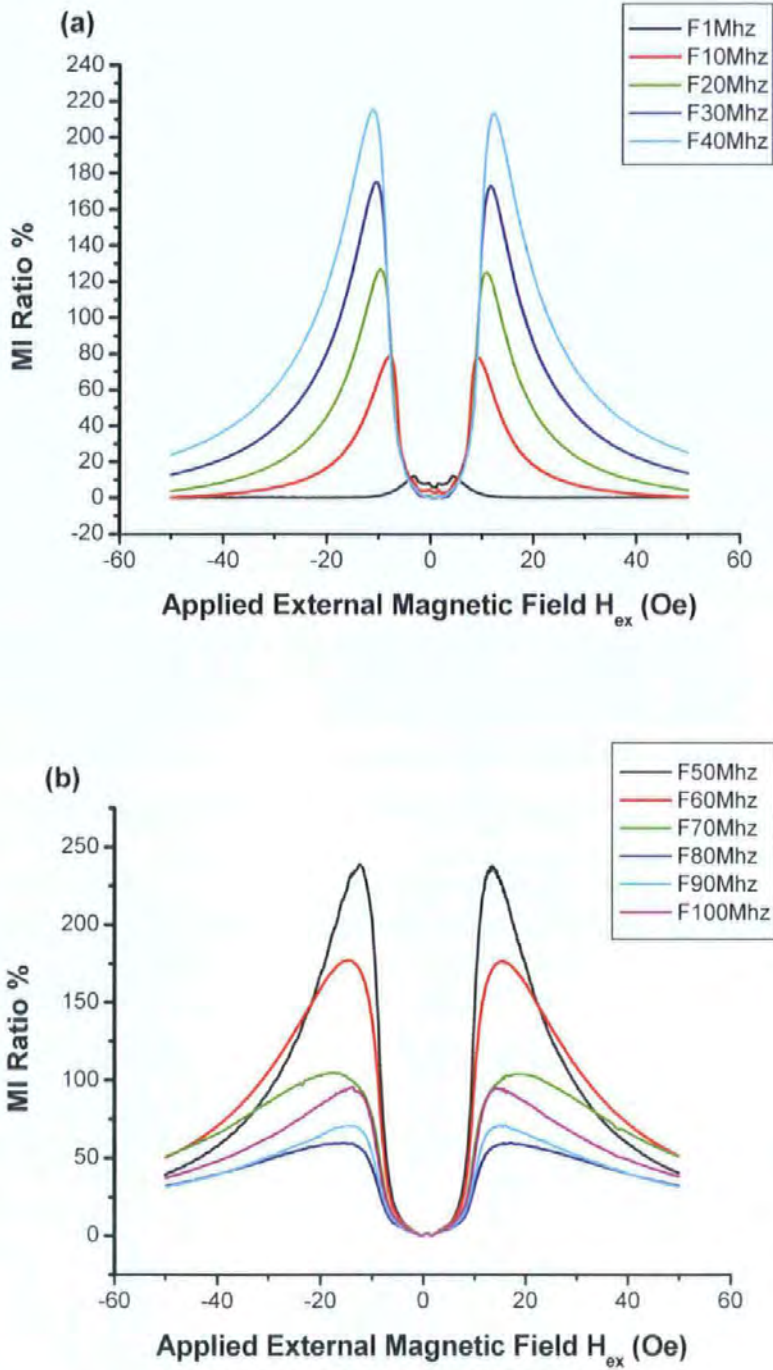
Figure 5.21   Plot of MI ratio vs. magnetic field in $Co_{70.2}Fe_{7.8}B_{22}$ / Cu serpentine 50μm in-plane width multi-layer, 1 to 40MHz (a), 50 to 100MHz (b).

The second amorphous thin films consisted of two outer magnetic layers with the composition CoSiB and Au inner lead sputtered onto a glass substrate. These samples use SiB to make the composition amorphous. Each layer thickness is 0.5μm. The transverse anisotropy was induced during the sputtering process, and was enhanced with a high vacuum heat annealing treatment. No insulation layer was present in these samples.

The 5mm length and 100um in-plane width sample displays two well defined peaks at $\pm H_K$, the anisotropy is surprisingly small around 3 Oe and does not vary significantly with increasing frequency. This is smaller than that in the previous CoFeB multi-layer. The anisotropy dispersion is extremely low in these samples leading to very sharp narrow peaks. The sensitivity to external field increases with frequency due to a larger inductive contribution from the magnetic layers to the total Impedance as with the NiFe multi-layer samples. The MI ratio reaches a peak at 50MHz with only slight reductions as frequency increases, as illustrated in Fig. 5.22. The maximum MI ratio for these dimensions is 120%, making it three times more sensitive than a NiFe / Au samples shown in Fig. 5.10 through 5.19. As a consequence of the low anisotropy field and dispersion the MI ratio changes with a high gradient (MI % / Oe) around 40% per Oe making the sample very sensitive to small increases in external field. The peak MI ratio is less than the previous CoFeB multi-layer (240%), but the gradient of MI ratio is much higher in the CoSiB multi-layers due to the low anisotropy field, making the sample sensitive to small changes of field, which is an important factor for sensors systems. On reduction of the width to 50μm the peak MI ratio is reduced significantly to a peak value of 50% at 100 MHz, as illustrated in Fig. 5.23. The edge effect reduces with increasing frequency, as indicated by the continuous rise in MI ratio with frequency. Figure 5.24 illustrates a short, wide sample of 2mm by 200μm in-plane width, and the general characteristic shape returns to the sharp peaks of the 100um in-plane width sample. The peak MI ratio is only slightly reduced to a maximum of 100% at 50MHz. Figure 5.25 illustrates another 2mm sample, but with a further reduction of in-plane width to 100μm, it displays a peak MI ratio of 40% at 70MHz. The peak magnitude of MI ratio in this 2mm 100μm sample is in the order of a 5mm by 100μm NiFe sample, illustrating that the CoSiB magnetic composition in combination with Au conductive layer is significantly more sensitive than NiFe, even when the dimensions of the thin film are reduced, this is mainly due to the increase in conductivity ratio between the CoSiB / Au compared to the NiFe / Au. This is important for producing miniature, sensitive multi-layer systems.
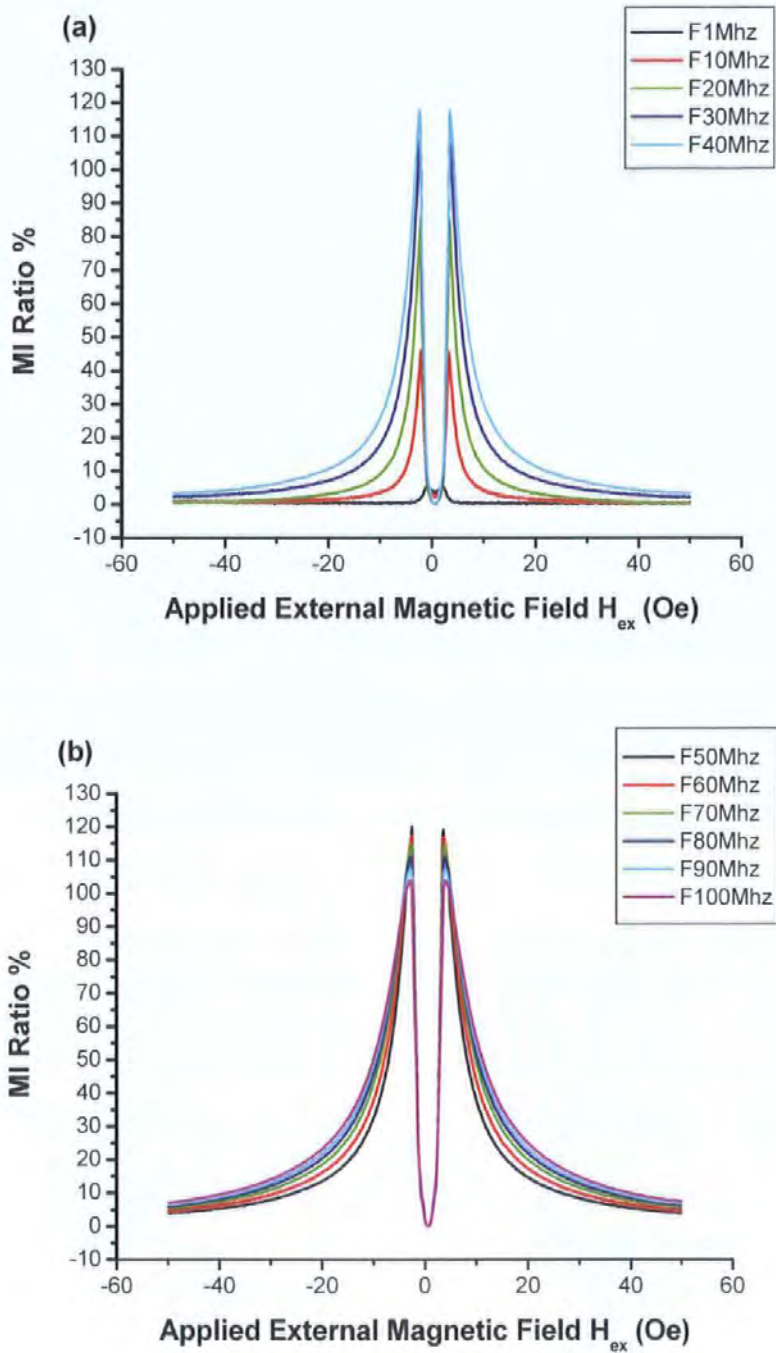
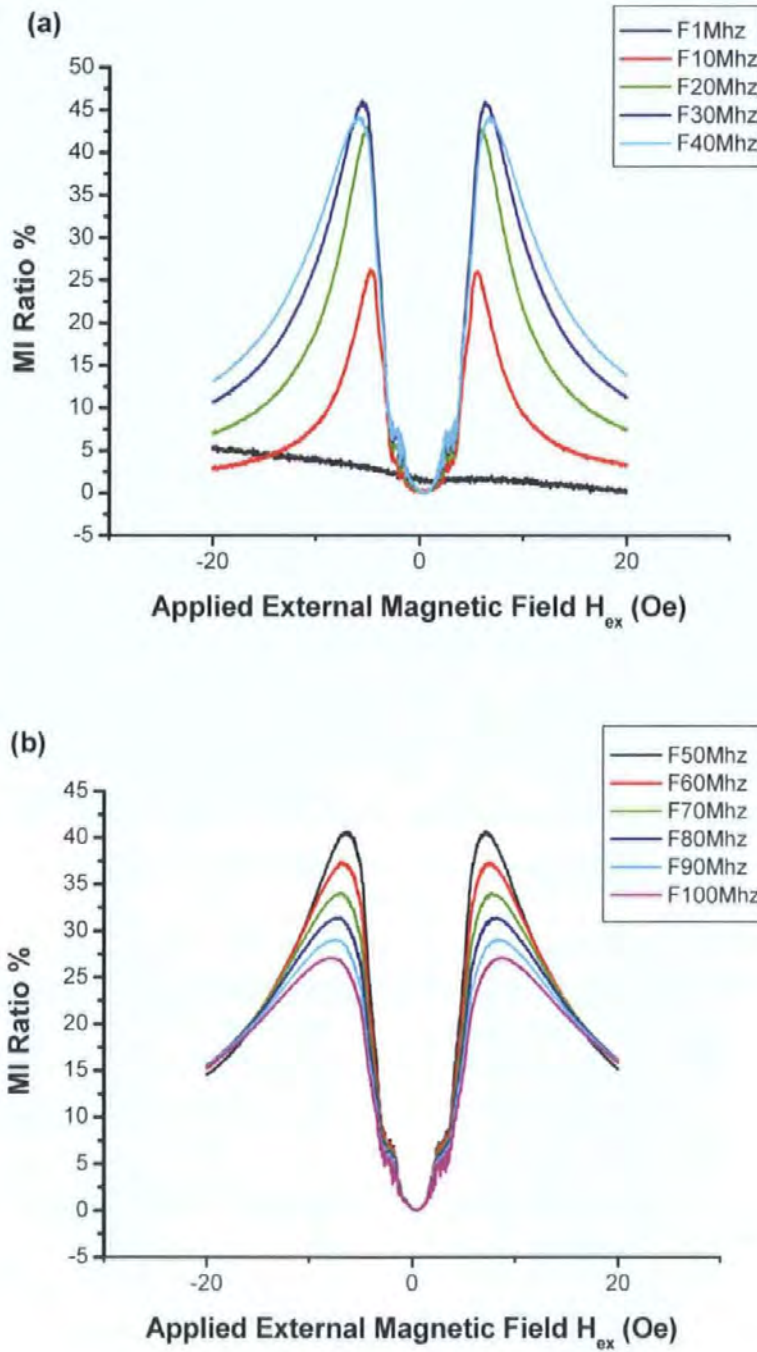*Figure 5.22   Plot of MI ratio vs. magnetic field in 5mm CoSiB / Au 100μin-plane width multi-layer, 1 to 40MHz (a), 50 to 100MHz (b).*
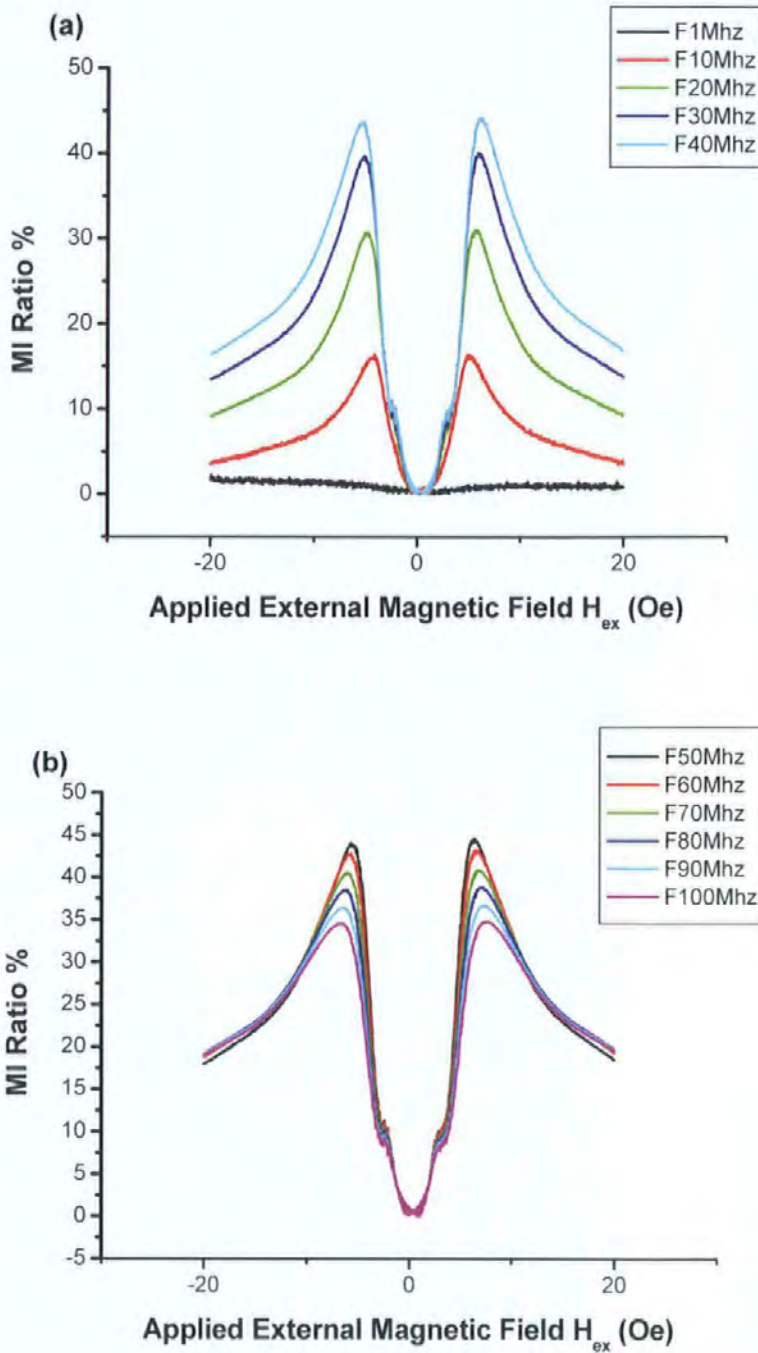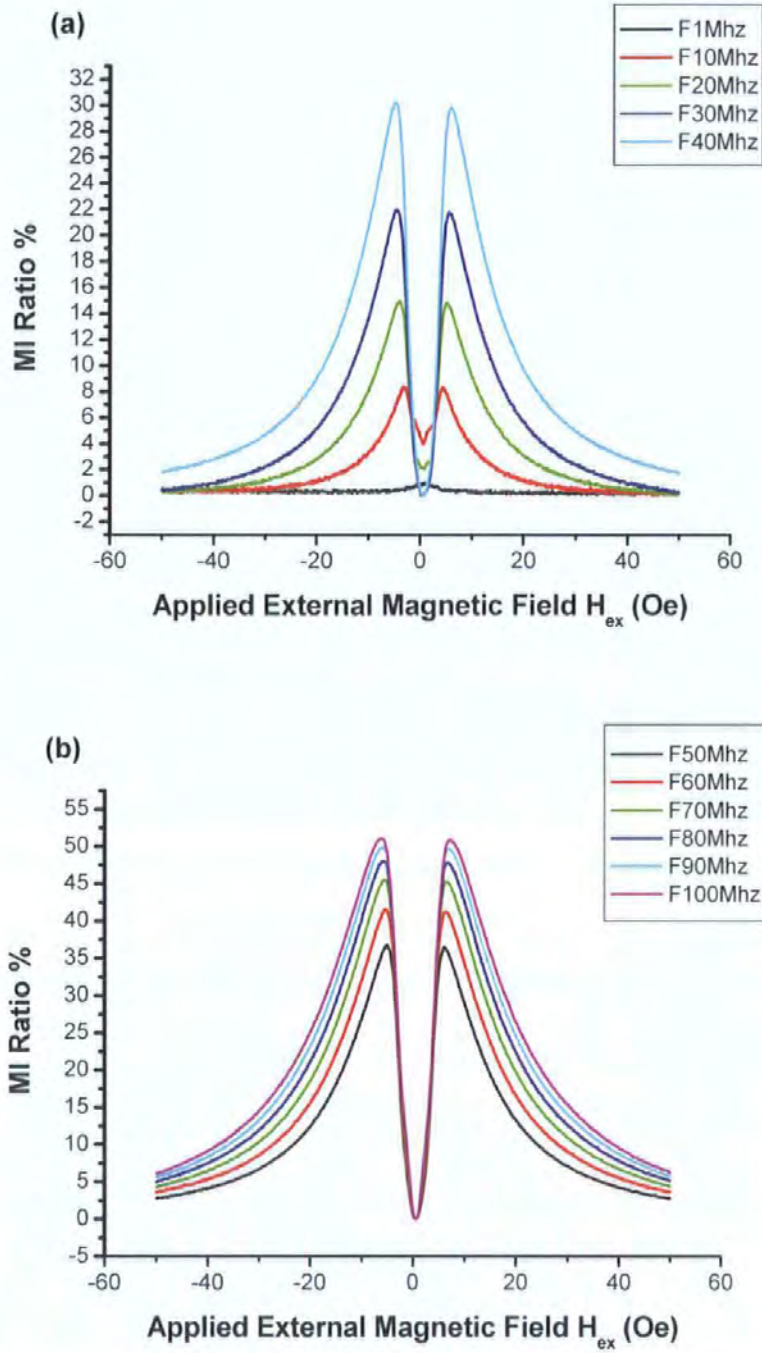
Figure 5.23   Plot of MI ratio vs. magnetic field in 5mm CoSiB / Au 50µ in plane width multi-layer, 1 to 40MHz (a), 50 to 100MHz (b).
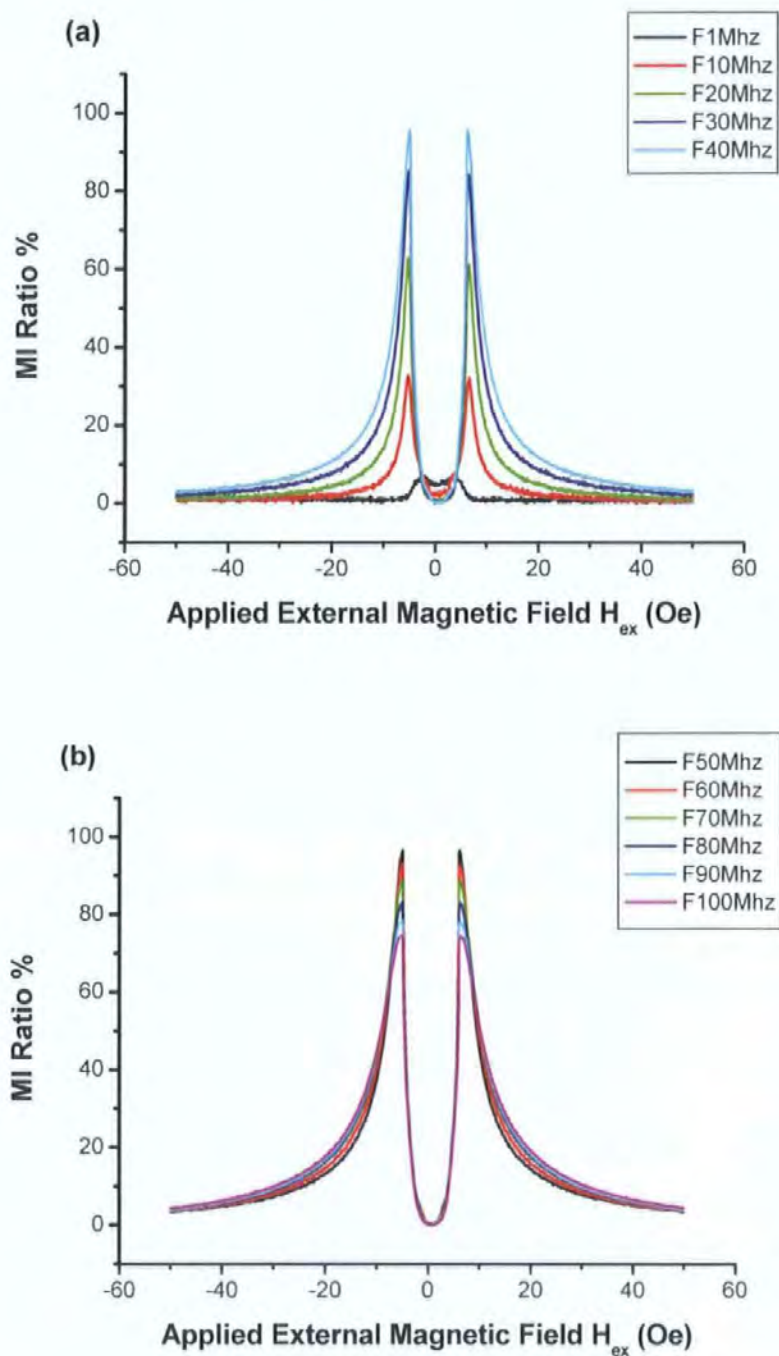
Figure 5.24   Plot of MI ratio vs. magnetic field in 2mm CoSiB / Au 200μ in plane width multi-layer, 1 to 40MHz (a), 50 to 100MHz (b).
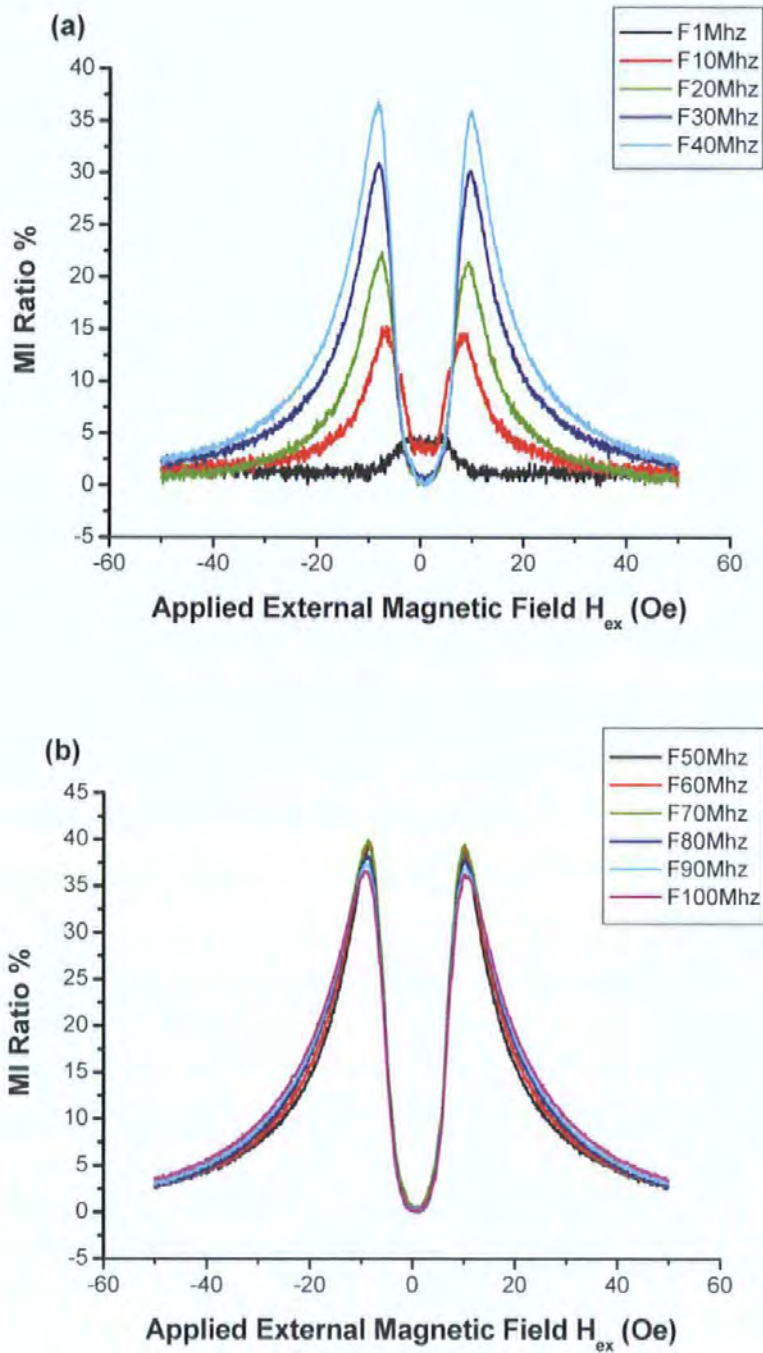
Figure 5.25   Plot of MI ratio vs. magnetic field in 2mm CoSiB / Au 100μ in plane width multi-layer, 1 to 40MHz (a), 50 to 100MHz (b).

It has been shown how different dimensions, geometries and materials can affect the sensitivity of the multi-layer film to an external field.   By using a longer, wider in-plane width thin film multi-layer which has been annealed after manufacture in an accurate vacuum method, a higher MI ratio can be achieved.

A lower anisotropy field is preferred in order to increase the gradient of the MI ratio, making the tin film more sensitive to smaller changes in external field. The larger dimensions are able to create an accurate homogenous anisotropy in the sample; the sample also suffers from less demagnetization fields and edge effects.

Additionally an insulating layer between the magnetic and conductive layers helps contain the flow of the current inside the conductor, which reduces the resistivity in the system. Further more the use of specific soft magnetic materials is able to increase the change of permeability in the sample and greatly increase the difference in conductivity between the magnetic and conducive in layer.

All of these factors combined are able to produce a magnetic transducer that is very sensitive to external magnetic fields when under the application of alternating current of a specific frequency, making the MI effect useful as a magnetic field sensing device and in reducing the size of the thin film for incorporation into integrated circuit (IC) technologies.

References

[1] Agilent AN 1287-1, "*Understanding the fundamental principles of vector network analysis*" Agilent application Note (1997).

[2] Agilent AN 1287-2, "*Exploring the architectures of network analysers*" Agilent application Note (1997).

[3] D. Makhnovskiy, "*Diagonal and Off-Diagonal Magneto Impedance In Ferromagnetic Microwires and Thin Films*", PhD Thesis, The University of Plymouth,(2003).

[4] T. Morikawa, Y. Nishibe, H. Yamadera, Y. Nonomura, M. Takeuchi, and Y. Taga, "*Giant magneto-Impedance effect in layered thin films*," IEEE *Trans. Magn.*, vol. 33, pp. 4367–4372, Sept. 1997.

[5] K. Hika, L. V. Panina, and K. Mohri, "*Magneto-Impedance in sandwich film for magnetic sensor heads*" IEEE *Trans. Magn.*, vol. 32, pp. 4594–4596, Sept. 1996.

[6] L. V. Panina and K. Mohri, "*Magneto-Impedance in multilayer films*" *Sens. Actuators A, Phys.*, vol. 81, no. 1–3, pp. 71–77, 2000.

[7] N. Jiang, K. Yamakawa, N. Honda, and K. Ouchi, "*A New Giant Magneto Impedance Head Using Magnetic Microstrip Lines*" IEEE Trans. Magn.34 1339, (1998).

[8] M. Takezawa, H. Kikuchi, M. Yamaguchi, and K. I. Arai, "*Miniaturization of high-frequency carrier-type thin-film magnetic field sensor using laminated film*" IEEE Trans. Magn. 36 3664, (2000).

[9]   R. L. Sommer, A. Gundel, and C. L. Chien, "*Magneto-impedance effects in multilayered permalloy materials*" J. Appl. Physics. 86, 1057 (1999).

[10]   D.P. Makhnovskiy, L. V. Panina, "*Size effect on magneto-impedance in layered films*" Sensor and actuators, A81, 91 (2000).

[11]   L. V. Panina , D.P. Makhnovskiy, D. J. Mapps, and D. S. Zarechnyuk, "*Two-dimensional analysis of magneto impedance in magnetic/metallic multilayers*" J. Appl. Physics. 89, 7221 (2001).

[12]   T. Morikawa, Y. Nishibe, H. Yamadera, Y. Nonomura, M. Takeuchi, J. Sakata, and Y. Taga, "*Enhancement of giant magneto-impedance in layered film by insulator separation*" IEEE Trans. Magn., vol. 32, pp. 4965–4967, Sept. 1996.

[13]   Y. Zhou, J. Yu, X. Zhoa, and B. Cai, "*Giant magneto Impedance in layered FeSiB/Cu/FeSiB films*", Journal of applied physics, Vol 89, Number 31 (2001).

[14]   Y. Nishibe, H. Yamadera, N. Ohta, K. Tsukada and Y Ohmura, "*Magneto Impedance effect of layered CoNbZr amorphous film formed on a polyimide substrtate*", IEEE Trans. Magn. MAG-39(1) 571, (2003).

Chapter 6. Asymmetrical Magneto Impedance in crossed anisotropy multi-layers and multi-layers with integrated coil

This chapter continues the experimental Magneto Impedance measurements undertaken on the thin film multi-layers with a specific anisotropy and multi-layers with an integrated coil. The samples were manufactured locally in the CRIST facility, and supplied by Stanley Electric Company Research and Design, Yokohama, Kanagawa 225, Japan. Here asymmetrical Impedance behaviour (with respect to applied magnetic field) is highlighted, which can be obtained in multi-layers with crossed anisotropy subjected to a DC bias current. Asymmetric and near linear MI behaviour is also obtained in multi-layers with a transverse anisotropy subjected to a small AC field produced by a planar coil integrated into film system.

6.1   Static   Asymmetric   Magneto   Impedance   in   crossed   anisotropy $Co_{70.2}Fe_{7.8}B_{22}$ / Cu multi-layers

The field behaviour of the Impedance is governed by the DC magnetic structure as explained in Chapter 3. It was then proposed theoretically that in multi-layers with an asymmetric arrangement of the magnetisation with respect to H_{ex} the Impedance will also show an asymmetric behaviour. Such asymmetric DC magnetisation process can be realised in multi-layers with a crossed anisotropy in the presence of a DC bias current I_b (see Chapter 3 for details). A similar magnetic configuration has been realised in the bilayer (without inner conductor) MI film with crossed anisotropy [1, 4-6] and wire with helical anisotropy induced by torsion stress [2] or annealing under torsion stress [3].

The multi-layer structures used in these measurements consisted of two outer magnetic layers with composition $Co_{70.2}Fe_{7.8}B_{22}$ and Cu inner lead sputtered onto a glass substrate. Each layer thickness is 0.5µm. Firstly uniaxial transverse anisotropy was induced during the sputtering process under a large uniform field of 200 Oe. The crossed anisotropy as shown in Fig. 6.1 was induced into the sample by current annealing in the presence of small longitudinal field.

This resulted in the anisotropy easy axes $\mathbf{n}_K$ having an angle $\pm\alpha$ with respect to the film long direction (z-axis). Altering the magnitude of the applied current could vary the angle of anisotropy α. Two types of sample where prepared, firstly a straight multi-layer of length 5mm with a width of 40µm and α of 15, 30 and 45 degrees and a serpentine configuration which was the same as the previous transverse samples illustrated in chapter 5, with an α of 66° measured by DC hysteresis loops.
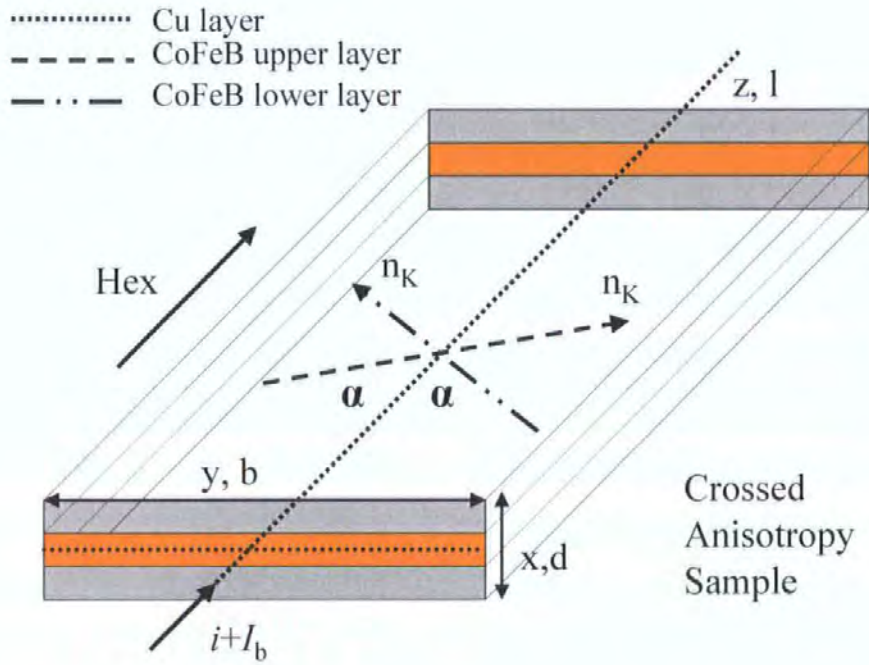
Figure 6.1   Crossed anisotropy film structure, principle quantities and directions.

Firstly, a sample in a serpentine configuration was investigated which allows an accurate measurement of the DC magnetization process. The anisotropy axis in the upper and bottom layers (designated as $\mathbf{n}_K$ in Fig 6.1) are at approximately 67° to the z-axis in this sample, which was estimated from DC hysteresis loops in the presence of a bias current I_b as shown in Fig. 6.2 The hysteresis of the sample was measured by using a pickup coil wound around the glass substrate of the sample (50 turns, 3mm diameter), and an identical compensation coil wrapped around a plain glass substrate connected to a differential amplifier. The effect of the application of I_b is to cause a shift in the loop towards negative fields (or positive, depending on the applied direction of I_b) and decrease the overall hysteresis area. The anisotropy angle is found from the shifting field, which is given by $H_b \tan\alpha = I_b \tan\alpha / 2b$ (b is the film width).
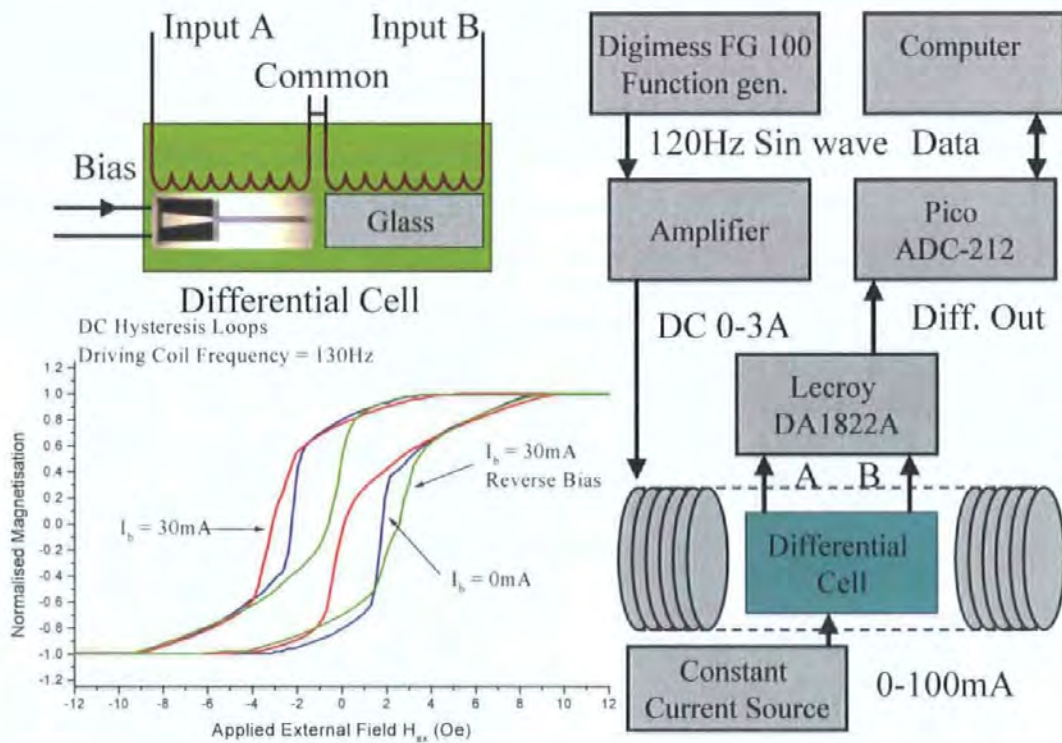
Figure 6.2   Schematic diagram of experimental configuration to measure the DC hysteresis loops of a crossed anisotropy sample with a DC bias current as a parameter and to identify the angle of anisotropy α. The hysteresis loops are shifted in the presence of I_b.

Figure 6.3 demonstrates the impedance vs, field behavior in this sample without a bias current I_b. In this case the reversible magnetization process remains symmetric, and the impedance characteristics of the serpentine sample resemble that of a transverse anisotropy samples with two symmetrical maxima.

However, the peaks are not pronounced at lower frequencies since it appears that both the domain and rotational processes give contributions to the impedance behavior. As the frequency is increased and the rotation component of permeability becomes dominant the maxima are clearly seen.

The MI ratio as a function of frequency has two maxima about 35% at 20 MHz and about 30% at 70 MHz. Such frequency behavior of the impedance should be attributed to a complicated dynamic magnetization process involving both domain wall displacements and magnetization rotation.
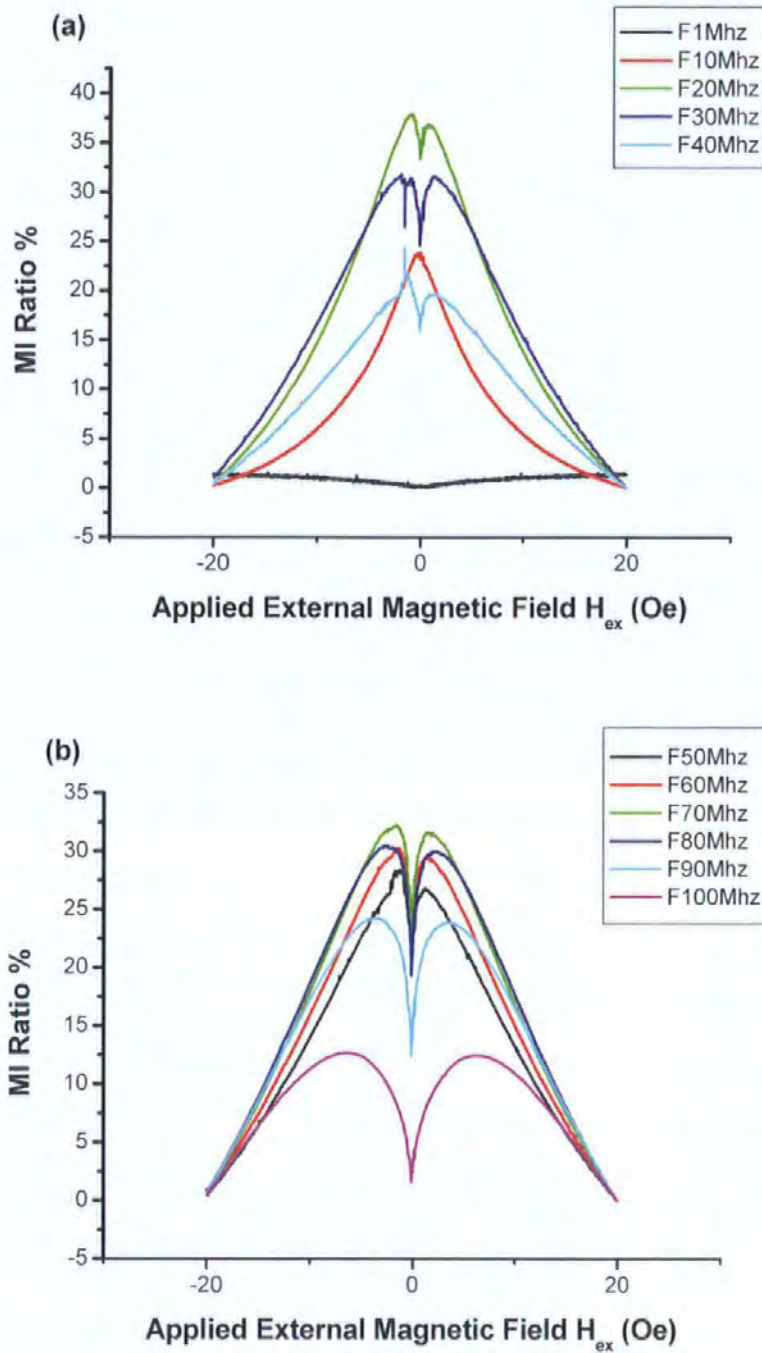
Figure 6.3   Plot of MI ratio vs. magnetic field of the $Co_{70.2}Fe_{7.8}B_{22}$ / Cu crossed anisotropy sample without a bias current 1 to 40MHz(a), 50 to 100MHz (b).

After a DC bias is applied to the sample, the reversal of magnetisation becomes asymmetric with respect to external field, due to the additional transverse bias field as seen in Fig. 6.2 and described in Section 3.3.2. The impedance plots for this case are shown in Fig. 6.4. For sufficiently large values of the bias current (I_b =25mA in Fig. 6.4) the impedance behaviour is characterised by a sharp increase seen near zero external field which should be attributed to the domain wall formation and a sharp increase in the domain permeability. As a result, the impedance has two maxima, one of which is enhanced and the other is strongly suppressed.

Such behaviour is most effective in the frequency region of 20-40 MHz. With increasing frequency, the two maxima becomes of a comparable magnitude. It is not quite clear why there is almost no hysteresis in MI behaviour. The maximum MI ratio for 10 MHz is nearly 50% and it increases up to more than 90% for 30 MHz .
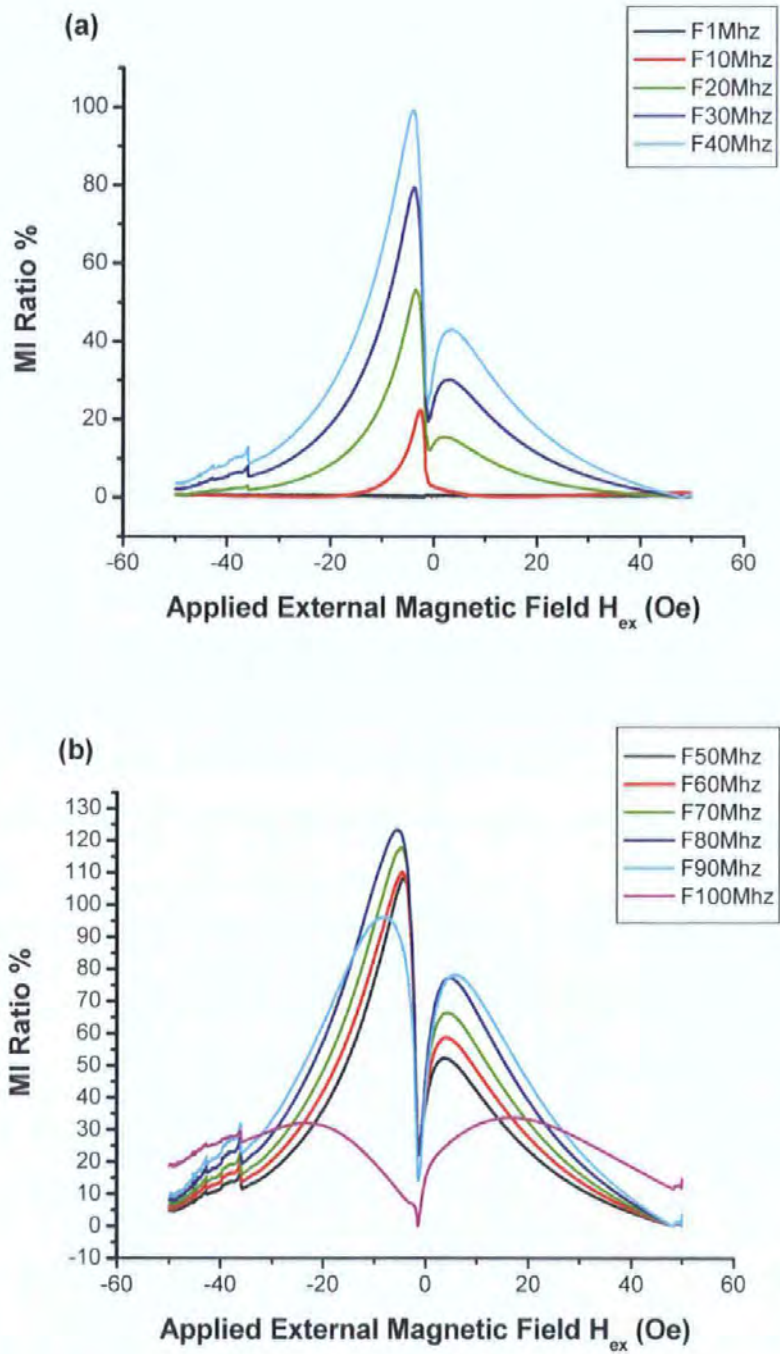
Figure 6.4   Plot of MI ratio vs. magnetic field of the $Co_{70.2}Fe_{7.8}B_{22}$ / Cu crossed anisotropy sample with a bias current of 25mA, 1 to 40MHz (a), 50 to 100MHz (b).

The second set of measurements, were carried out on the straight samples of 5mm length and 40μm in width, with varying angles of anisotropy α. The MI ratio vs. external field for these samples is shown with frequency as a parameter in Figs. 6.5 to 6.7. As before the bias field produces an asymmetrical magnetisation reversal in the samples leading to asymmetrical magnetisation plots with a sharp increase near zero field.

As α is decreased the MI ratio increase to 125% at $\alpha = 15°$ while its 75% at $\alpha = 30°$. It is interesting to notice that for $\alpha = 45°$ (Fig. 6.7) the transition to the higher peak occurs almost instantly producing highly sensitive characteristic. Rotational contributions are quite suppressed until 50MHz, the MI ratio is 55% at 100MHz. However, such a jump in the MI plot would be appropriate only for special switch type sensors. For the purpose of field measurements, the characteristics seen in Figs. 6.5 and 6.6 would be preferable.
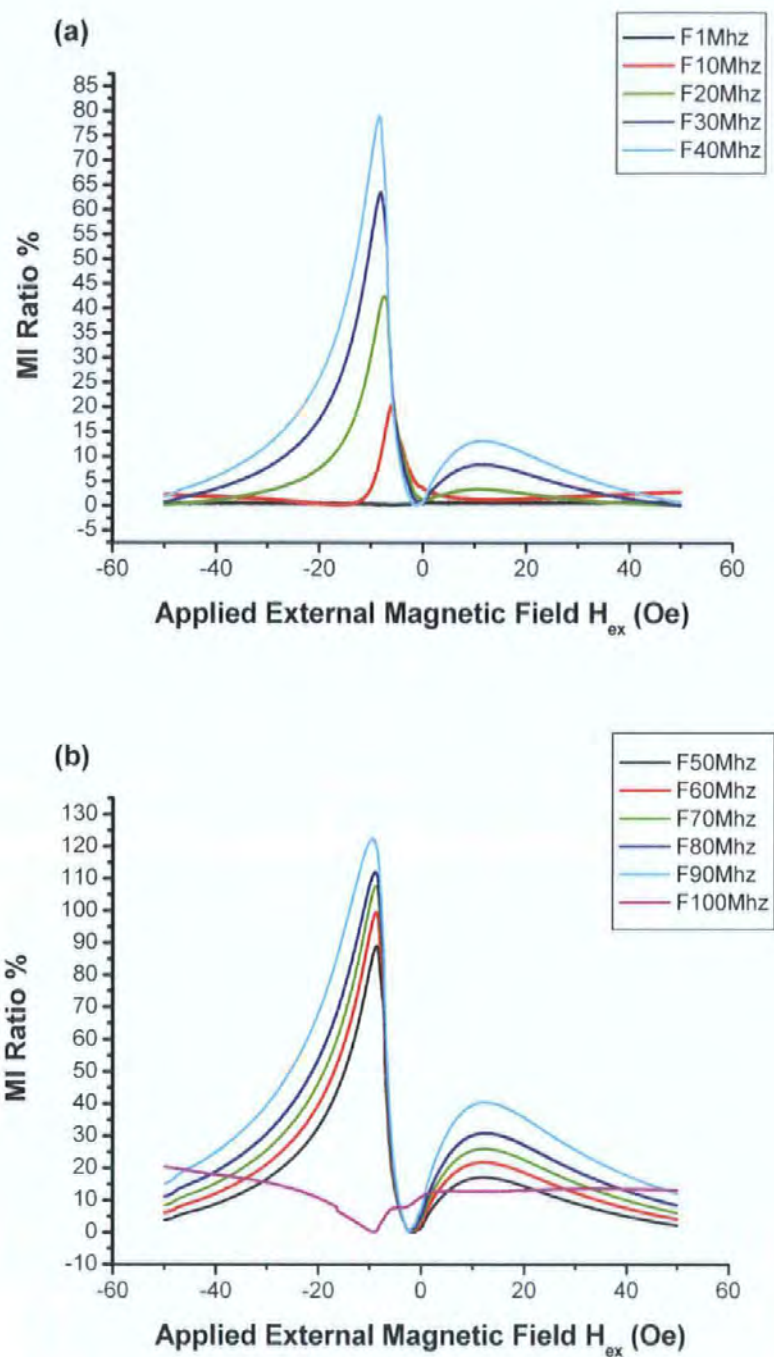
Figure 6.5   Plot of MI ratio vs. magnetic field of the $Co_{70.2}Fe_{7.8}B_{22}$ / Cu crossed anisotropy sample having the anisotropy angle of 15° with a bias current of 25mA, 1 to 40MHz (a), 50 to 100MHz (b).
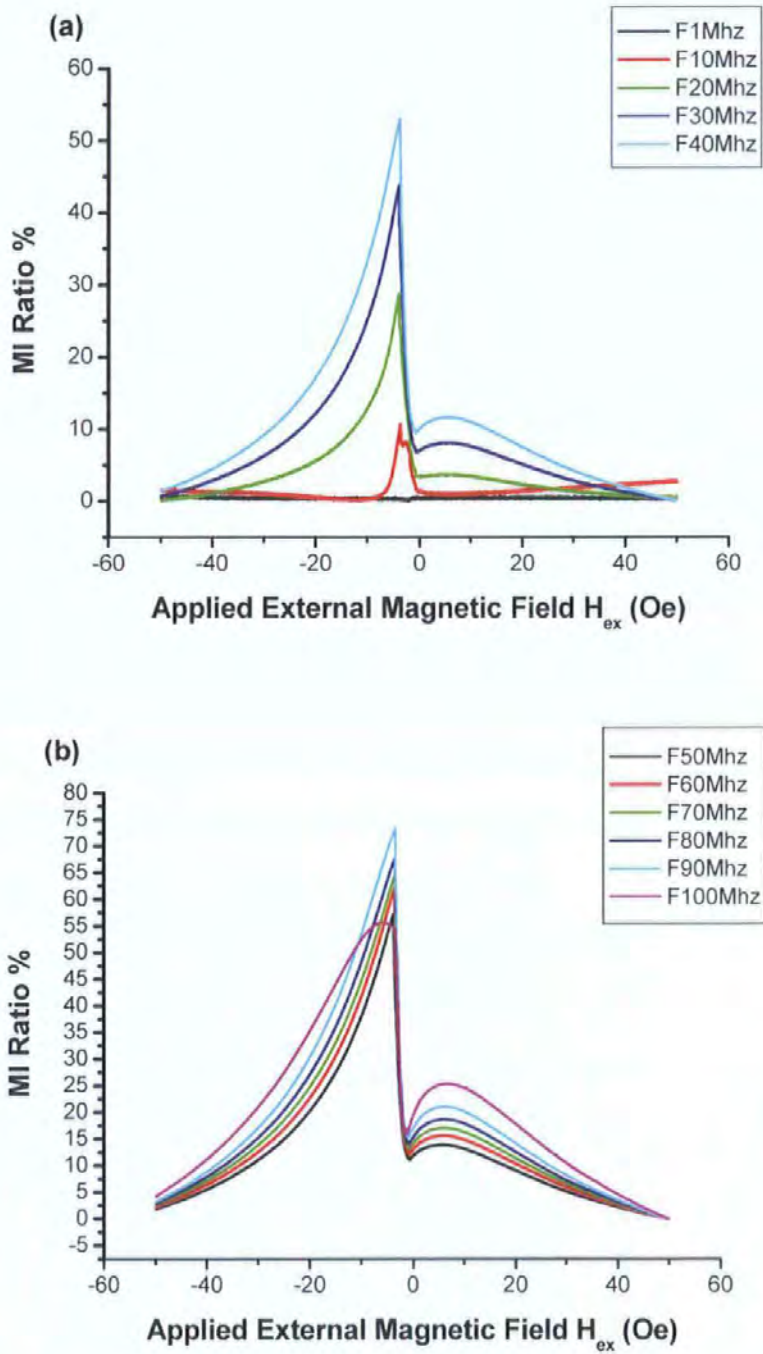
Figure 6.6   Plot of MI ratio vs. magnetic field of the $Co_{70.2}Fe_{7.8}B_{22}$ / Cu crossed anisotropy sample having the anisotropy angle of 30°   with a bias current of 25mA, 1 to 40MHz (a), 50 to 100MHz (b).
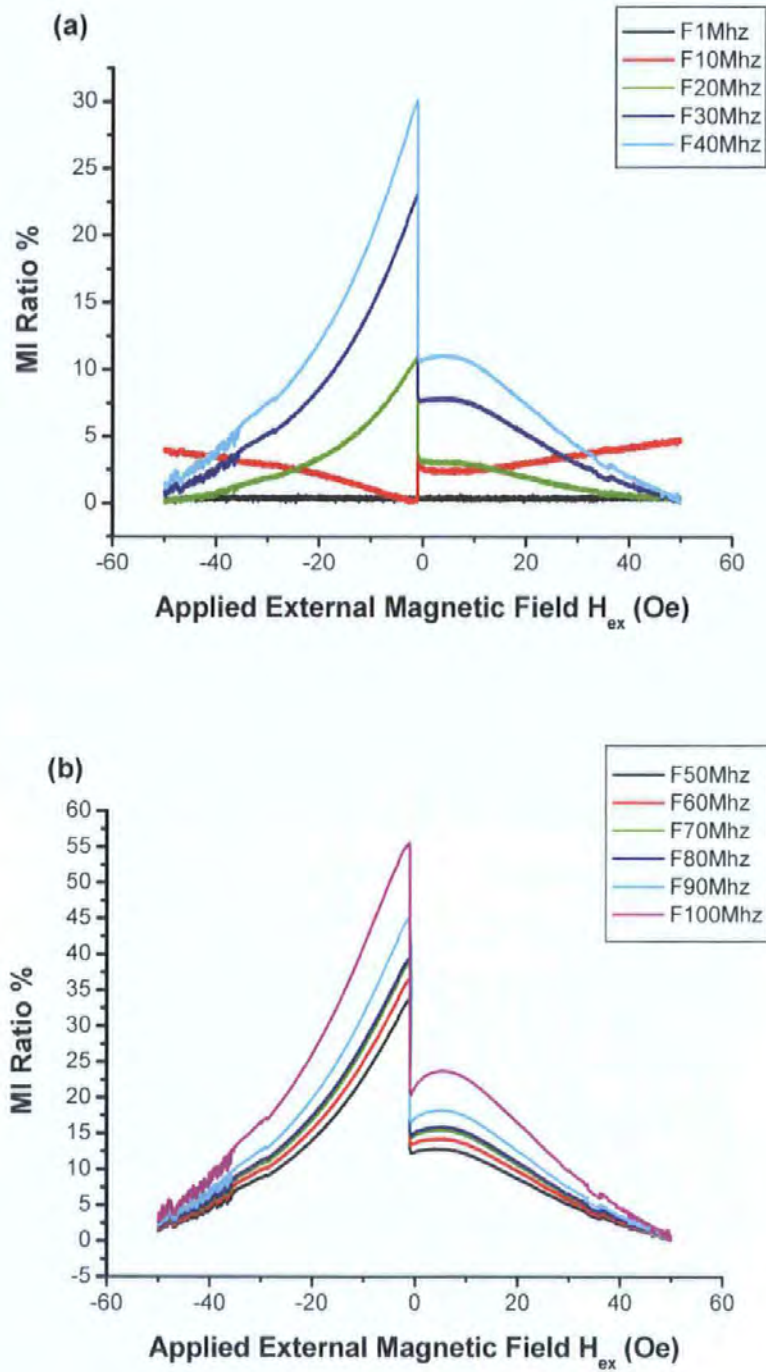
Figure 6.7   Plot of MI ratio vs. magnetic field of the $Co_{70.2}Fe_{7.8}B_{22}$ / Cu crossed anisotropy sample having the anisotropy angle of 45° with a bias current of 25mA, 1 to 40MHz (a), 50 to 100MHz (b).

6.2 Dynamical asymmetric off-diagonal Magneto Impedance in transverse anisotropy multi-layers with planar coil

The off diagonal component of impedance either ς_{zy} or ς_{yz} as described in chapter 3 can contribute to the voltage measured across the film and can produce its asymmetry with respect to the field direction without the need to induce a crossed anisotropy in the sample during manufacture. To distinguish this type of asymmetry from that discussed above it is referred to as dynamical asymmetry since it does not require a special DC magnetic configuration and can be obtained in the presence of an AC bias field which would mix together the diagonal and off diagonal components of the impedance tensor. This asymmetry occurs since the off-diagonal impedance is anti-symmetric with respect to the DC magnetization; where as the diagonal impedance is symmetric. It means that the off-diagonal response itself may be used for sensor design since it may have almost a linear behaviour at some field interval. In this section the off-diagonal response of a transverse anisotropy NiFe / Au / NiFe multi-layer with planar coil is illustrated. The sample has a dimension of 5mm length, 50 μm width, and a 1.5μm total thickness. The helical micro coil has 23 turns with a 50 μm width. The manufacturing process of the sample is described in Chapter 4.

The off-diagonal impedance is measured when the film is excited by AC current and the response is taken from the coil as explained in Chapter 3 9 (Fig. 3.3). In this case it is convenient to measure the forward transmitted power or S_{21} parameter which will be the ratio of the power picked by the helical micro coil around the multi-layer film to the AC power applied to the multi-layer film by the network analyser as described in Section 5.2.

The sample was measured from 1 to 100MHz with a DC bias current of 0 to 50mA. Without the bias current the diagonal response is very small as shown in Fig. 6.8 due to averaging over the transverse domains with the opposite magnetisation. With increasing DC bias the off-diagonal impedance increases. The DC bias which induces the transverse magnetic field eliminates domain structure which is a mandatory condition to get a substantially high off-diagonal response. The absolute value of the off-diagonal impedance increases almost 10 times in the presence of 10 mA bias field as seen in Fig. 6.9. However, if the bias current is further increased of more than 25 mA, the off-diagonal response decreases (Figs. 6.10, 6.11).
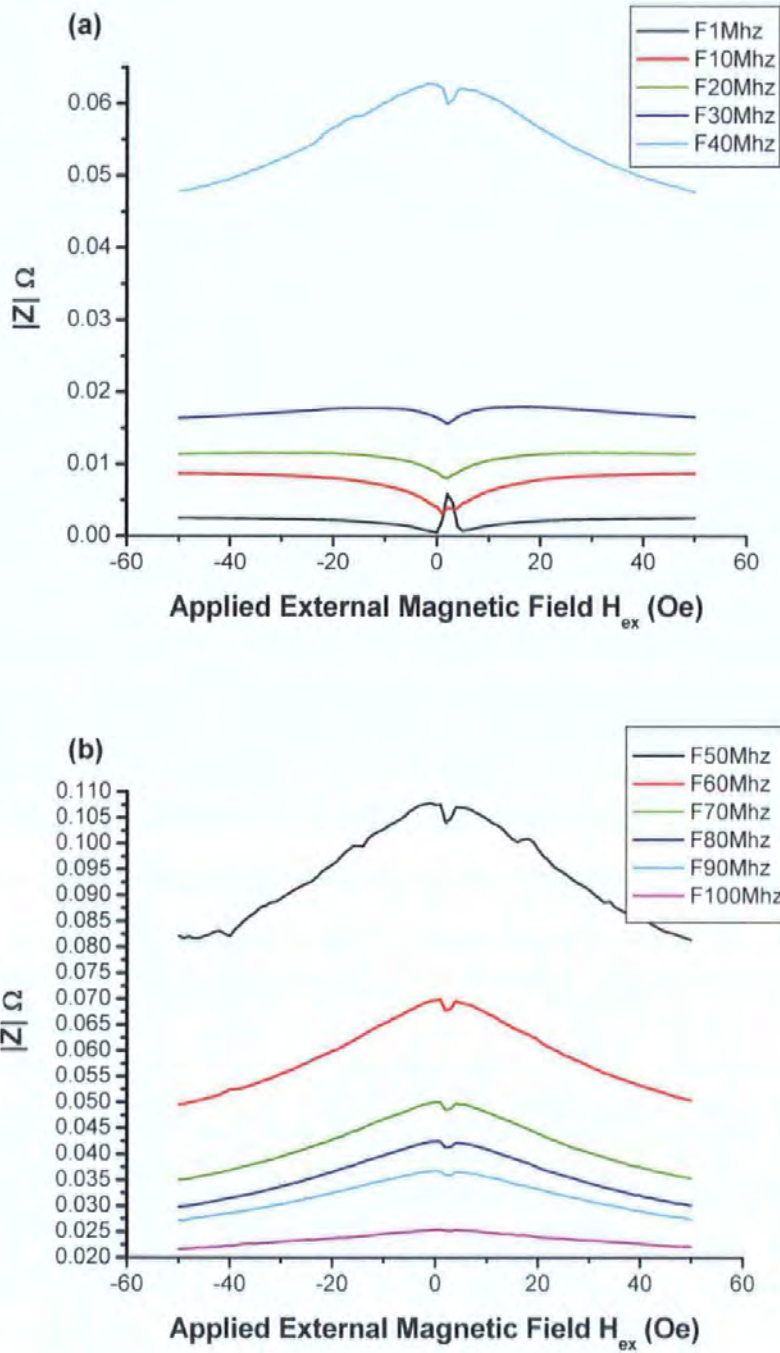
Figure 6.8   Plot of the off diagonal impedance magnitude vs. magnetic field of the NiFe / Au planar coil sample without a bias current 1 to 40MHz (a), 50 to 100MHz (b).
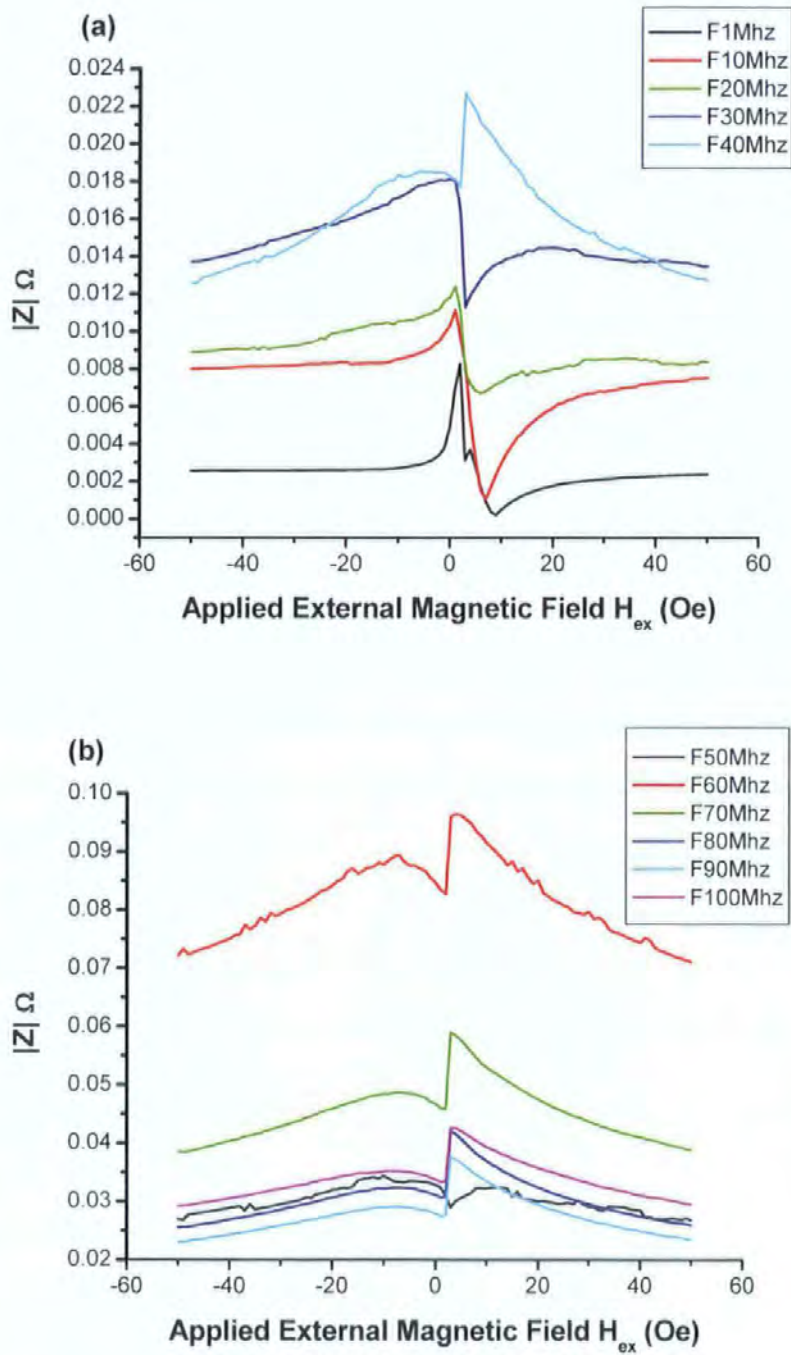
Figure 6.9   Plot of the off diagonal impedance magnitude vs. magnetic field of the NiFe / Au planar coil sample with a bias current of 10mA 1 to 40MHz (a), 50 to 100MHz (b).
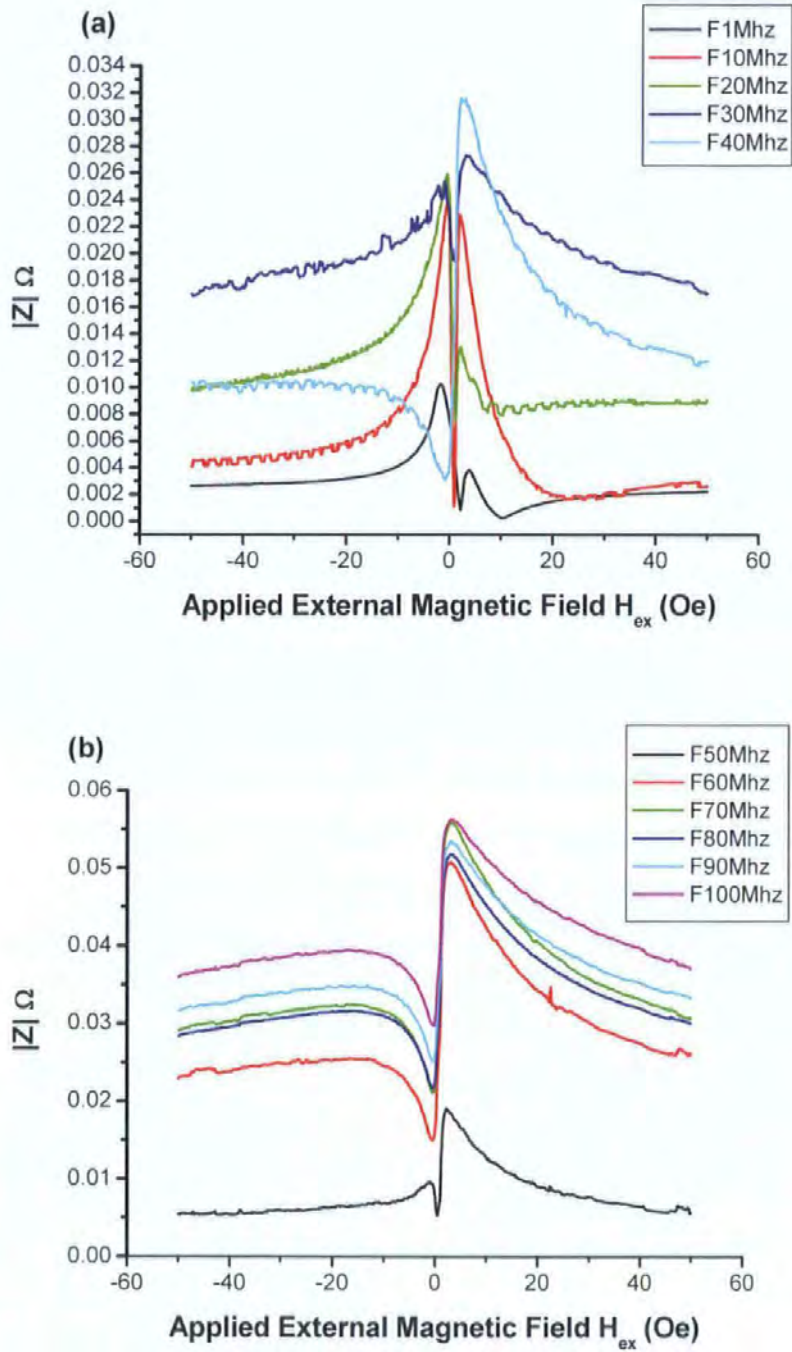
Figure 6.10   Plot of the off diagonal impedance magnitude vs. magnetic field of the NiFe / Au planar coil sample with a bias current of 25mA 1 to 40MHz (a), 50 to 100MHz (b).
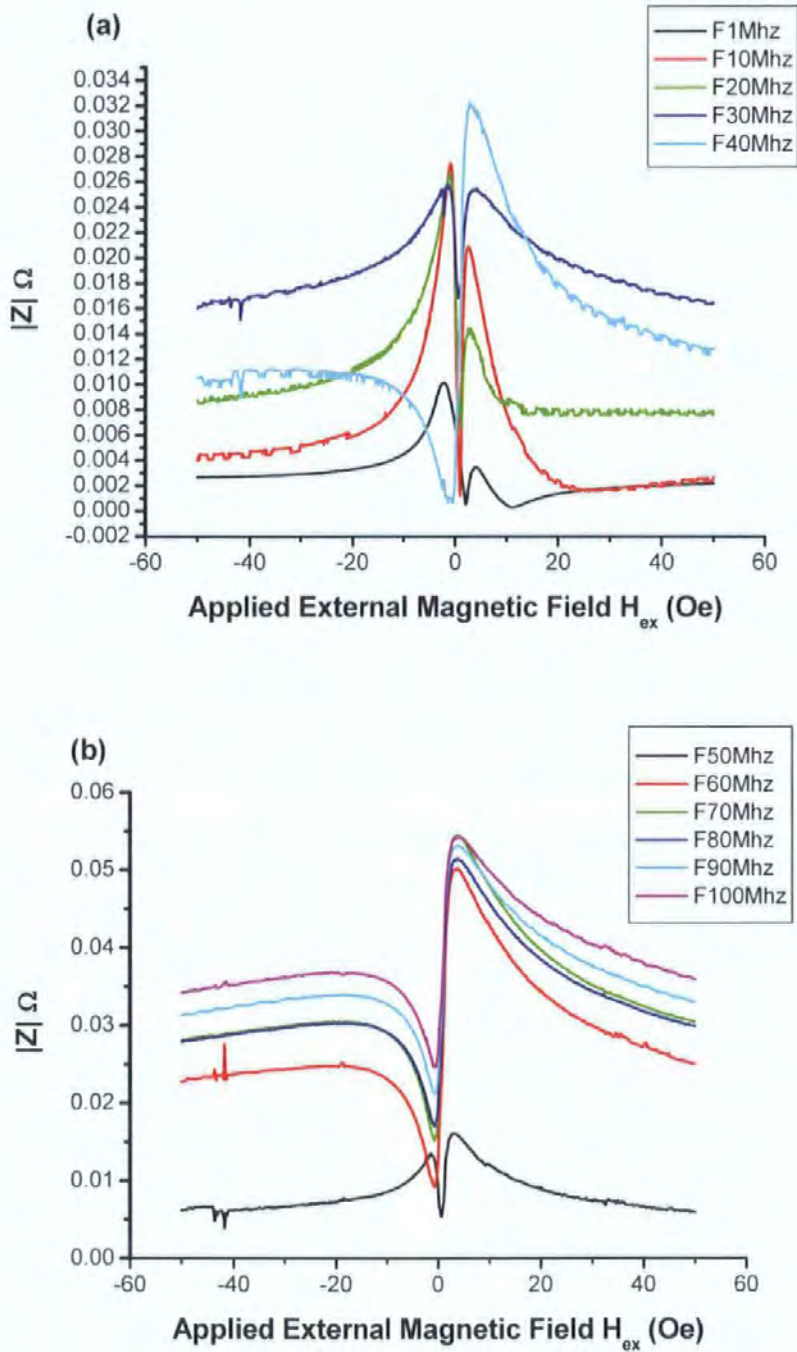
Figure 6.11   Plot of the off diagonal impedance magnitude vs. magnetic field of the NiFe / Au planar coil sample with a bias current of 40mA 1 to 40MHz (a), 50 to 100MHz (b).

This behaviour of the off-diagonal response can be illustrated considering a realistic domain structure shown in Fig. 6.12. Without a bias current, the contribution to the total off-diagonal response from the transverse domains with the opposite magnetisation is nulled, since in neighbouring domains the off-diagonal impedances have opposite signs being proportional to the transverse magnetisation. In this case only areas with closure domains may be responsible for the coil voltage.
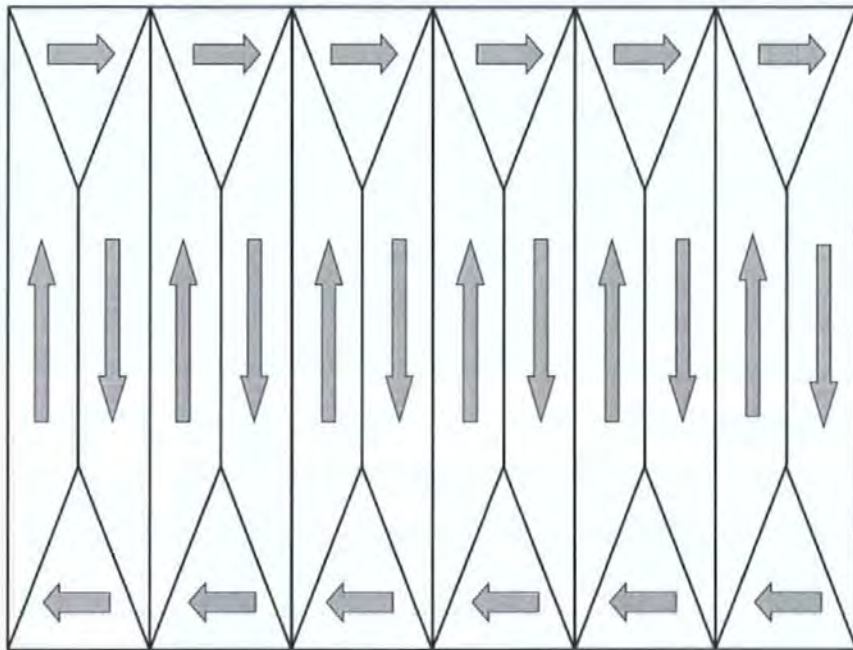
Figure 6.12   Stripe Domain structure of a film with transverse anisotropy.

The situation will change with the presence of a bias field. For $H_b \neq 0$, domains with the same direction of magnetization as H_b will grow, resulting in an uncompensated averaging. In addition, at a sufficient value of H_b the sample will become a single domain state. As a result, the effect of H_b significantly increases the off-diagonal response. However, for larger values of H_b the field sensitivity decreases due magnetostatic hardness increase.

In the case of a transverse anisotropy, the magnitude of the off-diagonal impedance has to be symmetrical with respect to the field, whereas the real and imaginary parts of this impedance (shown in Figs. 6.13 and 6.14) has to be anti-symmetrical with a linear portion in some field interval $\pm H$. There are some deviations from this behaviour which could be attributed to difficulties in this sample due to the large number of steps in the fabrication process. Very probably, the anisotropy has deviations from the transverse direction because the insulation layer acts as lamination which is known to change the domain structure. Nevertheless, the real and imaginary parts of the off-diagonal impedance demonstrate the field characteristics which could be easily adjusted to get a desired linear response in both field directions.

It should be noticed that in all the cases the magnitude of the off-diagonal impedance $|Z|$ is also very small compared to the measured values of the usual impedance. One reason for this is that the measurements are taken from a nearly pure inductive source such as the very small planar coil, the DC resistive component of which is very small, around 10 mΩ. Because of this, the results are presented as the actual impedances rather than the standard MI ratio.
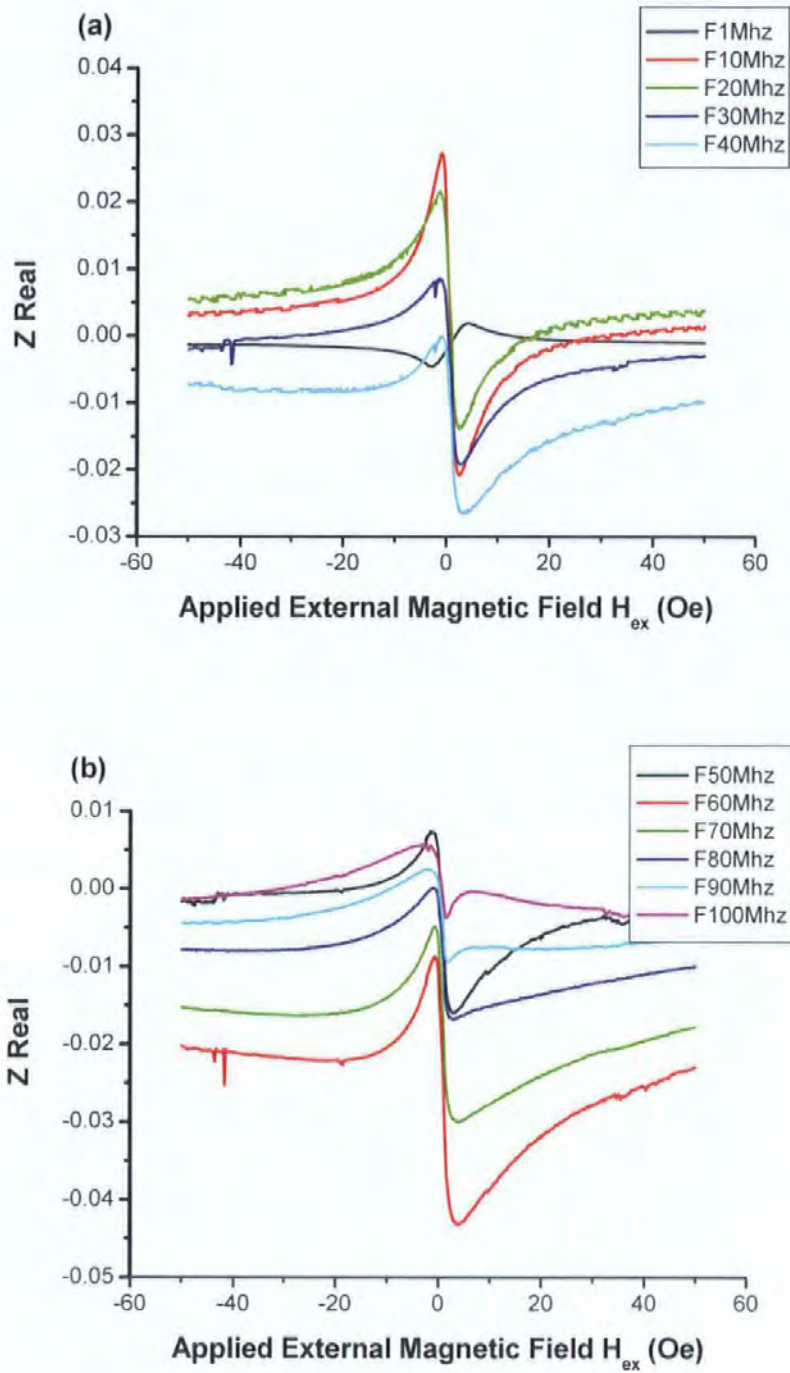
Figure 6.13   Plot of the real component of off-diagonal impedance vs.   magnetic field of the NiFe / Au transverse planar coil sample with a bias   current of 50mA 1 to 40MHz (a), 50 to 100MHz (b).
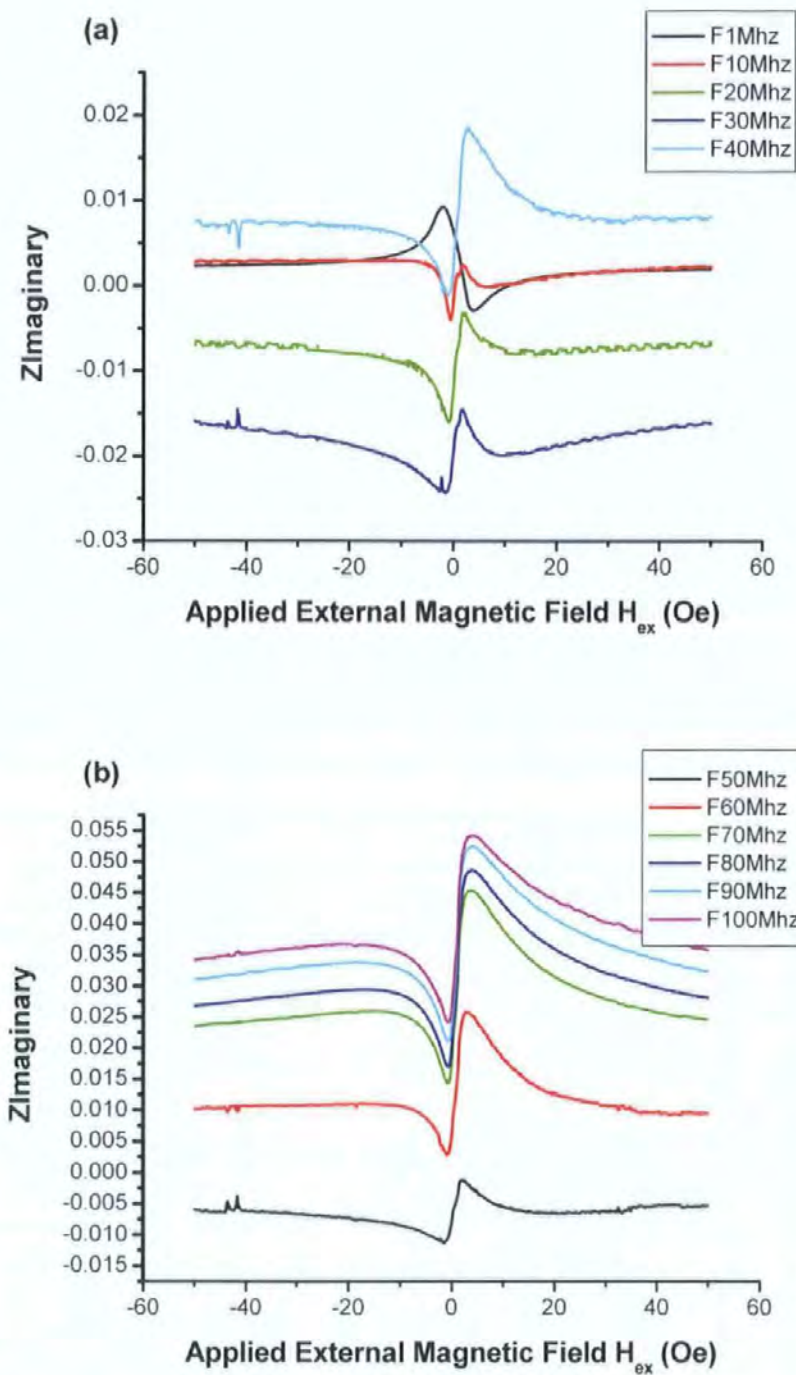
Figure 6.14   Plot of the imaginary component of off- diagonal impedance vs. magnetic field of the NiFe / Au planar coil sample with a bias current of 50mA 1 to 40MHz (a), 50 to 100MHz (b).

This work has demonstrated that film samples with a special crossed anisotropy and samples with an integrated coil are useful in tailoring the MI response with the specific purpose of obtaining linear characteristics with increased sensitivity. In the case of a crossed anisotropy samples, the linear bi-directional response can be obtained by using two identical films with an opposite DC current bias connected by differential amplifier. This process increases the directionality of field detection at the cost of reduction in magnitude of field detection. A good linear characteristic can be typically obtained in a certain range of frequencies and bias currents.

Samples with an integrated coil are able to go one further stage and produce a bi-directional response using one sample. However, in the present work such a response was obtained only for a very particular frequency of operation and applied bias current, as there was a difficulty to induce a proper transverse anisotropy during the manufacturing process, as the Al_2O_3 insulation layers could create inclusions into the NiFe. Furthermore, at microwave frequencies the matching of the very small complex impedance planar coil as a current source into a 50Ω system would be complex. In general, even thought two samples are required a crossed anisotropy multi-layer presents a better option as a magnetic field sensor transducer, as illustrated in detail in chapter 8.

References

[1]   K. Ueno, H. Hiramoto, K. Mohri, T. Uchiyama, and L.V. Panina, "*Sensitive asymmetrical MI effect in crossed anisotropy sputtered films*" IEEE Trans. Magn. 26, 3448 (2000)

[2]   L.V. Panina, K. Mohri, T. Uchiyama, K. Bushida, and M. Noda, "*Giant magneto-impedance in Co-rich amorphous wires and films*" IEEE Trans. Magn. 31, 1249 (1995)

[3]   V. A. Zhukova, A. Chizhik, J. Gonzalez, D. P. Makhnovskiy, L.V. Panina, D. J. Mapps, and A. P. Zhukov, "*Effect of annealing under torsion stress on the field dependence of the impedance tensor in amorphous wires*" J. Magn. Magn. Mater. 249, 324 (2002)

[4]   D. P. Makhnovskiy, A. S.Antonov, A. N. Lagarkov, and L. V. Panina "*Field-dependent surface impedance of a bilayer film with an antisymmetric bias magnetization*" J. Appl. Phys. Vol 84, 5698, 1998.

[5]   L. V. Panina, D. P. Makhnovskiy and K. Mohri. "*Analysis of Magneto-Impedance in Multilayers with Crossed Anisotropy*", J. Magn. Soc. Jpn. Vol 23, p925, 1999.

[6]   D. P. Makhnovskiy, A. N. Lagarkov, L. V. Panina, and K. Mohri. "*Effect of antisymmetric bias field on magneto-impedance in multilayers with crossed anisotropy*" Sens. Actuators A, vol. 81, p 106, 2000.

Chapter 7 Magnetic and Magneto Impedance sensors overview and comparison

Recent developments in the fields of computer peripherals, information apparatus, mechatronics such as: automobiles and industrial robots, power electronics, medical electronics, and industrial measurements require new high performance micro magnetic sensors to detect localized weak magnetic flux. [1,2]

This chapter will give a brief overview of several types of widely used magnetic sensors. The sensors are based on a large variety of different physical principles; the overview will highlight their particular physical characteristics and field detection magnitudes to allow comparison with a sensor based on the Magneto Impedance effect. These physical effects have been developed into sensors such as: search-coil magnetometer (inductive coil), Hall sensor, magneto-resistive (MR) and giant magneto-resistive (GMR) sensors, flux gate sensor, and super conducting quantum interference device (SQUID).

Various sensor technologies are currently needed since it is difficult to meet every industrial requirement utilising a single field sensing effect. Therefore the choice of an underlying physical principle is determined by specific conditions of magnetic field measurements such as the sensitivity and the detection range and the other properties such as physical dimensions, response speed, and power consumption of the sensor.

After the overview of the technology of the general magnetic sensor in use today, the aim is to demonstrate that a sensor based on the Magneto Impedance effect would be extremely versatile, as it combines the many attributes of other sensors and would be suitable for general field sensing ranges (10^{-3}Tesla and 10^{-6}Tesla) to near SQUID resolutions ($<10^{-9}$ Tesla but at room temperature).

A detailed historical review of the development and current sensor technology based on Magneto Impedance follows the magnetic sensor overview.

7.1   Magnetic sensor overview

The field detection range is the primary parameter of any magnetic field sensor, its range of detection must be suitable for the field being measured and the sensitivity must be high enough to ensure an accurate measurement within the range. Fig7.1 illustrates the types of magnetic sensor technology available and their detectable field ranges [1]. A sensor based on the Magneto Impedance effect is more suited for measurement of fields of a smaller magnitude or larger fields to a high sensitivity. It is not suitable for measurement of fields above 10 Oe, so the comparative review will concentrate on effects that can measure the smaller magnitude of detectable fields.

Magnetic Sensor Technology	Detectable Field Range (Oe)	
	Min	Max
Search Coil Magnetometer	10^{-8}	10^6
Flux Gate Magnetometer	10^{-7}	10^2
Optically Pumped Magnetometer	10^{-8}	1
Nuclear Procession Magnetometer	10^{-7}	10^2
SQUID Magnetometer	10^{-10}	10^{-4}
Hall Effect Sensor	1	10^6
(Giant) Magneto Resistive Magnetometer	10^{-6}	10^2
Magneto Diode	10^{-1}	10^4
Magneto Transistor	10^{-1}	10^4
Magneto Optical Sensor	1	10^6
Magneto Impedance Sensor	10^{-7}	10

Figure 7.1   Magnetic field sensor detection ranges

From Fig 7.1, it can be seen that SQUIDs, or Superconducting Quantum Interference Devices, are used to measure extremely small magnetic fields in the range of 10^{-10} to 10^{-4} Oe. They are currently the most sensitive vector magnetometers known being, with noise levels as low as $3\ fTHz^{-0.5}$. These magnetometers require cooling with liquid helium to a temperature of 4.2 K, or with liquid nitrogen to 77 K, to operate. Hence the packaging requirements to use them are rather stringent both from a thermal-mechanical as well as magnetic standpoint making them impractical for everything but the most sensitive field detection requirements [1, 2].

Some exotic sensors shown in the table, such as Optically Pumped and Nuclear Procession are quite complicated in execution due to the physical property they are based on and can be used only for the specific types of field detection, often in laboratories and medical applications. For example, optically pumped magnetometers use alkali metals from the first column of the periodic table such as cesium and potassium. To detect a field a cell containing the gaseous metal is polarized (or pumped) by exposure to light of a very specific wavelength. The light depopulates one electron energy level in the gas by pumping the electrons to a higher energy level. These electrons spontaneously decay to both energy levels, and eventually, a lower energy level is fully populated. Next, the cell is "depolarized" by shifting the electrons in the lower energy level back to their original position using lower wavelength RF power. The energy required to repopulate this energy level varies with the ambient magnetic field, according a principle called the *Zeeman* effect. Therefore, the frequency of the depolarizing RF power corresponds to the magnetic field value [1, 3].

The basic search-coil magnetometer is based on Faraday's law of induction, which states that the voltage induced in a coil of turns N is proportional to the changing magnetic field in the coil. This induced voltage creates a current that is proportional to the rate of change of field H_{ex}. The sensitivity of the search-coil is dependent on the permeability, $\tilde{\mu}$ of the core and the area S and number of turns of the coil. The voltage induced in the coil, V_c is given by:

$$V_c = -\tilde{\mu}\left(\frac{NS}{c}\right)\frac{\partial H_{ex}}{\partial t} \qquad (7.1)$$

Because search-coils work only when they are in a varying magnetic field or moving through one, they cannot detect static (DC) or slowly changing fields. They can be constructed to enable the detection of small fields at a compromise of dimensions. However they are inexpensive and easily manufactured are utilised in many industrial applications [1].

A fluxgate magnetometer is similar in construction to search coil, but adds a drive coil and magnetic core. The basic principle is to compare the drive-coil current needed to saturate the core in one direction as opposed to the opposite direction. The difference is due to the external field. Full saturation is not necessary; any nonlinearity will do. As the core approaches saturation, the signal picked up in the sense coil will show the nonlinearity. Under the application of a sine-wave to the drive coil, the sense coil would detect harmonics of the fundamental frequency; increasing in strength relative to the fundamental as the core becomes more saturated. A square wave can also be applied to the drive coil and asymmetries in the sense coil output indicate the presence of an external field. The technology of fluxgate magnetometers have been highly developed to include planar integrated circuit devices and highly sensitive fluxgates used in space missions such as CLUSTER and the Pioneer Venus Orbiter [1, 4].

The Giant Magneto Resistance Effect (GMR) is a quantum mechanical effect observed in thin film structures composed of alternating ferromagnetic and nonmagnetic metal layers. The effect causes a significant decrease in resistance from the resistance of when there is no field present to when a field is applied. In the zero field state, the magnetization of adjacent ferromagnetic layers are anti parallel due to a weak anti-ferromagnetic coupling between layers, when a field is applied the magnetization of the adjacent layers align. The spin of the electrons of the nonmagnetic metal align parallel or anti parallel with an applied magnetic field in equal numbers, and therefore suffer less magnetic scattering when the magnetizations of the ferromagnetic layers are parallel. Under the application of a DC drive current, the change of resistance can be measured and the field can be detected. Some developments of GMR include increased multilayer stacks and Spin valve. Both advancements use two or more (in the case of multilayer stacks) ferromagnetic layers are separated by a very thin non magnetic spacer. Spin-valve GMR is the configuration that is most industrially useful, as it is used in hard-drives[1, 5].

7.1.1   Sensor technology conclusions

After completing the overview of the types of sensors developed from different types of physical properties of magnetic field detection, they can be categorized by the different parameters that are associated with them as shown in Fig. 7.2. The sensors which utilize a DC current source are mainly based on quantum effects, whereas those with an AC current source are based on classical electrodynamics.

	Inductive coil	Fluxgates (parallel or orthogonal)	GMR sensor	MI sensor
Applied current: AC or DC	AC	AC	DC	AC
Principle of detection: resistance (R) or induced voltage (V)	V	V	R	R or V
Direction of Measured field with respect to the sensor surface	tangential	tangential	tangential	tangential
Direction of applied current with respect to the sensor surface	N/A	tangential (in the orthogonal-gated)	tangential	tangential
Anisotropy type with respect to the current or field drive direction	N/A	longitudinal for the parallel-gated and circumferential (transverse) for the orthogonal-gated	longitudinal in the free layer and transverse in the pinned layer	longitudinal, circumferential (transverse) or helical (crossed)
Measured field direction with respect to the anisotropy axis	N/A	longitudinal for the parallel-gated and transverse for the orthogonal-gated	transverse to the free layer anisotropy axis	longitudinal, transverse or crossed
Field drive direction with respect to the sample surface	N/A	tangential	N/A	Tangential
Field drive direction with respect to the anisotropy axis	N/A	longitudinal in the parallel-gated	N/A	longitudinal, transverse or crossed

Figure 7.2   Main parameters (left column) determining the sensing mechanisms [7].

From Fig. 7.2, it can be concluded that the MI sensors can satisfy the greatest number of parameters, which provide the ability to measure a wide variety of the field dependencies. The key parameters to a magnetic field sensor are highlighted in bold (left column). The MI sensors combine many features from others: AC excitation from the inductive coil sensor and fluxgates (but of much higher frequency, in the order of tens to hundreds of MHz), different polarizations of the AC excitation from the fluxgates, anisotropy from the MR and GMR, multi-layer structure (for multi-layer MI films) from the GMR. However, it may resemble the other sensors in terms of properties; it does not share their physical principles.

Chapter 3 has shown that the anisotropy of the sample plays a determining role in the forming of the MI field dependence, which can be further modified by the application of a DC bias field. Additionally, the applied AC excitation in the presence of a magnetic conductor give rise to the surface impedance tensor, which allows the measurement of diagonal or off-diagonal components. Therefore through a combination of anisotropy, bias field, different AC excitation and measuring methods results in various MI field dependencies. This huge range of field dependencies combined with the high sensitivity of the effect make GMI suitable for many current industrial applications.

7.2   Magneto Impedance sensor historical review

The basic requirements for a sensor based around a Magneto Impedance element is, to be able to produce the required excitation and bias signals to drive the sample, measure the change of voltage over the sample and calculate the change of magnitude (and direction) of the applied field from the corresponding voltage.

In an electronic sensor, the Magneto Impedance effect can be considered as a modulation of the amplitude of the applied excitation voltage by the variation of the impedance due to an external field. At RF frequencies this applied voltage is generally considered in the form of an applied power in decibels (dB) or milli-decibels (dBm). If the external field is constant (DC) then the voltage (power) will reduce by a constant amount. If the external field is time dependant, for example a sinusoid, then the applied power will be subjected to amplitude and phase modulation with the envelope generated by the time dependant waveform of the external magnetic field. Measurement of this change requires the recovery of the envelope from the carrier with a process called demodulation. This leaves a constant value for the DC field and the waveform of the time dependent field. From this the magnitude of the external field can be calculated from the transfer function of field vs. impedance of the sample. The specification or complexity of the MI sensor is dependant on the resolution, magnitude, range and frequency of field to be measured. Since its discovery in 1994, sensor design has developed from the need to design electronic equipment simply to observe the effect in magnetic materials, (which after further understanding of the effect has been replaced with the use of network and spectrum analysers), to sensors based on the effect for commercial applications, provided by the design of cheap low power MI sensors that can be integrated into existing electronic systems [8], or electronic systems that seek to measure a very specific application of MI. This section will take a historical approach to explain how different designs have tried produce an MI effect based magnetic field sensor. The primary investigations into MI magnetic sensors have mainly been carried out by Professor Mohri and his research group at the University of Nagoya, Japan.

His research has concentrated on the development of the MI-IC or Magneto Impedance Integrated Circuit, which is now in mass production for the use in mobile phones as a basic directional sensing and movement device.

7.2.1   MI sensor with sinusoid based oscillator

Chapter 3 has shown that a high frequency source of current is required to be applied to the multi-layer thin film in order to observe the effect. For all models, this is considered to be generated by, $i = i_0 \exp(-j\omega t)$ which is a constant amplitude and frequency, single harmonic sinusoid, in the MHz region. Generation of this perfect waveform in electronics is not possible, but various techniques have been undertaken to try to produce the highest approximation to this signal as possible. The stability of a sinusoidal oscillator is quantified by the measurement of the phase and amplitude noise of the source. This noise reduces the resolution of the sensor because it modifies the amplitude and frequency of the excitation signal. This will be interpreted by the measurement system as a change of impedance, and therefore a change of external field. In general, amplitude noise causes a more significant problem to a MI sensor, as the small variations in amplitude that are generally detected as a change in external field. In a good circuit design, amplitude noise can be removed by using automatic level control systems, or by passing the signal through a limiting amplifier, which are often built into IC based sinusoidal oscillators.

Phase noise, often quoted in dBc/Hz represents the equivalent noise power that would be received in a 1 Hz filter when the oscillator is modulated by an external system. In this case, the modulation would come from the change of impedance of the MI sample. Phase noise decreases with increased frequency of modulation, so generates the most noise for external fields in the kHz region or below. All oscillators generate harmonics of the base frequency that also must be removed before the excitation is applied to the MI sample, this can be achieved by conventional low pass filtering. The first observational electronic circuits, [9] simply used a basic FET resonance oscillator to produce the excitation and some balanced bridge configuration to measure the resulting change in voltage of the sample. The MI sample itself is included as a frequency-setting element in the oscillator. This approach leads to very high instability. The circuit is useful only as a basic effect observation system, which allowed the development of the theoretical aspects of the effect. In the same year, the first measurements of a differential sensor utilising the crossed magnetisation process to produce asymmetrical MI where undertaken. The effect was described as the double MI effect, and was used to produce a basic bi-direction linear response [10].

A small improvement on the circuit was presented in [11] when an oscillator based on Colpitts topography or configuration constructed from discrete components was used to provide the excitation, however the design still integrated the MI sample as a frequency setting component (L1 in Fig. 7.3), which is related to its inductance. As this inductive component would vary with the applied external field, the excitation frequency being applied to sample would also alter, this illustrates that the circuit shown in Fig. 7.3 is inherently unstable.
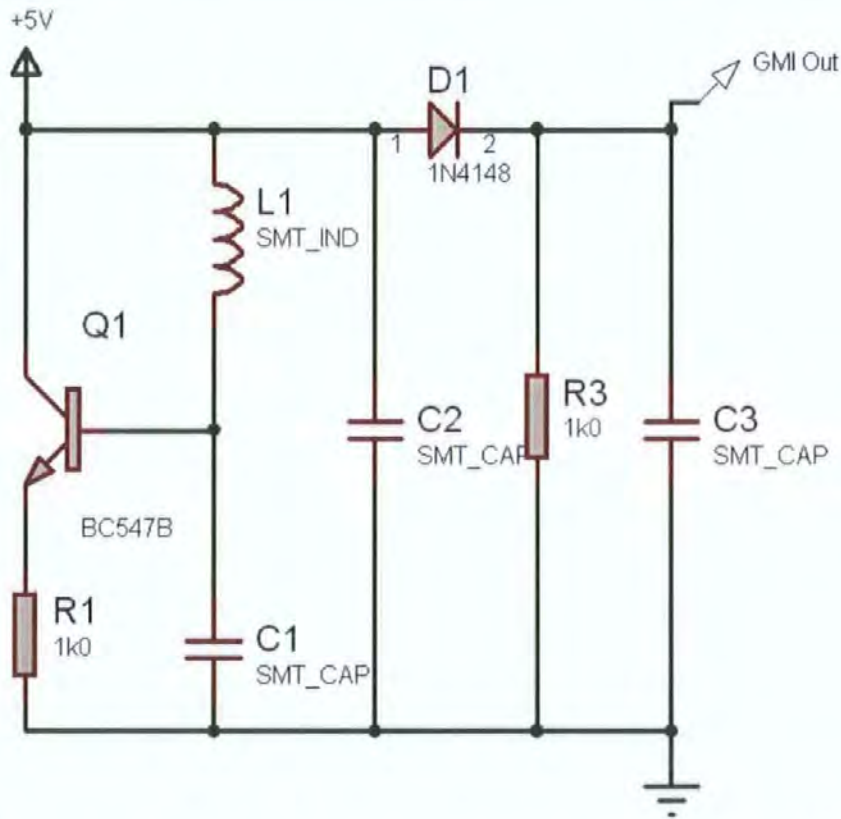
Figure 7.3   Schematic of Colpitts oscillator for producing sinusoidal excitation.

The equation for the frequency of resonance of the circuit above is given here as:

$$F_0 \cong \frac{1}{2\pi\sqrt{LC_1C_2/(C_1+C_2)}} \qquad (7.2)$$

The reason to initially include the MI sample in the circuit is to reduce the problems associated with radio frequency constraints on the rest of the circuit including connecting leads and PCB tracking.

An improvement was made to the circuit to maintain stability by adding a negative feedback path from the output of the oscillator to the sample by means of magnetic bias through a coil [12]. This feedback voltage applies a longitudinal external field to the sample providing an offset value; this means the bias field will always try to match the output of the system. This technique can provide very stable DC field detection, but the frequency response of the system is reduced, as the bias field will be slow to react and settle to the new value. This compromises the AC response in favour of a stable DC response.

Claims of field detection of a sinusoid with a magnitude $\approx 10^{-6}$ Oe at 1kHz within a shielded box, with 32,000x averaging in a dual coil differential system was reported in [13]. However, the measured waveform was distorted and did not produce an accurate signal, but was an important result for basic MI sensors.

7.2.2   MI sensor with CMOS pulse based oscillator

In 1997, the research group of Prof. Mohri began to experiment with a new form of excitation, in preference to a sinusoidal oscillator used in previous experiments. After discussing the sensitivity of the MI sensor within industry the Nagoya research group began to concentrate on developing a small, low cost, low power consumption sensor that would be able to be integrated easily into existing technologies. An oscillator based on the Colpitts oscillator, is quite large in topology and requires a reasonable amount of current to operate making it difficult to integrate into small scale integrated circuits (IC). Realising that the key to MI was the application of a high frequency current to the sample, the Nagoya group began to experiment with the application of pulses of current to the sample [14]. A pulse train consists of two components, a Root Mean Squared (RMS) value based on the amplitude of the signal and frequency of pulses, and a rise and fall time of the actual pulse, which can be made to be extremely fast in the order of 10ns. It is this second component that generates the high frequency change of current which produces the MI effect in the sample. The rise time provides an increasing field, and the fall time provides a decreasing field. The field produced in this manner is similar to a half duty cycle of a sinusoid field. It can be described more accurately from [15].

The driving function $I(t)$ is approximated by the Gaussian function, $I_0 \exp(-t^2/t_0^2)$,

With $t_0 = \int I(t)dt / I_0 \sqrt{\pi}$.

Then $V(t)$ has the form, in a single layer film, thickness t:

$$V(t) = \frac{I_0 t_0}{2\sqrt{\pi}} \int_{-\infty}^{\infty} Z(\omega) \exp[-j\omega t - (\omega^2 t_0^2/4)]d\omega \tag{7.3}$$

$$Z = R_{dc} \cdot jkt \coth(jkt) \tag{7.4}$$

$$k = \frac{(1+j)}{\delta_m} \qquad \delta_m = \frac{c}{\sqrt{2\pi\omega\sigma\mu_{ef}}} \tag{7.5}$$

The integral in Eq. (7.3) quickly converges at $|\omega| > 1/t_0$. If $\omega_0 = 1/t_0$ corresponds to a strong skin effect $(t/\delta_m(\omega_0) >> 1)$, the considerable contribution to the voltage response arises from the integration over the frequencies of the order of ω_0, where the impedance increases as $Z\alpha\sqrt{\omega\mu_{ef}}$.

This means that for a short current pulse, $t_0 << 2\pi(t/c)^2 \sigma\mu_{ef}$, the voltage response depends essentially on the magnetic properties.

A CMOS – IC based sensor for a single MI sample primarily consists of a chip containing six inverters. A sharp pulse of current with –3dB point of 10nS width is obtained in the power line of the multi-vibrator using just two of the six gates of the CMOS chip and a resistor and capacitor. The pulse is applied to the sample and is measured through a diode and low pass filter to produce a quasi-DC demodulated signal. The same strong negative feedback is applied using a feedback coil as with the previous Colpitts oscillator approach. The power consumption of the circuit is proportional to the oscillation frequency, f_{osc}, which is the rate at which the pulse occurs. The small power consumption of 0.5W can be obtained

for f_{osc} of 250Hz due to extremely low duty cycle of the signal train. This low power consumption was one of the main goals of the development of the technology. Field detection resolutions of $10^{-6} Oe$ equal the results produced by the previous oscillator technology [14] so the circuit maintains the sensitivity of MI.

The CMOS technology has continued to be developed by the Nagoya group, leading to the introduction of the synchronous rectification circuit [15] to replace diode rectification, as shown in Fig. 7.4.

Diode rectification is essentially a non-linear operation due to the voltage transfer function variation of the diode, with temperature and applied current so it could introduce instabilities in the circuit. The diode switch on voltage also poses problems for passing small signals, such as those measured from the coil. Essentially the pulse waveform is an entirely positive signal, except for digital ringing or noise, which produces some small negative voltage in the order of mV. The sinusoidal signal excitation required half wave rectification to remove the mirror envelope on the 2nd cycle of the sinusoidal current. This is not required for pulse excitation, so the synchronous rectifier simply "chops" the coil waveform to include only the signal due to magnetic response, removing ringing and other distortions. As the signal is passed into an integrator to produce a quasi-DC value, the area under the voltage waveform is important, so any extra signals must be minimised. The process is controlled by utilising a pulse generated from the same process producing the excitation signal, so the signals are synchronous. The width of the control pulse is set by the using a variable resistor. The same field resolution is claimed as the previous sensor, $10^{-6} Oe$ but the temperature stability is increased to 0.6% of the full-scale value for an operating temperature of room temperature to $80°C$.
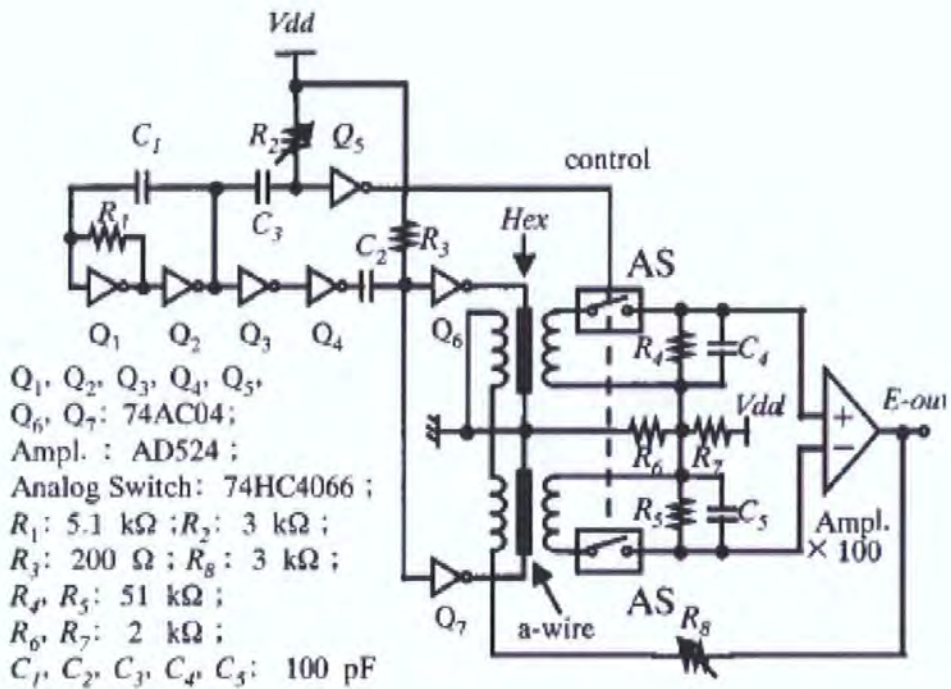
Figure 7.4   Schematic of a differential CMOS-IC with synchronous rectification.

The latest development from the Nagoya group in partnership with Aichi Steel is the development of the MI-IC. This is the same CMOS-IC circuit shown in Fig 7.4, but it has successfully been miniaturised and integrated into an IC package. According to the data sheet published in 2002 [16], the device operates from a single MI wire sample with planar coils to bias and measure the external field. The device will be available in both single axis (x) and dual axis (x,y) configurations specifically developed for earths field detection as a compass. The synchronous rectification has been replaced with a sample and hold device for better peak detection. The linear output from the IC is designed to be sampled by an ADC to allow simply integration into other electronic systems. The specifications are as follows:

Field detection range of $\pm 0.2mT$ ($\pm 2Oe$), with a resolution of $4mV/\mu T$, frequency detection of AC fields up to 1 kHz and a maximum power consumption of 100mW.

This chip represents a large advance for the field of MI sensors for simple commercial industrial operations, and may replace GMR or fluxgates in some areas. A huge and comprehensive list of potential application areas has been published by the Nagoya research

group in [6], the development of MI-IC may allow these applications to be realised. Most importantly, this chip has already been integrated into mobile phones in the Asian market to provide a basic compass facilities and interactive controls based on movement.

However, the limiting factor of the noise generated by CMOS–IC pulse excitation means that it will never be suitable for extremely small magnitude, in the order of nano Telsa measurements, which GMI has the potential to realise.

References

[1]   J. E. Lenz, "*A review of magnetic sensors*" Proc. IEEE Trans. Magn. **78**, 973 (1990).

[2]   R. Leiner, D. Koelle, F. Ludwig, J. Clarke, "*Superconducting quantum interference devices: State of the art and applications*" Proc. IEEE, **92** (2004), 1534 – 1548.

[3]   "*Short Review of Optically Pumped Scalar Magnetometers*" GEM Systems, Inc.

[4]   Gao Zu-Cheng, R.D. Russell, "*Fluxgate Sensor Theory: Sensitivity and Phase Plane Analysis*", IEEE Trans GE-25 (1987) 862 – 870.

[5]   J. Daughton, J. Brown, E. Chen, R. Beech, A. Pohm, W. Kude, "*Magnetic field sensors using GMR multilayer*" Proc. IEEE Trans. Magn **30**, Issue 6, Part 1-2, (1994), 4608 – 4610.

[6]   K.Mohri, *Fellow*, T. Uchiyama, L. P. Shen, C. M. Cai, L. V. Panina, Y. Honkura and M. Yamamoto "*Amorphous Wire and CMOS IC-Based Sensitive Micromagnetic Sensors Utilizing Magnetoimpedance (MI) and Stress-Impedance (SI) Effects*", IEEE Trans. Magn. **38**, 3063 (2002).

[7]   D. Makhnovskiy, "*Diagonal and Off-Diagonal Magneto Impedance In Ferromagnetic Microwires and Thin Films*", PhD Thesis, The University of Plymouth,(2003).

[8]   Y. Kohtani, M. Yamamoto, H. Honkura, and K. Mohri, "*Development of MI sensors using amorphous wire for automobiles*" presented at the Annu. Conf. Magn. Soc. Jpn., 2001, paper 26pD-4.M.

[9]   Y. Yoshida, T. Uchiyama, K. Mohri and S. Ogha, "*Quick Response Field Sensor Using 200MHz Amorphous MI element FET Multivibrator Resonance Oscillator*", *IEEE Trans Magn* **29** (1993), 3177-3179.

[10]   K. Kawashima, T. Kohzawa, H. Yoshida and K. Mohri, "*Magneto-Inductive effect in torsion-annealed amorphous wires and MI sensors*", *IEEE Trans Magn* **29** (1993), 3168-3171.

[11]   K. Mohri, L. V. Panina, T. Uchiyama, K. Bushida, and M. Noda, "*Sensitive and Quick response Micro magnetic sensor utilising magneto impedance in Co rich amorphous wires*", IEEE Trans. Magn. **31**, 1266 (1995).

[12]   K. Bushida, K. Mohri, and T. Uchiyama, "*Sensitive and Quick response Micro magnetic sensor using magneto amorphous wire element Colpitts Oscillator*", IEEE Trans. Magn. **31**, 3134 (1995).

[13]   K. Bushida, K. Mohri, T. Kanno, D. Katoh, and A. Kobayashi, "*Amorphous Wire MI sensor for gradient field detection*", IEEE Trans. Magn. **32**, 4944 (1996).

[14]   T. Kanno, K. Mohri, T. Yagi, T. Uchiyama and L. P. Shen, "*Amorphous Wire MI sensor using CMOS-IC Mulivibrator*", IEEE Trans. Magn. **33**, 3358 (1997).

[15]   M. Noda, L. V. Panina, and K. Mohri, "*Pulse Response Bistable Magneto-Impedance Effect in Amorphous Wires*", IEEE Trans. Magn. **31**, 3167 (1995).

[16]   MI-IC-2DL-LGA   datasheet,   Aichi   steel   corporation,   (2002)

Chapter 8. Magneto Impedance sensor design and technology

It has been shown that the MI effect has the potential to be a very sensitive magnetic transducer in an electronic sensor device. However, transferring theoretical measurements into a practical commercial sensing device that can produce a superior performance to current sensors in a number of critical areas is a challenge.

The development of the MI-IC sensor [1] by the Aichi steel and Prof. K. Mohri's research group, has commercialised one aspect of magnetic field sensing. A miniature low power IC can be incorporated into many electronic devices to provide basic magnetic field sensing for direction of the earths magnetic field and low frequency AC fields. However the technology is limited by the pulsed excitation method of producing the high frequency driving current, and the basic means of demodulating pulsed current to obtain the modulating magnetic field.

The pulse contains a very large number of harmonics spread throughout the spectrum, not just multiples of the carrier. This generates unwanted harmonic noise in the modulating spectrum of the pulse which masks the wanted modulating signal of the external field. This noise ultimately reduces the resolution and magnitude of small field detection of the pulse excitation method. Additionally, the frequency of the pulse train develops an RMS or constant DC value of voltage to the MI sample. This produces a transverse DC bias field in the sample, which depending on the anisotropy can cause the MI effect to be weakened. If a DC bias field is required, the variation of the pulse train frequency is limited resulting in a lack of control in the applied DC bias field.

The negative feedback method of biasing the sample with the output of the sensor allows the system to become stabilised at the expense of frequency response to the external field as it is limited by the bandwidth of the amplifier. Additionally, driving an inductive load to ground has complicated frequency dependant variables which are not designed into the system, as it relies on a simple resistor to control the value of applied current and hence field.

The demodulation technique is based on simple diode or switching to remove the negative noise pulses on the modulated pulse signal, after that a simple resistor and capacitor network is used to hold the peak value of the pulse so it can be measured by the output amplifier. This method is limited due a number of factors including the forward voltage loss on the diode, the voltage loss over the internal resistance of the switch and the bandwidth of the switch itself, it needs to be able to pass the high frequency pulse characteristics through it to preserve the modulating envelope. This further limits the frequency response of the system. The capacitor and resistor network has a time constant, and a frequency of applied signal higher or lower than this will not fully charge the network, and hence the peak value is not maintained, the so called voltage droop of the network describes the loss of current while before the next current pulse charges it again. Therefore the system can only be accurate at one frequency range of operation.

The aim of this course of work was to investigate means of producing magnetic field detection methods to identify the ultimate resolution and magnitude of field detection utilising the MI effect. This chapter illustrates the methods and technology required to achieve a sub-nano Tesla resolution and magnitude (10^{-6} Oe) of external AC field, from 10Hz to over 100MHz and DC field detection. After identifying the limitations of pulsed excitation, the work was carried out with the use of sinusoidal excitation and Radio Frequency (RF) design criteria.

The use of sinusoidal excitation of this type was proposed simultaneously in early works of Ref [10-11]. The experimental configuration utilizes a low phase noise oscillator working in the range of 370MHz and a phase shifted differential combination method to provide carrier suppression to allow the measurement of the modulating external field signal. The method in this current work measures the reflected power produced by the modulating external field signal on the carrier as a means of carrier suppression.

8.1   Practical design considerations

In a perfect electrical system the oscillator would be a pure sinusoidal tone with no variations in frequency, amplitude or phase or harmonics. When this sinusoid is applied to a MI element any variations in the sinusoid would be due to modulation of the external field. In practice this is not possible and the unwanted variations are added to the system as noise which limits the magnitude and resolution of field detection.

A practical oscillator suffers from both, higher harmonics and also stochastic fluctuations in amplitude and frequency, which are called noise. Since the noise spectrum of an oscillator around the oscillation frequency always has sidebands, as shown in Fig 8.1, it is possible to describe the signal with noise by the following expression:

$$V(t) = [A_0 + a(t)]\cos[\omega_c t + \phi(t)] \tag{8.1}$$

Where $a(t)$ and $\phi(t)$ are random signals. $a(t)$, describes the AM noise, $\phi(t)$ is called phase noise and $d\phi/dt$ FM noise. The use of the term phase noise is only meaningful when the maximum phase deviation does not exceed 2π rad. In the vector diagram, Fig. 8.1(b), the noise-free carrier is represented by a vector of constant length which rotates with a constant velocity and the noise by an extra vector with varying amplitude and phase with respect to the original signal. The component of the latter which lies in the direction of the carrier vector describes the AM noise and the orthogonal component the FM noise.

Usually it is assumed that the total noise power is small compared with the power at the central frequency f_c. A common measure for the noise at a certain frequency f_m in the sideband is then the power in the bandwidth $\delta f = f_c - f_m$, divided by the bandwidth δf taken in dB units relative to the carrier wave power (referred to as dBc), or

$$\text{Oscillator noise ratio} = \frac{P(f_m)}{P(f_c)\delta f}[dBc/Hz] \tag{8.2}$$
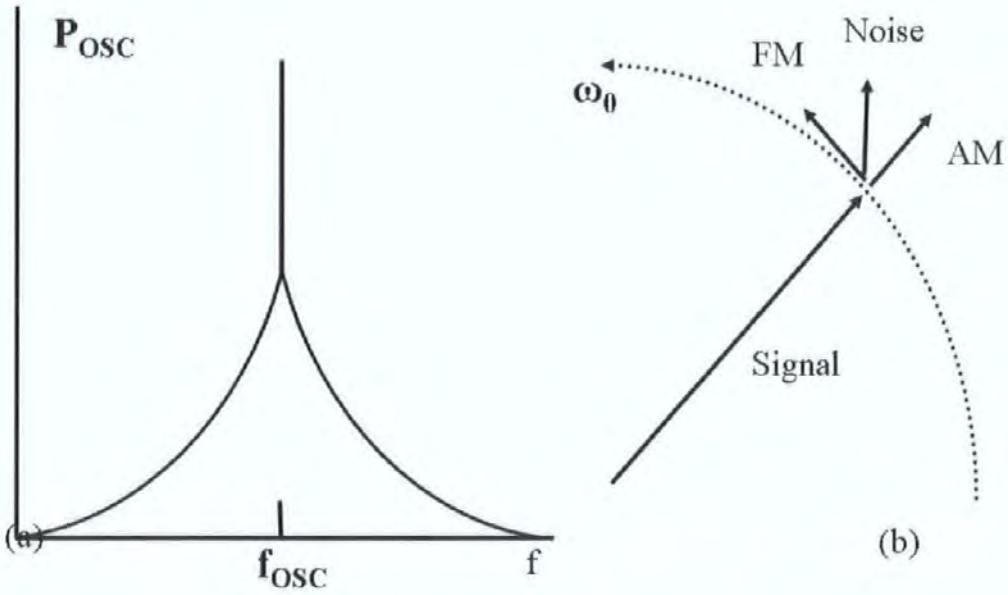
Figure 8.1   Oscillator noise: (a) spectrum; (b) vector diagram.

This is specified for AM and FM separately. Usually the noise is measured in one sideband so it should correctly be called the single-sideband oscillator noise ratio. For FM noise another measure is commonly used, the root mean square frequency deviation Δf_{RMS}, that is the root of the average quadratic frequency deviation in a specified bandwidth divided by that bandwidth. A similar definition holds for $\Delta\phi_{RMS}$. Here too the distance from the carrier frequency must be specified. The relation with the FM noise power where P_{FM} is the power of the FM deviation and P_c is the carrier power is,

$$(\Delta\phi_{RMS})^2 = \left(\frac{\Delta f_{RMS}}{f_m}\right)^2 = 2\frac{P_{FM}}{P_c} \tag{8.3}$$

The sources of noise in practical oscillators originate from: noise in the active element; noise in the bias current to the active element; and noise in the lossy parts of the passive circuit, which are thermal noise based. [2] – [7]

Not only the noise around the oscillation frequency but also low frequency noise sources are important. The low frequency noise sources owing to the non-linear properties of the active element, are up converted to the sidebands of the oscillator. The up conversion is related to the modulation sensitivity, that is the extent to which the oscillation frequency depends on the bias current. Any oscillator which is modulated via the bias current is also sensitive to the noise in the bias current. The $1/f$ noise in the bias current and the active element are therefore important quantities to understanding the amount of noise in the oscillator as a whole. For the purpose of improving the sensitivity of a MI based magnetic field sensor the reduction of $1/f$ and thermal noise of the bias current of the oscillator is critical to performance.

When the AC carrier signal is modulated by the external magnetic field in the MI element, means of recovering that modulation information are required in the sensing device in order to determine the quantities of the external field. The noise of this recovery element will represent the minimum present in any detection circuit.

The limits of operation in a perfect sinusoidal source and detection system would be thermal noise, which is a number of magnitudes higher than any intrinsic magnetic noise produced by the MI element itself. Further more, the up conversion of low frequency $1/f$ and thermal noise within the oscillator produces many magnitudes higher noise than then minimum thermal noise of the perfect system. Therefore in order to produce the highest sensitivity of MI sensor it is critical to reduce the phase noise of the oscillator to a minimum and reduce the limits of the system to thermal noise, which can be achieved by careful component selection, low noise circuit design and good engineering practice.

8.2   Practical implementation of a sinusoidal source and detection

In this section the methods of producing a low noise sinusoidal source for a portable device will be discussed. In this case a portable device is defined as requiring a small size, low power, low cost sinusoidal source. The oscillator will then be used as the current source for application to a Magneto Impedance element in order to generate the skin effect within the sample. Simple commercial devices were improved in performance by the application of novel electronic techniques to reduce the effect of noise at source. The circuits were manufactured, tested and phase noise measured using a Rhode and Schwarz FSU 60GHz spectrum analyser (1 Hz measurement bandwidth, -158dBm noise floor) with embedded phase noise software.

8.2.1   Oscillation circuits

Two different oscillation technologies were evaluated, an advanced Colpitt's oscillator Integrated Circuit (IC) the Maxim 2605 and a surface acoustic wave (SAW) based IC that was embedded into a simple transmitter device designed for short range RF communications, the Radiometrix 433MHz TX2 .

MAX2605 to 2609 are compact, high-performance intermediate-frequency (IF) voltage-controlled oscillators (VCOs) designed specifically for demanding portable wireless communication systems. They combine monolithic construction with low-noise, low-power operation in a tiny 6-pin SOT23 package. Each device covers a range of carrier frequency generation.

These low-noise VCOs feature an on-chip varactor and feedback capacitors that eliminate the need for external tuning elements, making the MAX2605-MAX2609 ideal for portable systems. Only an external inductor is required to set the oscillation frequency. In addition, an integrated differential output buffer is provided for driving a mixer or prescaler.

The buffer output is capable of supplying up to -8dBm (differential) with a simple power match. It also provides isolation from load impedance variations.

Three different implementations of this circuit were manufactured and tested. Firstly the differential output were combined to produce a single output signal which was buffered for two MI elements from a single source. Secondly the differential signals were no combined an just buffered separately to produce a dual output capable of driving two MI elements from a single source. Thirdly passive low pass filters were applied to reduce the harmonic composition of the output sinusoidal excitation before it was combined differentially for a single output.

Commonly, the circuits were voltage regulated to 3.3V DC by an Analog TPS79133 voltage regulator. A Maxim 6001 voltage reference was applied to the frequency voltage control pin of the Maxim 2605 to keep the sinusoidal frequency constant. An inductor was selected to produce an output frequency of between 40 and 85MHz, which covered the range of highest MI ratio of the MI elements to be used with this current source. The signals are combined or buffered using Maxim 2470 high speed operation amplifiers.

The outputs are matched to 50Ω impedance using the appropriate matching network component values specified in the VCO datasheet for the output frequency. The buffers are matched to 50 Ω using a resistor; a blocking capacitor is used to remove the DC component, which could cause an unwanted transverse field to be generated in the sample. The sinusoidal sources were connected to external devices by using SMA connectors. Figs. 8.2 to 8.4 illustrate the schematic of the circuits.
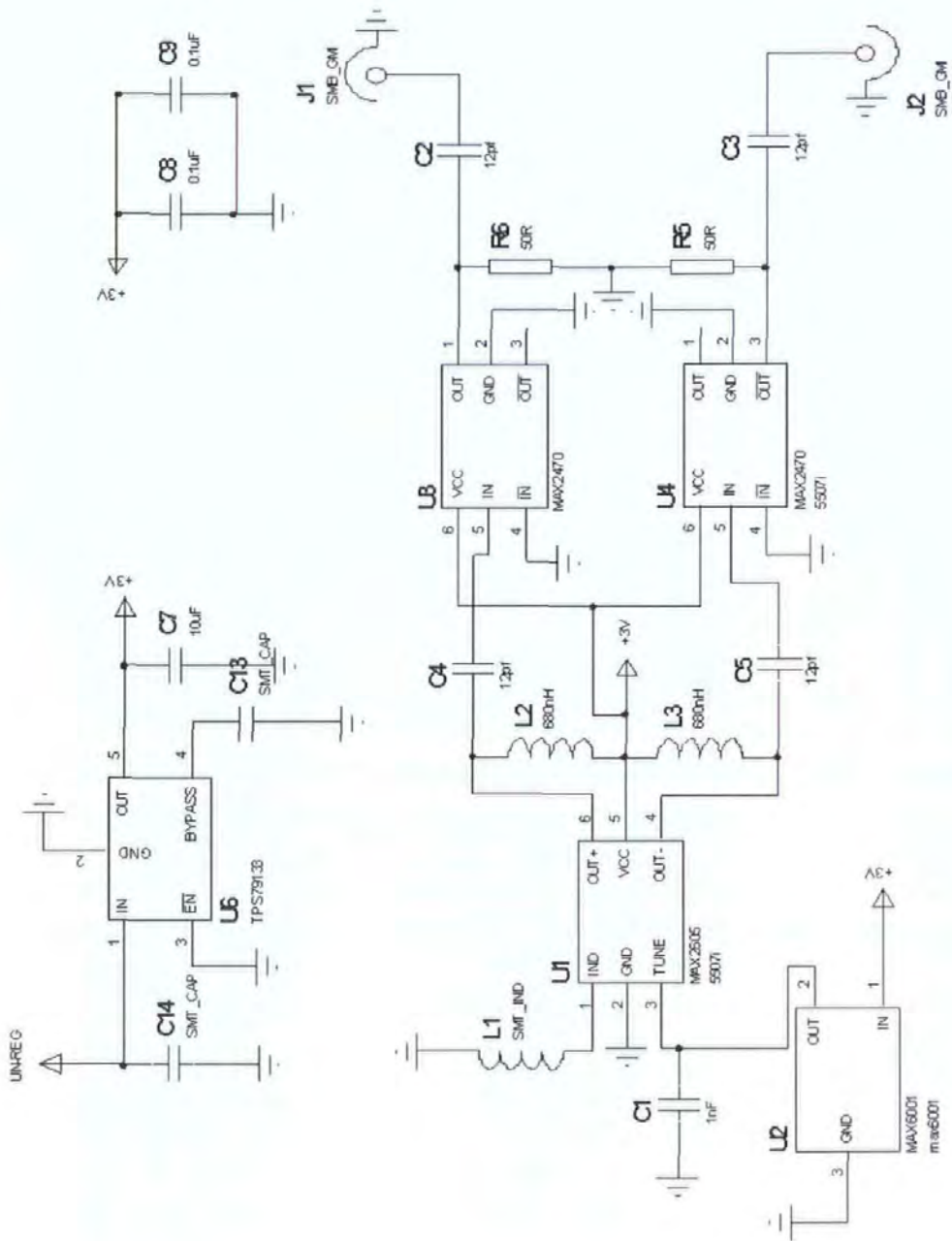
Figure 8.2   Maxim 2605 non-differential outputs.
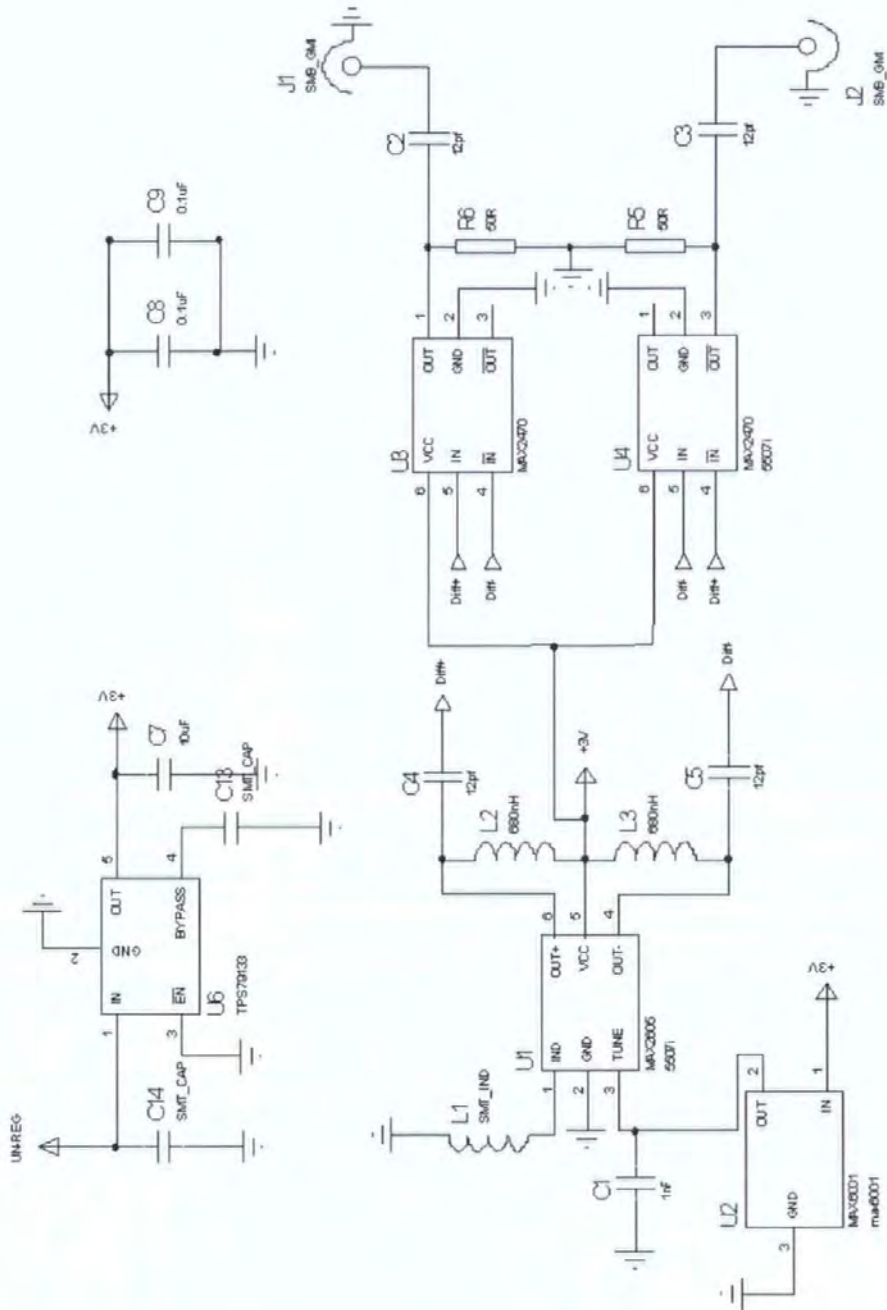
Figure 8.3   Maxim 2605 differential outputs.
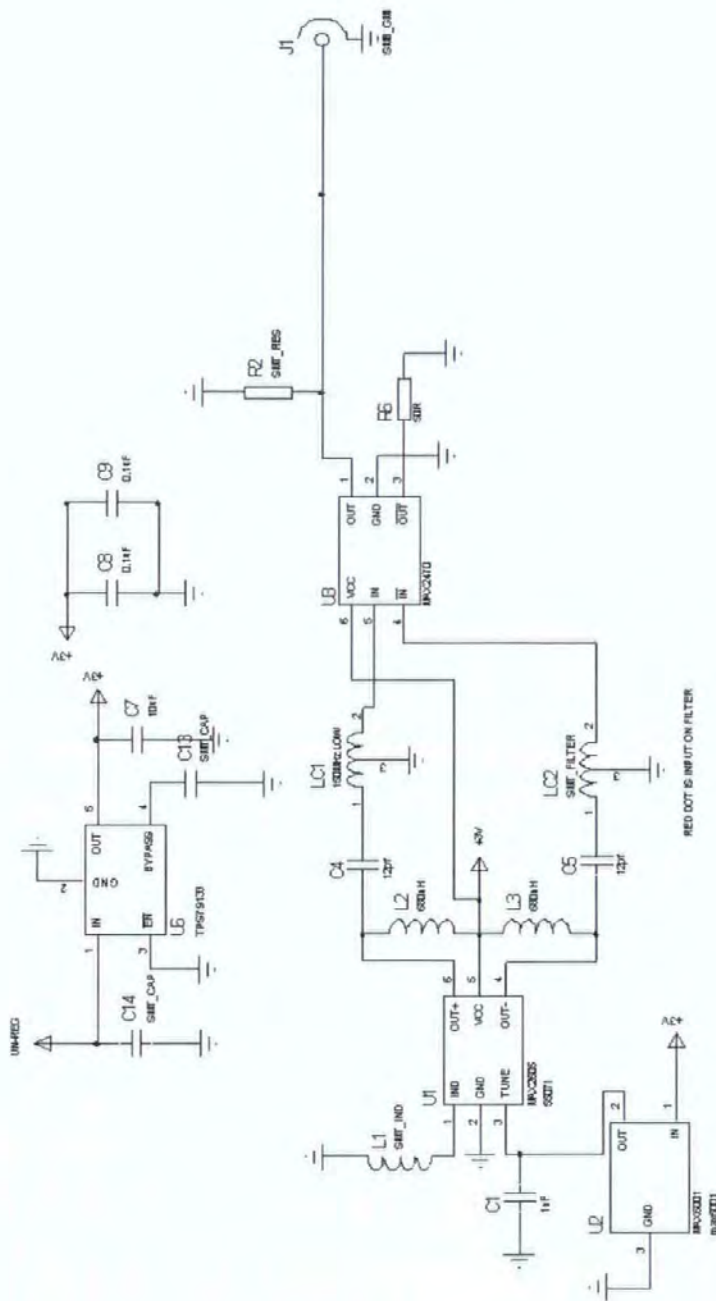
Figure 8.4   Maxim 2605 differential output with low pass filters.

The PCBs were designed to reduce the RF effects of stray capacitance and inductance at this relatively low frequency of 45 to 100MHz. Track widths and component placement were carefully considered as well as the use of a large low inductance ground plane. Fig. 8.5 illustrates the PCB layout at increased size for detail.
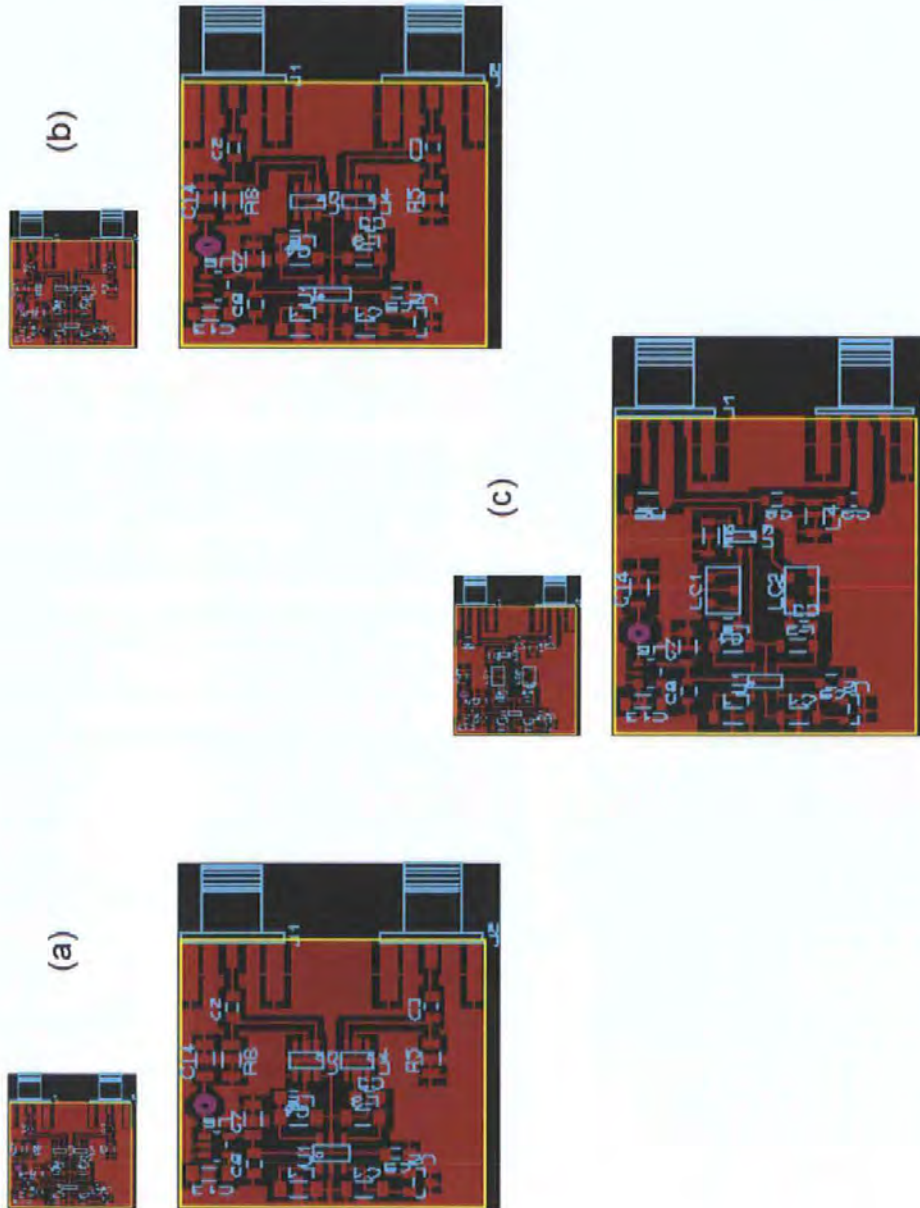
Figure 8.5   PCB implementation of (a) non differential output, (b) differential output an (c) non differential output with low pass filters.

The Radiometrix TX2 transmitter module is a two stage, SAW controlled FM transmitter operating between 2 and 6 V and is available in 433.92MHz and 418.00 MHz versions. The 433.92 MHz can deliver +9 dBm from a 5V supply at 12mA, the module physically measures 12 x 32 x 3.8 mm. Its functional schematic is shown in Fig. 8.6
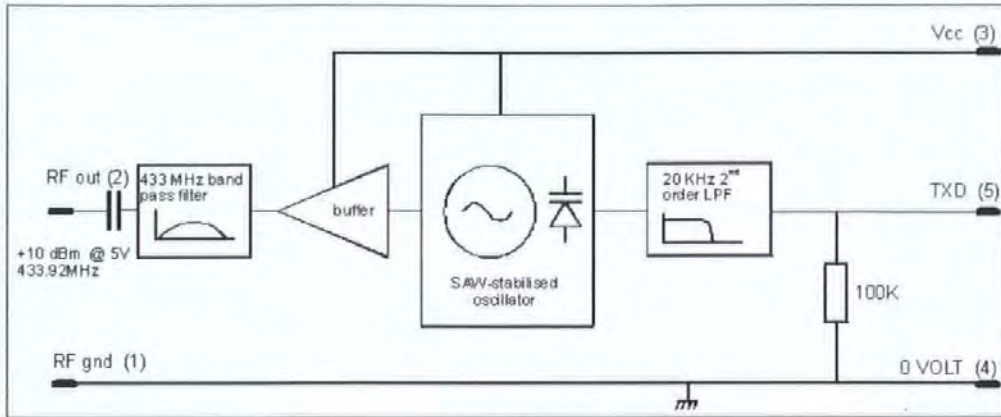
Figure 8.6   Function block diagram of the transmitter module.

This makes the Radiometrix device ideal for portable applications, and to drive an MI element at a higher excitation current frequency. As the oscillator is a plug-in module it required very little additional components in order to complete the oscillator circuit. Analog devices TPS79101 was used to provide a regulated 5V supply to the Radiometrix module, the device is designed to receive digital data to frequency modulate onto the carrier. As this was not required the digital circuit was connected to 5V to maintain constant carrier amplitude. The circuit was connected to other devices by means of a SMA connector as before. The circuit and PCB layout is shown in Fig. 8.7.
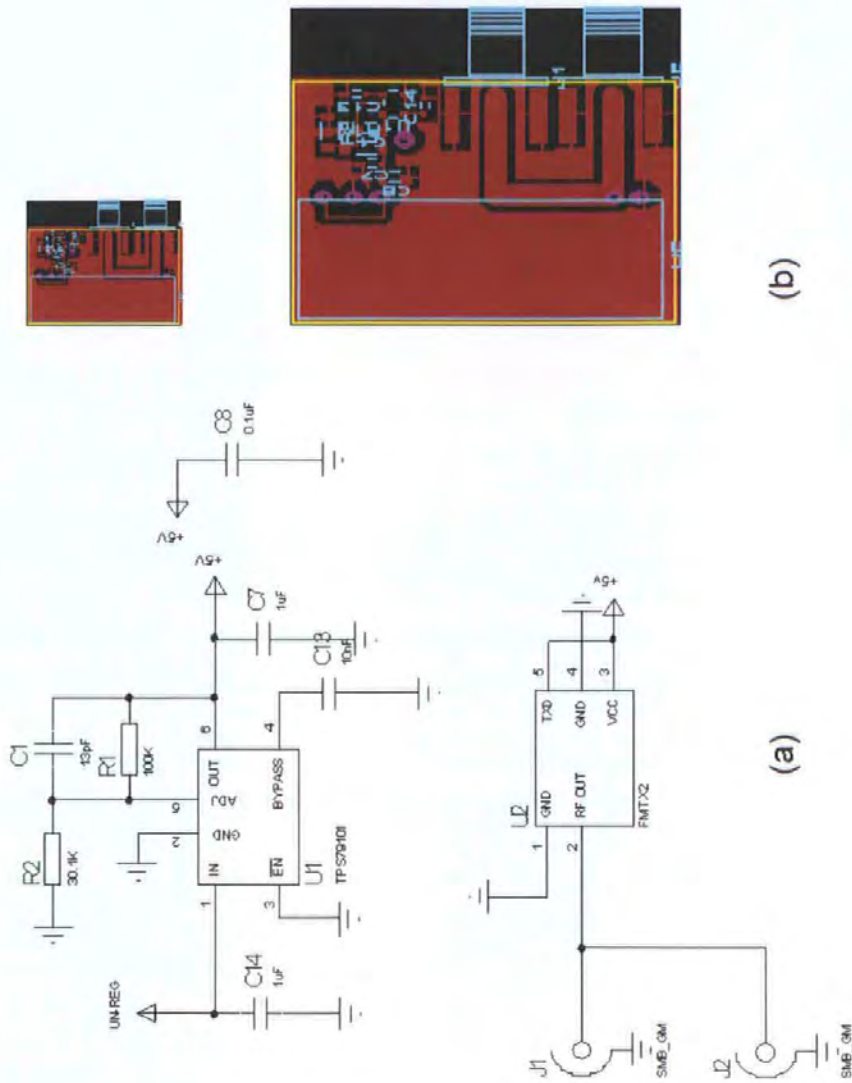
Figure 8.7   Radiometrix module (a) schematic, (b) PCB layout.

8.2.2   Reduction of 1/f noise in oscillator circuits

Any low frequency noise that is present on the DC power supply of the oscillator will be up converted in the oscillator through its bias current, increasing the sideband noise, as shown in the previous section. Even by selecting the best voltage regulators and decoupling capacitors, the effect cannot be significantly reduced and an active approach is required.

Many voltage regulators have excessive levels of output noise including voltage spikes from switching circuits and high flicker noise levels from unfiltered references. Ordinary three-terminal regulators will have several hundred nanovolts per root-hertz of white noise and some reference devices exceed one microvolt per root-hertz. DC to DC converters and switching regulators may have switching products ranging into the millivolt range covering a wide frequency spectrum.

The traditional approach to reducing such noise products to acceptable levels could be so called the "brute force" approach - a large-value inductor combined with a capacitor or a clean-up regulator inserted between the noisy regulator and load.

The active approach to noise reduction is based on the fact that the noise voltage is many orders of magnitude below the regulated voltage, even when integrated over a fairly wide bandwidth. For example, a 10 volt regulator might exhibit 10 μV of noise in a 10 kHz bandwidth - six orders of magnitude below 10 volts. Naturally, the noise current that flows in a resistive load due to this noise voltage is also six orders of magnitude below the DC. By adding a tiny resistor, R, in series with the output of the regulator and assuming that a circuit somehow manages to reduce the noise voltage at the load to zero, the noise current from the regulator may be calculated as V_n / R. If the resistor is 1Ω then, in this example, the noise current will be $10\mu V / 1\Omega = 10\mu A$.

If a current-sink can be designed to sink this amount of AC noise current to ground at the load, no noise current will flow in the load. By amplifying the noise with an inverting transconductance amplifier with the right amount of gain, the required current sink may be realized. The required transconductance is simply $-1/R$ where R is the tiny series resistor.

The following circuit illustrated in Fig. 8.8 is designed for filtering the 5 volt supply used on the Radiometrix module and is based on the design produced by Wenzel associates inc. The shunt will greatly reduce white noise, spurious signals, and line-related signals on the power supply; the attenuation can exceed 40 dB with careful construction. The values are not critical except that the gain of the amplifier should be very near the ratio of the transistor emitter resistor to the series shunt resistor. In this case the gain is 14.3 which is close to the 15Ω of the emitter. The OPA21 is a dual low noise operational amplifier that is used to measure the shunt noise. It is dual so either two supplies can be provided or in can be cascaded to further reduce the noise.
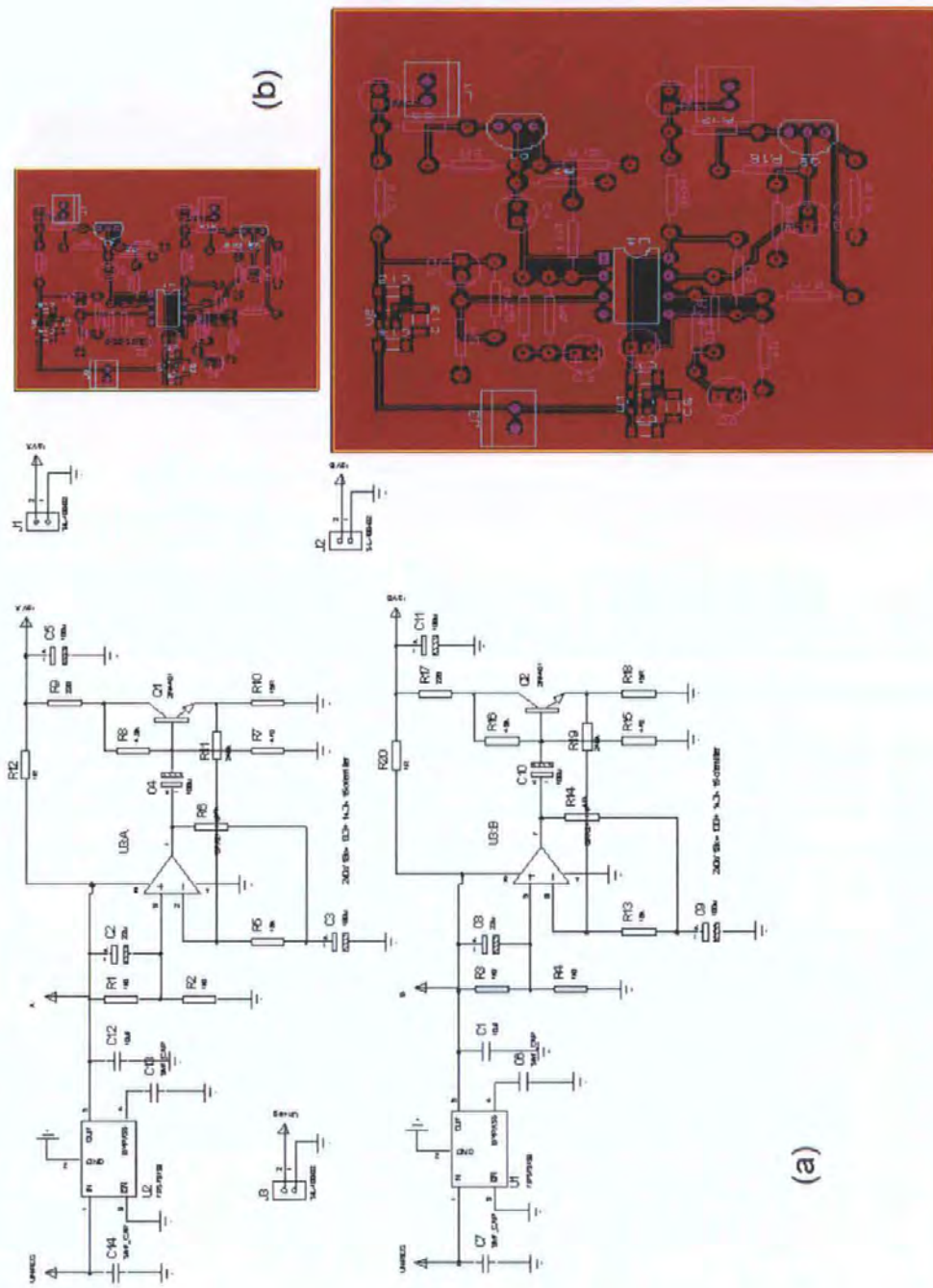
Figure 8.8   Dual 5V active filter DC supply (a) schematic, (b) PCB layout.

8.2.3   Measurement of phase noise in the implemented oscillator circuits

Firstly the Maxim 2605 oscillator circuits were measured using a spectrum analyzer. The sinusoidal current frequency was set to 100MHz using an external inductor on the circuit.

The first devices to be tested were the differential and non-differential buffered outputs with no low pass filters. They had very similar results illustrating the differential combination was not required. The phase noise performance was at a offset of 1 kHz -50 dBc/Hz, falling to -120 dBc/Hz at 1MHz offset from the carrier. This complies with the datasheet specification of the phase noise measured by Maxim. Harmonics at 200 and 300MHz are visible in the spectrum at around -90 dBc/Hz. The output power directly measured into the spectrum analyzer was 6 dBm at a 1MHz offset the noise level is over 120 dBm lower than the carrier as shown in Fig. 8.9.
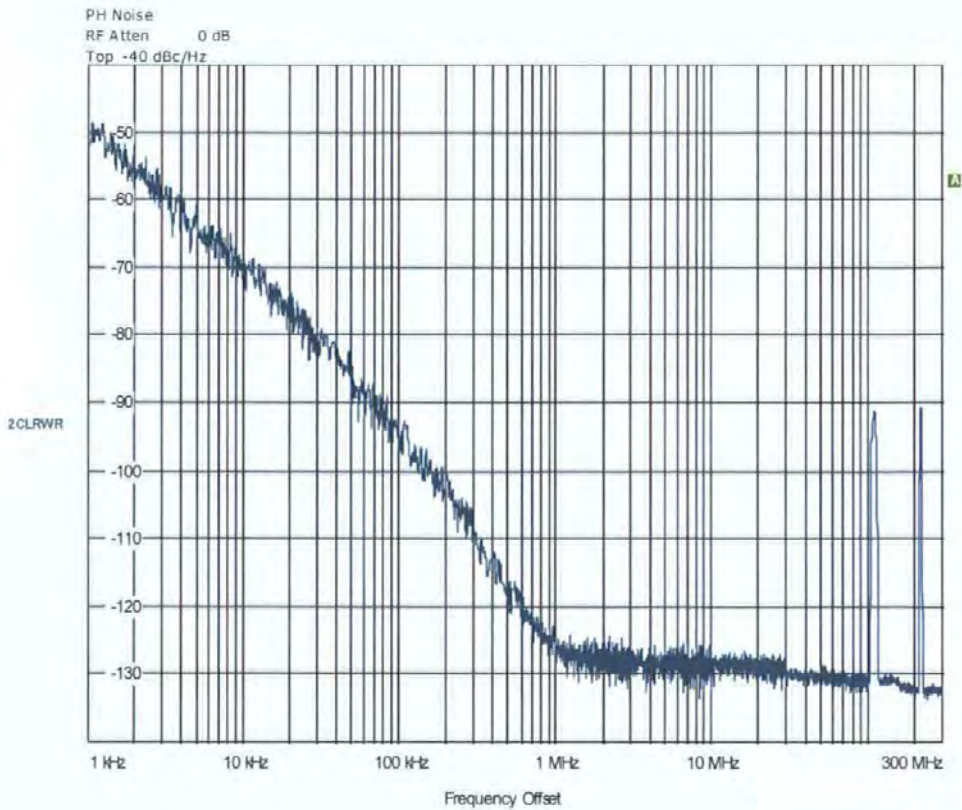
Date: 22.JUL.2005 17:18:02

Figure 8.9   Phase noise of a Maxim 2606 differential output VCO at 100MHz.

By adding the low pass filters to the Maxim 2606, before they were combined differentially, had a small effect on reducing the in band phase noise. The phase noise performance was at a offset of 3 kHz -60 *dBc/Hz*, falling to -130 *dBc/Hz* at 1MHz offset from the carrier. Harmonics at 200 and 300MHz are visible in the spectrum at around -95 *dBc/Hz*. The output power directly measured into the spectrum analyzer was 6 *dBm* at a 1MHz offset the noise level is over 130 *dBm* lower than the carrier as shown in Fig. 8.10
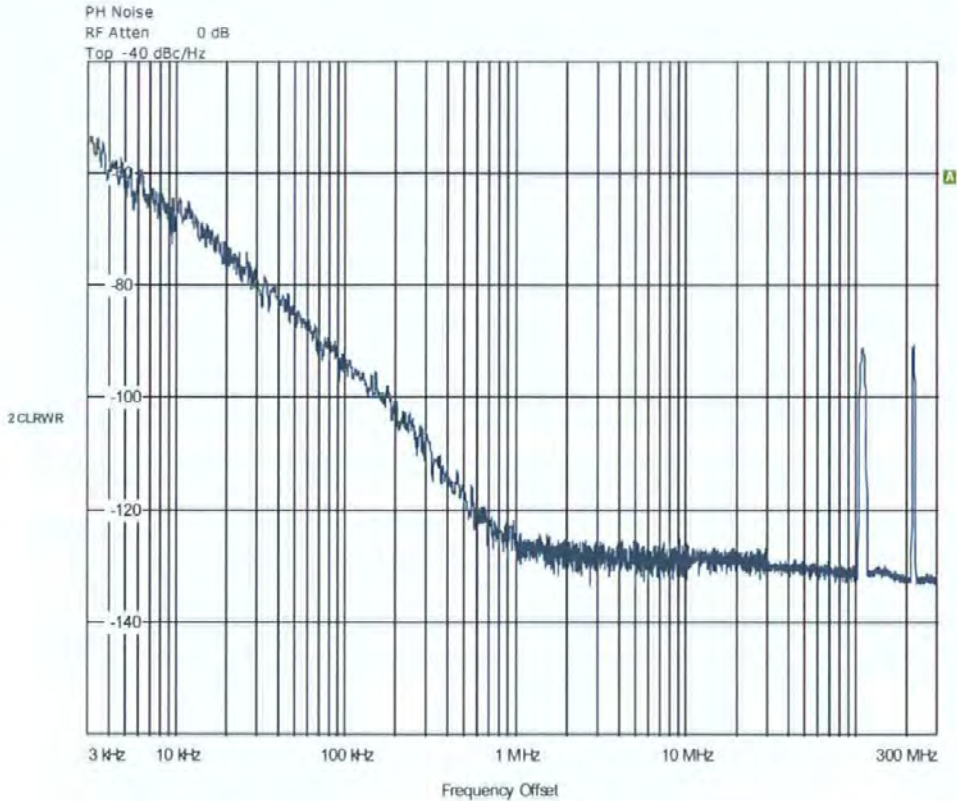
Date: 22.JUL.2005 17:33:35

Figure 8.10   Phase noise of a Maxim 2606 differential output VCO at 100MHz with low pass filters.

The magnitude of the phase noise limits the minimum resolution and magnitude of the modulating magnetic field in the MI element. This oscillator would be suitable for high sensitivity measurements of modulating fields of 1 MHz of higher where the sideband of the oscillator noise is reduced to the levels of the general system noise.

Secondly, the 433Mhz Radiometrix module was measured with and without the cascaded active noise reduction DC power supply. The output power directly measured into the spectrum analyzer was $6.6\,dBm$, the harmonics at 866 and 1.2GHz are visible in the spectrum at around $-60\,dBc/Hz$ as shown in 8.11.
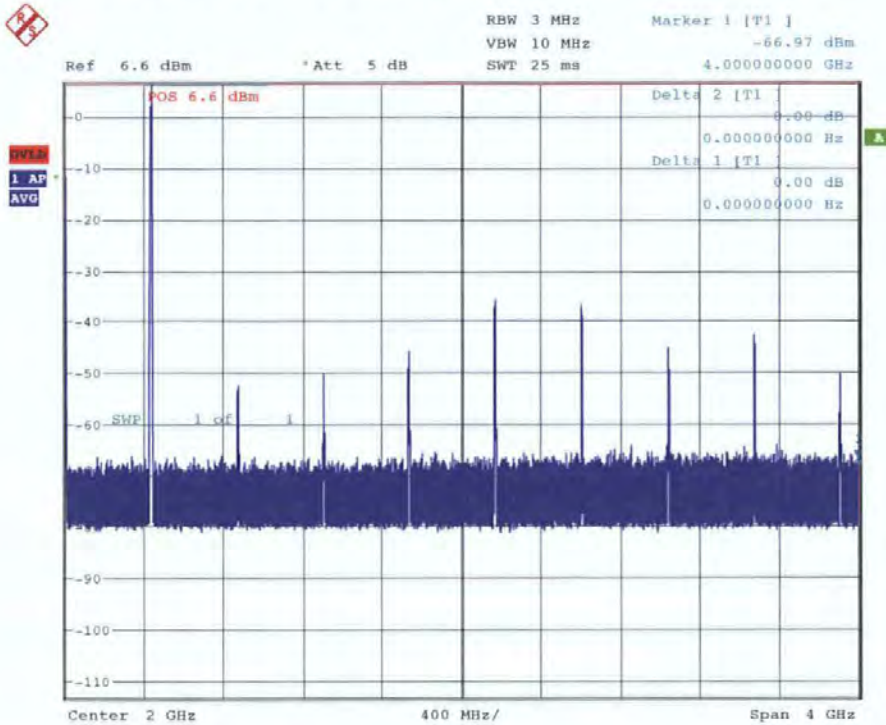
Date: 22.JUL.2005 17:44:52

Figure 8.11   Output spectrum of the 433MHz Radiometrix module.

The phase noise performance without the noise reduction power supply was many orders better than the Maxim 2606 VCO. This is due to SAW filtering and basic Phase Lock Loop (PLL) provided on the module. However, the device costs approximately ten times the price of the Maxim 2606 and has a much larger package. At a offset of 300 Hz the phase noise is -100 dBc/Hz (50 dB improvement), falling to -140 dBc/Hz at 1MHz offset from the carrier, and less than -150 dBc/Hz at large offset frequencies a shown in Fig. 8.12. These excellent results are primarily due to the extremely low noise floor of the spectrum analyser; in most conventional systems a -120 dBm noise floor is common. However the important result is that high sensitivity measurements can be made on lower frequency magnetic fields than was possible with the Maxim VCO as the sideband noise is dramatically reduced.

PH Noise
RF Atten   10 dB
Top -80 dBc/Hz

-90

-100

2CLRWR

-120

-130

-140

-150

-160

300 Hz 1 kHz   10 kHz   100 kHz   1 MHz   10 MHz   300 MHz

Frequency Offset
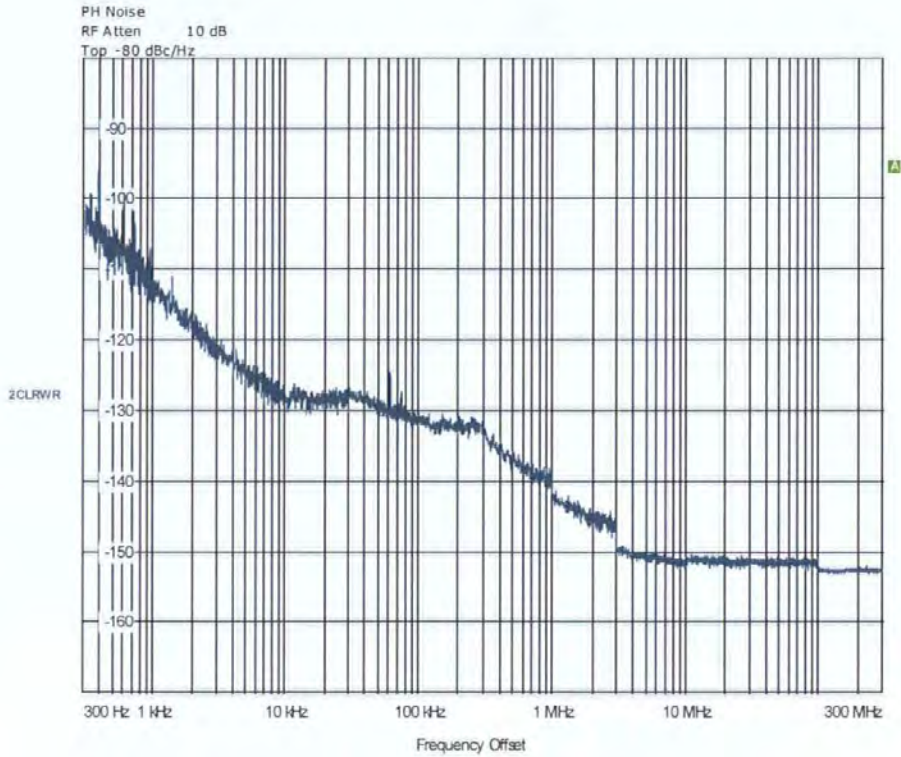
Date: 22.JUL.2005   16:51:39

Figure 8.12   Phase noise of the 433MHz Radiometrix module.

By introducing the active noise reduction power supply a slight reduction in phase noise is observed at higher frequencies, it is primarily designed to reduce low frequency noise, which cannot easily be measured on the spectrum analyzer as it is very sensitive and cannot lock correctly at such low measurement bandwidths. However even at 1KHz around 5 dB reduction in noise is created as shown in Fig. 8.13. The low frequency improvement will be better illustrated when the device is used for low frequency field measurements.

PH Noise
RF Atten   5 dB
Top -90 dBc/Hz
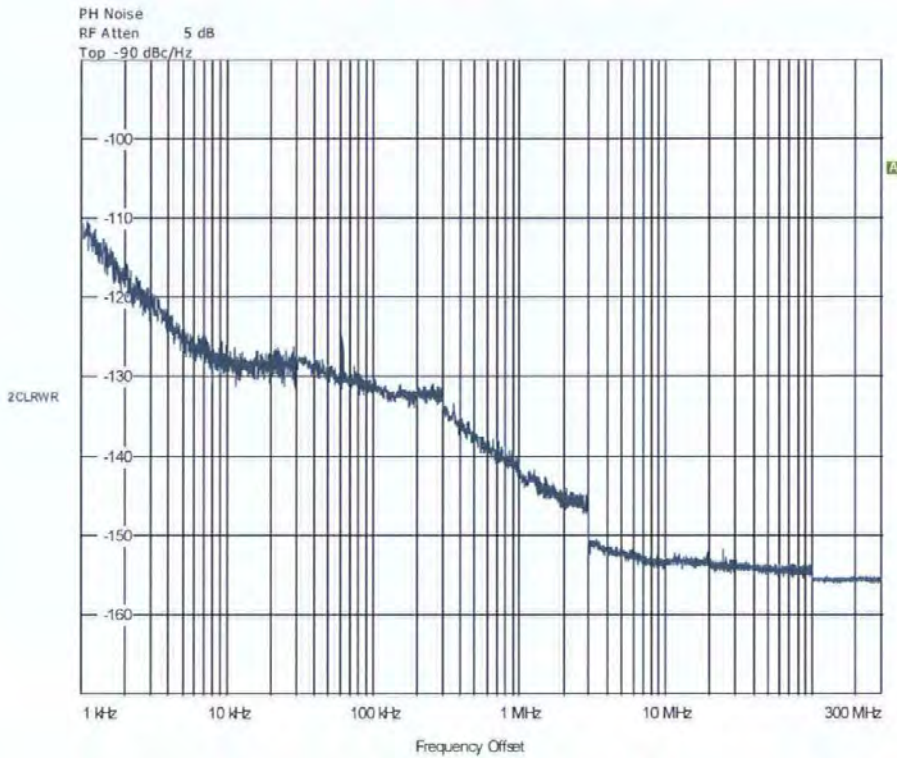
Date: 22.JUL.2005 17:43:16

Figure 8.13   Phase noise of the 433MHz Radiometrix module with active noise reduction power supply.

8.2.4   Detection and demodulation methods

Two different power detection and demodulation devices were evaluated, Linear technologies LT5507 which is based directly on a Schottky diode peak detector and an Analog electronics AD8307 which is based on logarithmic amplifier technology.

The LTC5507 integrates several functions to provide RF power detection over frequencies up to 1000MHz. These functions include an internally compensated buffer amplifier, an RF Schottky diode peak detector and level shift amplifier to convert the RF signal to DC. The LTC5507 can be used as a self-standing signal strength measuring receiver for a wide range of input signals from –34dBm to 14dBm for frequencies up to 1000MHz. The LTC5507 can be used as a demodulator for AM and ASK modulated signals with data rates up to 1.5MHz. In this application the LTC5507 can be used for detecting relatively high magnitude magnetic fields to high resolution with a maximum frequency of around 1.5MHz.

The AD8307 is the first logarithmic amplifier in an 8-lead (SOIC-8) package. It is a complete 500 MHz monolithic demodulating logarithmic amplifier based on the progressive compression (successive detection) technique, providing an dynamic range of 92 dB to ±3 dB law-conformance and 88 dB to a tight ±1 dB error bound at all frequencies up to 100 MHz. It is extremely stable and easy to use, requiring no significant external components. A single-supply voltage of 2.7 V to 5.5 V at 7.5 mA is needed, corresponding to a power consumption of only 22.5 mW at 3 V. In this application the AD8307 can be used to detect large magnitude fields to very high resolutions or very small magnitude fields at any modulating frequency up to the carrier.

For evaluation, both circuits were implemented on a single PCB sharing a common Analog TPS79133 as before. The LTC5507 requires a few capacitors to match the input frequency and to produce the peak detection; the AD8307 required an input matching network, which was calculated from the suggested data sheet values and some external capacitors to set the lower frequency demodulation cut off. The schematic and PCB layout is shown in Fig. 8.14
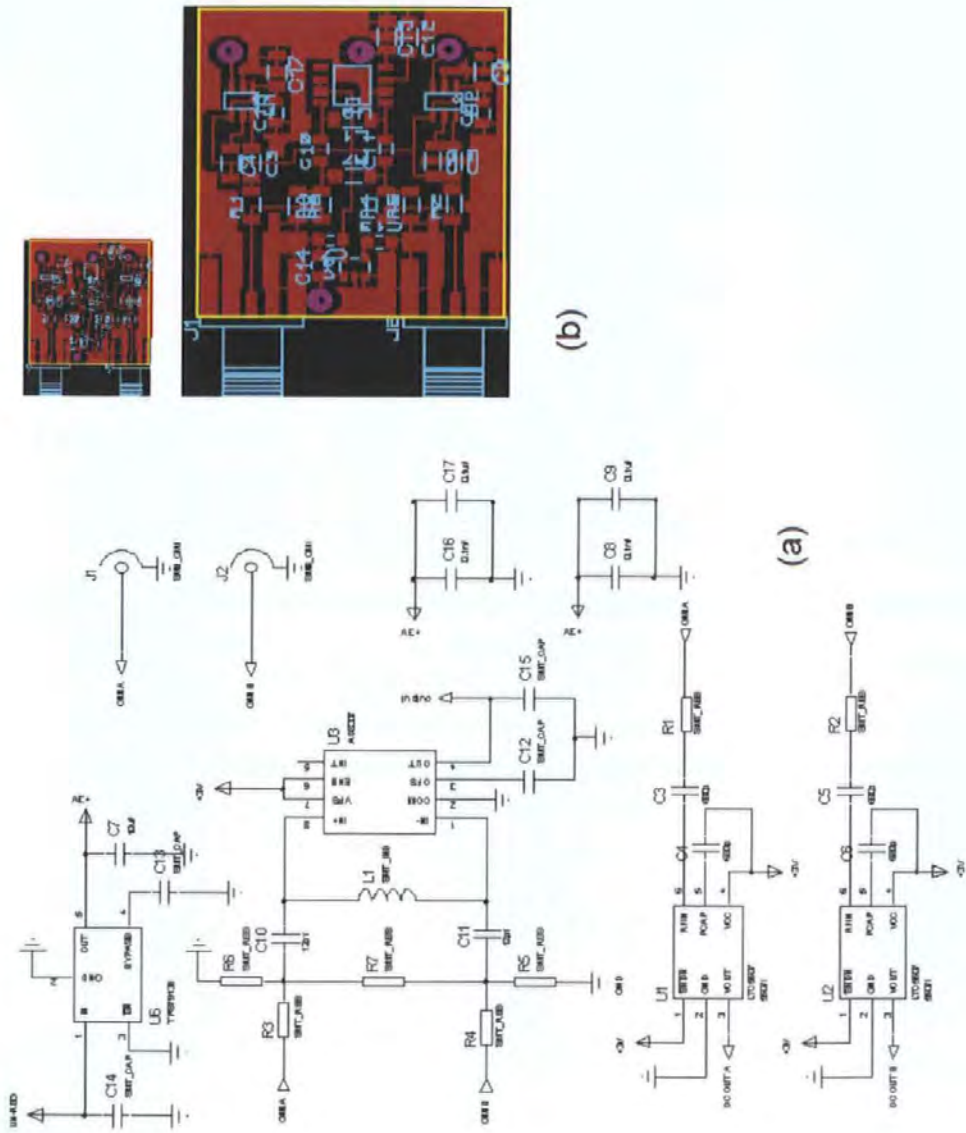
Figure 8.14   (a) Schematic of the LT5507 and AD8307detection circuits, (b) PCB layout.

8.3   Magnetic sensors utilizing Magneto Impedance

After completion of the sinusoidal generation and detection circuits, they can be combined together with the Magneto Impedance elements produced during the course of this work to produce Magneto Impedance sensor devices. Two devices are presented which were developed to use different magnetic anisotropy multi-layers, firstly with two crossed anisotropy elements and secondly with a single transverse anisotropy sample.

8.3.1   Sub-nano tesla differential magnetic field sensor utilizing Asymmetrical Magneto Impedance in multi-layer films

In Chapter 6, static and dynamical asymmetrical Magneto Impedance was measured experimentally.   Dynamical asymmetrical Magneto Impedance was shown to be more sensitive, but would present unusual complex impedance to the output of an oscillator and input to a detection device in comparison to 50Ω and would require complicated matching techniques. A similar bi-directional response could be obtained if two crossed anisotropy samples where combined differentially, as each sample is only sensitive in one particular field direction.

Initially, this is illustrated by combining a copy of the measured sample data after it is reversed to be sensitive in the opposite direction to the original field, for a frequency of 40 and 85MHz. At 85MHz the differential response is around twice as large but the smaller anisotropy angle samples suffer from large distortions because the sensitive linear response does not exactly start at the zero field strength so distortion is created. This differential outputs are shown in Figs. 8.15 and 8.16

This means the samples would not be able to be used to measure small fields due to non-linearity in the response but could be used for accurate measurements at a specific higher field measurement such as $\pm 10Oe$. However, the $\alpha = 45°$, the non-linearity is very small and could be easily corrected with a small longitudinal "tuning" DC bias to each sample to ensure the sensitive linear region begins at $0Oe$. This would then produce a continuous linear response in both field directions. The response is smaller, but not by an order of magnitude, and could be corrected in a good sensor design. [9]
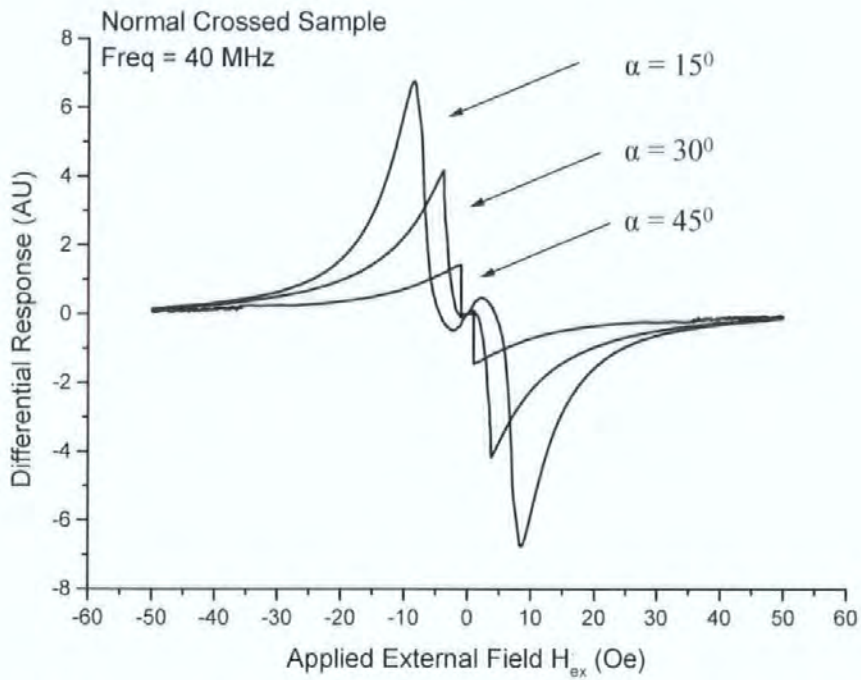
Figure 8.15   Differential output of combined measured data of crossed anisotropy samples with different anisotropy angles at 40MHz.
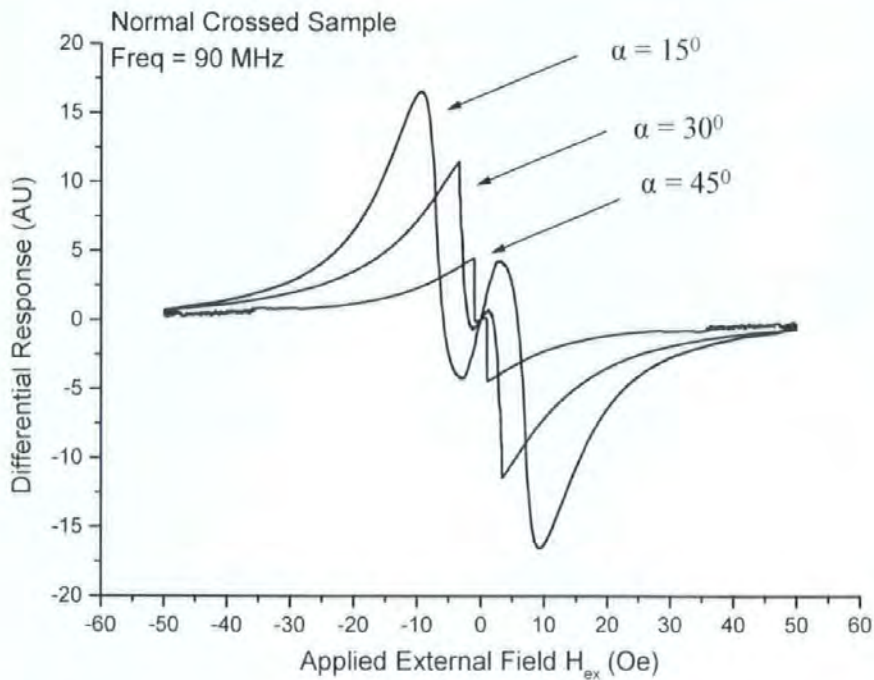
Figure 8.16   Differential output of combined measured data of crossed anisotropy samples with different anisotropy angles at 90MHz.

The sinusoidal based differential sensor design consists of the following stages, as illustrated in the block diagram in Fig. 8.17. (A) A Maxim 2605 Voltage Controlled Oscillator (VCO) configured into the differential output with low pass filters as described in section 8.2.1, this was configured to give an excitation current frequency of 90 MHz by using an external inductor and voltage reference corresponding with the more sensitive combined differential output response shown in Fig. 8.16.

All signal measurements were performed by the use of a HP4195A spectrum analyzer set to 100kHz bandwidth with 10dB input signal attenuation. The VCO produces a sinusoid with amplitude of 1.45mV; the noise at the fundamental was measured as 40nV/√Hz. The differential signals were combined in a pair of wide bandwidth amplifiers, (B), to provide the actual sinusoidal waveform. The amplitude of the waveform is 2.1mV and noise at the fundamental is 25nV/√Hz after the differential stages. This provided a pair of accurate excitation signals for the AMI samples. In order to decrease the effect of the harmonics of the signal, a pair of passive network low pass filters (C) with a –3dB point of 100MHz were used to reduce the harmonic content. The signal is then further amplified in a pair of RF power amplifiers (D). The sinusoidal signal is increased in amplitude to 25mV (No load), with a noise of 3μV/√Hz.

The measuring cell (H) consists of two close characteristic $\alpha = 45°$ crossed anisotropy elements, which are connected in parallel to ground. Each sample is driven by a separate sinusoidal output from the RF amplifiers and a feedback constant current source to produce the 25mA DC bias current required to produce the AMI effect. The AMI elements are biased oppositely to one another, making one sample sensitive to positive fields and the other sensitive to negative fields. When the samples are placed inside an AC longitudinal sensed field of ± 20Oe, the change of impedance of the sample causes a modulation of the amplitude of the applied excitation signal.

The small changes in impedance of the sample are measured by the LTC5507 power detector described in section 8.2.4 (E). The output is an offset DC level, based on the average amplitude of the signal, with a small variation which matches response of the sample measured on the HP8753E. This DC level is passed into a unity gain buffer amplifier (F) to ensure the current drive is sufficient for the instrumentation amplifier.

The responses are then combined differentially in the instrumentation amplifier (G), by inverting the signal on the negative input and adding it to the signal on the positive input, noise common to both inputs is removed. The resulting waveform is then amplified by 10 to produce an output level suitable for further signal processing.
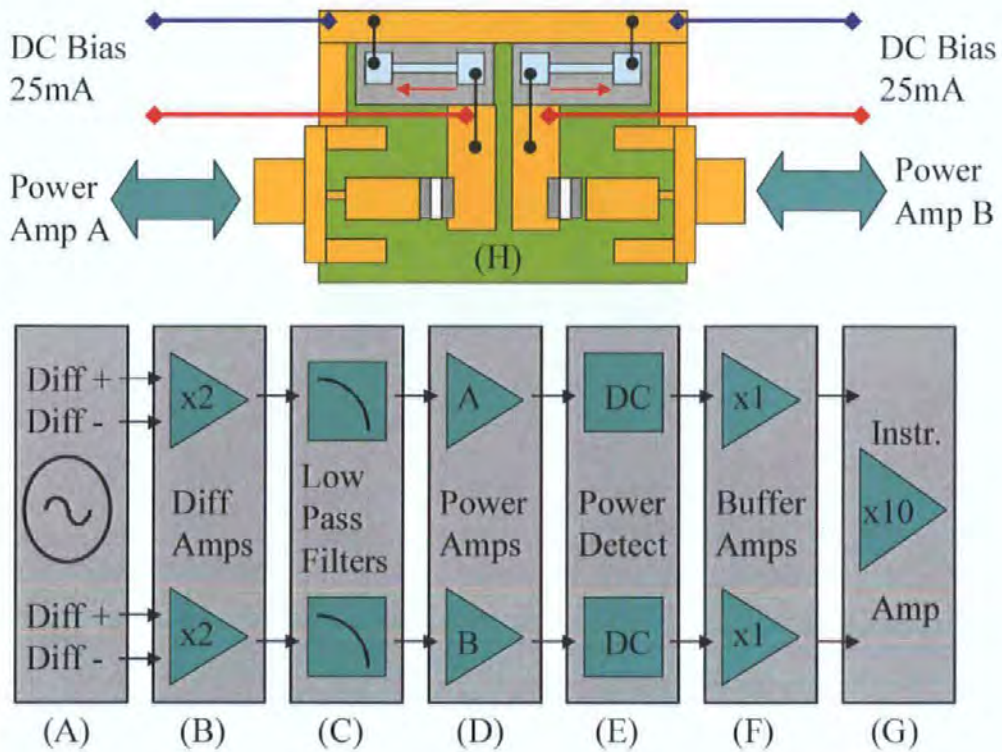
Figure 8.17   Differential sensor block diagram.

The sensor was built in both AC and DC coupled variants, as the LT5507 produces an average DC level based on the size of the power of the signal, for example the change of impedance doesn't reduce the Maxim input power to less than its minimum detection power, the unwanted DC component must be removed to allow just the AC variation to be processed and amplified. A DC coupled version allows a constant field (such as a permanent magnet) or average power of an AC signal to be measured.

The sensor operation is essentially a combination of the Maxim 2605 VCO and the LTC5507 peak detector with some additional amplification to produce a larger sinusoidal excitation current in the samples, and an instrumentation amplifier to combine the differential signals. The circuit diagram, PCB layout and final circuits are illustrated in Figs. 8.18 to 8.19.
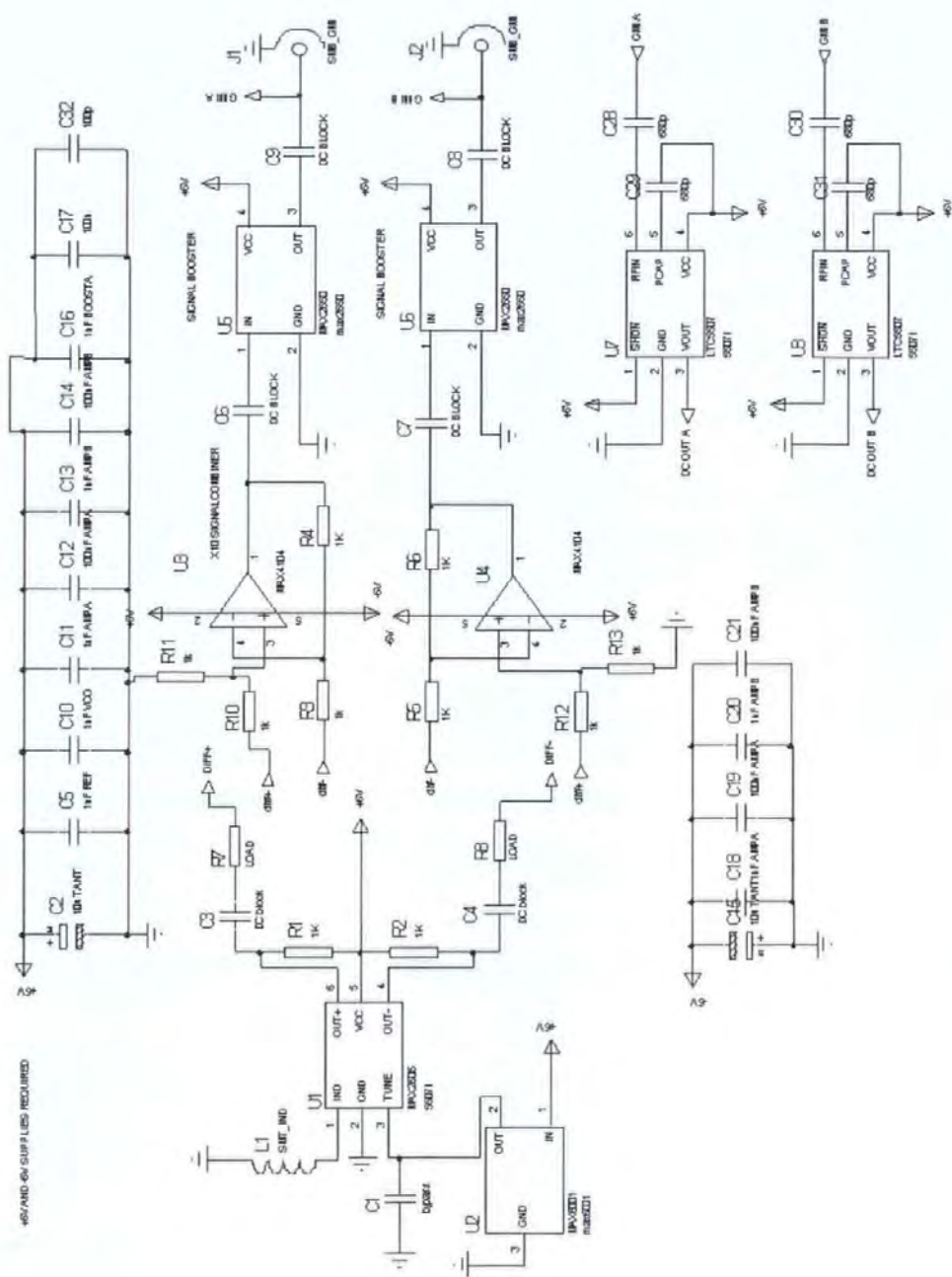
Figure 8.18   Differential sensor schematic, VCO and peak detection circuits.
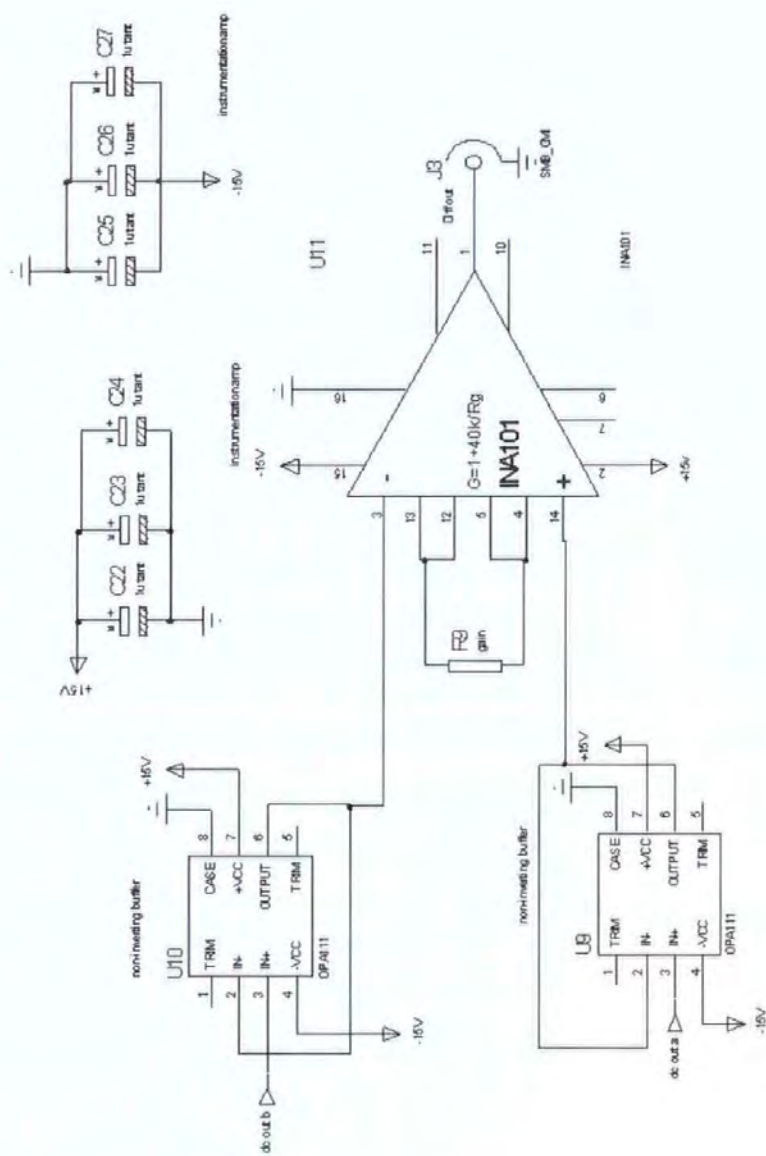
Figure 8.19   Differential sensor schematic, buffer amplifiers and instrumentation amplifier.
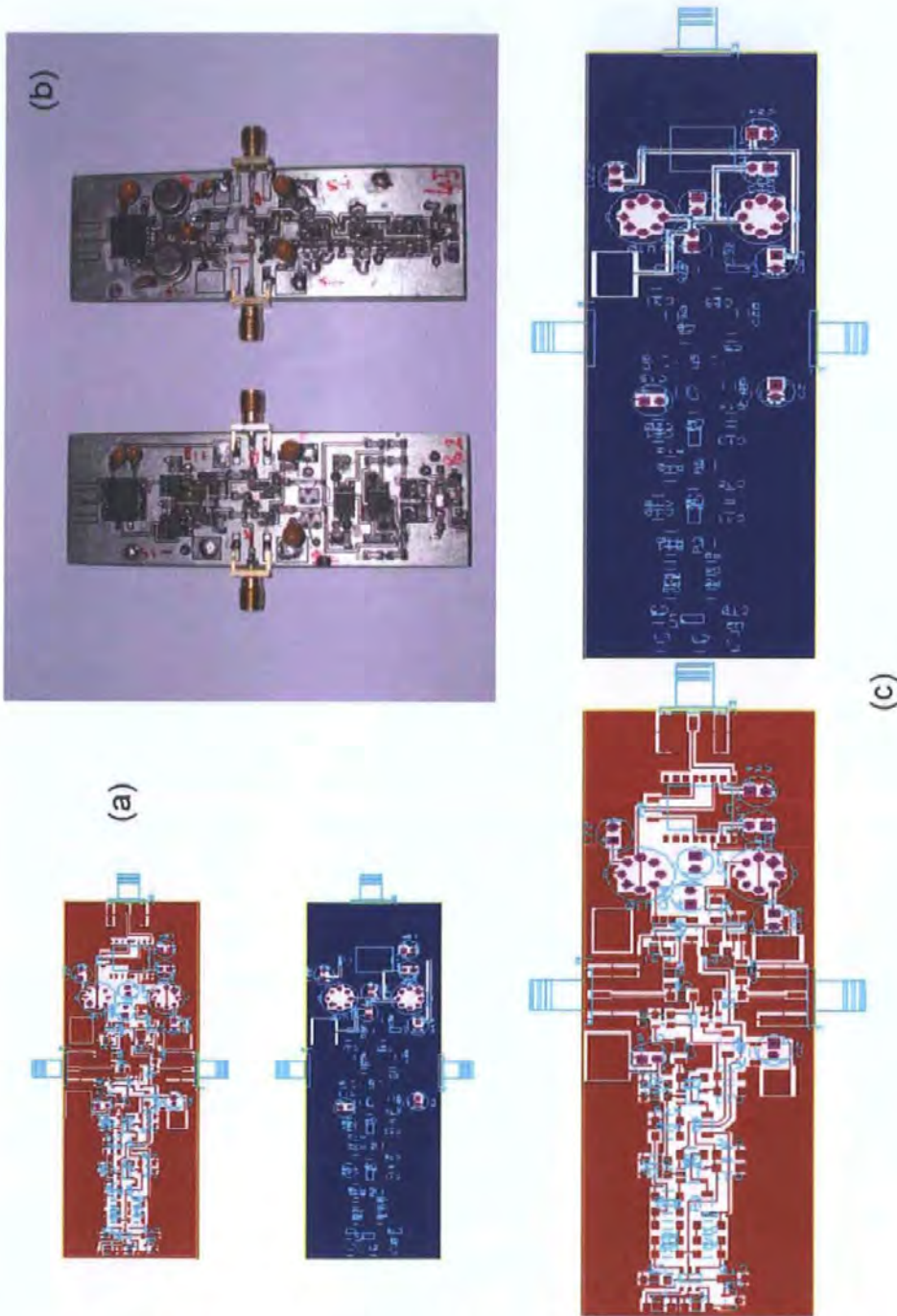
Figure 8.20   Differential sensors PCB layout (a) actual size (b) completed circuits, (c) detailed PCB illustration top and bottom copper views.

Figure 8.21 shows the output of the instrumentation amplifier for a pair of samples with the anisotropy $\alpha = 45°$.   This closely matches the previous HP8753E measured data shown in Fig. 8.16   The differential response is near linear in the field interval ± 1Oe with loss of sensitivity around the zero point.   This small distortion could be corrected with the

addition of a longitudinal magnetic bias applied to the substrate for each sample [10]. The output of the instrumentation amplifier was measured as ~600mV/Oe for a gain of 10 with a noise magnitude of $1.226\mu V/\sqrt{Hz}$ DC coupled. The SNR was calculated as, SNR = $20\log_{10}$ (Voltage Signal / Voltage Noise). For 100 kHz bandwidth this gives 20 $\log_{10}$ (600mV / $387.7\mu V$) = 63.8 dB.

This corresponds to a maximum effective resolution for AC and DC fields in of 1μ Oe for field strengths of magnitude $\sim 2Oe$ when the maximum change of impedance and therefore the maximum change of power occurs in the sinusoidal excitation current. For this sensor design, as the magnitude of applied external field is reduced, the resolution is reduced correspondingly, making it useful for large field high resolution measurements, or small magnitude field detection.
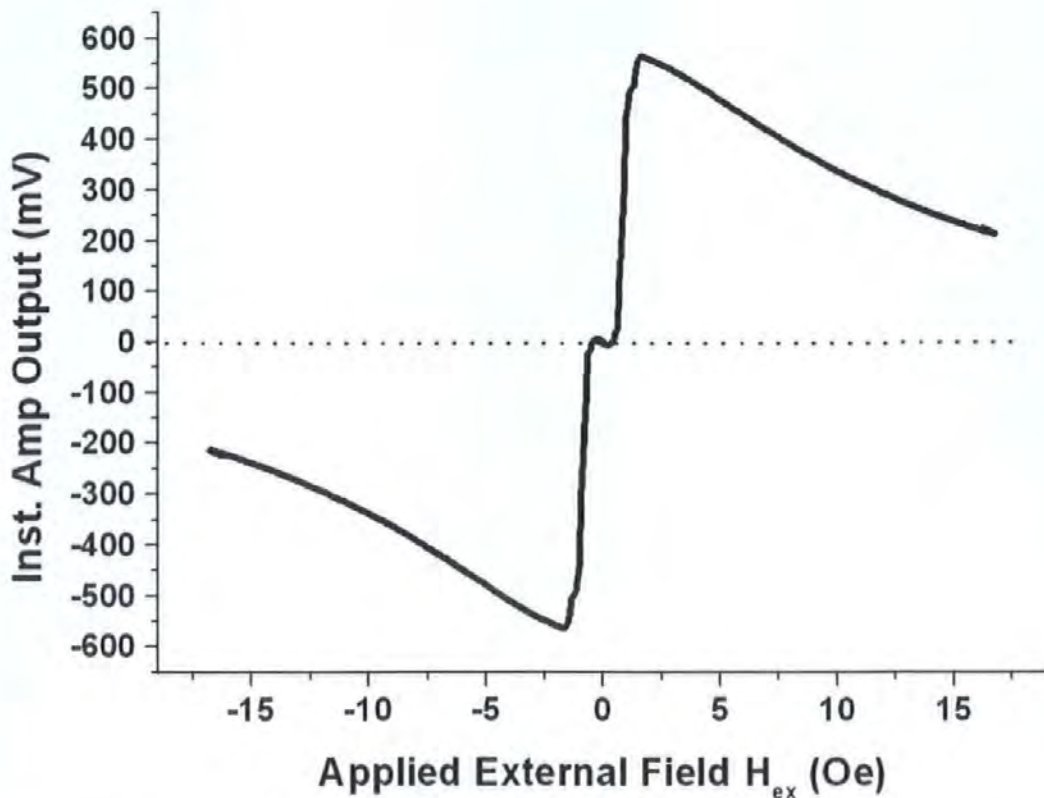
Figure 8.21   Output of the instrumentation amplifier for $\alpha = 45°$ sample and an excitation frequency of 90MHz.

8.3.2 AC biased sub-nano tesla magnetic field sensor for low frequency applications utilizing Magneto Impedance in multi-layer films

For the second sensor design a different specification of external magnetic field would be measured, namely extremely small magnitude (sub-nano Telsa) and low frequency (less than 20Hz). This was driven by the desire to use the sensitivity of Magneto Impedance for large signal bio-medical signal detection. In order to achieve this goal a significant improvement in the phase noise of the oscillator and detection methods of the sensor would have to be made.

As the signal was of a small magnitude a single transverse anisotropy sample was utilized as a transducer with a DC bias to select the most sensitive operating point. Further more, in a significant improvement of the detection process, the sample would be matched to 50Ω complex impedance at the DC bias operating point, and connected to an active isolator before de-modulation by a high dynamic range logarithmic amplifier. Additionally in order to improve the low frequency response of the sensor, the field to be measured would be up converted using an injection AC biasing technique and lock-in amplifier. Therefore a $10Hz$ signal could be up converted to $10kHz \pm 10Hz$ where the phase noise of the Oscillator is a number of magnitudes lower than at $10Hz$. After demodulation of the carrier signal by the logarithmic amplifier, as the injected AC modulating signal is known it can be amplified in an extremely accurate way by a lock-in amplifier to provide large gain. The resulting spectrum can then be measured on a spectrum analyser.

For optimal sensor design, the MI element was a multi-layered film with transverse anisotropy having two outer magnetic layers with composition NiFe, an Al_2O_3 insulation layers and a Au inner made on glass substrate, with dimensions $l = 5mm$, $d = 2.5\mu m$ and $b = 200\mu m$. The outer layers and the inner lead are of thickness $0.5\mu m$ and the insulating layer is of 80 nm. The MI element was hand picked for its performance at this frequency from numerous measured samples. The element dimensions were selected based on model analysis of flux leakage across the inner conductive layer due to edge effects and all the experimental results illustrated in Chapter 5.

The sample was characterized by utilizing a measurement system based on a Hewlett Packard HP8753E network analyzer. The measurements were made for a frequency of 433.75MHz, and an external longitudinal DC field of $\pm50Oe$ varied over 10,000 steps giving a $0.01Oe$ resolution. The sample was then DC biased using a permanent magnet (5 Oe) to the most linear portion on the characteristic curve, and the impedance was transformed to 50Ω by the use of T-matching network at the bias point for utilization with the sensor design. Figure 8.22 shows the measured impedance of the sensor element as a function of DC field cantered at 50Ω. The impedance has an overall change of 135% with a sensitivity of 15%/Oe and a linear behaviour in the field interval $-2.5Oe$ and $5Oe$. This characteristic itself is one of the best reported on MI in multilayers of similar dimensions and composition.
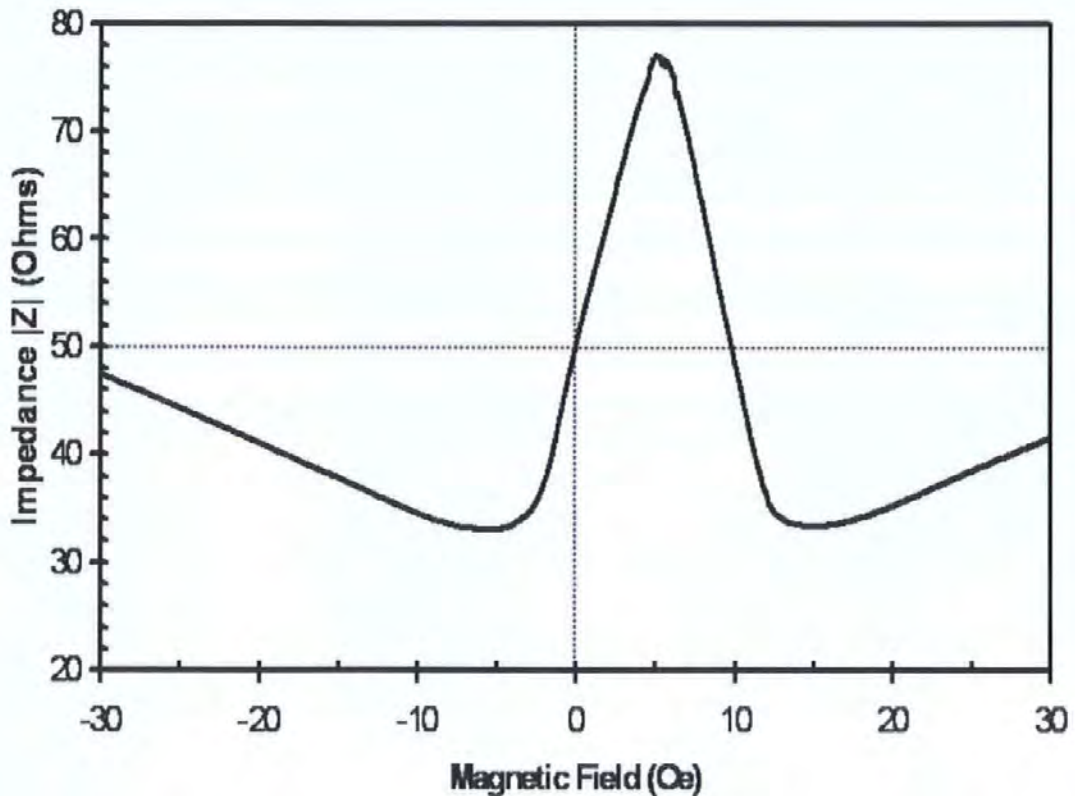
Figure 8.22   Impedance of the multilayer film biased with $5Oe$ and matched to 50Ω.

The sensor front end system is in essence designed as a single frequency network analyzer to measure the magnitude of the incident reflected power produced by a mismatch in complex impedance between the source and load. This approach is novel in Magneto Impedance sensor technologies; all previous sensor systems do not couple the reflected or transmitted power for measurement. When impedance of the MI element matches the impedance of the source (50Ω) the maximum amount of power is transferred to it. If the MI element is mismatched, some of the incident power is reflected back towards the source, this can be isolated, measured and converted to a change in applied longitudinal AC field. The incident power or carrier is produced by the Radiometrix Surface Acoustic Wave (SAW) filtered crystal oscillator circuit described in section 8.2.1

The reflected power is separated from the incident power by means of a directional coupler based on an active op-amp design which provides a non-magnetic coupling approach for lower noise which was based on a design by Wenzel Inc. This design was modified and updated for new operational amplifier technologies to allow it to work at frequencies that would be utilized in this sensor. It was originally conceived for low frequencies below 100MHz where magnetic coupling approaches required large values and components, however since 1991 when the article was been published, operation amplifier technology has increased to allow $-3dB$ bandwidths greater than $433MHz$ making, with some careful RF design, the technology useful to this sensor design.

Suitable for small signal applications, the active circulator is excellent for matching and tuning antennas, amplifiers, and oscillators. The purpose of the circulator is to absorb all energy entering a port and to pass that energy on to the next port. High reverse isolation ensures that the energy flows in one direction around the circulator and that the impedance of one port is not affected by the other ports. A traditional microwave circulator uses the non-linear properties of ferrite immersed in a magnetic field whereas this circuit uses high speed operational amplifiers. For the circulator to work properly, each port must exhibit the characteristics of a Thevenin equivalent consisting of a 50 ohm resistor and a voltage source with a voltage twice as large as the voltage arriving at the previous port.

The factor of two makes up for the drop across the Thevenin resistance when a 50 ohm load is connected. First, the 50 ohm resistance results from the two, 100 ohm resistors leading to virtual grounds -that is points that are held at a fixed voltage regardless of the current.

The Thevenin voltage source is a little less obvious since the two 100 ohm resistors are connected to two different voltages that average to the desired factor of two. Each op-amp amplifies the input signal by 3.236 which is applied to one of the resistors. A voltage divider drops this voltage down to 0.764 which is applied to the positive input of the next op-amp. Since the other resistor is connected to the feedback node of this op-amp, it sees the same 0.764 size signal. The average of 3.236 and 0.764 gives the desired factor of two. The differential gain is set so that signals leaving a port terminated with 50 ohms will generate no output at the following port.

A load impedance other than 50 ohms generates a reflection which is passed on to the next port. Crucially this means the active circulator working in an isolation mode will only transmit the mismatched power due to the MI element varying from 50Ω at the frequency of the variation, and the magnitude of power relating to the magnitude of variation. The unwanted carrier power is suppressed and the variation is amplified, as is illustrated in Fig. 8.23
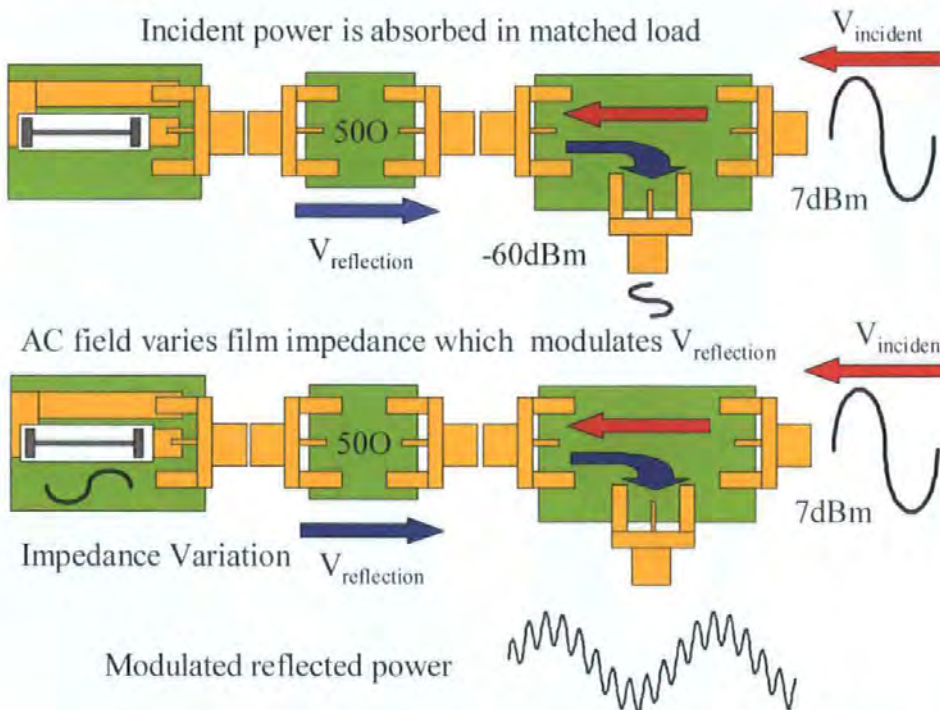
Figure 8.23   Amplification of modulated power due to active isolator technique.

By connecting the Radiometrix amplifier to the active circulator and applying a 50Ω termination the reduction in carrier power can be measured and is illustrated in Fig. 8.24, in this case the carrier is reduced by 50dB which is a number of magnitudes higher than a conventional magnetic circulator / isolator.
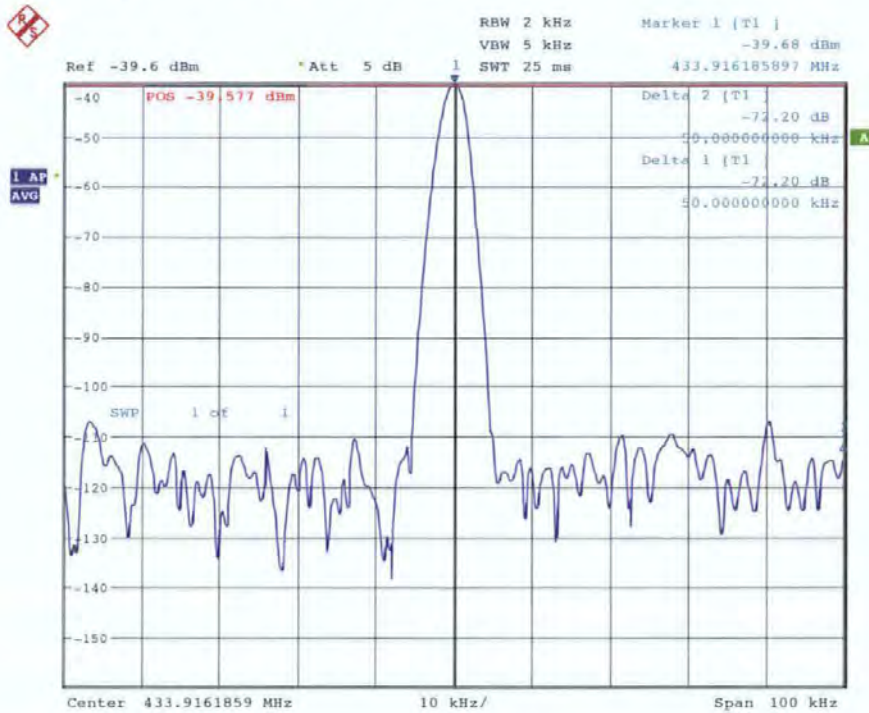
Date: 22.JUL.2005 17:49:28

Figure 8.24   Suppression of carrier frequency due to active isolator, original carrier power 6.6dB.

The active circulator circuit was made from Maxim 4305 operational amplifiers and precision surface mount resistors; the circuit was connected to others by the standard SMA connectors. The schematic, PCB and actual circuit are illustrated in Fig. 8.25.

Additionally, the phase noise of the system with the 50Ω broadband termination compared to the 50Ω matched MI sample could be measured and compared on the spectrum analyser. The broadband terminator reduced the carrier signal by 50dB and the MI element by 45dB, illustrating that the matching network was producing a close match to 50Ω at 433MHz. However the phase noise performance of the Magneto Impedance element was better than the broad band terminator by around 7dB as the noise floor was −120dBm compared to −113dBm as is illustrated in Figs. 8.26 and 8.27.

219
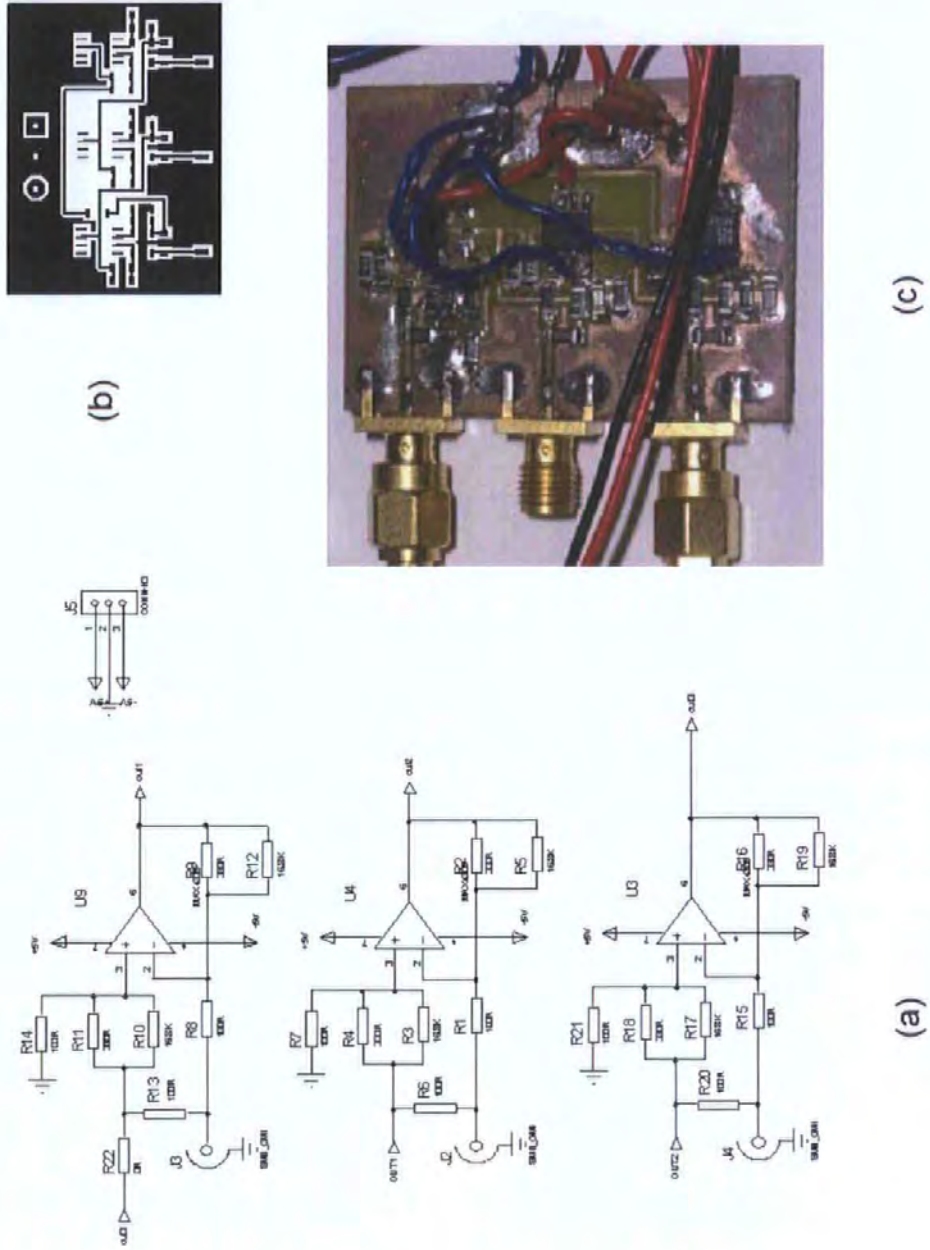
Figure 8.25   Active isolator (a) schematic, (b) PCB layout and (c) actual circuit.
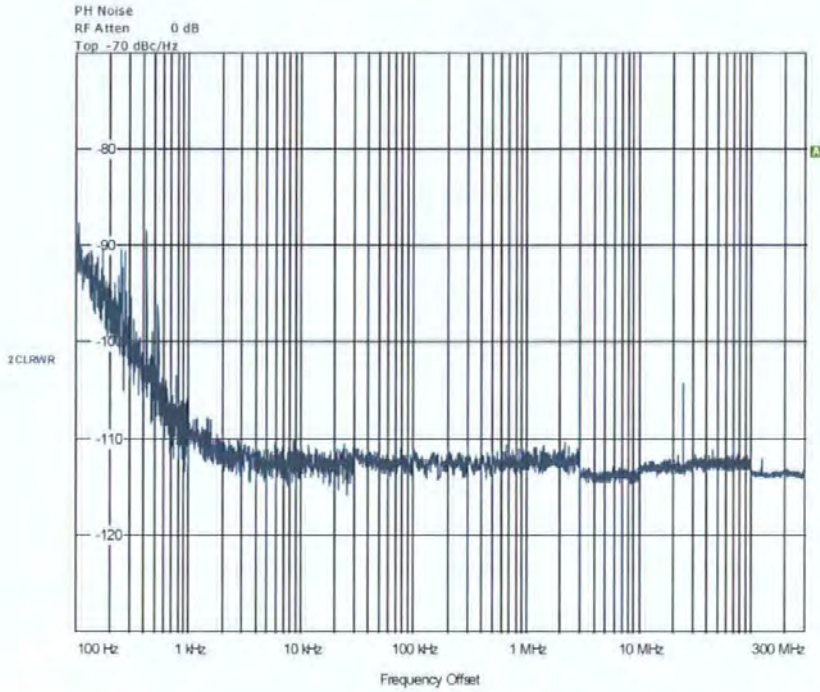
Date: 22.JUL.2005 18:10:24

Figure 8.26   Phase noise of the active isolator systems, with the Radiometrix oscillator and a 50Ω broadband terminator.
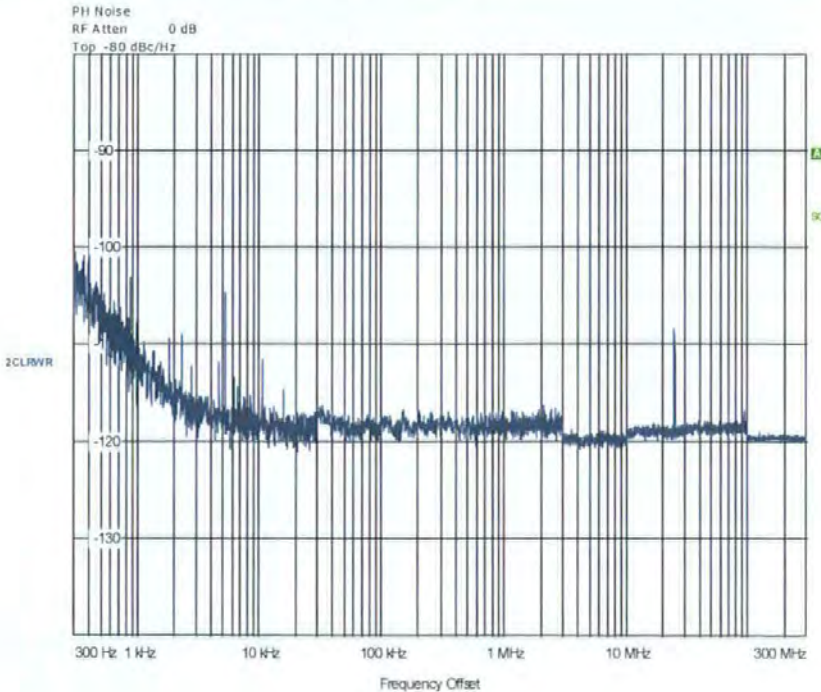
Date: 26.JUL.2005 13:09:07

Figure 8.27   Phase noise of the active isolator systems, with the Radiometrix oscillator and a 50Ω matched Magneto Impedance element.

The modulated reflected power is then demodulated by the AD8307 filtered, amplified and measured using a spectrum analyzer to find the signal-to-noise ratio of the modulated power to noise floor. The magnitude and resolution of field detection at that modulation frequency can then be determined by converting the power in dBm to a RMS voltage at 50Ω.

The AC modulation current is produced by a solenoid with two coils, calibrated to 0.38mA per Oe, driven by a higher frequency AC modulation current and a lower frequency AC field for measurement. At low frequencies (<100Hz) the phase noise (1/f) of the oscillator producing the carrier limits the performance of the sensor [10],[11] and has been shown in section 8.2.3. A technique to overcome this problem is to firstly modulate the low frequency AC field to be measured with a locally produced high frequency field (1 to 5 kHz). The second local modulation field shifts the measurement field of interest to a higher frequency offset from the local modulation. This modulation field ideally needs to be higher in magnitude than 1MHz, however, it is difficult to drive extremely low currents at such higher frequencies into a large inductive, low resistance load, while maintaining a constant amplitude and phase of current. Therefore the system is running at an optimum level to maintain a precise stable driving current in the solenoids. The system is reviewed in Fig. 8.28
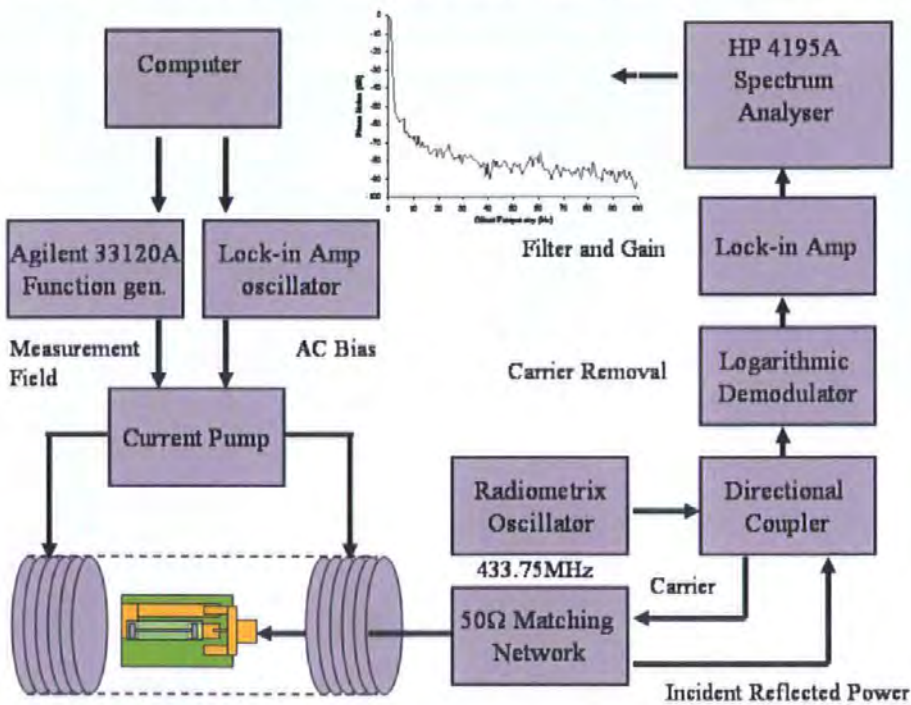
Figure 8.28   AC bias for low frequency measurement system block diagram.

The oscillator of the lock-in amplifier was used to generate a sinusoidal signal of 0.142V to 1µV RMS at frequencies of 1 kHz, 100 Hz and 20 Hz. This corresponds to an AC measurement field of 0.37 to 3µ Oe RMS in the solenoid.

For a large field of 0.37Oe at 1kHz a signal to noise ratio (SNR) of 86dB was obtained, this corresponds to a resolution detection of 1.84 x 10^{-5} Oe. Reducing the field magnitude down to 3µ Oe decreased the signal to noise ratio to 18dB, corresponding to a resolution of detection of 3.73 x10^{-7} Oe. At 100Hz, the large field performance is reduced to a resolution of 8.14 x 10^{-5} and the small field performance to 1.46 x 10^{-6} Oe this is confirmed by the small increase in phase noise of the oscillator over that bandwidth. Performance at 50Hz is illustrated in Fig. 8.29

However, by reducing the frequency to 20Hz a large change in performance is observed, large field resolution falls to 2.18 x 10^{-4} Oe and the smallest magnitude of field of measurement is 3.3 x 10^{-4} Oe with a signal to noise ratio of 13dB giving a resolution of 6.6 x 10^{-5} Oe.

Under direct measurement sub-nano Tesla magnitude and resolution is only available at frequencies greater than 100 Hz, due to the phase noise of the carrier generating oscillator. The upper limits of the demodulation resolution depend on the of the measurement circuit, so in this case in the magnitude of 200MHz.

However, this performance is already several orders of magnitude more sensitive than the previous sensor design presented over a several magnitudes increase in bandwidth of operation, and recently published Magneto Impedance sensor technologies. The full table of results is presented in Fig. 8.30
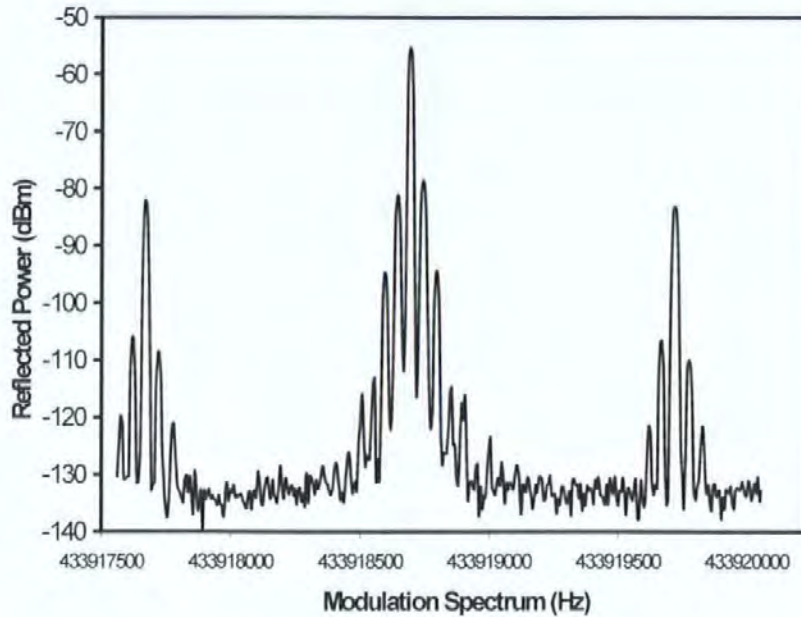
Figure 8.29   Modulation spectrum of the carrier with a 1kHz and 50Hz external field.

1KHz	RMS Coil current (A)	AC Field Magnitude (RMS) Oe	Magnitude (dBm)	Noise Floor (/10 offset)	Signal to Noise
	1.41E-02	3.70E-01	-0.106976	-8.62E+01	8.61E+01
	1.89E-03	4.96E-02	-8.26035	-8.09E+01	7.26E+01
	3.78E-06	9.95E-05	-12.0294	-6.57E+01	5.37E+01
	3.52E-07	9.26E-06	-29.4931	-62.5598	3.31E+01
	1.25E-07	3.29E-06	-41.4665	-6.38E+01	2.24E+01
	1.13E-07	2.97E-06	-43.8831	-6.19E+01	1.80E+01
100Hz	RMS Coil current (A)	AC Field Magnitude (RMS) Oe	Magnitude (dBm)	Noise Floor (/10 offset)	Signal to Noise
	1.40E-02	3.69E-01	-11.1125	-8.42E+01	7.31E+01
	1.89E-03	4.97E-02	-22.1257	-8.48E+01	6.26E+01
	3.75E-06	9.87E-05	-20.423	-66.2976	4.59E+01
	1.20E-06	3.16E-05	-27.9648	-58.585	3.06E+01
	1.00E-06	2.63E-05	-31.0414	-5.76E+01	2.65E+01
	1.00E-06	2.63E-05	-34.5138	-6.00E+01	2.55E+01
20Hz	RMS Coil current (A)	AC Field Magnitude (RMS) Oe	Magnitude (dBm)	Noise Floor (/10 offset)	Signal to Noise
	1.40E-02	3.68E-01	-11.3933	-73.7365	6.23E+01
	1.88E-03	4.95E-02	-30.5834	-7.44E+01	4.38E+01
	3.75E-06	9.87E-05	-21.3135	-5.99E+01	3.86E+01
	1.15E-06	3.03E-05	-29.2173	-4.22E+01	1.30E+01
	1.66E-06	4.36E-05 noise			
1KHz	Magnitude V	mV		Detection Levels	Field resolution
	220.869731	1.10E-02		2.02E+04	1.84E-05
	86.39080129	0.020162065		4.28E+03	1.16E-05
	55.9776938	0.115725749		4.84E+02	2.06E-07
	7.496007323	0.166530966		4.50E+01	2.06E-07
	1.888687048	0.143722579		1.31E+01	2.50E-07
	1.429980128	0.179432043		7.97E+00	3.73E-07
100Hz	Magnitude V	mV		Detection Levels	Field resolution
	62.20997147	1.37E-02		4.54E+03	8.14E-05
	17.50652717	1.29E-02		1.35E+03	3.67E-05
	21.29781264	0.108294151		1.97E+02	5.02E-07
	8.938095738	0.263169165		3.40E+01	9.30E-07
	6.272129292	0.295750169		2.12E+01	1.24E-06
	4.205280818	0.223606798		1.88E+01	1.40E-06
20Hz	Magnitude V	mV		Detection Levels	Field resolution
	60.23099008	4.60E-02		1.31E+03	2.81E-04
	6.611728355	4.25E-02		1.56E+02	3.18E-04
	19.22250587	0.226313261		8.49E+01	1.16E-05
	7.737844576	1.733604406		4.46E+00	6.79E-06

Figure 8.30   Measurement results of direct external AC magnetic field modulation.

To improve the performance of the sensor for low frequency fields, the lock-in amplifier is used to produce fields of 5 kHz and 1 kHz at a magnitude of 0.37Oe, and an Agilent 33120A is used to produce the measurement field at 20 and 10Hz for comparison with the direct measurement. Using an AC bias field of 5 kHz, a 20Hz measurement field of magnitude 0.186 Oe had a signal to noise ratio of 60 dB giving a resolution of 1.71×10^{-4} Oe, small magnitude field detection was increased to 1.27×10^{-5} Oe with a resolution of 4.78×10^{-6} Oe.

Reducing the measurement field to 10Hz reduced the large field resolution to 2.01×10^{-4} Oe and small field magnitude detection to 1.35×10^{-5} with resolution to 5.27×10^{-6} Oe.

Secondly, using an AC bias field of 1 kHz, a 20Hz measurement field of magnitude 0.186 Oe had a signal to noise ratio of 56 dB giving a resolution of 2.59×10^{-4} Oe, small magnitude field detection was 5.30×10^{-5} Oe with a resolution of 1.86×10^{-5} Oe.

Reducing the measurement field to 10Hz reduced the large field resolution to 2.71×10^{-4} Oe and small field magnitude detection to 4.53×10^{-5} with resolution to 9.33×10^{-6} Oe.

A typical modulation spectrum of a 5 kHz AC bias with a 20Hz modulation spectrum (magnitude 2.58×10^{-2}) is illustrated in Fig. 8.31 A full table of the frequency measurement results are shown in Fig. 8.32.
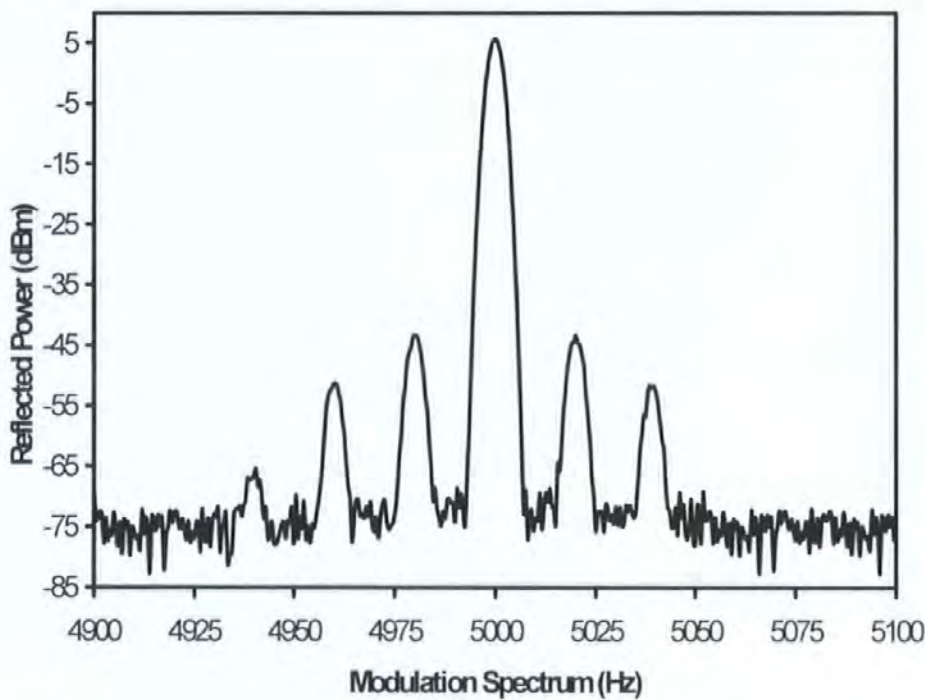

Figure 8.31   Modulation spectrum of a 5 kHz AC bias signal with a 20 Hz measurement field and harmonics.

5KHz AC Bias
20Hz

RMS Coil current (A)	RMS Magnitude (Oe)	Magnitude (dBm)	Noise Floor (/10 offset)	Signal to Noise
7.05E-03	1.86E-01	-1.61E+01	-7.68E+01	6.07E+01
2.21E-03	5.81E-02	-2.81E+01	-7.68E+01	4.87E+01
9.81E-04	2.58E-02	-3.82E+01	-7.68E+01	3.85E+01
3.09E-04	8.13E-03	-4.86E+01	-7.71E+01	2.86E+01
1.70E-06	4.46E-05	-57.7418	-75.3645	1.76E+01
4.82E-07	1.27E-05	-6.66E+01	-7.51E+01	8.47E+00

5KHz AC Bias
10Hz

RMS Coil current (A)	RMS Magnitude (Oe)	Magnitude (dBm)	Noise Floor (/10 offset)	Signal to Noise
7.02E-03	1.85E-01	-16.6453	-7.59E+01	5.93E+01
2.20E-03	5.79E-02	-2.79E+01	-7.59E+01	4.80E+01
9.78E-04	2.57E-02	-3.83E+01	-7.59E+01	3.76E+01
3.08E-04	8.12E-03	-4.79E+01	-7.59E+01	2.80E+01
1.72E-06	4.53E-05	-5.73E+01	-7.59E+01	1.87E+01
5.12E-07	1.35E-05	-6.50E+01	-7.59E+01	1.10E+01

1KHz AC Bias
20Hz

RMS Coil current (A)	RMS Magnitude (Oe)	Magnitude (dBm)	Noise Floor (/10 offset)	Signal to Noise
6.72E-03	1.77E-01	-1.85E+01	-7.52E+01	5.67E+01
2.02E-03	5.32E-02	-3.36E+01	-7.65E+01	4.30E+01
1.33E-05	3.51E-04	-4.36E+01	-7.47E+01	3.11E+01
4.34E-06	1.14E-04	-5.46E+01	-7.63E+01	2.16E+01
2.02E-06	5.30E-05	-6.31E+01	-7.22E+01	9.09E+00

1KHz AC Bias
10Hz

RMS Coil current (A)	RMS Magnitude (Oe)	Magnitude (dBm)	Noise Floor (/10 offset)	Signal to Noise
7.02E-03	1.85E-01	-1.94E+01	-7.61E+01	5.67E+01
2.20E-03	5.79E-02	-3.37E+01	-7.61E+01	4.24E+01
9.78E-04	2.57E-02	-4.41E+01	-7.61E+01	3.20E+01
3.08E-04	8.12E-03	-5.35E+01	-7.61E+01	2.26E+01
1.72E-06	4.53E-05	-6.24E+01	-7.61E+01	1.37E+01

5KHz AC Bias
20Hz

Magnitude V	mV	Detection levels	Field Resolution
35.17021329	3.24E-02	1.08E+03	1.71E-04
8.846266164	3.24E-02	2.73E+02	2.13E-04
2.741006101	3.25E-02	8.44E+01	3.06E-04
0.833825173	0.031098182	2.68E+01	3.03E-04
0.289998	3.81E-02	7.61E+00	5.86E-06
0.104739381	3.95E-02	2.65E+00	4.78E-06

5KHz AC Bias
10Hz

Magnitude V	mV	Detection levels	Field Resolution
32.90182607	3.57E-02	9.21E+02	2.01E-04
8.96700539	3.57E-02	2.52E+02	2.30E-04
2.716689487	3.57E-02	7.60E+01	3.39E-04
0.899911915	3.57E-02	2.52E+01	3.22E-04
0.30667615	3.57E-02	8.58E+00	5.27E-06
0.126443061	3.57E-02	3.54E+00	3.81E-06

1KHz AC Bias
20Hz

Magnitude V	mV	Detection levels	Field Resolution
26.58489823	3.89E-02	6.84E+02	2.59E-04
4.676382237	3.33E-02	1.41E+02	3.78E-04
1.48547382	4.12E-02	3.61E+01	9.72E-06
0.414390702	3.43E-02	1.21E+01	9.45E-06
0.155770424	5.47E-02	2.85E+00	1.86E-05

1KHz AC Bias
10Hz

Magnitude V	mV	Detection levels	Field Resolution
23.83691249	3.49E-02	6.82E+02	2.71E-04
4.622373154	3.49E-02	1.32E+02	4.37E-04
1.394071351	3.49E-02	3.99E+01	6.45E-04
0.471194272	3.49E-02	1.35E+01	6.02E-04
0.169589907	3.49E-02	4.85E+00	9.33E-06

Figure 8.32   Measurement results of an AC modulated external AC magnetic field.

226

A thin-film MI sensor was produced based on the measurement of the modulation of the incident reflected power due to an external AC magnetic field. Direct field measurement performance at 1kHz is a resolution of 3.73×10^{-7} Oe. AC biased performance at 5kHz of a 20Hz field is a resolution of 5.27×10^{-6} Oe, and at 10Hz of 9.33×10^{-6} Oe. The achieved low frequency magnetic field resolution is at least one order of magnitude higher than that reported for MI pulse-circuit elements. Provided that the phase noise of the oscillator at lower frequencies is suppressed and the measurements are taken in a magnetically screened room, the performance of the sensor could be further improved, to the limits of intrinsic thermal noise present in any system, since the magnetic noise of the MI element is a number of orders of magnitude lower than the thermal noise. [12]

References

[1]   http://www.aichi-mi.com/ - products and datasheets

[2]   A. Hajimiri and T. H. Lee, *"A General Theory of Phase Noise in Electrical Oscillators"*, IEEE Journal of solid-state electronics, vol. 33, no 2, 1998

[3]   E. J. Baghdady, R. N. Lincoln, and B. D. Nelin, *"Short-term frequency stability: Characterization, theory, and measurement,"* Proc. IEEE, vol.53, pp. 704–722, July 1965.

[4]   L. S. Cutler and C. L. Searle, *"Some aspects of the theory and measurement of frequency fluctuations in frequency standards,"* Proc. IEEE, vol. 54, pp. 136–154, Feb. 1966.

[5]   D. B. Leeson, *"A simple model of feedback oscillator noises spectrum,"* Proc. IEEE, vol. 54, pp. 329–330, Feb. 1966.

[6]   J. Rutman, *"Characterization of phase and frequency instabilities in precision frequency sources; Fifteen years of progress,"* Proc. IEEE, vol. 66, pp. 1048–1174, Sept. 1978.

[7]   A. A. Abidi and R. G. Meyer, *"Noise in relaxation oscillators,"* IEEE J. Solid-State Circuits, vol. SC-18, pp. 794–802, Dec. 1983.

[8]   P. Delooze, L. V. Panina, D. J. Mapps, K. Ueno, and H. Sano, *"CoFeB-Cu layered film with crossed anisotropy for asymmetrical magnetoimpedance,"* IEEE Trans. Magn., vol. 39, pp. 3307–3309, Sept. 2003.

[9]   Y. Nishibe and N. Ohta, *"Thin film magnetic field sensor utilizing magneto impedance effect,"* R&D Rev. Toyota CRDL, vol. 35, no. 4. 2000.12.

[10]   H. Mawatari, H. Kikuchi, S. Yabukami, M. Yamaguchi, and K. I. Arai, "*High-frequency-carrier type thin film magnetic field sensor for AC detection*", J. Magn. Soc. Jpn., vol. 27, pp. 414–418, Apr. 2003.

[11]   S. Yabukami, H. Mawatari, Y. Murayama, T. Ozawa, K. Ishiyama, and K. I. Arai, "*High-Frequency Carrier Type Thin-Film Sensor Using Low-Noise Crystal Oscillator*", *IEEE Trans. Magn.* vol. 40, pp. 2670-2672, 2004.

[12]   Delooze, P. Panina, L.V. Mapps, D.J. "*AC biased sub-nano-tesla magnetic field sensor for low-frequency applications utilizing magnetoimpedance in multilayer films*" IEEE Trans. Magn. vol. 41, pp. 3652 - 3654, 2005.

Chapter 9. Conclusions and future work

This chapter aims to underline the main achievements of the present work and consider future work in continuation of this research area.

The first stage of the research was dedicated to the understanding of magnetic properties of ferromagnetic materials and to the depth of knowledge required to study the origins of the Magneto Impedance effect. This course of guided reading provided strong foundation and is thoroughly presented in Chapter 2, illustrating the knowledge acquired.

With this strong foundation, the study of magneto impedance effect could begin through acquisition of the various implementations of the theoretical effect presented in papers and reviews. The results of this review are presented in Chapter 3.

In Chapter 4, in order to clarify and test the theoretical results, and also to produced MI elements with improved characteristics, training was provided in high vacuum manufacturing techniques and a review of manufacturing methods was undertaken before beginning an extensive programme of manufacturing of thin films that were then utilized during the course of this work.

With this in place, measurement of multi-layer samples with various types of materials, anisotropies, geometries and dimensions was carried out in order to produce sensitive, miniaturised thin films for sensor applications. The new combinations of materials, anisotropies and geometries produced exciting results in all areas. For MI samples with a transverse anisotropy, which generally is the widest published body of work, MI ratios of *135% over a large useable frequency range of 500MHz in NiFe and CoSiB multi-layers*, and MI ratios of *240% in $Co_{70.2}Fe_{7.8}B_{22}$ multi-layers over a useable frequency range of 50MHz* were presented. In particular, in conjunction with Stanley Electric Company R&D, sensitive static crossed anisotropy samples were produced, a relatively new field of published work, in which MI ratios of *120% in $Co_{70.2}Fe_{7.8}B_{22}$ multi-layers over a useable frequency range of 50MHz* were presented. The results of this crossed anisotropy study were published in [1], and the full range of results are presented in Chapters 5 and 6.

With these results it was possible to tailor the response and produce samples for specific applications, which in turn could be used as *sensitive magnetic transducers* in electronic sensor circuits. A simple possible replacement Magneto Impedance thin-film

element for magneto resistive technologies was demonstrated, as a *read head in longitudinal recording medium* in [2]. For this purpose, the newly published crossed anisotropy multi-layers results played an important role in achieving high sensitivity with respect to transverse external magnetic fields typical in longitudinal recording medium.

An extensive study in magnetic sensor technology was undertaken to understand all of the available effects and specialised electronic techniques required to produce and measure them. Furthermore, a critical review of the current Magneto Impedance sensor pulse excitation technology was carried out including manufacturing and experimental measurements of published electronic circuits. This review is fully illustrated in Chapter 7. From these reviews, the theoretical operation of oscillators and sinusoidal demodulators and detectors and their sources of noise were undertaken to further improve knowledge in these areas.

In the final Chapter 8, two different sensor designs are presented, with the second significantly improving on the performance of the first. The first sensor, which the results were presented in [3] concentrates on utilizing two asymmetrical Magneto Impedance (AMI) sensor elements combined differentially. The sensor is driven by a sinusoidal current of 90 MHz biased with a DC current. For AMI film element of 5mm long, 40μm wide and having anisotropy angle of 45° the field detection resolution is in the magnitude of *1μ Oe for both AC and DC for fields of ~ 2Oe magnitude. The maximum response speed is in the order of 1MHz.* These published results in themselves are equal in performance to the best previously published Magneto Impedance Sensors.

After completion of the initial sensor, a shift in the use of Magneto Impedance to the measurement of low frequency fields was identified, primarily due to published results on magneto impedance sensors reaching resolutions and magnitude detection of large bio-medical signals at higher frequencies. Firstly, extensive research was undertaken to improve the phase noise of the oscillator and sensitivity of the detection mechanism using *novel RF techniques* to improve the sensitivity at high frequencies, and secondly a method to improve the low frequency sensitivity by *AC biasing the MI element* with a magnetic field.

By taking the active 1/f noise reduction technique and applying it to normal portable commercial oscillator the phase noise was reduced to that of more expensive laboratory units. Using the concept of the active isolator and developing it to operate at higher frequencies, approaching that of traditional microwave circulators, a new method of carrier suppression

231

was utilised, which has scope for operation in many applications beyond areas of this work. By matching the MI element to 50Ω, the change of impedance could still be measured and utilised but now the element could easily and effectively be interconnected to standard RF equipment and measuring systems. By up converting a lower frequency field with a know modulating signal of a higher frequency it was possible to use lock in amplification techniques and other traditional signal processing techniques to improve the measurement performance external to the sensor itself. The combination of all these techniques in one sensor provided a leap forward that yielded several orders of magnitude improvement in sensitivity compared to previously published MI based sensor measurements.

A thin-film MI sensor was produced based on the measurement of the modulation of the incident reflected power due to an external AC magnetic field. *Direct field measurement performance at 1kHz produced a resolution of 3.73 x 10^{-7} Oe, AC biased performance at 5kHz of a 20Hz field is a resolution of 5.27 x 10^{-6} Oe, and at 10Hz of 9.33 x 10^{-6} Oe.* The achieved low frequency magnetic field resolution is at least *one order of magnitude* higher than that reported for MI pulse-circuit elements.

Theoretical analysis of the noise in the system shows that direct improvement in performance could be produced provided that the phase noise of the oscillator at lower frequencies is suppressed and the measurements are taken in a magnetically screened room. The first stage of further work would be to design a system utilising laboratory based equipment for all stages of the sensor. At that stage it is considered to be a measurement system rather than a sensor unit. With continued improvement of the electronic components utilized in this novel method of Magneto Impedance sensor presented in this work, the possibility of measuring bio magnetic signals of the human body at room temperature becomes a distinct reality, beginning with detection of large particles in the human body before moving on to the large field components of the human heart. Further work is required in parallel on the thin film elements themselves, the present work needs to be extended to include new materials, dimensions and manufacturing techniques. Depending on application and the type of field to be measured, the thin film requires tailoring to that application, for instance the construction of arrays of sensors for mapping the vector rather than scalar magnitude of field. Development of a commercial MI based sensor a specialised industrial application would be the best continuation of this current work.

List of related publications

[1]   P. Delooze, L. V. Panina, D. J. Mapps, K. Ueno, and H. Sano, *"CoFeB-Cu layered film with crossed anisotropy for asymmetrical magneto impedance"* IEEE Trans. Magn. vol. 39, pp. 3307–3309, Sept. 2003.

[2]   P. Delooze, L. V. Panina, D. J. Mapps, K. Ueno, and H. Sano, *"Effect of transverse magnetic field on thin-film magneto impedance and application to magnetic recording"*, Elsevier Science, 2003.

[3]   P. Delooze, L. V. Panina, D. J. Mapps, K. Ueno, and H. Sano, *"Sub-nano tesla resolution differential magnetic field sensor utilizing asymmetrical magnetoimpedance in multilayer films"* IEEE Trans. Magn. vol. 40, pp. 2664–2666, July. 2004.

[4]   P. Delooze, L. V. Panina, D. J. Mapps ,*"AC biased sub-nano-tesla magnetic field sensor for low-frequency applications utilizing magneto impedance in multilayer films"* IEEE Trans. Magn. vol. 41, pp. 3652 - 3654, 2005.

Appendix A

CoFeB–Cu Layered Film With Crossed Anisotropy for Asymmetrical Magnetoimpedance

Paul Delooze, Larissa V. Panina, Desmond J. Mapps, Kasuhiko Ueno, and Hiroyuki Sano

Abstract—This paper reports experimental results on sensitive (up to 25%/Oe) asymmetric magnetoimpedance (AMI) in magnetic/metallic multilayers with crossed anisotropy, excited by a sinusoidal current (1–100 MHz) biased with a dc current. The film structure having two outer magnetic layers $Co_{70.2}Fe_{7.8}B_{22}$ and Cu inner lead is made on a glass substrate using dc sputtering. Each layer thickness is 0.5 μm. The magnetic anisotropy in the upper film is crossed with respect to that in the lower one, which is achieved by current annealing in a longitudinal magnetic field. The AMI characteristics are found by measuring the S_{11} microwave parameter using a HP8753 spectrum analyzer. The asymmetric behavior of the impedance is more pronounced at relatively low frequencies of about a few megahertz where the impedance-field characteristics are caused by domain-wall dynamics. The obtained results present a very good compromise on size, sensitivity, and linearity.

Index Terms—Asymmetry, crossed anisotropy, multilayers, magnetoimpedance.

I. INTRODUCTION

THE RECENT increasing interest in magnetoimpedance (MI) in thin films is justified by sensor technology needs such as miniaturization, and compatibility with integrated circuit technology. The MI effect is based on the property of the high-frequency complex impedance changing enormously under the application of a dc (or lower frequency) magnetic field. [1] The impedance change ratio per Oersted in amorphous microwires is in the range of 10–100%/Oe at megahertz frequencies [2], [3]. This sensitivity is at least one order of magnitude higher than that of giant magnetoresistive (MR) materials. However, the MI wires have much greater dimensions: 10–50 μm in diameter and a few millimeters long. When decreasing the sensor element size, the maintenance of such high sensitivity becomes a problem. Special thin-film structures are employed to improve the MI performance in miniature elements (thickness <1 μm, in-plane size <200 μm, and length <5000 μm). [4] In principle, they consist of two outer magnetic layers and an inner highly conductive lead. The MI ratio in these systems has been proven to be much greater compared with that in a similar ferromagnetic single layer. For example, in CoFeSiB–Cu–CoFeSiB multilayers of several mi-
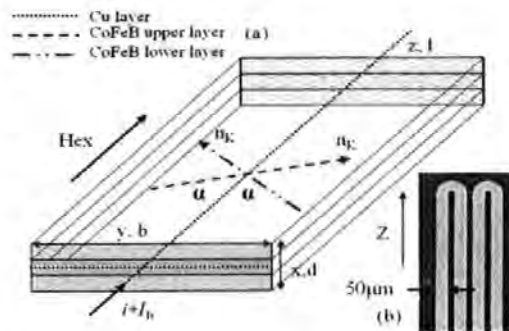
crometers thick, the impedance change ratio is more than 300% for a frequency of 10 MHz and a dc magnetic field of about 10 Oe. [5] Furthermore, special types of magnetic anisotropy can be realized in layered systems to improve sensitivity and linearity. The theoretical analysis predicts that cross-anisotropy films (magnetic anisotropy in the upper film is crossed with respect to that in the lower one) exhibit asymmetric MI (AMI) characteristics. [6], [7] The concept of AMI was confirmed for two-layer magnetic films [8]. This paper reports experimental results on sensitive AMI in three-layer films having two outer CoFeB magnetic layers with crossed anisotropy and Cu inner lead, excited by a sinusoidal current biased with a dc current. It is demonstrated that AMI can be used to obtain a near-linear voltage response with enhanced sensitivity, which is of a particular interest for magnetic sensor applications.

II. THEORY

In magnetic/metallic multilayers [see Fig. 1(a)], the large change in impedance occurs at frequencies, when the skin effect is not essential. The resistivity of amorphous CoFeB alloy is about 50 times larger than that of Cu, therefore, the resistance of the multilayer structure is mainly determined by the inner lead resistance R_m. Then, the inductive term of the impedance which comes largely from the flux change in the magnetic layers can become dominant at relatively low frequencies. The expression for the impedance can be written in the form

$$Z = R_m - j\omega\Phi/cI \tag{1}$$

where $i = i_0 \exp(-j\omega t)$ is the ac current flowing along the inner lead (z direction), ω is the frequency, and Φ is the total transverse (in-plane y direction) magnetic flux generated by the current i in the magnetic layers. The magnetic flux Φ is defined

Fig. 1. (a) Film structure and principle quantities and directions. (b) Sample in-plane view.
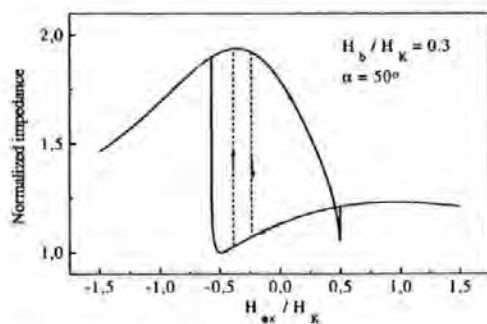
Fig. 2. Theoretical impedance plots (normalized to the saturation value) for $\alpha = 50\,^\circ$ in single-domain films. The dashed lines show the generalization for equilibrium magnetization flip due to domain processes.

Fig. 3. Hysteresis loops versus H_{ex} with the bias current I_b as a parameter.

via an average transverse permeability μ_t. Then, the expression for the impedance reads [4]

$$Z = R_m \left(1 - 2j\mu_t \frac{d_1 d_2}{\delta_1^2} \right) \qquad (2)$$

where d_1 and d_2 are the thickness of the inner lead and magnetic layers, respectively, and δ_1 is the skin depth in the inner lead. Expression (2) shows that depending on the value of μ_t, the MI ratio in the sandwich film can be very large even at relatively low frequencies when $\delta \gg d_1, d_2$.

The impedance field behavior is determined by the field dependence of the ac transverse permeability μ_t, which depends on the equilibrium magnetization M_0. We consider a case when the anisotropy axes in the ferromagnetic layers are directed at an angle $\pm \alpha$ to the z direction, respectively for the upper and lower magnetic layers, as shown in Fig. 1(a). In this system, the magnetization process for M_0 as a function of the longitudinal field ($H_{ex} \parallel z$) exhibits asymmetry in the presence of dc bias current I_b, which induces a circulatory field $H_b(x > 0) = -H_b(x < 0)$ [6], [7]. Then, the permeability parameter and impedance also change differently for positive and negative H_{ex}, as shown in Fig. 2, where the theoretical impedance plots are given for single-domain layers (considering rotational magnetization processes only) for $\alpha = 50\,^\circ$, $H_b/H_K = 0.3$, H_K is the anisotropy field. This behavior can be generalized for the case of the magnetic layers with domain structure considering that M_0 reverses at lower H_{ex} due to the domain-wall motion, as shown by dashed lines.

In this work, AMI was investigated in multilayered films having two outer magnetic layers with composition $Co_{70.2}Fe_{7.8}B_{22}$ and a Cu inner lead made on glass substrates using dc sputtering. The sputter rates are 17 nm/min and 50 nm/min, background pressure and Ar gas pressure are 3×10^{-5} Pa and 0.1 Pa, respectively. During the deposition process, the temperature of the substrate is 35 °C, and a constant magnetic field of 200 Oe is applied in the transverse direction to the MI element in order to add uniaxial anisotropy. Finally, a crossed anisotropy can be induced in the sample by current annealing in a longitudinal field at a temperature of 215 °C. The value of the applied current and field can be varied to produce different angles of crossed anisotropy in the sample, in this case, 30 mA and 11.8 Oe, respectively. The sample in-plane view and magnetic configuration is shown in Fig. 1.
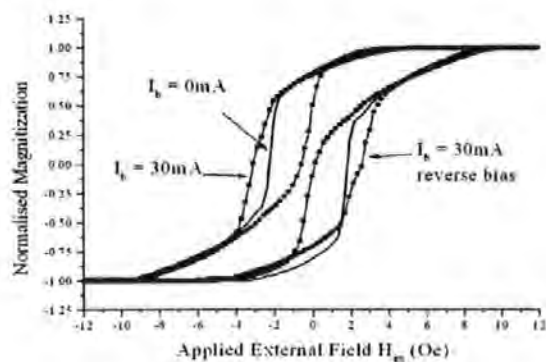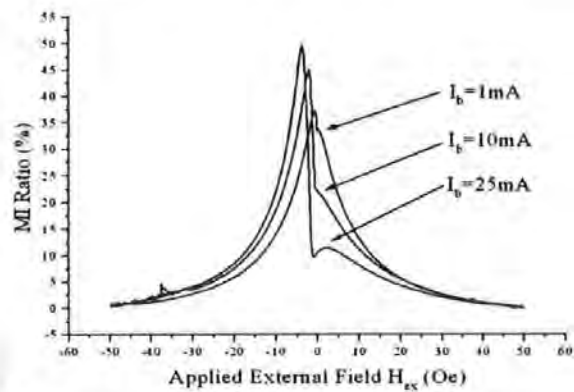

Fig. 4. MI ratio versus H_{ex} with I_b as a parameter at a frequency of 10 MHz.

The anisotropy axis in the upper and bottom layers [designated as n_K in Fig. 1(a)] are at approximately 67° to the length direction (z axis), which was estimated from dc hysteresis loops in the presence of a bias current I_b as shown in Fig. 3. The hysteresis of the sample was measured by using a pickup coil wound around the glass substrate of the sample (50 turns, 3-mm diameter), and an identical compensation coil wrapped around a plain glass substrate connected to a differential amplifier. The effect of the application of I_b is to cause a shift in the loop toward negative fields (or positive, depending on the applied direction of I_b) and decrease the overall hysteresis area. The anisotropy angle is found from the shifting field, which is given by $H_b \tan \alpha = I_b \tan \alpha / 2b$ (b is the film width).

III. MEASUREMENT AND RESULTS

In order to characterize the MI effect in the multilayer thin films, a measurement system was designed which is based on Hewlett Packard HP8753 network analyzer. The network analyzer determines the way the sample under test modifies the signal flowing through it by using S-parameters (scattering parameters).

The measurements were made for frequencies of 1 to 100 MHz, with an applied bias current I_b of 0 to 100 mA and an external field H_{ex} of ± 50 Oe. The film impedance is found via measuring the S_{11} parameter (input reflection) and converting it to an equivalent parallel impedance.
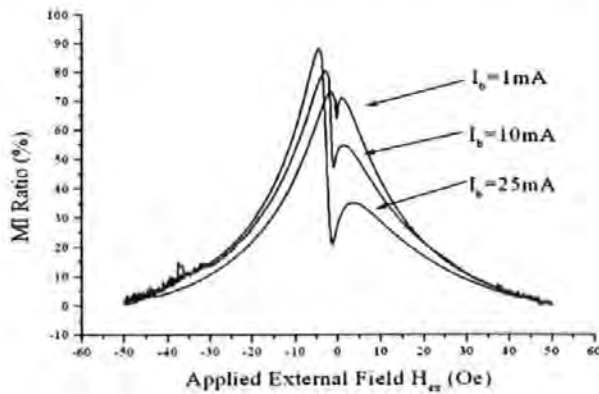
Fig. 5. MI ratio versus H_{ex} with I_b as a parameter at a frequency of of 30 MHz.

Fig. 6. Differential response produced from the combination of two identical samples biased in opposite directions.

Fig. 4 shows how applying I_b to the sample modifies the asymmetrical response for frequencies of a few megahertz. Here, we introduce the MI ratio, defined as MI = 100% $(|Z| - |Z_{sat}|)/|Z_{sat}|$, where Z_{sat} is the impedance measured at the maximal value of H_{ex}.

When no bias current is applied, the response produces a single peak which is situated at the 0-Oe field point. The value of impedance rolls off until the saturation value is reached (16 Ω). As I_b is increased, the peak position is shifted to negative fields, whereas the change of impedance is suppressed for positive fields. This is consistent with the results of the dc loop measurements and with the theoretical plot shown in Fig. 2 (with dashed lines). Surprisingly, no hysteresis is seen in the experiment. For $I_b = 25$ mA, the maximum MI ratio of 50% occurs at a field strength of -3.7 Oe with a sensitivity of 25%/Oe between -1.7 and -2.7 Oe.

As the frequency of excitation is increased to around 30MHz, the following MI characteristics are produced in the sample, as shown by Fig. 5. The response still displays asymmetry, but the second peak is now present for positive fields. Additionally, the maximum MI ratio has increased to nearly 90%.

This change in the characteristic response can be attributed to increasing contribution of rotational effects to the ac permeability μ_t.

IV. SENSOR

AMI can be used to obtain a linear characteristic. For this purpose, it is required to combine the responses of two samples, each biased in opposite directions. It is essential that the 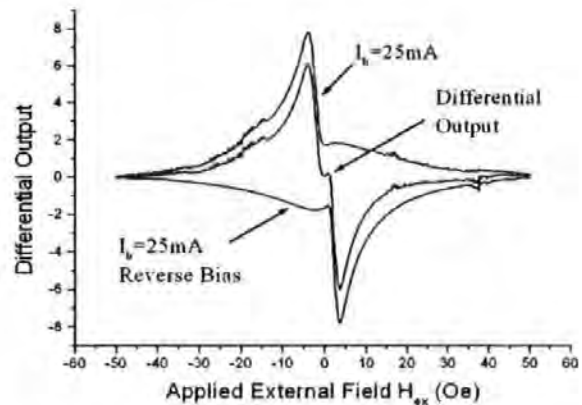response in one field direction remains as suppressed as possible. Additionally the transition point should begin at the 0-Oe point in both samples to produce a continuous response. This could be practically realized as the angle of anisotropy α field can be varied during manufacture in order to control the position of the peak. Using the 10-MHz 25-mA response for both samples, the sensing element response in Fig. 6 can be produced. This response would allow high-resolution field measurements to be made in the range of ± 3.7 Oe, with only a small reduction in the maximum MI ratio and loss of sensitivity around the 0 field point.

REFERENCES

[1] L. V. Panina, K. Mohri, K. Bushida, and M. Noda, "Giant magnetoimpedance and magnetoinductive effects in amorphous alloys," *J. Appl. Phys.*, vol. 76, pp. 6198–6203, 1994.
[2] M. Vazquez and A. Hernando, "A soft magnetic wire for sensor applications," *J. Phys. D: Appl. Phys.*, vol. 29, pp. 939–949, 1996.
[3] D. P. Makhnovskiy, L. V. Panina, and D. J. Mapps, "Field-dependent surface impedance tensor in amorphous wires with two types of magnetic anisotropy: Helical and circumferential," *Phys. Rev. B*, vol. 63, pp. 144 424–40, 2001.
[4] L. V. Panina and K. Mohri, "Magnetoimpedance in multilayer films," *Sensors Actuators A*, vol. 81, pp. 71–77, 2000.
[5] T. Morikawa, Y. Nishibe, and H. Yamadera, "Giant magnetoimpedance effect in layered thin films," *IEEE Trans. Magn.*, vol. 33, pp. 4367–4369, Dec. 1997.
[6] L. V. Panina, D. P. Makhnovskiy, and K. Mohri, "Analysis of magnetoimpedance in multilayers with crossed anisotropy," *J. Mag. Soc. Jpn.*, vol. 23, pp. 925–930, 1999.
[7] D. P. Makhnovskiy, L. V. Panina, A. N. Lagar'kov, and K. Mohri, "Effect of antisymmetric bias field on magnetoimpedance in multilayers with crossed anisotropy," *Sensors Actuators A*, vol. 81, pp. 91–93, 2000.
[8] K. Ueno, H. Hiramoto, K. Mohri, T. Uchiyama, and L. V. Panina, "Sensitive asymmetrical MI effect in crossed anisotropy sputtered films," *IEEE Trans. Magn.*, vol. 36, pp. 3448–3450, Dec. 2000.

Effect of transverse magnetic field on thin-film magneto impedance and application to magnetic recording

P. Delooze[a], L.V. Panina[a,*], D.J. Mapps[a], K. Ueno[b] and H. Sano[b]

[a]Department of Communication and Electronic Engineering, University of Plymouth, Drakes Circus, Plymouth, Devon, PL4 8AA, United Kingdom.

[b]Stanley Elect Co R&D, Yokohama, Kanagawa 225, Japan.

Abstract. A potential of using the magnetoimpedance thin-film element as a read head in longitudinal recording medium is demonstrated. For this purpose, cross-anisotropy in magnetic layers plays an important role to achieving high sensitivity with respect to transverse external magnetic fields typical in longitudinal recording medium. A sputtered CoFeB/Cu/CoFeB film of 1.5 $\propto$m thick exhibits a sensitivity of about 10%/Oe for transverse fields in the frequency range of 30-40MHz.

Recent progress in thin-film magnetoimpedance (MI) has raised a question of the application of this effect as sensing technology to magnetic recording. Normally, the MI structures show the greatest sensitivity for magnetic fields applied in parallel with high frequency current [1-3]. This is in the direction orthogonal to that from the recording medium [4]. Therefore, the major step is to investigate how high frequency impedance of thin film materials changes in orthogonal fields. This paper considers the effect of a transverse magnetic field H_t (with respect to the high frequency current) on the impedance of three-layer film having two outer CoFeB layers and an inner Cu lead. Each layer thickness is 0.5 microns and the film width is 50 microns. In the case of a transverse anisotropy in magnetic layers, the MI behavior in a longitudinal field $H_\parallel$ shows two maximums situated at $\pm H_K$, where H_K is the anisotropy field. The application of a transverse field H_t originated from a dc current flowing along with the high frequency one does not change the appearance of the MI characteristics suppressing the sensitivity to $H_\parallel$. As a result the impedance as a function of H_t changes little when $H_\parallel$ is small, showing major variations around $H_\parallel \approx H_K$, as shown in Figure 1(a). The situation is quite different for a cross anisotropy film in which the anisotropy in the upper film is crossed with respect to that in the lower film [5,6]. When no H_t is applied, the impedance vs. $H_\parallel$ shows a single peak which is situated at the 0 field point. As H_t is increased the peak position is shifted to negative fields, whereas the change of impedance is suppressed for positive fields. In this case the effect of the transverse magnetic field on impedance is the greatest at $H_\parallel = 0$, illustrated by Fig. 1(b).

In order to use the MI element as a read head in longitudinal magnetic storage media, the sample must be oriented as shown by Fig. 2 (a). The z-axis, in which the high frequency current flows, lies perpendicular to the magnetic domains of the track. The film length l in this direction would be limited by the track width. The film thickness d (along the x-axis) is parallel to the magnetic domains. Its dimensions would be limited by the size of the magnetic domains. On the other hand, the MI ratio decreases with decreasing d being only about 15% for $d = 0.1$ $\propto$m. The y-axis, which is along the width b of the MI element, extends from the surface of the track. For given l

and d, the value of b is limited by the demagnetising effect and ac flux leakage [3]. Practical head design is beyond the scope of this paper.
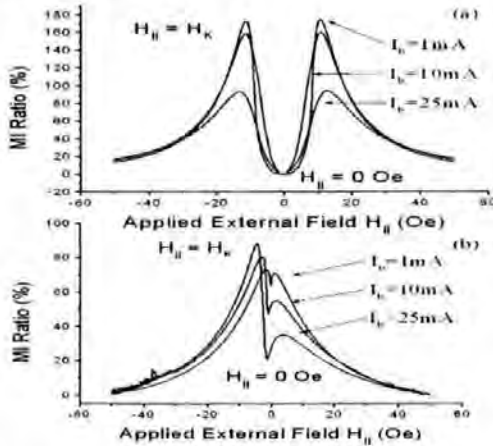

Fig. 1. MI plots vs. $H_\parallel$ at 30MHz with I_b as a parameter, (a) transverse anisotropy, (b) crossed anisotropy.

The MI head would be biased by a constant DC current, shown as I_b in Fig. 2, in order to set an operating point with the highest gradient of $H_\parallel = 0$. When the head is over a magnetic domain, an intermediate value of the operating point impedance would be measured. This is because no magnetic fields emanate from the interior of the magnetised domain itself. As the MI head passes over the domain walls that exist between oppositely magnetised domains, the field H_t produced by uncompensated magnetic poles is equivalent to an additional current I_t in the MI element.

Depending on the direction of the transverse field, this will add or subtract from the operating point current, causing an increase or decrease of the impedance. This would be measured in a synchronous system and converted to the corresponding information bit, shown by Fig. 2 (b). This system of operation is very similar to that for the current magnetoresistive read heads [4].
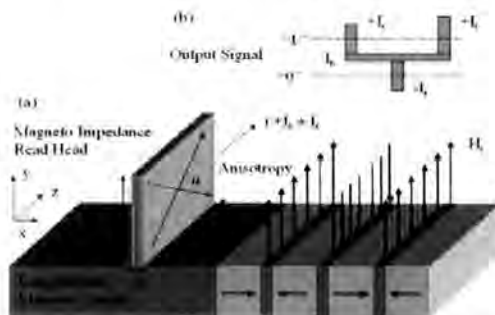

Fig. 2. (a) Geometry of the MI element for read head in longitudinal magnetic media. (b) Output signal variation due to the effect of H_t.
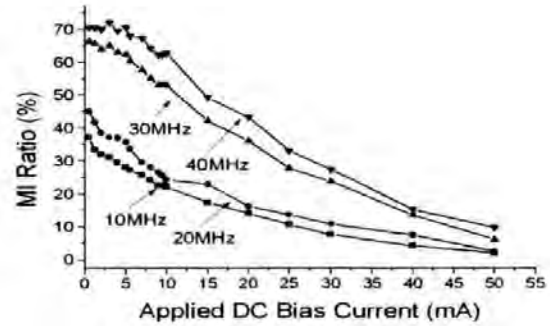

Fig. 3. MI ratio vs. I_b at $H_\parallel = 0$ with frequency of the driving current as a parameter.

In order to characterize the effect of H_t in the multilayer thin film, a measurement system was designed which is based on Hewlett Packard HP8753E network analyzer. The network analyzer determines the way the sample under test modifies the signal flowing through it by using S-parameters (forward transmision parameters). The measurements were made for frequencies of 1 to 100MHz, with an applied bias current, I_b of 0.5 to 50mA and an external field $H_\parallel$ of $\pm$ 50 Oe, to obtain the impedance saturation value Z_{sat} (the impedance measured at the maximal value of $H_\parallel$). Here we introduce the MI ratio, which is defined as $MI = 100\%(|Z| - |Z_{sat}|)/|Z_{sat}|$. This is required as the saturation impedance changes with frequency preventing a direct comparison between the values. As frequency is increased, the value of the initial MI ratio also increases, and conversely as the bias current is increased the MI ratio drops, which reduces the impedance, as shown in fig. 3. For a high frequency current in the range of 30-40 MHz the MI ratio falls by 35% after the current is increased to 25mA and by 60% when it is increased further to 50mA. By setting the operating point to 25mA an orthogonal field of $\pm$3Oe ($H_t = I_t/2b$) produced by the media would cause a $\pm$30% change in impedance in the sample.

We conclude that crossed anisotropy multilayered films may have potential for magnetic recording applications in the form of a sensitive read head. All samples used in this paper were kindly provided by Stanley Elect Co R&D.

References
[1] T. Morikawa, Y. Nishibe et al, *IEEE Trans. Magn.* 32, (1996) 4965.
[2] K. Hika, L. V. Panina and K. Mohri, IEEE Trans. Magn, 32, (1996) 4594.
[3] L. V. Panina and K. Mohri, *Sensors and Actuators* A, 81, (2000) 71-76.
[4] C.H. Tsang, et al. *IBM Journal of Research and Dev.* 42, (1998) 103-117.
[5] D. P. Makhnovskiy, L. V. Panina, and K. Mohri , *J Mag Soc Jpn*, 23, (1999) 925-930.
[6] P. Delooze, et al, IEEE Trans Magn, 2003 (in print)

Sub-Nano Tesla Resolution Differential Magnetic Field Sensor Utilizing Asymmetrical Magnetoimpedance in Multilayer Films

Paul Delooze, Larissa V. Panina, Desmond J. Mapps, Kasuhiko Ueno, and Hiroyuki Sano

Abstract—Asymmetrical magnetoimpedance (AMI) in multilayer thin films with cross anisotropy has been used for the development of a low noise, sensitive and quick response miniature magnetic sensor. The sensor is driven by a sinusoidal current of 90 MHz biased with a dc current. For an AMI film element of dimensions 5-mm long, 40-μm wide, and having an anisotropy angle of 45°, the field detection resolution is in the order of 1-μ Oe for both ac and dc fields of magnitude 1 Oe. The maximum response speed is in the order of 1 MHz.

Index Terms—Crossed anisotropy, differential sensor, magnetoimpedance, multilayers.

I. INTRODUCTION

SENSITIVE and quick response magnetic sensors are required for many industrial applications needing a field detection resolution down to 10^{-6} Oe (sub-nano Tesla range). A series of magnetoimpedance (MI) sensors utilizing pulse excitation of amorphous wires has been developed to achieve this target [1]. However, the MI wire element has limitations in miniaturization, mass productivity and compatibility with integration technology. Thin-film technology is needed to avoid these limitations. Recent results on MI in magnetic/metallic multilayers with cross anisotropy have demonstrated very high field sensitivity of the impedance change of more than 30%–50%/Oe, which is in the range of that in wires [2], [3]. Furthermore, by applying a dc bias current, asymmetrical MI (AMI) can be realized which is very useful for obtaining a linear sensor. In the present paper, we have developed a thin-film AMI sensor with estimated field resolution detection of 10^{-6} Oe. Additionally the AMI in films with different anisotropy angles and sensor performance are discussed as well.

II. CROSSED ANISOTROPY SAMPLES

For optimal sensor design, AMI was investigated in multilayered films consisting of two outer magnetic layers with compo-
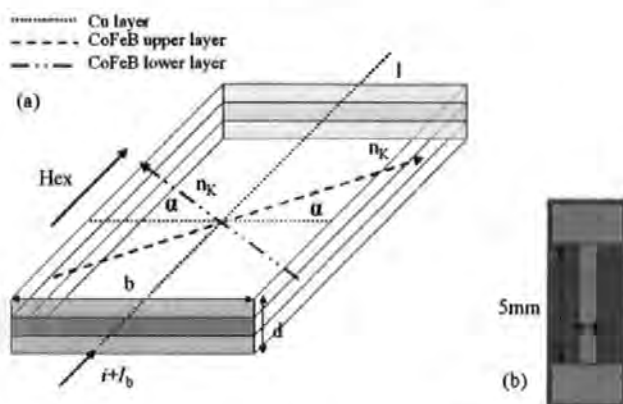
Fig. 1. (a) Film structure and principle quantities and directions. (b) Sample in-plane view.

sition $Co_{70.2}Fe_{7.8}B_{22}$ and a Cu inner lead made on glass substrates (see Fig. 1). Each layer is 0.5 μm thick and 5 mm long, produced by using a dc sputtering technique. During the deposition process, the temperature of the substrate is 35 °C, and a constant magnetic field of 200 Oe is applied in the transverse direction to the MI element in order to add uniaxial anisotropy. Finally, a crossed anisotropy can be induced in the sample by current annealing in a longitudinal field at a temperature of 215°C. The value of the applied current and field can be varied to produce different angles α, of crossed anisotropy in the sample (with respect to transverse direction as shown in Fig. 1). Three variations of magnetic anisotropy, $\alpha = 15°$, $\alpha = 30°$, and $\alpha = 45°$, and three variations of film width $b = 40$ μm, $b = 60$ μm, and $b = 110$ μm were manufactured. The samples were characterized by utilizing a measurement system based on a Hewlett Packard HP8753E network analyzer. The measurements were made for frequencies of 1–100 MHz, with an applied bias current, I_b of 0 and 25 mA and an external field H_{ex} of ± 50 Oe varied over 10 000 steps giving a 0.01 Oe resolution. The film impedance is found via measuring the S_{11} parameter (input reflection) and converting it to equivalent parallel impedance [4].

The impedance field behavior of the sample is determined by the field dependence of the ac transverse permeability μ_t, which in turn depends on the equilibrium magnetization M_0. With crossed anisotropy and an additional transverse field H_b induced from the presence of the dc bias current I_b, the mag-

netization process for M_0 as a function of the longitudinal field ($H_{ex} \parallel 1$) as shown in Fig. 1, exhibits asymmetry [5]. Therefore, the permeability parameter and impedance also changes differently for positive and negative H_{ex}.

When no bias current I_b is applied to the sample, the impedance versus H_{ex} shows a shallow symmetrical response with only a small change of impedance. Applying I_b of 25 mA produces a highly sensitive MI response in one field direction and a flat response in the opposite direction.

Then, by combining the two samples response's measured data obtained for opposed directions of I_b, using a computer a simulation of a near linear MI characteristic can be obtained for certain anisotropy angles, as shown in Fig. 2. The best linearity and sensitivity (45% per 1 Oe) is achieved for $\alpha = 45°$, $b = 40 \mu m$ and a frequency of 90 MHz. This makes this sample suitable for field sensing applications with maximum magnitude of ± 1 Oe. However, without a suitable form of longitudinal magnetic bias, the fundamental AMI characteristic is insensitive to small magnitude fields (>1-m Oe). It should be noticed that as the width b is decreased from 110 to 40 μm, the MI ratio is observed to increase for all the samples. This very important result for sensor miniaturization is probably related to a better established anisotropy due to the shape effect.

III. SENSOR DESIGN AND MEASUREMENT TECHNIQUES

The proposed sensor design is based on a sinusoidal current excitation biased with a dc current. This is different from currently developed MI sensor circuits utilizing a CMOS-IC to produce a sharp pulse excitation. This pulse excitation method which combines low and high frequency harmonics (in effect, ac and dc excitation) seems to be a very effective method: cheap, simple, low power consuming, making it suitable for portable designs. This sensor circuit with amorphous wires as MI elements has a field resolution of 10^{-6} Oe, but only for ac field detection. Further improvements in field resolution are questionable. The problems with these sensor circuits are related to utilizing a large number of harmonics and rather unstable low frequency bias, temperature deviations and digital ringing which all produce additional noise in the circuit limiting its resolution. Sinusoidal excitation based on voltage controlled oscillators (VCOs) or temperature compensated crystal oscillators (TCXOs) have temperature compensation leading to highly stable, single harmonic signal sources. They are very low noise, in the order of $10 nV/\sqrt{Hz}$, but they are costly and require higher power consumption. To produce the AMI response in the sample it must be dc biased with a constant current, which must remain stable as the impedance of the sample varies with external field. With pulse excitation this is generated with low frequency harmonics (equivalent to the rms value of the pulse train), which is difficult to control. With a separate dc supply based on a feedback constant current source, this bias current can be precisely set, increasing the sensors resolution. Again this introduces an additional cost and increased power consumption. With sinusoidal excitation, specialized Power and RF magnitude/phase detectors can be used to measure the effect of the change of impedance in the sample to a high resolution with low noise. The current technique with pulse excitation is to use synchronous
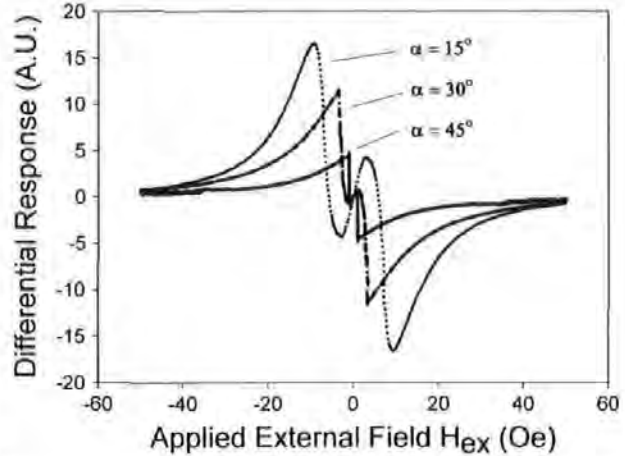

Fig. 2. Differential responses obtained by combining two MI plots with opposite dc bias current for different anisotropy angles, α. The excitation frequency is 90 MHz, $b = 40 \mu m$ and $I_b = 25$ mA.

rectification and a peak hold circuit. This method experiences nonlinearity's due to switch timing and the time constant of hold circuit. It is necessary to use a differential based sensor as the AMI samples only experience a useful change of impedance in one field direction. The outputs of the two samples are subtracted from one another to produce a response that is sensitive in both field directions on a single axis. Additionally any noise that is common (and in phase) to both samples will be cancelled out during the differential process, enabling the detection of fields to a higher resolution.

IV. SENSOR IMPLEMENTATION

The sinusoidal based differential sensor design consists of the following main stages, as shown in the block diagram in Fig. 3. All signal measurements were performed by the use of a HP4195A spectrum analyzer set to 100-kHz bandwidth with 10-dB input signal attenuation. (A) A VCO, this was configured to give an excitation voltage with a frequency of 90 MHz and amplitude of 1.45 mV; the noise at the fundamental was measured as 40 $nV/\sqrt{Hz}$. The differential signals were combined in a pair of amplifiers, (B), to provide the actual sinusoidal waveform. The amplitude of the waveform is 2.1 mV and noise at the fundamental is 25 $nV/\sqrt{Hz}$ after the differential stages. This provided a pair of accurate excitation signals for the AMI samples. In order to decrease the effect of the harmonics of the signal, it is passed through a pair of passive network low pass filters (C) with a -3-dB point of 100 MHz. The signal is then further amplified in a pair of RF power amplifiers (D). The sinusoidal signal is increased in amplitude to 25 mV (No load), with a noise of 3 $\mu V/\sqrt{Hz}$. This isolated buffer method of sinusoidal excitation experiences none of the problems of using the AMI sample as part of a Colpitts Oscillator or other multivibrator circuits [5].

The measuring cell (H) consists of two identical AMI elements, which are connected in parallel to ground. Each sample is driven by a separate sinusoidal output from the RF amplifiers and a dc bias current source. The AMI elements are biased oppositely to one another, making one sample sensitive to positive
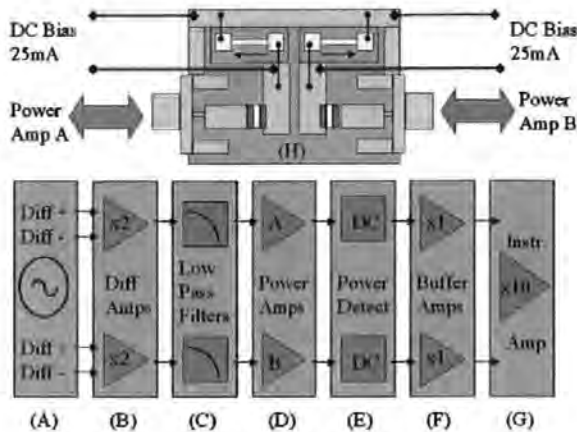
Fig. 3. Block diagram of a sinusoidal based differential sensor and sample measuring cell.

Fig. 4. Output of the instrumentation amplifier for a $\alpha = 45°$, $b = 40\ \mu m$ sample with $I_b = 25$ mA and an excitation frequency of 90 MHz.

fields and the other sensitive to negative fields. When the samples are placed inside an ac longitudinal sense field of ± 20 Oe at 120 Hz, the change of impedance of the sample causes a modulation of the amplitude of the applied excitation signal.

The small changes in impedance of the sample are measured by the power detector (E). The output is an offset dc level, based on the average amplitude of the signal, with a small variation which matches characteristic response of the sample measured on the HP8753E. The responses are then subtracted from one another in the instrumentation amplifier (G), by inverting the signal on the negative input and adding it to the signal on the positive input, noise common to both inputs is removed. The resulting waveform is then amplified by ten to produce an output level suitable for further signal processing.

V. RESULTS

Fig. 4 shows the output of the sensor's instrumentation amplifier for a pair of matched samples with an anisotropy angle, $\alpha = 45°$. This closely matches the previous computer simulation made from the HP8753E measurements as shown in Fig. 2. The differential response is near linear in the field interval ± 1 Oe with expected loss of sensitivity around the zero point. The output of the instrumentation amplifier was measured using the as ~ 600 mV/Oe for a gain of 10 with a noise magnitude of 1.226 $\mu V/\sqrt{Hz}$ (0.001 Hz component) and the noise floor of the sensor was of a similar magnitude. The resolution of the sensor can be defined by the signal-to-noise ratio (SNR). This shows how small an increment in output signal caused by an external field can be before it is indistinguishable from the background noise of the sensor. The SNR was calculated as, $SNR = 20 \log_{10}$ (voltage signal/voltage noise). For 100-kHz bandwidth, this gives $20 \log_{10}$ (600 mV/387.7 μV) = 63.8 dB. This corresponds to a maximum effective resolution of 1 μ
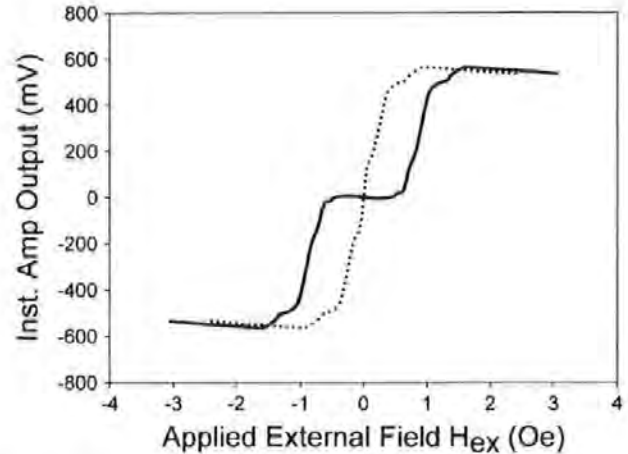
Oe for external ac and dc fields with a magnitude in the order of 1 Oe. With further development, the loss of sensitivity to small magnitude external fields could be corrected with the addition of a longitudinal magnetic bias applied to the substrate for each sample either produced by an additional magnetic layer [7]. This would allow the high resolution of the sensor to be utilized for sub-nano Tesla magnitude measurements, as shown on Fig. 4 by the dotted line.

In summary, we have developed a low-noise, highly sensitive sensor circuit based on AMI. The high field resolution in a miniature sensor is achieved due to the high sensitivity and linearity of the fundamental AMI characteristics for a certain anisotropy angle in combination with the low-noise sinusoidal excitation and precise dc biasing.

REFERENCES

[1] K. Mohri *et al.*, "Amorphous wire and CMOS IC-based sensitive micromagnetic sensors utilizing magnetoimpedance (MI) and stress-impedance (SI) effects," *IEEE Trans. Magn.*, vol. 38, pp. 3063–3068, Sept. 2002.

[2] L. V. Panina, D. P. Makhnovskiy, and K. Mohri, "Analysis of magnetoimpedance in multilayers with cross anisotropy," *J. Magn. Soc. Jap.*, vol. 23, pp. 925–930, 1999.

[3] K. Ueno, H. Hiramoto, K. Mohri, T. Uchiyama, and L. V. Panina, "Sensitive asymmetrical MI effect in crossed anisotropy sputtered films," *IEEE Trans. Magn.*, vol. 36, pp. 3448–3450, Sept. 2000.

[4] P. Delooze, L. V. Panina, D. J. Mapps, K. Ueno, and H. Sano. "CoFeB–Cu layered film with crossed anisotropy for asymmetrical magnetoimpedance," *IEEE Trans. Magn.*, vol. 39, pp. 3307–3309, Sept. 2003.

[5] L. V. Panina, D. P. Makhnovskiy, and K. Mohri, "Analysis of magnetoimpedance in multilayers with crossed anisotropy," *J. Mag. Soc. Jap.*, vol. 23, pp. 925–930, 1999.

[6] Y. Yoshida, T. Uchiyama, K. Mohri, and S. Ogha, "Quick response field sensor using 200 MHz amorphous MI element FET multivibrator resonance oscillator," *IEEE Trans. Magn.*, vol. 29, pp. 3177–3179, Nov. 1993.

[7] Y. Nishibe and N. Ohta, "Thin film magnetic field sensor utilizing magneto impedance effect," *R&D Rev. Toyota CRDL*, vol. 35, no. 4. 2000.12

AC Biased Sub-Nano Tesla Magnetic Field Sensor for Low-Frequency Applications Utilizing Magnetoimpedance in Multilayer Films

Paul Delooze, Larissa V. Panina, and Desmond J. Mapps

Department of Communications and Electronic Engineering, University of Plymouth, Drake Circus, Plymouth PL4 8AA, U.K.

A sensitive magnetic sensor based on the measurement of reflected incident power from magnetoimpedance (MI) multilayer-film element incorporated into 50 Ω matching network has been produced. The film system was fabricated by radio-frequency sputtering having two outer magnetic layers (NiFe), insulation layers (AlO$_3$), and inner conductor Au. For optimized layer parameters, an MI ratio of 135%, sensitivity 15%/Oe, and linearity within -2.5 and 5 Oe was obtained at a frequency of 434 MHz. An ac sense magnetic field applied to the MI element results in a small amplitude modulation signal due to the impedance variation, which can be measured on the carrier signal. For the sense field frequency of 1 kHz, the resolution of 3.73×10^{-7} Oe was achieved. To improve the field resolution at lower frequencies (<100 Hz), the use of an ac bias technique has been proposed. For a sense field of 20 and 10 Hz with 5 kHz ac bias, field resolutions of 4.78×10^{-6} Oe and 5.27×10^{-6} Oe, respectively, have been obtained.

Index Terms—AC bias, magnetoimpedance, multilayer, transverse anisotropy.

I. INTRODUCTION

SENSITIVE, high-frequency (ac) magnetic sensors are required for many industrial applications with the field detection magnitude and resolution down to 10^{-6} Oe (sub-nano Tesla range). A series of magnetoimpedance (MI) sensors utilizing pulse excitation of amorphous wires has been developed to achieve this target [1]. However, the MI wire element has its limitations in miniaturization, mass production, and compatibility with integrated technology. MI elements based on thin-film technology are needed to avoid these limitations. Results on MI in magnetic/metallic multilayers with cross anisotropy have demonstrated very high field sensitivity in the same range as an MI wire element [2]. Further studies have reported sensitivities in magnitude of 10 n Oe at frequencies greater than 1 kHz [3], [4]. This resolution of detection puts GMI sensors in the range of relatively large bio magnetic signals such as magnetocardiography (~0.1 μOe) which are normally measured by superconducting quantum interference devices (SQUIDs). Recent interest in MI has concentrated on the measurement of low-frequency magnetic fields (<10 Hz) while maintaining the required sensitivity. In this paper, we discuss a technique to enable MI for low-frequency field detection.

II. EXPERIMENTAL CONFIGURATION

A. Thin-Film Sensor Element

For optimal sensor design, MI was investigated in multilayered films with transverse anisotropy, having two outer magnetic layers with composition NiFe, an AlO$_3$ insulation layers and an Au inner made on glass substrate, with dimensions $l = 5$ mm, $d = 2.5$ μm, and $b = 200$ μm. The outer layers and the inner lead are of thickness 0.5 μm and the insulating layer is of 80 nm. Fig. 1 shows an illustration of the sensor element struc-
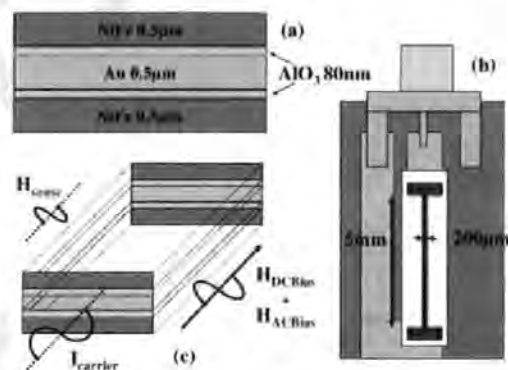

Fig. 1. (a) Sensor element structure, (b) top view, and (c) excitation and biasing quantities.

ture along with the excitation and biasing quantities. The element was manufactured using radio-frequency (RF) sputtering. During the deposition process the temperature of the substrate is 35 °C, and a constant magnetic field of 200 Oe is applied in the transverse direction to the MI element in order to establish a uniaxial transverse anisotropy. The element dimensions were selected based on model analysis of flux leakage across the inner conductive layer due to edge effects. The flux leakage produces an effective ac demagnetization factor that reduces permeability making the sample less sensitive to external fields as the width is reduced [5]. The insulating layers such as SiO$_2$ or AlO$_3$ between the conducting and magnetic layers typically help to improve the MI effect [6] causing the driving current to flow only in the inner layer which enhances the MI ratio. If NiFe and Au layers are sputtered on top of each other, the diffusion processes evens out the resistivity across the system and the current tends to be distributed more uniformly. The sample was characterized by utilizing a measurement system based on a Hewlett-Packard HP8753E network analyzer. The measurements were made for a frequency of 433.75 MHz, and an external longitudinal dc field of ±50 Oe varied over 10 000 steps
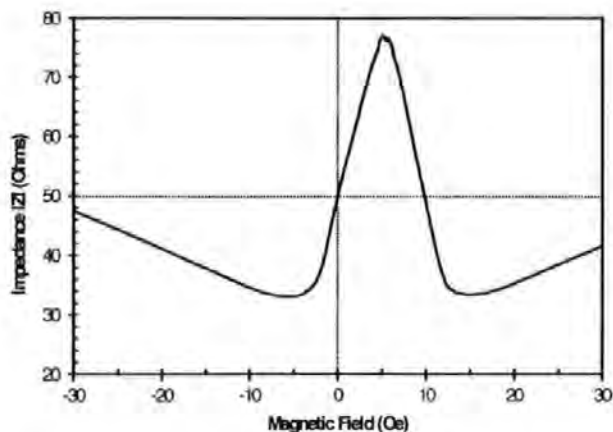
Fig. 2.   Impedance of the film-system, biased with 5 Oe and matched to 50 Ω.

Fig. 3.   Illustration of the input reflection measurement system.

giving a 0.01 Oe resolution. The film impedance is found via measuring the S_{11} parameter (input reflection) and converting it to equivalent parallel impedance. The sample was then dc biased using a permanent magnet (5 Oe) to the most linear portion on the characteristic curve, and the impedance was transformed to 50 Ω by the use of T-matching network at the bias point for utilization with the sensor design. Fig. 2 shows the measured impedance of the sensor element as a function of dc field centered at 50 Ohm. The impedance has an overall change of 135% with a sensitivity of 15%/Oe and a linear behavior in the field interval −2.5 Oe and 5 Oe. This characteristic itself is one of the best reported on MI in multilayers of similar dimensions.

B. Input Reflection Sensor

The sensor measurement system illustrated in Fig. 3 is designed as a single frequency network analyzer to measure the magnitude of the incident reflected power produced by a mismatch in complex impedance between the source and load. When impedance of the MI element matches the impedance of the source (50 Ω) the maximum amount of power is transferred to it. If the MI element is mismatched, some of the incident power is reflected back toward the source; this can be isolated, measured, and converted to a change in applied longitudinal ac field. The incident power or carrier is produced by a surface acoustic wave (SAW) filtered crystal oscillator designed for low power, portable applications with an output of 7 dbm, phase noise of −53 dBc at 10 Hz, −95 dBc at 100 Hz, −110 dBc at 1 kHz. The reflected power is separated from the incident power by means of a directional coupler based on an active op-amp design which provides a nonmagnetic coupling approach for lower noise. With no external field, the carrier is suppressed by 60 dB. An ac external field causes variation in the 50 Ω impedance of the sensor element, which is measured as an AM modulation on the suppressed carrier in the reflected incident power. This is then demodulated, filtered, amplified, and measured using a spectrum analyzer to find the signal-to-noise ratio (SNR) of the modulated power to noise floor. The magnitude and resolution of field detection at that modulation frequency can then be determined by converting the power in dBm to a root-mean-square (rms) voltage at 50 Ω. The ac modulation current is produced by a solenoid with two coils, calibrated to
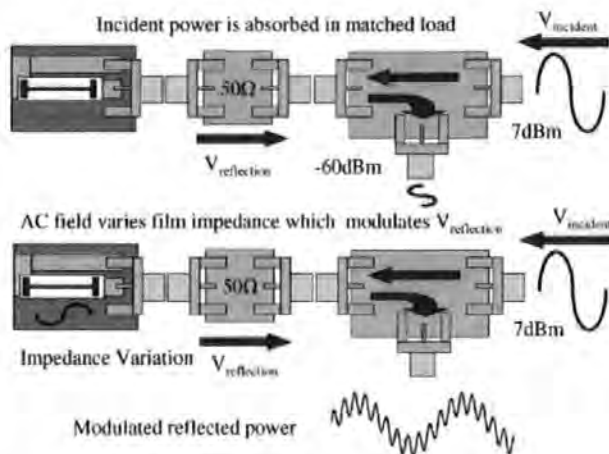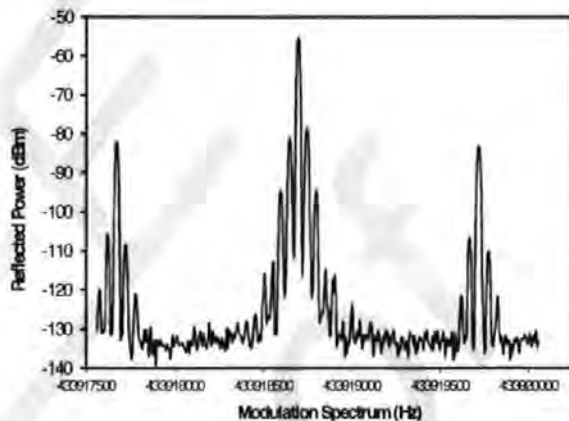

Fig. 4.   Modulation spectrum of the carrier (434 MHz) with a 1 kHz and 50 Hz external field.

0.38 mA per Oe, driven by a higher frequency ac modulation current and a lower frequency ac field for measurement. At low frequencies (<100 Hz), the phase noise $(1/f)$ of the oscillator producing the carrier limits the performance of the sensor [3], [4]. A technique to overcome this problem is to firstly modulate (chop) the low frequency ac field to be measured with a locally produced high-frequency field (1 to 5 kHz). The second local modulation field shifts the measurement field of interest to a higher frequency offset from the local modulation. This allows the measurement of the low frequency field in the spectrum of the oscillator that is not affected by the phase noise. Fig. 4 illustrates the modulation spectrum of a 1 kHz modulation field and a 50 Hz measurement field with no amplification. All measurements were taken in a nonmagnetically shielded room.

III. EXPERIMENTAL RESULTS

A. Direct Measurements

The oscillator of the lock-in amplifier was used to generate a sinusoidal signal of 0.142 V to 1 μV rms at frequencies of 1 kHz, 100 Hz, and 20 Hz. This corresponds to an ac measurement field of 0.37 to 3 μOe rms in the solenoid. For a large field of 0.37 Oe at 1 kHz, an SNR of 86 dB was obtained; this corresponds to a resolution detection of 1.84×10^{-5} Oe. Reducing

the field magnitude down to 3 μOe decreased the SNR to 18 dB, corresponding to a resolution of detection of 3.73×10^{-7} Oe. At 100 Hz, the large field performance is reduced to a resolution of 8.14×10^{-5} and the small field performance to 1.46×10^{-6} Oe; this is confirmed by the small increase in phase noise of the oscillator over that bandwidth. However, on reducing the frequency to 20 Hz a large change in performance is observed, large field resolution falls to 2.18×10^{-4} Oe and the smallest magnitude of field of measurement is 3.3×10^{-4} Oe with a SNR of 13 dB giving a resolution of 6.6×10^{-5} Oe. Under direct measurement sub-nano Tesla magnitude and resolution is only available at frequencies greater than 100 Hz, due to the phase noise of the carrier generating oscillator.

B. AC Biased Measurements

To improve the performance of the sensor for low-frequency fields, the lock-in amplifier is used to produce fields of 5 kHz and 1 kHz at a magnitude of 0.37 Oe, and an Agilent 33120 A is used to produce the measurement field at 20 and 10 Hz for comparison with the direct measurement.

Using an ac bias field of 5 kHz, a 20 Hz measurement field of magnitude 0.186 Oe had an SNR of 60 dB giving a resolution of 1.71×10^{-4} Oe, small magnitude field detection was increased to 1.27×10^{-5} Oe with a resolution of 4.78×10^{-6} Oe. Reducing the measurement field to 10 Hz reduced the large field resolution to 2.01×10^{-4} Oe and small field magnitude detection to 1.35×10^{-5} with resolution to 5.27×10^{-6} Oe. Secondly, using an ac bias field of 1 kHz, a 20 Hz measurement field of magnitude 0.186 Oe had an SNR ratio of 56 dB giving a resolution of 2.59×10^{-4} Oe, small magnitude field detection was 5.30×10^{-5} Oe with a resolution of 1.86×10^{-5} Oe. Reducing the measurement field to 10 Hz reduced the large field resolution to 2.71×10^{-4} Oe and small field magnitude detection to 4.53×10^{-5} with resolution to 9.33×10^{-6} Oe. A typical modulation spectrum of a 5 kHz ac bias with a 20 Hz modulation spectrum (magnitude 2.58×10^{-2} Oe) is illustrated in Fig. 5.

The introduction of the ac bias field for the modulation of lower frequency measurement fields has increased the performance of small field detection by an order of magnitude for both 20 and 10 Hz measurements. Detection of fields lower than 10 Hz was possible but was limited by the 3 Hz bandwidth of the spectrum analyzer.

IV. CONCLUSION

A thin-film MI sensor was produced based on the measurement of the modulation of the incident reflected power due to
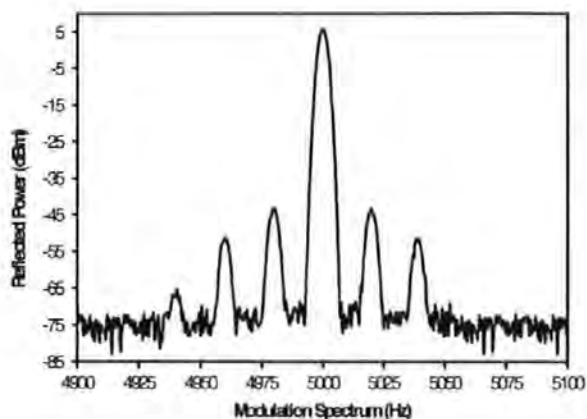

Fig. 5. Modulation spectrum of a 5 kHz ac bias signal with a 20 Hz measurement field and harmonics.

an external ac magnetic field. Direct field measurement performance at 1 kHz is a resolution of 3.73×10^{-7} Oe, ac biased performance at 5 kHz of a 20 Hz field is a resolution of 5.27×10^{-6} Oe, and at 10 Hz of 9.33×10^{-6} Oe. The achieved low-frequency magnetic field resolution is at least one order of magnitude higher than that reported for MI pulse-circuit elements. Provided that the phase noise of the oscillator at lower frequencies is suppressed and the measurements are taken in a magnetically screened room, the performance of the sensor could be further improved.

REFERENCES

[1] K. Mohri et al., "Amorphous wire and CMOS IC-based sensitive micromagnetic sensors utilizing magneto impedance (MI) and stress-impedance (SI) effects," IEEE Trans. Magn., vol. 38, no. 5, pp. 3063–3068, Sep. 2002.

[2] P. Delooze, L. V. Panina, D. J. Mapps, K. Ueno, and H. Sano, "Sub-nano tesla differential magnetic field sensor utilizing asymmetrical magneto impedance in multilayer films," IEEE Trans. Magn., vol. 40, no. 4, pp. 2664–2666, Jul. 2004.

[3] H. Mawatari, H. Kikuchi, S. Yabukami, M. Yamaguchi, and K. I. Arai, "High-frequency-carrier type thin film magnetic field sensor for AC detection," J. Magn. Soc. Jpn., vol. 27, pp. 414–418, Apr. 2003.

[4] S. Yabukami, H. Mawatari, Y. Murayama, T. Ozawa, K. Ishiyama, and K. I. Arai, "High-frequency carrier type thin-film sensor using low-noise crystal oscillator," IEEE Trans. Magn., vol. 40, no. 4, pp. 2670–2672, Jul. 2004.

[5] L. V. Panina, D. Zarechnuk, D. P. Makhnovskiy, and D. J. Mapps, "Two-dimensional analysis of magnetoimpedance in magnetic/metallic multilayers," J. Appl. Phys., vol. 89, pp. 7221–7223, 2001.

[6] T. Morikawa et al., "Enhancement of giant magneto-impedance in layered film by insulator separation," IEEE Trans. Magn., vol. 32, no. 5, pp. 4965–4967, Sep. 1996.